Word Count of thesis: .....*38525 (actual true word count, 59k including numeric expressions, equations, bibliography and code)*.....

Declaration

This work has not previously been accepted in substance for any degree and is not being concurrently submitted in candidature for any degree.

Signed ..... (candidate)
Date .....

Statement 1

This thesis is the result of my own investigations, except where otherwise stated. Where ***correction services** have been used, the extent and nature of the correction is clearly marked in a footnote(s).

Other sources are acknowledged by footnotes giving explicit references. A bibliography is appended.

Signed ..... (candidate)
Date .....

[*this refers to the extent to which the text has been corrected by others]

Statement 2

I hereby give consent for my thesis, if accepted, to be available for photocopying and for inter-library loan, and for the title and summary to be made available to outside organizations.

Signed ..... (candidate)
Date .....

NUMERICAL SIMULATION OF HYDRAULIC FRACTURES. VARIOUS LEAK-OFF REGIMES AND MULTIFRACTURING

PIOTR KUŚMIERCZYK

PhD dissertation

September 2015 – version 1.0

Piotr Kuśmierczyk: *Numerical simulation of hydraulic fractures. Various leak-off regimes and multifracturing* , PhD dissertation, © September 2015

CONTENTS

[September 10, 2015 at 14:04 – classicthesis version 1.0]

1 INTRODUCTION

To begin with, this first introductory Chapter should serve as an introduction to fracturing problems. The brief outline of the process, main challenges and ideas, as well as its real life significance are outlined in Section 1.1. Then the existing solutions for single fracture problems are reviewed in Section 1.2, and more advanced multifracturing problems follow in Section 1.4. The text presented here should be interpreted as an overview of methods and important results existing in the literature, and used to put the next Chapters in the right context. Finally in Section 1.4 should lay out what this work is trying to achieve.

[September 10, 2015 at 14:04 – classicthesis version 1.0]

1.1 INTRODUCTION TO HYDROFRACTURING

To begin, lets start with a brief explanation of what hydrofracturing is, and why it was created. Natural gas and oil have been the main fossil fuels in use for the past century. These were initially extracted from conventional deposits, underground pockets of trapped hydrocarbons. Figure 1 shows various types of oil and gas reservoirs, where an example of conventional gas and oil deposits are shown. These deposits were relatively easy to access, when a rig was drilled the pressure would often force a violate burst of stored fossil fuel. A very accurate (but over dramatic) cinematization of these early days oil industry could even be seen in a number of Hollywood productions [1]. Even in the recent history there are examples of oil and gas uncontrollably forcing its way to the surface: Kuwait 1991, Gulf of Mexico 2010 or Nefteyugansk 2015, to name just a few major ones. It could be mistaken that extraction of liquid fossil fuels is just about capturing this uncontrollable flow of a free natural resource.

Unfortunately, in reality oil and gas acquisition is a complex multiphysics problem. In an attempt to introduce the overall complexity, lets begin with pressure, porosity and permeability. The deeper underground we go the higher the formation pressure, at depths of a few kilometers the weight of the above material will add up to a multitude of the atmospheric pressure. Porosity is a measure of how much of a rock is open space, a proportion of pores to solid matter, and even at these great depths, there pores might be filled with some hydrocarbonate fluid. Finally permeability is a measure of the ease with which a fluid (oil or gas) can move through a porous rock. A conventional reservoir would therefore be made of a filled porous rock, such as sandstone, covered by some other impermeable rock layer. The drilled well would create a path that would direct a pressure driven viscous flow of oil or gas to the surface, which could be modeled by Darcy's Law [74]. These type of reservoirs are still operational, and contribute the major part of world oil and gas production, however many are depleted or running dry.

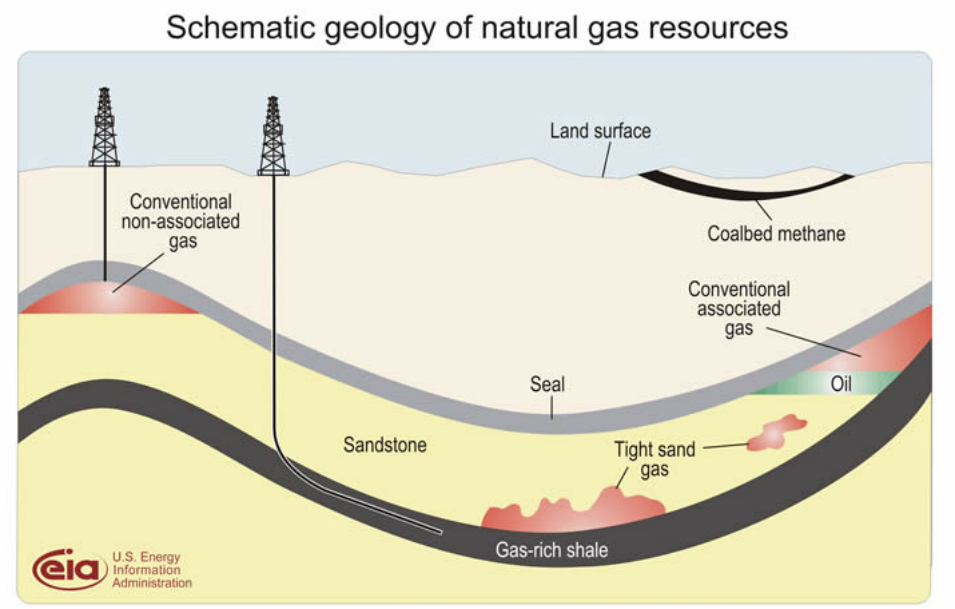

Figure 1: Schematic geology of natural gas resources (source [99])

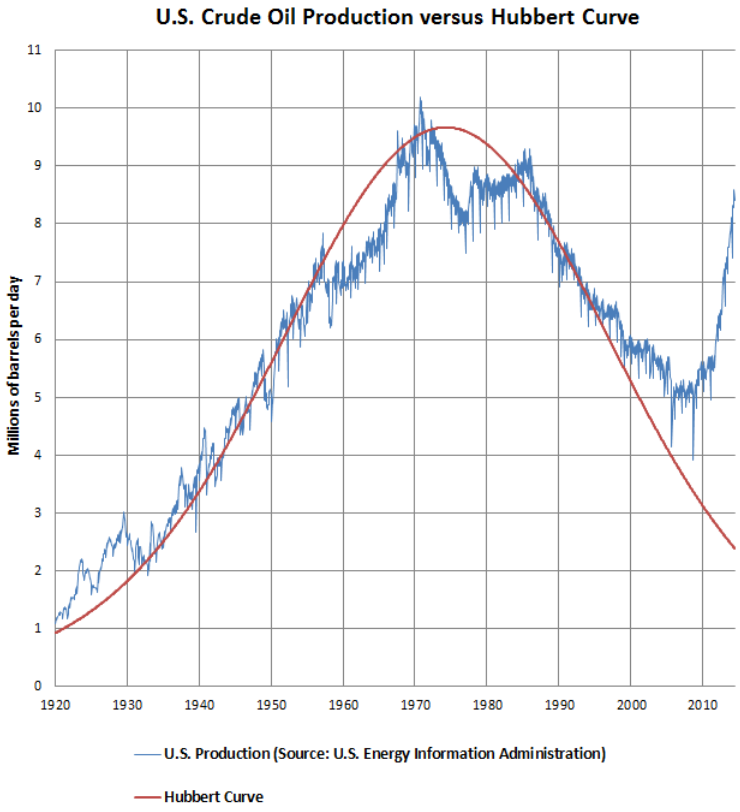

Figure 2: Oil production in USA throughout past century (source [101])

The output of conventional oil and gas fields could have been described by Hubbert Curve [34], a model that assumes a peek in production followed by a steady decline. In the US (see Figure 2) these maximum production output appeared to occur in the 1970s. Therefore as known techniques of hydrocarbons extraction were proving to be insufficient, efforts to find new ways of obtaining oil were made. The first pioneering papers on the topic of hydrofracturing [20, 30, 33, 35, 39, 70, 76, 87] were published during that peek production time, as the industry realized the need to use new, unconventional methods of hydrocarbon recovery to meet the growing supply.

In its broadest definition, *hydraulic fracturing refers to a problem of a fluid driven fracture propagating in a brittle medium*. It is a naturally occurring process observable in formation of magma dykes [81, 58, 59] or subglacial drainage of water [91]. The possible applications also go beyond petroleum industry: disposal of waste drill cuttings underground [67], geothermal reservoirs exploitation [77] or coalbeded methane extraction. It is not the only reservoir stimulation method available, some other techniques involve washing away remaining fossil fuels with specially prepared foam [69]. A typical hydrofracturing fracturing job, as shown on Figure 3, could be done in the following stages:

- Drilling of a vertical well, or preparation of an existing one if stimulating depleted reservoir. The wells walls must be prepared to withstand massive pressures without unanticipated leak to the ground waters.
- Drilling of a long horizontal section that spans throughout target resource rich rock formation, which could be some gas rich shale as shown on Figure 1. It is a fairly recent technique that requires proper horizontal drilling heads.
- Preparation of initial fractures with directed explosive charges.
- Pumping of fracturing fluid. This could go on for days, and requires substantial reserves of water, chemical additives, and powerful pumps[1].
- Mixing in proppant. This hard solid additive spreads inside fractures and prevents them from closing, after pumping is stopped. Sand, or other granulate material such as ceramic grains can be used, provided it is hard enough to hold drained fracture walls opened.
- And finally moving on to production phase, capturing hydrocarbons that flow out of the created fractures.

The process is indeed very sophisticated and expensive, but pays off. Due to its application, the Hubbert Curve has been beaten [15] and the popularized in the mass media forecast of fossil fuel depletion appears to be postponed for the next century. Indeed over the past decade natural gas production in the US alone increased by over 50% [92] due to the recent shale gas boom. This was achieved by widespread application of hydrofracturing. Shale gas deposits, as opposed to conventional sandstones, have natural gas trapped in pores of non permeable shale formations (see Figure 1 again). Hydrofracturing, pumping fluid under extremely high pressures opens new

1 Apparently to extract oil one must first burn some oil

fractures, and creates pathways for the natural gas to escape these pores in shale and flow all the way to the surface.

This work should cover only a single stage of the hydrofracturing process, the numerical modeling of fracture propagation due to fluid pumping. Although it is only a single stage of this large multiphysics problem, modeling fracture propagation is already a sufficient enough challenge on its own to produce interesting and novel research. The previous physical concepts: pressure, porosity and permeability of the reservoir will now be coupled with incompressible viscous fluid dynamics, fracture mechanics and complex non static geometries into a dynamic mathematical model. This will cover the evolution of short initial fractures located right at the drilled wellbore, to an underground system of multiple fractures, that could span over several kilometers. The engineering and geological challenges of choosing right drilling place, preparing a sufficient horizontal well at depths of up to a few kilometers, and maintaining later production will not be covered here.

The problem of proppant mixing and transportation, that follows immediately after the stage of fracture propagation will not be mentioned here. Taking proppant into consideration would introduce even more physical properties and processes, which would extend the overall complexity beyond manageable level. Even the oldest and relatively simple proppant model by Einstein [27], might not describe the actual physical process correctly [45], but would make fluid viscosity dependent on proppant concentration, thus add yet another variable. Furthermore other thermal and chemical processes would need to be taken care of as these also affect fluid viscosity, therefore it is reasonable to exclude these and simply assume uniform constant viscosity of the fracturing fluid.

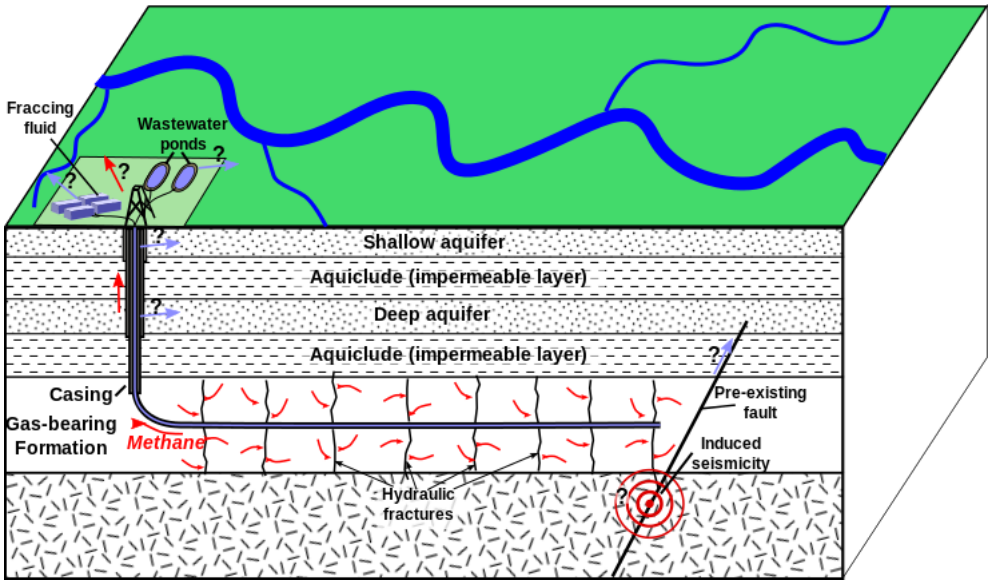

Figure 3: A schematics of hydrofracturing job (source [97])

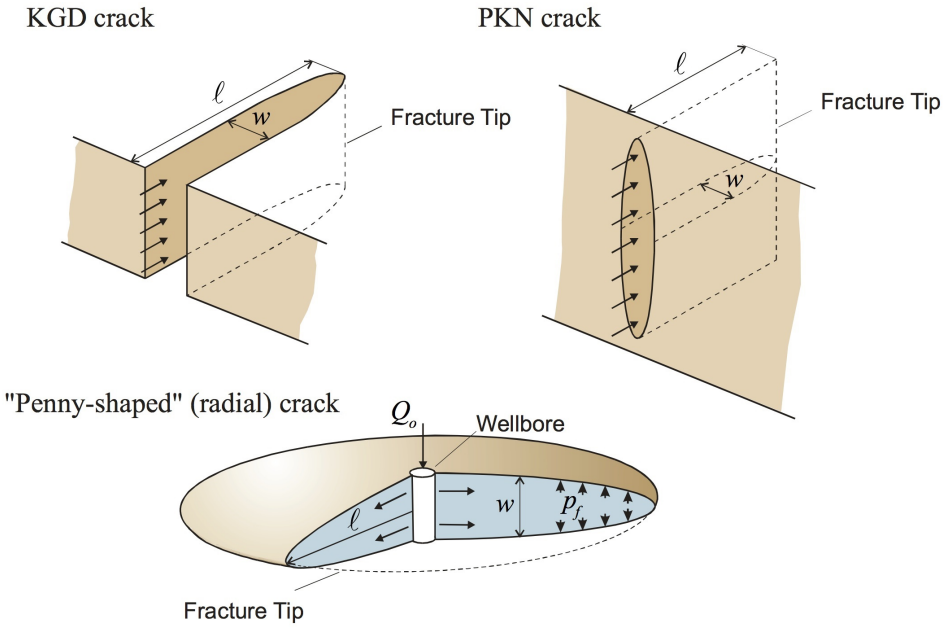

Figure 4: The three classical models of hydraulic fracture: KGD (plane strain), PKN and Radial (as originally depicted in [13])

1.2 OVERVIEW OF SINGLE FRACTURE MODELS

There are three classical single hydraulic fracture model, as shown on Figure 4:

- Radial. Describes evolution of a "Penny-shaped" crack, was introduced by Sneddon [85]. This horizontal fracture that propagates evenley in all directions.
- KGD. Developed independently by [30] and [39]. Similar to PKN, vertical fracture of fixed height that propagates horizontally in one direction.
- PKN. Based on an adaptation of Sneddon's solution [86]. Named after Pekrings, Kern [76] and [70]. A fracture of fixed height and elliptical cross section propagating horizontally, in one direction.

All these models attempt to account for coupled mechanics governing the hydrofracturing processes:

- solid mechanics equations, describing the rock deformation induced by the fluid pressure
- fracture mechanics criteria defining the conditions for fracture propagation

- equations for the fluid flow within the fracture and the *leak-off* [2] to the surrounding rock formation

The computational challenges of these models result from several factors:

- strong non-linearity introduced by the Poiseuille equation describing the fluid flow
- in the general case, a non-local relationship between the fracture opening and the net fluid pressure
- moving boundaries of the fluid front and the fracture contour
- degeneration of the governing PDE at the fracture front
- possible lag between the crack tip and the fluid front

For the purpose of this work *only PKN model will be considered.* The first numerical solution by Nordgren [70] was based on a few assumptions. The shape of crack was assumed to be elliptical as a solution for the plain strain equation. Rock toughness and fluid lag at the crack tip was ignored. Carter law [14], a simplified one dimensional formula, was chosen to govern fluid leak-off. This resulted in PKN formulation being a relatively simple model, that allowed to predict single fractures under certain conditions, however many questions about its accuracy and properties have risen over the past years.

The initial crack length was assumed to be nonzero: $l(0) = l_* > 0$. For the initial stage of crack propagation inertia term[3] should be included, thus all classical model that do not include inertia would not be credible anyway. But this simplification can be justified as hydrofracturing is a relatively slow process that might begin from already existing fractures, naturally present or artificially created with directed charges [25]. The reasoning behind zero tougheners ($K_{IC} = 0$) is that the resistance of propagation medium is so small, that the energy dissipated by the fracture extension is negligible compared to the energy dissipated[4] in the viscous fluid flow [3], moreover in [23] it has been proven that *radial hydraulic fractures in impermeable rocks generally propagate in the viscosity regime* [5] *, and that the toughness regime is relevant only in exceptional circumstances.* Furthermore PKN model assumes constant fracture height, which was changed in more recent pseudo 3D models. These P3D models take into account that a fracture can propagate through medium with multiple horizontal layers

2 Not all the pumped fluid remains inside fracture. *Leak-off* refers to the fluid volume that was lost, leaked through pores into the surrounding rock formation.

3 No mass is included, hence Newton's second law of motion is not applied.

4 Lost to overcome the viscous forces.

5 Term *viscosity regime* refers to fluid resistance to flow being the most dominant force in the process, *toughness regime* could occur with very hard rock formation and low viscosity fluid.

of different properties, so fracture height can also be made a variable in the problem [60].

Significant improvements to PKN model were introduced by Kemp in [38]. Asymptotic analysis of the solution near the crack tip for impermeable medium model was presented as well as an approximate solution for the zero leak-off case, with accuracy to the first four leading asymptotic terms. In [38], probably for the first time, the speed equation was efficiently implemented in the model. The fourth degree of the crack opening (w^4) was considered as the variable and used in numerical computations. Finally Kemp suggested to use a special tip element, compatible with the asymptotic behavior of the solution, within Finite Volume (FV) scheme.

It should be noticed that a major part of existing publications can be linked to the University of Minnesota [13], including the work done by Kovalyshen [41, 40] which introduced further improvements to PKN model. Extension of the zero leak off solution [38] to the full series representation was given by Kovalyshen in [41]. For the leak-off function defined by the Carter law the two leading terms of asymptotics were found, to take into account the multi-scale arguments suggested by [29]. However FV scheme with special tip element was again used as the computation method.

This trend to use FV based methods was questioned by Linkov in [56] where the speed equation was reintroduced. This concept was indirectly presented in [87] and utilized by [38], but later abandoned. Linkov discovered that the hydraulic fracture problem may exhibit ill posed properties, and to eliminate this problem a number of techniques were proposed.

- speed equation to trace the crack front instead of the usually applied total flux balance condition.
- the so-called ε-regularization technique which consists of imposing the computational domain boundary at a small distance behind the crack tip.
- a new boundary condition to be imposed in the regularized formulation.
- a new dependent variables: the particle velocity and the crack opening cubed, that exploits the asymptotic behavior of the solution.
- the spatial coordinates moving with the crack front and evaluation of the temporal derivative under fixed values of these coordinates.

This sparkled a series of publications redefining the conventional approach to the PKN model [54, 57, 55, 65, 106, 107, 44] where Finite Differences method were used to deal the with governing PDEs. Initially

it was shown that for the case of leak-off vanishing near the crack tip a great improvement over previous methods can be achieved by using a proper form of boundary condition and a modified dependent variable [65]. Then the paper [44], that is integrated as a part of this work, proved that also in the case of singular Carter law [14] leak off the suggestions of Linkov are very beneficial. Other works in this series [106, 107] sought to use more promising numerical algorithms, and apply this strategies to the KGD model.

The context of single hydraulic models and their development was described. This should be treated as a brief overview that outlines most important issues and challenges. For further reading there is a number of introductory publications on both theoretical and numerical aspects of single hydraulic fracture models such as: [2, 80], as well as a number of printed books [25, 93] that start at an elementary level of non hydraulic fracture mechanics and builds up to the formulation of the single fracture models.

1.3 INTO MULTIFRACTURING

So far the traditional models assumed existence of only one fracture. Although this assumption worked fine in reservoir treatment planing for decades, and were verified through some simple experiments [11, 52], these are simplified best guesses rather than actual understanding of what is exactly happening underground. The classical models could relay be trying to mimic systems of multiple fractures [83], that under favorable circumstances could form a single dominant fracture. Meanwhile a number of other technologies were developed to aid and monitor treatment process. These included microcosmic mapping, detecting minor seismic activity associated with fracture front movement [18], and surface displacement detection [24]. As more and more fracturing data became available, attempts to include these in the simulations were made, unfortunately single fracture models could not account for all the extra information.

One needs to acknowledge that the uniform medium assumption not very accurate, in fact the opposite should be expected for most reservoirs. In reality rock formations are far from being perfect fixed height two dimensional mediums, at a very least some defects should be considered such as pre-existing natural fractures, that are of great interest in shale rich formations [48]. These natural preexisting fractures should have an effect on propagating hydraulic fractures, possibly resulting in opening of new hydraulic fractures [42, 109]. Before the treatment, the naturally exiting fractures alone form a discreet fracture network [94, 108], and it should be expected that the treatment will not produce a perfect single fracture, but rather be influenced by these preexisting fractures. Furthermore to optimize the hydrofracturing process a number of fractures are initiated simultaneously [24, 10], to achieve greater coverage of the fractured reservoir. Therefore in order to make a more accurate model one needs to take account for multiple fractures, which could be done by building a more complex model based on existing theoretical single fracture solutions.

While a single simple fracture propagation is relativity easy to compute with proper usage of implicit methods and numerical formulation [2], to improve on these into a multifracture model is a much more complex challenge. The mathematical formulation must be extended to account for multiple fractures interactions, while the performance should not be drastically affected by multiplying the problem size. On top of that the effort required to handle and display data is much greater when more than one fracture is considered. These factors alone should be accounted for the variety of hydrofracturing models that appeared over the few past years, that are capable of dealing with multiple fractures.

To list a few example solutions, lets first begin with a model given by Ghani [31]. It is a relatively straightforward solution that allows for a hydraulic fracture to propagate freely in a inhomogeneous discretization of 2D plane, depicted Figure 5d. Other solutions however tend to put much stricter constrains on fracture path and shape. The influence of nearby fractures can result in shadowing[6], which is observable in some solutions, including the most recent ones by Bunger [12]. The most developed models available, are actually commercial software used by oil consulting companies, such as Schlumberger (works of Kresse and Weng [43, 42, 18]) or Itasca (Damjanac [21]), which attempt to produce comprehensive simulation of treatment process.

All these models are based on existing single fracture solutions, but none uses the formulation derived from the speed equation nor $\epsilon-$reguralization [65], or two term asymptotics boundary condition [44]. Additionally the source code of these solutions is not publicly available, nor any truly free licenses exist. These leaves an open space for new solutions which are thoroughly tested in terms of accuracy, based on some reliable formulations, and given away for free and unrestricted usage.

6 A fracture growth may be inhibited by the presence of other nearby fractures, this phenomena is sometimes called shadowing

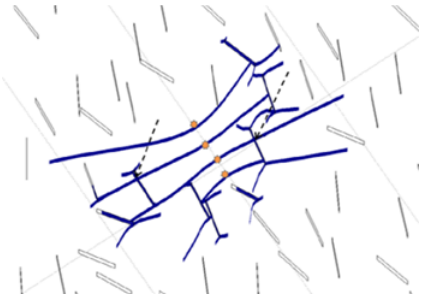

(a) Kresse [43, 42]

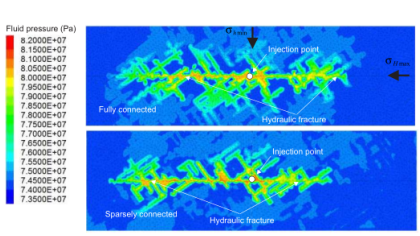

(b) Damjanac [21]

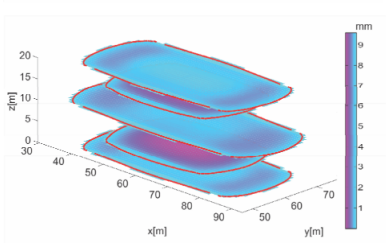

(c) Bunger [12]

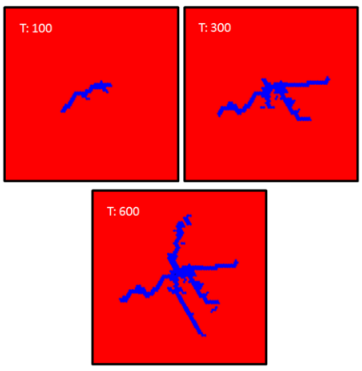

(d) Ghani [31]

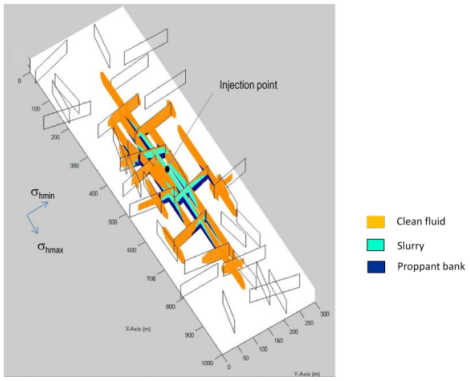

(e) Cipolla [18]

Figure 5: Samples of various multifracturing solutions as a quick comparison of the general trend. The original renderings of the solutions are shown in [43, 42, 21, 18, 31, 12].

1.4 AIM OF THIS WORK

So far this introduction Chapter has shown the economic motivation behind hydrofracturing, the techniques for single fracture modeling, and the attempts to model more complex reservoirs with multi fracture models.

Reservoir stimulation can be an expensive and uncertain task. Choosing the right place to drill, and performing the fracturing properly, is hard and without adequate planning the whole enterprise is very likely to fail. The industry attempts to eliminate this risk by developing computer models that predict what the results might be. This work will attempt to make yet another prototype model that answers a part the of more general question: will this well produce any oil or gas ?

The answer is not a simple yes or no, but rather a combination of multiple results, where each of them carries a bit of information. The single fracture models mentioned in Section 1.2 give a prediction about how deeply the rock formations can be penetrated. This does not tell much about the cost, risks or result production, but provides one piece of the puzzle.

This work should concentrate on exploring the existing models and finding their applications which can be generalized in the following tasks:

- Studying the PKN model of a single fracture, and attempting to improve its theoretical formulation.
- Implementing code that can efficiently handle single fracture problems.
- Extending the single fracture formulation into multiple fracture formulation, multifracturing, that can handle more complex problems
- Building a software solution, that utilizes all this new ideas, to model the process of hydraulic fracture growth.

All of the above have been attempted a number of times, and so multiple solutions already exist. However all the solutions are different in accuracy, performance, applicability, scalability and even availability. Thus the work here does not outright seek to produce better result, but rather to make an alternative that uses different methods and approaches to produce different, yet compatible solutions, that are freely available for others to use[7].

7 Provided as it is, with a strong and justified belief that it works, but no written guarantees, aka GPL

2 PKN MODEL REFORMULATION

The first challenge of this work will be to reformulate the original PKN model formulation. Recently the speed equation was reintroduced by Linkov [56], although it was originally used by Kemp [38]. Previously the majority of hydrofracturing problems were solved using finite volume methods, but thanks to the speed equation it is now possible to solve these using finite difference methods. This chapter will prepare the theoretical mathematical background upon which new finite difference based solutions can be later constructed. Hopes are that such a new formulation would not only be more straightforward, but would also lead to improved overall modeling of hydraulic fracture propagation.

A significant part of this Chapter was done under mentoring[1] by other research group members, as it repeats published article [44], and can be traced back to previous works [65, 54]. It would be however impossible not to include these previous findings, without loosing essential prerequisite information, needed to understand the new formulation. The Sections in this Chapter achieve the following:

- Section 2.1 is a general outline of background works on PKN model, including the previously known idea to use the crack tip asymptotics.
- Section 2.2 presents a new way to formulate the problem using fracture width w as the problem variable (29), probably the first formulation to use the asymptotic term directly. Furthermore simplification of carter law (Subsection 2.2.1) and dereviation of further asymptotic terms (Subsection 2.2.2) is presented.
- Section 2.3 reuses U variable formulation [54], bringing it in line with the other formulations of this Chapter.
- Section 2.4 introduces a new variable Ω, and a new formulation compatible with the previous w and U variable formulation.
- Section 2.5 explores the old speed equation related tip boundary condition (Subsection 2.5.1), to introduce improved two term boundary condition (Subsection 2.5.2).

1 As opposed to the next Chapters where more and more work would be done completely independently.

[September 10, 2015 at 14:04 – classicthesis version 1.0]

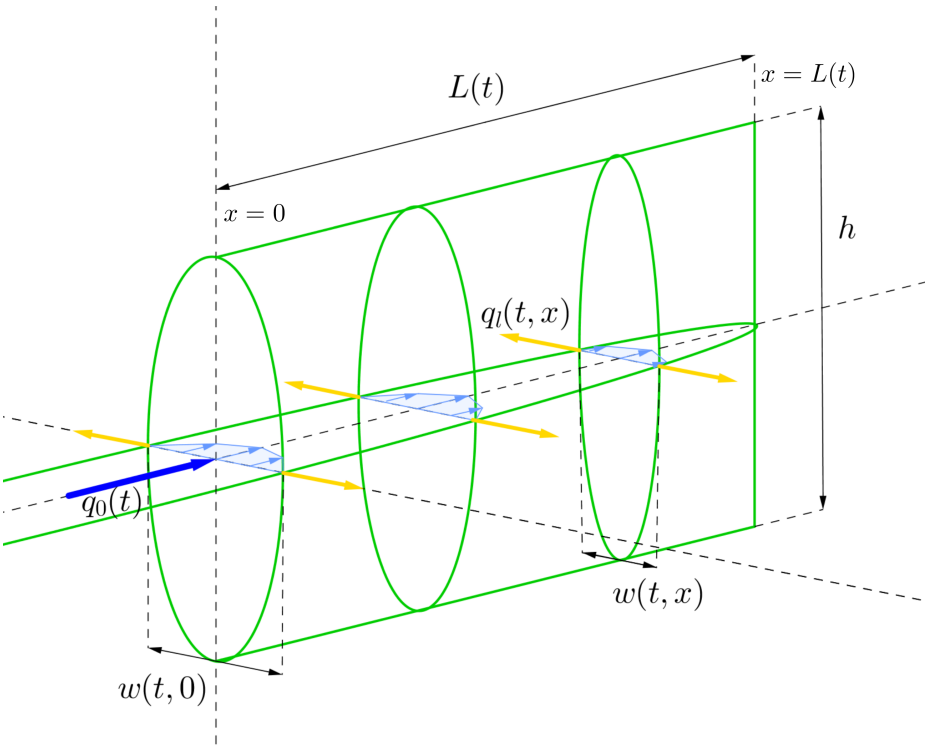

Figure 6: PKN model geometry.

2.1 PRELIMINARY RESULTS

2.1.1 *PKN Model original formulation*

PKN model is essentially a 1D model, with a single horizontal axis of propagation x as shown on Figure 6. Numerous descriptions of this model are already available [44, 65, 70, 40], thus the one provided here should outline the most important aspects in context of this Thesis. Consider a symmetrical crack of the length $2l$ situated in the plane $x \in (-l, l)$, where the length $l = l(t)$ is one of the solution components changing as a result of the fluid flow inside the crack. The initial crack length is assumed to be nonzero: $l(0) = l_* > 0$. The crack is fully filled by a Newtonian fluid pumped at some known rate $q_0(t)$ at the crack mouth $x = 0$.

The Poiseulle equation for the Newtonian fluid flow in a narrow channel is written in the form:

$$q = -\frac{1}{M} w^3 \frac{\partial p_{net}}{\partial x}, \tag{1}$$

where $q = q(t,x)$ is the fluid flow rate and $w = w(t,x)$ is the crack opening, while $p_{net} = p_{net}(t,x)$ is the net fluid pressure, that is, the difference between the fluid pressure p_{fluid} inside the fracture and

the confining stress σ_0[2]. The constant M involved in the equation is defined as $M = 12\mu$, where μ stands for the dynamic viscosity (for example see [54]).

The continuity equation, accounting for the crack expansion and the leak-off of the fluid is:

$$\frac{\partial w}{\partial t} + \frac{\partial q}{\partial x} + q_l = 0, \quad t > 0, \quad 0 < x < l(t), \tag{2}$$

where $q_l = q_l(t, x)$ is the volume rate of fluid loss to the surrounding formation in the direction perpendicular to the crack propagation direction (x-axis).

Although the definition of leak-off as *the volume of fluid lost to the surrounding medium* is well defined, the choice of function that describes this quantity is subject to further interpretation. Indeed various works choose to use different functions to represent this physical phenomena [40, 70, 42, 65], so a sensible choice is to consider multiple possible representations and be able to switch these at will. In this work the following leak-off versions are considered:

$$q_l(t, x) = q_l^{(j)}(t, x) + q_j^*(t, x), \quad j = 1, 2, 3, \tag{3}$$

where:

$$q_l^{(1)} = \frac{C_1(t)}{\sqrt{t - \tau(x)}}, \quad q_l^{(2)} = \frac{C_2(t) p_{net}}{\sqrt{t - \tau(x)}}, \quad q_l^{(3)} = C_{31}(t) p_{net} + C_{32}(t), \quad 0 < x < l(t). \tag{4}$$

Here C_1, sometimes denoted as C_L, is assumed to be a known constant defined experimentally[3] [14] . Recently C_L was estimated analytically for a poro-elastic material by Kovalyshen [40]. The pressure proportional $q_l^{(2)}$ refers to modified law given by Clifton [19], which is a more accurate version of Carter Law that takes pressure difference in to account. Function $\tau(x)$ contains information on the process history (it is explored in greater detain later in Section 3.8). It defines the time at which the fracture tip reaches the point x and can be computed as inverse of the crack length:

$$\tau(x) = l^{-1}(x), \quad x > l_*. \tag{5}$$

Other constants in (4), $C_j(t) = C_j(t, w, p)$, $(j = 2, 3)$ may depend on the solution itself but are bounded functions in time. Finally, the

2 $p_{net} = p_{fluid} - \sigma_0$, where constant background stress σ_0 is assumed to be uniform over the entire fracture length, but this assumption will challenged in the following Chapters

3 C_L is given in $\frac{m}{\sqrt{s}}$ as an experimental 1D measure of how fast fluid soaks into the rock medium.

terms q_j^*, $(j = 1,2,3)$ in (4) are assumed to be negligible in comparison with $q_l^{(j)}$ near the crack tip. Note that application of the Carter leak-off law [14] which is a simplified model of established fluid diffusion through the fracture walls, is rather questionable at the initial stage of the crack propagation [70, 49, 61].

As the first task of this work is to build formulation for a general numerical scheme, the collection of possible leak-off representations given in (4) covers the main spectrum of possible behaviors used in the hydrofracturing simulations [40].

The system of equations (1) - (2) should be supplemented by the elasticity equation. The simplest relationship used in the PKN formulation is used:

$$p_{net} = kw, \tag{6}$$

with a known proportionality coefficient $k = \frac{2}{\pi h}\frac{E}{1-\nu^2}$ found from the solution of a plane strain elasticity problem for an elliptical crack of fixed height h [70], this h is also the height of fractured rock formation . For this model to be valid it is further required that $h >> w$, [70] and generally it is expected that $L >> h >> w$ or other type of model geometry, such as radial, could be more suitable [40][4]. Constants E and ν are the Young modulus and the Poisson ratio, respectively.

On substitution of the Poiseulle equation (1) and elasticity relationship (6) into the continuity equation (2), one obtains well known lubrication (Reynolds) equation defined in a trapezoidal domain ($t > 0,\ 0 < x < l(t)$):

$$\frac{\partial w}{\partial t} - \frac{k}{M}\frac{\partial}{\partial x}\left(w^3\frac{\partial p_{net}}{\partial x}\right) + q_l = 0. \tag{7}$$

Since the system has its natural symmetry with respect to variable x and the equations are local, it is convenient to consider only half (symmetrical part) of the interval $[0, l(t)]$ instead of the full crack length $[-l(t), l(t)]$.

The initial conditions for the problem are:

$$l(0) = l_*, \quad w(0,x) = w_*(x), \quad x \in (0, l_*). \tag{8}$$

The boundary conditions consist of: known fluid injection rate at the crack mouth, q_0, zero crack opening and zero fluid flux rate at the crack tip:

$$q(t,0) = q_0(t), \quad w(t,l(t)) = 0, \quad q(t,l(t)) = 0. \tag{9}$$

4 PKN model is still technically valid if $h >> L >> w$, but sometimes a more physically plausible approach would be to consider a radial fracture that is converted to PKN type once $L > h$. Nevertheless tests shown later in Section 3.9 clearly show that $L >> h >> w$ is the dominant regime, and radial model only fits very well if the first initial fracture originated from a point source q_0.

Note that this formulation looks overdetermined[5] as the governing equation (7) is of the second order with respect to spatial variable. This issue shall be discussed later in Section 2.2.

Finally, by consecutive integration of equation (7) over time and then space, one can also derive the formula for global fluid balance:

$$\int_0^{l(t)} [w(t,x) - w_*(x)]dx - \int_0^t q_0(t)dt + \int_0^{l(t)} \int_0^t q_l(t,x)dtdx = 0, \tag{10}$$

where it is accepted that $w_*(x) = 0$ when $x > l_*$ and $l'(t) \geq 0$.

It has been shown in [54], that the crucial role in analysis of the problem is played by the particle velocity defined as:

$$V(t,x) = \frac{q}{w}, \quad t > 0, \quad 0 \leq x \leq l(t), \tag{11}$$

which indicates the average velocity of fluid flow through the cross-sections of the fracture.

Under the assumption that *the crack is fully filled by the fluid and sucking, ejection or discharge through the front can be neglected, the fluid velocity defines the crack propagation speed and the following speed equation is valid* [38, 56, 57] [6]:

$$l'(t) = V\left(t, l(t)\right), \quad t > 0. \tag{12}$$

Moreover, for physical reasons, one can deduce that the fluid velocity at the crack tip is finite:

$$0 \leq V\left(t,x\right) < \infty, \quad t > 0, \quad x \leq l(t). \tag{13}$$

Note that, allowing the crack propagation speed to be infinite, one has to simultaneously include the inertia term in the equations[7]. Thus, the estimate (13) is a direct consequence of neglecting the acceleration terms.

2.1.2 *Asymptotics behavior of the solution and its consequences*

As was mentioned in [87], the fact that both w and q are present in (11), creates serious difficulties when trying to use the fluid velocity as a variable. However, as shown in *[56, 57, 54, 55, 64]*, proper usage of fluid velocity may be extremely beneficial. First, it allows one to

5 The order system, here second (7) with respect to x, should match the number of boundary conditions, where there are three conditions in (9)

6 In fact, the speed equation in this form is valid only under the assumption of zero spurt loss at the crack tip [70]

7 There is no mass involved, hence no inertia term $F = ma = m\dot{V}$ is present to cancel out infinite velocity. In fact it is known that fracturing processes take hours and are rather slow by nature.

replace the two boundary conditions at the crack tip (9) with a single one additionally incorporating information from the speed equation (12), (13).

Indeed, the boundary conditions (9) in view of (1) and (6) lead to the estimate:

$$w(t,x) = o\left((l(t)-x)^{\frac{1}{4}}\right), \quad x \to l(t), \tag{14}$$

which does not necessarily guarantee (13). However, further analysis of the problem, for different leak-off functions (see [41, 38] and Appendix 2.2.2), shows that the particle velocity is bounded near the crack tip and the crack opening exhibits the following asymptotic behavior:

$$w(t,x) = w_0(t)\big(l(t)-x\big)^{\frac{1}{3}} + w_1(t)\big(l(t)-x\big)^{\alpha} + o\big((l(t)-x)^{\alpha}\big), \quad x \to l(t), \tag{15}$$

with some $\alpha > 1/3$. For the classical PKN model for an impermeable solid (or when leak-off vanishes near the crack tip at least as fast as the crack opening) the exponent $\alpha = 4/3$ was found in [38] and [65]. For the case of the singular Carter's type leak-off, the exponent $\alpha = 1/2$ was determined in [41].

Note that the asymptotics (15) shows that the fluid velocity is indeed bounded near the crack tip. Moreover,

$$V(t,x) = V_0(t) + V_1(t)\big(l(t)-x\big)^{\beta} + o\big((l(t)-x)^{\beta}\big), \tag{16}$$

as $x \to l(t)$, where $\beta = \alpha - 1/3$ and

$$V_0 = \frac{k}{3M} w_0^3(t), \quad V_1 = \frac{k}{M}\left(\alpha + \frac{2}{3}\right) w_0^2(t) w_1(t). \tag{17}$$

As follows from Section 2.2.2, $V(t,x)$ may not be so smooth near the crack tip as one could expect and the exponent β in (16) plays an important role here. Indeed, if $\beta \geq 1$ then $V(t,\cdot) \in C^1[0,l(t)]$ and the particle velocity function is smooth enough near the crack tip. However, this happens only in the special case of $\alpha = 4/3$ when $V_x(t,x)$ is bounded near the crack tip. In case of singular leak-off ($0 < \beta < 1$), the particle velocity near the crack tip is only of the Hölder type $V(t,\cdot) \in C^1[0,l(t)) \bigcap H^{\beta}[0,l(t)]$. In Section 2.2.2 the exact form of the asymptotic expansion (15) is presented, which yields the aforementioned smoothness deterioration of V near the crack tip for the singular leak-off models.

Note that estimate (15) (or equivalently (16)) enforces the condition (13). Thus, in view of (11), the pair of conditions $(9)_2$ and $(9)_3$

is equivalent to $(9)_2$ and (15). This discussion clearly illustrates why accounting for asymptotic behavior of the solution in form (15) is of crucial importance for effective numerical realization of any algorithm utilized in hydrofracturing [37, 29]. On the other hand, the fact that the particle velocity function is smooth enough near the crack tip has been one of the important arguments to use *the speed equation and proper variable approach* as the basis for improvement of the existing numerical algorithms [56]. It should be emphasized that behavior of $V(t, x)$ near the crack tip may have serious implications when using ε-regularization technique (Section 2.5). Therefore, one of the aims of this work is show that, regardless of possible smoothness of the particle velocity near the crack tip, the approach proposed in [56, 57, 54, 55] and [65] is still efficient[8].

8 Since now singular Carter leak-off (4) is allowed , the behavior of particle velocity at the crack tip be altered.

2.2 NORMALIZED FORMULATION

Lets normalize the problem by introducing the following dimensionless variables:

$$\tilde{x} = \frac{x}{l(t)}, \quad \tilde{t} = \frac{t}{t_n}, \quad t_n = \frac{M}{kl_*}, \quad \tilde{w}_*(\tilde{x}) = w_*\left(\frac{x}{l_*}\right),$$

$$\tilde{w}(\tilde{t},\tilde{x}) = \frac{w(t,x)}{l_*}, \quad \tilde{V}(\tilde{t},\tilde{x}) = \frac{t_n}{l_*}V(t,x), \quad L(\tilde{t}) = \frac{l(t)}{l_*},$$

$$l_*^2\tilde{q}_0(\tilde{t}) = t_n q_0(t), \quad l_*\tilde{q}_l(\tilde{t},\tilde{x}) = t_n q_l(t,x), \tag{18}$$

where $\tilde{x} \in (0,1)$ and $L(0) = 1$.

Using this notation, one defines the normalized particle velocity as:

$$\tilde{V}(\tilde{t},\tilde{x}) = -\frac{\tilde{w}^2}{L(\tilde{t})}\frac{\partial\tilde{w}}{\partial\tilde{x}}. \tag{19}$$

The conservation law (2) in the normalized domain is rewritten in the following manner:

$$\frac{\partial\tilde{w}}{\partial\tilde{t}} = \frac{1}{L(\tilde{t})}\left[\left(\tilde{x}\tilde{V}(\tilde{t},1) - \tilde{V}(\tilde{t},\tilde{x})\right)\frac{\partial\tilde{w}}{\partial\tilde{x}} - \tilde{w}\frac{\partial\tilde{V}}{\partial\tilde{x}}\right] - \tilde{q}_l(\tilde{t},\tilde{x}). \tag{20}$$

The leading terms of the asymptotic estimate of the leak-off function from (4) are now:

$$\tilde{q}_l^{(1)}(\tilde{t},\tilde{x}) = \frac{\tilde{C}_1(\tilde{t})D(\tilde{t})}{\sqrt{1-\tilde{x}}}, \quad \tilde{q}_l^{(2)}(\tilde{t},\tilde{x}) = \frac{\tilde{C}_2(\tilde{t})D(\tilde{t})}{\sqrt{1-\tilde{x}}}\tilde{w}(\tilde{t},\tilde{x}),$$

$$\tilde{q}_l^{(3)}(\tilde{t},\tilde{x}) = \tilde{C}_{31}(\tilde{t})\tilde{w}(\tilde{t},\tilde{x}) + \tilde{C}_{32}(\tilde{t}). \tag{21}$$

Here, the function

$$D(\tilde{t}) = \sqrt{\frac{L'(\tilde{t})}{L(\tilde{t})}}, \tag{22}$$

is introduced in Section 2.2.1, where the remainder between the normalized total flux and the leading term (21) has been estimated. Thus the normalized term $\tilde{q}_j^*(\tilde{t},\tilde{x})$ vanishes near the crack tip faster than the solution itself.

Finally, normalized initial conditions (8) and boundary conditions (9) are:

$$L(0) = 1, \quad \tilde{w}(0,\tilde{x}) = \tilde{w}_*(\tilde{x}), \quad x \in (0,1), \tag{23}$$

and

$$-\frac{1}{L(\tilde{t})}\tilde{w}^3\frac{\partial\tilde{w}}{\partial\tilde{x}}(\tilde{t},0) = \tilde{q}_0(\tilde{t}), \quad \tilde{w}(\tilde{t},1) = 0. \tag{24}$$

The global fluid balance (10) can be written as:

$$L(\tilde{t})\int_0^1 \tilde{w}(\tilde{t},x)dx - \int_0^1 \tilde{w}(x,0)dx - \int_0^{\tilde{t}} \tilde{q}_0(t)dt + \int_0^{\tilde{t}} L(t)\int_0^1 \tilde{q}_l(t,x)dxdt = 0. \tag{25}$$

For convenience, from now on the "$\sim$" symbol should be omitted, and all dependent and independent variables will only be consider as the respective dimensionless values.

Note that the particular representation (20) of Reynolds equation highlights an essential feature of the problem - it is singularly perturbed near the crack tip. Indeed, both coefficients in front of the spatial derivatives on the right-hand side of the equation (20) tend to zero at $x = 1$. Thus, the asymptotic behavior of the solution near the crack tip ($x \to 1$)

$$w = w_0(t)\,(1-x)^{\frac{1}{3}} + w_1(t)\,(1-x)^{\alpha} + o\left((1-x)^{\alpha}\right), \tag{26}$$

$$V = V_0(t) + V_1(t)\,(1-x)^{\alpha-\frac{1}{3}} + o\left((1-x)^{\alpha-\frac{1}{3}}\right), \tag{27}$$

represents nothing but the boundary layer[9]. Moreover, normalizing (17) one obtains:

$$V_0(t) = \frac{1}{3L(t)} w_0^3(t). \tag{28}$$

The terms w_0, w_1 and V_0, V_1 in (26) and (27) are different from those in (15) and (16). In fact, the former should be written with "$\sim$" symbol.

On substitution of (19) into (20), one eliminates the particle velocity function from Reynolds equation:

$$\frac{\partial w}{\partial t} = \frac{1}{L^2(t)}\left[\frac{1}{3}w_0^3 x\frac{\partial w}{\partial x} + 3w^2\left(\frac{\partial w}{\partial x}\right)^2 + w^3\frac{\partial^2 w}{\partial x^2}\right] - q_l. \tag{29}$$

Here w_0 is the multiplier of the first term of the asymptotic expansion (15). This form of lubrication equation exhibits the same degenerative properties as (20). Also the coefficients appearing in front of the leading terms tend to zero near the crack tip.

The speed equation (12) defining the crack propagation speed is given in the normalized variables as:

$$L'(t) = V_0(t), \quad t > 0. \tag{30}$$

Taking into account (28), the latter can be rewritten in the following form:

$$\frac{d}{dt}L^2 = \frac{2}{3}w_0^3(t), \qquad t > 0. \tag{31}$$

9 The boundary layer concept was introduced by Ludwig Prandtl at [78], refers to the fluid in immediate vicinity of a bounding surface, here the crack tip

This equation serves to determine the unknown value of the crack length $L(t)$. It has been shown in [65] that (31) offers advantages over the standard approaches based on the global fluid balance equation (25).

As a result of the foregoing transformations, one can formulate a system of PDEs describing the hydrofracturing process. The system is composed of two operators:

$$\frac{d}{dt}w = \mathcal{A}_w(w, L^2), \quad \frac{d}{dt}L^2(t) = \mathcal{B}_w(w), \tag{32}$$

where $\mathcal{A}_w$ is defined by the right-hand side of equation (29) with the boundary conditions (24), while the second operator $\mathcal{B}_w$ is given by (31). The system is equipped with the initial conditions:

$$L(0) = 1, \quad w(0, x) = w_*(x), \quad x \in (0, 1). \tag{33}$$

2.2.1 *Carter type leak off simplification*

Consider the transformation of the Carter law described by (4) when applying the normalization (18). Assume that:

$$\frac{1}{\sqrt{t - \tau(x)}} = \frac{D(t)}{\sqrt{1 - \tilde{x}}} + R(t, \tilde{x}), \tag{34}$$

where function $D(t)$ is defined in (22) while the remainder R is estimated later in (37).

To find function $D(t)$, and thus to obtain the exact form of equation (22), it is enough to compute the limit:

$$D^2(t) = \lim_{\tilde{x} \to 1} \frac{1 - \tilde{x}}{t - \tau(x)} < \infty. \tag{35}$$

This can be done by utilising L'Hopital's rule, taking into account that $x \to L(t)$ as $\tilde{x} \to 1$,

$$\tau(x) = \tau\left(L(t)\tilde{x}\right) = L^{-1}(L(t)\tilde{x}), \tag{36}$$

and that the crack length is a smooth function of time ($L \in C^1$ at least). The last fact immediately follows from the problem formulation in terms of evolution system (32).

Having the value of $D(t)$ we can estimate the remainder $R(t, \tilde{x})$ when $\tilde{x} \to 1$, or, what it is equivalent to when $x \to l(t)$ (or $t \to \tau(x)$). For this reason, we search for a parameter $\xi \neq 0$ which guarantees that the limit:

$$A = \lim_{\tilde{x} \to 1} \frac{R(t, \tilde{x})}{(1 - \tilde{x})^{\xi}} =$$

$$\lim_{\tilde{x}\to 1}\frac{1}{2\xi(1-\tilde{x})^{\xi-1}}\left(\frac{D(t)}{(1-\tilde{x})^{3/2}}-\frac{L(t)\tau'(x)}{(t-\tau(x))^{3/2}}\right)$$

does not approach to zero or infinity. Thanks to this assumption, we can write

$$\frac{1}{\sqrt{t-\tau(x)}}=\frac{D(t)}{\sqrt{1-\tilde{x}}}+A(1-\tilde{x})^{\xi}+o\left((1-\tilde{x})^{\xi}\right), \tag{37}$$

when $\tilde{x}\to 1$, or equivalently $x\to l(t)$. Taking the last estimate into account A can be expressed as:

$$A=\lim_{\tilde{x}\to 1}\frac{1}{2\xi(1-\tilde{x})^{\xi-1}}\left(\frac{D(t)}{(1-\tilde{x})^{3/2}}-\frac{L(t)\tau'(x)}{t-\tau(x)}\frac{D(t)}{\sqrt{1-\tilde{x}}}\right)-$$

$$\frac{AL(t)}{2\xi}\lim_{\tilde{x}\to 1}\frac{(1-\tilde{x})\tau'(x)}{t-\tau(x)}(1+o(1)).$$

Now, on substitution of $\tau'(x)=1/L'(t)$ at $x=L(t)$ and (35) into the limit one has obtained:

$$A=\lim_{\tilde{x}\to 1}\frac{D(t)}{2\xi(1-\tilde{x})^{\xi-1/2}}\left(\frac{1}{1-\tilde{x}}-\frac{L(t)\tau'(x)}{t-\tau(x)}\right)-\frac{AL(t)D^2(t)}{2\xi L'(t)}.$$

Applying (35) and (22) here gives:

$$\frac{1+2\xi}{2\xi}A=\lim_{\tilde{x}\to 1}\frac{D(t)}{2\xi(1-\tilde{x})^{\xi-1/2}}\left(\frac{1}{1-\tilde{x}}-\frac{L(t)\tau'(x)}{\sqrt{t-\tau(x)}}\frac{D(t)}{\sqrt{1-\tilde{x}}}\right)$$

$$-\frac{AD(t)L(t)}{2\xi}\lim_{\tilde{x}\to 1}\frac{\tau'(x)\sqrt{1-\tilde{x}}}{\sqrt{t-\tau(x)}}.$$

By repeating the same process one more time we have:

$$(2+2\xi)A=\lim_{\tilde{x}\to 1}\frac{D(t)}{(1-\tilde{x})^{\xi}}\left(\frac{1}{\sqrt{1-\tilde{x}}}-\frac{L(t)\tau'(x)D(t)}{\sqrt{t-\tau(x)}}\right).$$

Finally by eliminating the square root with use of (37) we obtain (after some algebra)

$$(3+2\xi)A=D(t)\lim_{\tilde{x}\to 1}\frac{1-L(t)\tau'(x)D^2(t)}{(1-\tilde{x})^{\xi+1/2}}.$$

This relationship gives a finite value[10] of A if $\xi=1/2$ and, as a result, we find:

$$A=\frac{1}{4}D^3(t)L^2(t)\tau''(L(t))=-\frac{1}{4}\frac{L''(t)}{L'(t)}\sqrt{\frac{L(t)}{L'(t)}}.$$

10 $(1-\tilde{x})^1$ appears in the denominator, and after some algebra cancels out with context of the numerator

2.2.2 *The details of crack tip asymptotics*

2.2.2.1 *Solving for α_0*

Lets start by writing just the first term of the asymptotic expansion (45):

$$w(t,x) = w_0(t)(1-x)^{\alpha_0} + O\left((1-x)^{\alpha_1}\right), \quad x \to 1 \tag{38}$$

By speed equation (19) it can be deduced that the first term of asymptotic expansion for speed function (46) is given by:

$$V(t,x) = \frac{\alpha_0 k}{ML(t)} w_0^3(t)(1-x)^{3\alpha_0-1} + O\left((1-x)^{\alpha_1+2\alpha_0-1}\right), \quad x \to 1 \tag{39}$$

Or alternatively it can be written as:

$$V(t,x) = v_0(t)(1-x)^{\beta_0} + O\left((1-x)^{\beta_1}\right), \quad x \to 1 \tag{40}$$

Where $v_0 = \frac{\alpha_0 k}{ML(t)} w_0^3(t)$ and $\beta_0 = 3\alpha_0 - 1$.

Interestingly $V(t,1)$ can take three values depending on the value of β_0 :

$$V(t,1) = \begin{cases} v_0(t) & if\ \beta_0 = 0 \\ 0 & if\ \beta_0 > 0 \\ \infty & if\ \beta_0 < 0 \end{cases} \tag{41}$$

It can be concluded that if $V(t,1)$ is to have a meaningful value at $x = 1$ the power a_0 must be chosen such so $\beta_0 = 3\alpha_0 - 1 = 0$ hence $\alpha_0 = \frac{1}{3}$. This will make sure the fracture tip can be propagating at finite speed, following the *zero fluid lag* assumption.

If $V(t,1)$ was zero and $\alpha_0 > \frac{1}{3}$ then there would be no fluid movement at crack tip and no crack propagation. If $\alpha_0 < \frac{1}{3}$ then $V(t,1)$ would be infinite and no straightforward physical interpretation can follow. Therefore the only sensible choice is to set $\beta_0 = 0$ so:

$$V(t,1) = v_0(t)(1-1)^0 = v_0(t) \tag{42}$$

hence it can be said that the crack tip propagates at speed $v_0(t)$. Additionally the value of $v_0(t)$ can be associated with $w_0^3(t)$ to obtain:

$$v_0(t) = \frac{k}{3ML(t)} w_0^3(t) \tag{43}$$

Now having found the value of $\alpha_0 = \frac{1}{3}$ for one term expansions (38) and (40) these can be substituted into (20) to obtain:

$$w_0'(t)(1-x)^{\frac{1}{3}} = \frac{1}{3L(t)}\left(w_0(t)v_0(t)(1-x)^{\frac{1}{3}}\right) - DC(t)(1-x)^{-\frac{1}{2}} + O\left((1-x)^{\alpha_1-1}\right) \quad x \to 1 \tag{44}$$

If next power was such so $\alpha_1 > \frac{4}{3}$, then this expansion would be complete, that is further terms would of higher order than $O(1-x)^{\frac{1}{3}}$. However introduction of leak off function might complicate this problem. The term $(1-x)^{-\frac{1}{2}}$ originating from leak off function $q_l^{(1)}$ (4) (or $(1-x)^{-\frac{1}{6}}$ if pressure proportional Carter type leak version $q_l^{(2)}$ (4)) is the most significant in (44) and must be matched with $O\left((1-x)^{\alpha_1-1}\right)$. This means more terms must be found to clear this expansion. For this first step the values $\alpha_0 = \frac{1}{3}$ and $\beta_0 = 0$ are concluded.

2.2.2.2 *Finding further asymptotic terms*

Asymptotic expansion for the crack opening and the fluid velocity near the crack tip in the normalized variables (18) can be written in the following general forms:

$$w(t,x) = \sum_{j=0}^{N} w_j(t)(1-x)^{\alpha_j} + O((1-x)^{\varrho_w}), \quad x \to 1, \tag{45}$$

and

$$V(t,x) = \sum_{j=0}^{N} V_j(t)(1-x)^{\beta_j} + O((1-x)^{\varrho_V}), \quad x \to 1, \tag{46}$$

with $\varrho_w > \alpha_n$, $\varrho_V > \beta_n$, $\alpha_0 = 1/3$, $\beta_0 = 0$ and some increasing sequences $\alpha_0, \alpha_1, \ldots, \alpha_n$ and $\beta_0, \beta_1, \ldots, \beta_n$. Note that the asymptotics are related to each other by the speed equation (19) and thus, regardless of the chosen leak-off function, we can write

$$\sum_{j=0}^{N} V_j(t)(1-x)^{\beta_j} + \ldots = \tag{47}$$

$$\frac{1}{3L(t)} \sum_{k=0}^{N} \sum_{m=0}^{N} \sum_{j=0}^{N} \alpha_j w_j(t) w_m(t) w_k(t) (1-x)^{\alpha_j+\alpha_m+\alpha_k-1}.$$

In line with the discussion after equation (16), only terms such that $\beta_j \leq 1$ are of interest, restricting to the smallest $\varrho_V > 1$, since the values of β_j are combinations of a sum of three consequent components

of the exponents α_j. However, since $\alpha_0 = 1/3_0$ is now known one can write (compare with (17)):

$$V_0(t) = \frac{1}{3L(t)} w_0^3(t), \tag{48}$$

$$V_1(t) = \frac{1}{L(t)} \left(\alpha_1 + \frac{2}{3}\right) w_0^2(t) w_1(t), \quad \beta_1 = \alpha_1 - \frac{1}{3}. \tag{49}$$

To continue the process one now needs to compute the value of the exponent α_1 as it is not clear a priori which value determining the next exponent $\beta_2 = \min\{2/3 + \alpha_2, 1/3 + 2\alpha_1\}$ is larger. To do so lets rewrite the continuity equation (20) in the form:

$$\frac{\partial w}{\partial t} + \frac{V_0(t)}{L(t)}(1-x)\frac{\partial w}{\partial x} = \frac{1}{L(t)} \frac{\partial \big(w(V_0 - V)\big)}{\partial x} - q_l(t,x). \tag{50}$$

Here, the terms on the left-hand side of the equation are always bounded near the crack tip, while those on the right-hand side can behave differently depending on the chosen leak-off function (4). Consider the following three cases of q_l behavior.

1. Assume first that

$$q_l(t,x) = o\big(w(t,x)\big), \quad x \to 1.$$

This case includes the impermeable rock formation. Analyzing the leading order terms in the equation (50), it is clear[11] that $w(V_0 - V) = O((1-x)^{4/3})$, as $x \to 1$. This, in turn, is only possible for $\beta_1 = 1$ and, therefore, $\alpha_1 = 4/3$. Finally, comparing the left-hand side and the right-hand side of the equation it is obtained:

$$w_0'(t) = \frac{w_0(t)}{3L(t)}\big(V_0(t) + 4V_1(t)\big), \quad V_1(t) = \frac{2}{L(t)} w_0^2(t) w_1(t). \tag{51}$$

This case has been considered in [54] and [65].

2. Now assume that the leak-off function is estimated by the solution as $O\big(w(t,x)\big)$, or equivalently:

$$q_l(t,x) \sim \Upsilon(t) w_0(t) (1-x)^{1/3}, \quad x \to 1,$$

11 Following (26) the right hand side of (50) is $O((1-x)^{1/3})$, on the left side $q_l(t,x) = 0$ for impermeable rock, so $\frac{\partial \left(w(V_0-V)\right)}{\partial x} = O((1-x)^{1/3}) \Rightarrow w(V_0 - V) = O((1-x)^{4/3})$

then the previous results are related to the values of α_1 and β_1 and, therefore, the equation of $V_1(t)$ (51) remains unchanged, while the first one becomes:

$$w_0'(t) = \frac{1}{3L(t)} w_0(t)\big(V_0(t) + 4V_1(t)\big) - \Upsilon(t) w_0(t). \tag{52}$$

This case corresponds to $q_l^{(3)}$ 21 when $C_{32} = 0$ and $\Upsilon(t) = kC_{31}(t)$.

3. General form of leak-off function:

$$q_l(t,x) = \Phi(t)(1-x)^\theta + o((1-x)^{1/3}), \quad x \to 1,$$

where $-1/2 \le \theta < 1/3$. Here, one can conclude that $w(V_0 - V) = O((1-x)^{1+\theta})$, as $x \to 1$ or equivalently, $\beta_1 = \theta + 2/3$, and $\alpha_1 = 1 + \theta$. Moreover, in this case:

$$(1+\theta) w_0 V_1 = L(t)\Phi(t), \quad V_1(t) = \frac{1}{L(t)} \left(\theta + \frac{4}{3}\right) w_0^2(t) w_1(t), \tag{53}$$

and, thus

$$w_1(t) = \frac{3L^2(t)\Phi(t)}{(4+3\theta)(1+\theta) w_0^3(t)}. \tag{54}$$

Note that the particle velocity function is not smooth in this case near the crack tip, its derivative is unbounded and exhibits the following behavior:

$$\frac{\partial V}{\partial x} = O\big((1-x)^{\theta - 1/3}\big), \quad x \to 1.$$

To formulate an expression similar to (51) or (52), one needs to continue asymptotic analysis of the equation (50) incorporating the available information. Although the analysis can be done for the general case, only three variants should be considered (compare with (4)), respectively: $\theta = 0$, $\theta = 1/3 - 1/2 = -1/6$ and $\theta = -1/2$.

When $\theta = 0$, $\alpha_1 = 1$ and $\beta_1 = 2/3$, returning to the equation (47), one concludes that $\beta_2 > 1$ and, therefore,

$$w_0'(t) = \frac{1}{3L(t)} w_0(t) V_0(t). \tag{55}$$

This case corresponds to $q_l^{(3)}$ (21) when $\Phi(t) = C_3^{(2)}(t) w_0(t)$ and $C_3^{(1)} = 0$.

If $\theta = -1/6$, then $\alpha_1 = 5/6$ and $\beta_1 = 1/2$. In this case the function $\Phi(t)$ can be written as $\Phi(t) = C_2 D(t) w_0(t)$ (compare to $q_l^{(2)}$ (21)) and again equation (47) gives $\beta_2 > 1$, while equation (50) leads to

$$w_0'(t) = \frac{1}{3L(t)} \big(w_0(t) V_0(t) + 4 w_1(t) V_1(t)\big). \tag{56}$$

Summarizing, in both mentioned above cases, there exists a single term in asymptotics of the particle velocity which has singular derivative near the crack tip. Moreover, those terms (w_1 and V_1, respectively) are fully defined by the leak-off function $\Phi(t)$ and the coefficient w_0 in front of the leading term for the crack opening in (54) and (53).

The situation changes dramatically when $\theta = -1/2$ (Carter law). We now have $\alpha_1 = 1/2$ and $\beta_1 = 1/6$ and $\Phi(t) = C_1 D(t)$. In this case, however, $\beta_2 < 1$ and the asymptotic analysis must be continued further to evaluate all terms of the particle velocity which exhibit non-smooth behavior near the crack tip. The full details of this derivation should be omitted there, instead final results are presented in a compact form. The first six exponents in the asymptotic expansions (45) and (46), that introduce the singularity of w_x, are:

$$\alpha_j = \frac{1}{2} + \frac{j}{6}, \quad \beta_j = \frac{j}{6}, \quad j = 1, 2, \dots, 6.$$

$$w_j(t) = \kappa_j \frac{\Phi^j(t) L^{2j}(t)}{w_0^{4j-1}(t)}, \quad V_j(t) = \psi_j \frac{\Phi^j(t) L^{2j-1}(t)}{w_0^{4j-3}(t)},$$

where $j = 1, 2, \dots, 5$ and

$$\kappa_1 = \tfrac{12}{7}, \quad \psi_1 = 2, \quad \kappa_2 = -\tfrac{270}{49}, \quad \psi_2 = -\tfrac{24}{7},$$

$$\kappa_3 = \tfrac{9768}{343}, \ \psi_3 = \tfrac{828}{49}, \ \kappa_4 = -\tfrac{2097252}{12005}, \ \psi_4 = -\tfrac{5136}{49},$$

$$\kappa_5 = \tfrac{1081254096}{924385}, \quad \psi_5 = \tfrac{1234512}{1715}.$$

2.3 REFORMULATION OF THE PROBLEM IN PROPER DEPENDENT VARIABLES. FIRST APPROACH

In [54] and later in [65] it has been shown that the dependent variable

$$U(t,x) = w^3(t,x) \tag{57}$$

is more favorable for the solution of the system (32)(33) than the crack opening itself. This idea is based on the fact that, according to the asymptotics of the solution near the crack tip, the dependent variable U is much smoother than w. In the case of an impermeable solid, the solution U is analytic in the closed interval $[0,1]$ (see [54]). However, the type of leak-off function is of significant importance here. Thus, adopting asymptotic representation (26), one can see that for $x \to 1$

$$U = U_0(t)(1-x) + U_1(t)(1-x)^{\frac{2}{3}+\alpha} + o((1-x)^{\frac{1}{3}+2\alpha}), \tag{58}$$

where the coefficients $U_0(t)$ and $U_1(t)$ are directly related to those appearing in the crack opening formulation:

$$U_0(t) = w_0^3(t), \quad U_1(t) = w_0^2(t)w_1(t). \tag{59}$$

Depending on the type of leak-off described in (4), the exponent in the second asymptotic term $\frac{2}{3}+\alpha$ may take value of $3/2$, $11/6$ or 2. Thus in the first two cases, the transformation (57) no longer results in polynomial representations of asymptotic expansion for U. For this reason, the advantage of the approach using variable U in more general cases, when the leak-off is singular near the crack tip, should still be confirmed. On the other hand, at least two factors work in favor of this formulation. First, the spatial derivative of U is not singular and, second, the particle velocity is given by a linear relationship:

$$V(t,x) = -\frac{1}{3L(t)}\frac{\partial U}{\partial x}. \tag{60}$$

The governing equation (20) in terms of the new variable can be written in the normalized domain $x \in (0,1)$ as:

$$\frac{\partial U}{\partial t} = \frac{1}{L(t)}\left[(xV(t,1) - V(t,x))\frac{\partial U}{\partial x} - 3U\frac{\partial V}{\partial x}\right] - 3U^{\frac{2}{3}}q_l, \tag{61}$$

Similarly to (29) the particle velocity function may be eliminated from the lubrication equation:

$$\frac{\partial U}{\partial t} = \frac{1}{3L^2(t)}\left[xU_0\frac{\partial U}{\partial x} + \left(\frac{\partial U}{\partial x}\right)^2 + 3U\frac{\partial^2 U}{\partial x^2}\right] - 3U^{\frac{2}{3}}q_l. \tag{62}$$

Note that equations (61)-(62) are of a very similar structure to those evaluated for the crack opening w. They exhibit the same degenerative nature near the crack tip.

Finally, boundary conditions (24) transform to:

$$-\frac{\sqrt[3]{U(t,0)}}{3L(t)}\frac{\partial}{\partial x}U(t,0) = q_0(t), \quad U(t,1) = 0, \tag{63}$$

while the speed equation (31) takes the following form:

$$\frac{d}{dt}L^2 = \frac{2}{3}U_0(t), \qquad t > 0. \tag{64}$$

The system of PDEs equivalent to (32) is now defined as:

$$\frac{d}{dt}U = \mathcal{A}_U(U, L^2), \quad \frac{d}{dt}L^2(t) = \mathcal{B}_U(U). \tag{65}$$

The operator $\mathcal{A}_U$ is described by (62) with boundary conditions (63), while the second operator $\mathcal{B}_U$ is given by (64). Finally, the initial conditions are similar to those in the previous formulation (23):

$$L(0) = 1, \quad U(0,x) = w_*^3(x), \quad x \in (0,1). \tag{66}$$

2.4 REFORMULATION OF THE PROBLEM IN PROPER DEPENDENT VARIABLES. SECOND APPROACH

The aforementioned formulation of the problem in terms of the dependent variable U has one considerable drawback. It is well known that for different elasticity models and different hydrofracturing regimes one has various asymptotic behaviors of the solution near the crack tip [3]. For example, for exact equations of elasticity theory and the zero toughness condition ($K_{IC} = 0$), the exponent of the leading term of w varies from $\frac{2}{3}$, for the Newtonian fluid, to 1, for the ideally plastic fluid. Thus, the same reformulation to the type of the proper variable might be inconvenient, or even impossible.

For this reasons, another dependent variable will be introduced. Although it does not transform the asymptotic behavior of the solution in such a smooth manner as it has been done previously when adopting U, this variable has its own advantages. Namely, lets consider a new dependent variable Ω defined as follows:

$$\Omega(t,x) = \int_x^1 w(t,\xi)d\xi. \tag{67}$$

This variable is not directly related to any particular asymptotic representation of $w(x,t)$, however it assumes that $w \to 0$ for $x \to 1$. As a result the form of governing equations for Ω remain the same regardless of $w(x,t)$ asymptotics, i.e. this formulation has a general (universal) character. Note, that in case of U the optimal way of transformation for the lubrication equation essentially depends on the exact form of asymptotic expansion (the leading term) for w.
Another advantage of Ω comes from the fact that it has clear physical and technological interpretation. Namely, it reflects the crack volume measured from the crack tip.

Asymptotics of the function Ω near the crack tip takes the following form:

$$\begin{aligned}\Omega(t,x) = \Omega_0(t)(1-x)^{\frac{4}{3}} + \Omega_1(t)(1-x)^{\alpha+1} \\ +o((1-x)^{\alpha+1}), \quad x \to 1,\end{aligned} \tag{68}$$

where the coefficients $\Omega_0(t)$ and $\Omega_1(t)$ are related to those in (26):

$$\Omega_0(t) = \frac{3}{4}w_0(t), \quad \Omega_1(t) = \frac{1}{\alpha+1}w_1(t). \tag{69}$$

Thus, similarly to U, the new variable is smoother than the crack opening, w, and the first singular derivative of Ω is that of the second order.

By spatial integration of (20) from x to 1 and substitution of (67) one obtains:

$$\frac{\partial \Omega}{\partial t} = -\frac{1}{L(t)}\left[\left(V(t,x) - xV(t,1)\right)\frac{\partial \Omega}{\partial x} + V(t,1)\Omega\right] - Q_l, \tag{70}$$

where the monotonicity of $L'(t) > 0$ has been taken into account and

$$Q_l(t,x) = \int_x^1 q_l(t,\xi)d\xi.$$

Here, the particle velocity (19) is computed in the manner:

$$V(t,x) = \frac{1}{3L(t)}\frac{\partial}{\partial x}\left(\frac{\partial \Omega}{\partial x}\right)^3 \quad . \tag{71}$$

By eliminating $V(x,t)$ from the equation (70) we derive a new formula for the lubrication equation:

$$\frac{\partial \Omega}{\partial t} = -\frac{1}{L^2(t)}\left[\left(\frac{\partial \Omega}{\partial x}\right)^3\frac{\partial^2 \Omega}{\partial x^2} + \frac{64}{81}\Omega_0^3\left(\Omega - x\frac{\partial \Omega}{\partial x}\right)\right] - Q_l. \tag{72}$$

The boundary conditions (24) are expressed in the following way:

$$-\frac{1}{L(t)}\left(\frac{\partial \Omega}{\partial x}\right)^3\frac{\partial^2 \Omega}{\partial x^2}(t,0) = q_0, \quad \frac{\partial \Omega}{\partial x}(t,1) = 0. \tag{73}$$

Interestingly, the first boundary condition, directly substituted into the lubrication equation (70) can be equivalently rewritten in the form

$$\frac{\partial \Omega}{\partial t}(t,0) = -\frac{64}{81^2 L(t)}\Omega(t,0)\Omega_0^3(t) + \frac{q_0(t)}{L(t)} - Q_l(t,0), \tag{74}$$

This condition, in turn, represents nothing but the local (in time) flux balance condition. To verify this, it is enough to apply the time derivative to the equation (25). Furthermore it appears much easier for implementation into a numerical procedure than (73), but may lead to some increase of the problem stiffness, as shown later in Section 3.1 .

It is easy to check, by using the governing equation (70) and limiting values of all its terms for $x \to 1$, that a weaker boundary condition

$$\Omega(t,1) = 0 \tag{75}$$

is equivalent to the original one (73). Finally, the speed equation (31) in the Ω formulation assumes the following form:

$$\frac{d}{dt}L^2(t) = \frac{128}{81}\Omega_0^3(t). \tag{76}$$

This way another system of PDEs is obtained, that is composed of two operator relations:

$$\frac{d}{dt}\Omega = \mathcal{A}_\Omega(\Omega, L^2), \quad \frac{d}{dt}L^2(t) = \mathcal{B}_\Omega(\Omega), \tag{77}$$

where, as previously, $\mathcal{A}_\Omega$ is defined by (29) with boundary conditions (73) or (74) and (75). The second operator, $\mathcal{B}_\Omega$, is given by equation (76). Here the initial conditions are obtained from (23):

$$L(0) = 1, \quad \Omega(0, x) = \Omega_*(x) \equiv \int_x^1 w_*(\xi)d\xi. \tag{78}$$

2.5 ε-REGULARIZATION AND THE RESPECTIVE TIP BOUNDARY CONDITIONS

2.5.1 *One term condition*

Consider a spatial domain of the problem reduced in accordance with the ε-regularization technique to the interval $x \in [0, 1-\varepsilon]$, where ε is a small parameter. This so-called ε-regularization technique, was originally introduced in [56] for the system of spatial coordinates moving with the fracture front, and in [65] the authors efficiently adopted this approach for the normalized coordinate system. As the result a mesh, $\{x_i\}_{i=1}^{N}$, will be composed of N points with $x_1 = 0$ and the last point $x_N = 1-\varepsilon$, separated from the tip by ε. Example of such meshes are shown in Appendix A.1.

With ε-regularization the Dirichlet boundary condition (63) is replaced with an approximate one:

$$U(t, 1-\varepsilon) = 3\varepsilon L(t) V(t, 1), \tag{79}$$

The value of the crack propagation speed $V(t, 1)$ (and simultaneously the particle velocity at a fracture tip) was suggested to be computed from the speed equation (64) in its approximated form:

$$V(t, 1) = -\frac{1}{3L(t)} \frac{\partial U}{\partial x}(t, 1-\varepsilon). \tag{80}$$

The pair of conditions (79) and (80) has shown an excellent performance in terms of solution accuracy and, as has been proven in [65], reduced the stiffness of dynamic system in case of leak-off function vanishing near the crack tip. One can check that for such a leak-off model numerical error introduced by using the approximate conditions, instead of the exact ones, is of the order $O(\varepsilon^2)$, and the other improvements following usage of this method were shown in [54, 65].

The above conditions can be written in an equivalent form. Indeed, one can merge (79) and (80) into a single condition of the third type:

$$U(t, 1-\varepsilon) + \varepsilon \frac{\partial U}{\partial x}(t, 1-\varepsilon) = 0. \tag{81}$$

Interestingly, the latter condition is nothing but the consequence of a direct utilization of the information about the leading term of asymptotics of the solution near the crack tip (compare with (58)).

Analogously, one can define the respective pairs of boundary conditions in the regularized formulations. Considering the dependent variable w one should take (31) together with the condition

$$w(t, 1-\varepsilon) + 3\varepsilon \frac{\partial w}{\partial x}(t, 1-\varepsilon) = 0, \tag{82}$$

while analyzing the system based on the dependent variable Ω, the speed equation (76) should be accompanied by

$$4\Omega(t, 1-\varepsilon) + 3\varepsilon\frac{\partial\Omega}{\partial x}(t, 1-\varepsilon) = 0. \tag{83}$$

2.5.2 *General two term condition*

For each of the problem formulations a boundary condition for the crack tip at $x = 1-\varepsilon$ must be specified. These as follows from (81), (82) and (83) are in fact very similar and can be generalized, for the dependent variables $w(t,x)$, $U(t,x)$ and $\Omega(t,x)$ a common notation $f(t,x)$ with convention $f_k = f(t,x_k)$ should now follow.

So far the presented regularized boundary conditions following the proposition of Linkov [56] are based on the leading term of the asymptotic expansion. But as shown in Section 2.2.2 the Carter leak off (4) introduced terms will introduce large disturbance to the problem, which will dramatically affect the accuracy (as proven later in Section 3.4). To properly account for the second term, that under likely circumstances might be as significant as the first term, a modification of this approach which consists of two asymptotic terms will be proposed.

According to (26), (58) and (68), the following asymptotics approximation is acceptable in the proximity of the crack tip ($x \in [x_{N-2}, 1]$):

$$f(t,x) = e_1^{(f)}(t)(1-x)^{\alpha_1} + e_2^{(f)}(t)(1-x)^{\alpha_2}. \tag{84}$$

The values of α_1 and α_2 are known and depend on the chosen variable and the behavior of the leak-off function. Assuming that the last two points of the discrete solution (x_{N-1}, f_{N-1}) and (x_N, f_N) lie on the solution graph $(x, f(t,x))$, one can obtain $e_1^{(f)}$ and $e_2^{(f)}$ by solving the flowing system of two equations:

$$\begin{aligned} e_1^{(f)}(t)(1-x_{N-1})^{\alpha_1} + e_2^{(f)}(t)(1-x_{N-1})^{\alpha_2} &= f_{N-1} \\ e_1^{(f)}(t)(1-x_N)^{\alpha_1} + e_2^{(f)}(t)(1-x_N)^{\alpha_2} &= f_N \end{aligned} \tag{85}$$

The equations (85) when solved yield $f(t,x)$ and consequently allow to obtain boundary condition at $x = 1-\varepsilon$. Function $f(t,x)$ can be used to extrapolate extra point x_{N+1}, and then use that point in some three point discretization shame which would essentially lead to:

$$f_{N+1} + b_N^{(f)} f_N + b_{N-1}^{(f)} f_{N-1} = 0 \tag{86}$$

Where $b_j^{(f)} = b_j^{(f)}(x_{N-1}, x_N, x_{N+1})$. (one can always use one less ODE, to match with indexing scheme and system size presented in

[44, 65]). However it is also possible to use $f(t,x)$ to obtain $\frac{\partial f}{\partial x}$ and $\frac{\partial^2 f}{\partial x^2}$ directly, and this approach will be preferred later[12].

The presented approach is a direct generalization of that proposed in [56]. Indeed, if one takes $e_2 = 0$ in the representation (84) then the pair of the equations (81) and (80) follows immediately. If $\alpha_2^{(f)} - \alpha_1^{(f)} = 1$, which means that the leak-off function q_l is bounded near the crack tip, the second asymptotic term provides a small correction. However, in the case of the Carter law, when $\alpha_2^{(f)} - \alpha_1^{(f)} = 1/6$, it brings an important contribution.

The obtained coefficient $e_1^{(f)}$ from (84) is substituted into corresponding speed equation (31), (64) or (76) to give the ordinary differential equations for the crack length:

$$\frac{d}{dt}L^2 = \frac{2}{3}\left(e_1^{(w)}\right)^3, \quad \frac{d}{dt}L^2 = \frac{2}{3}e_1^{(U)},$$
$$\frac{d}{dt}L^2(t) = \frac{128}{81}\left(e_1^{(\Omega)}\right)^3. \tag{87}$$

Note that the right-hand sides of the equations define the boundary operators $\mathcal{B}_w$, $\mathcal{B}_U$ and $\mathcal{B}_\Omega$ from (32), (65) or (77), respectively.

One can observe that for all variable formulations the generalized form of tip boundary condition is very similar.

In the case of the dependent variable U, apart from the representations (84) of the boundary condition near the crack tip in the linear form:

$$\begin{aligned} e_1^{(U)}(t)(1-x_{N-1})^{\alpha_1^{(U)}} + e_2^{(U)}(t)(1-x_{N-1})^{\alpha_2^{(U)}} &= U_{N-1} \\ e_1^{(U)}(t)(1-x_N)^{\alpha_1^{(U)}} + e_2^{(U)}(t)(1-x_{N-})^{\alpha_1^{(U)}} &= U_N \end{aligned} \tag{88}$$

one can use a nonlinear one, adopting the relationship between this dependent variable and the crack opening w:

$$\begin{aligned} e_1^{(w)}(t)(1-x_{N-1})^{\alpha_1^{(w)}} + e_2^{(w)}(t)(1-x_{N-1})^{\alpha_2^{(w)}} &= \sqrt[3]{U_{N-1}} \\ e_1^{(w)}(t)(1-x_N)^{\alpha_1^{(w)}} + e_2^{(w)}(t)(1-x_N)^{\alpha_1^{(w)}} &= \sqrt[3]{U_N} \end{aligned} \tag{89}$$

Similar exchange of underlying $e_1^{(f)}$ and $e_2^{(f)}$ could be also done with Ω variable, but it would be less intuitive to write ($\frac{\partial}{\partial x}$ vs $\sqrt[3]{}$) .Note that the two terms representation (88) of the function U is less informative than the same representation for the functions w (or Ω). The Carter type term is cleared by the second term of expansion $\alpha_2^{(w)} - 1 = -\frac{1}{2}$

12 An extensive practical study of many crack tip boundary condition variations was made to arrive at this conclusion.

(2.2.2), while in case of U the two term expansion of w, (26) after cubing produces:

$$U(t,x) = w_0^3(1-x) + w_0^2 w_1 (1-x)^{\frac{2}{3}+\alpha_2^{(w)}} + w_0 w_1^2 (1-x)^{\frac{1}{3}+2\alpha_2^{(w)}} + w_1^3 (1-x)^{3\alpha_2^{(w)}} + o\left((1-x)^{min(\frac{2}{3}+\alpha_3^{(w)}, \frac{1}{3}+2\alpha_2^{(w)})}\right) \tag{90}$$

Thus taking two terms of U only accounts for w_0^3 and $w_0^2 w_1$, while two components $w_0^2 w_1$and w_1^3 are lost.

Therefore, using the modified condition (88), one can expect a better solver performance.

3

PKN MODEL NUMERICAL WORK

Having reformulated the classical PKN model in previous Chapter 2 it is time to implement and test the new ideas. Therefore this Chapter focuses on numerical programing, testing, and comparing results.

- Section 3.1 analyzes problem stiffens, and proves that the PKN problem formulation is indeed stiff.
- Section 3.2 outlines the numerical procedure prepared for stiff ODE solvers.
- Section 3.3 shows results of hundreds of tests with various initial conditions, the reliability is tested here.
- Section 3.4 shows that the developed code produces accurate results when tested against numerical benchmarks. The accuracy gains are mostly attributed to the better, new, two term asymptotic boundary condition at the crack tip.
- Section 3.5 is a comparison with results by other authors obtained by other means. Here it is implied that the accuracy of this work is greater than these of other authors.
- Section 3.6 explains some implementation details which allowed to gain further accuracy and performance gains.
- Section 3.8 presents algorithms for dealing with closing fracture and leak off phenomena.
- Section3.9 shows outcomes of using real life inputs in a single fracture simulation.

The Appendix A.4 includes some sample source code, a bare minimum required to reproduce single fracture simulations.

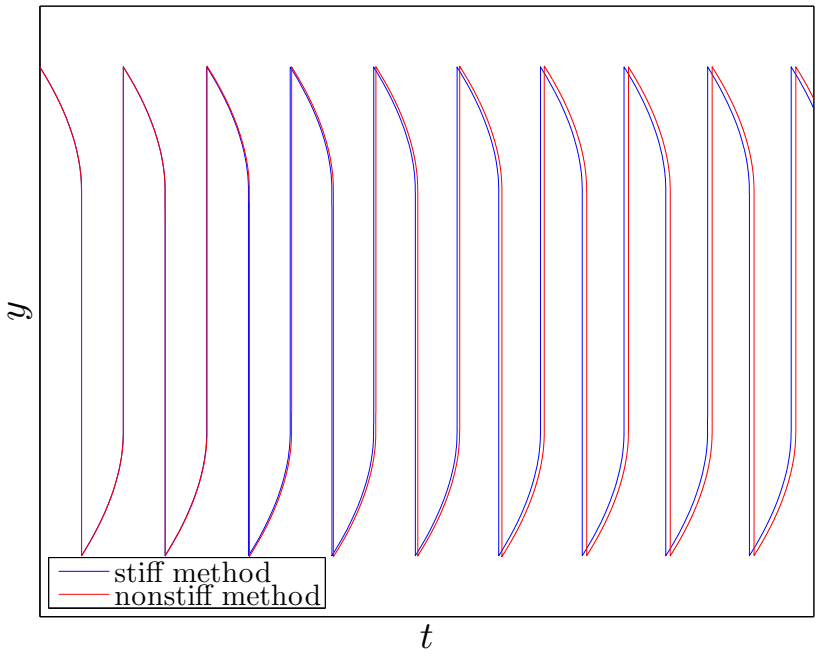

Figure 7: Two solutions to a van der Pol Equation problem [104]. Nonstiff method results in oscillations that fall out of sync, compared to the more accurate stiff method.

3.1 STIFFNESS ANALYSIS

Before attempting to solve the single fracture formulation presented in previous Chapter 2, lets perform a stiffness analysis of the problem. Stiffens is a phenomena that is rather hard to define. Certain models may result in systems of equations that are not numerical stable[1] when attempted to solve with nonstiff numerical methods [102]. A good example of such systems can be based on the van der Pol Equations [104]. Solutions to these are osculations, with very sharp turning points. When a nonstiff method is used it is much harder for the method to correctly detect turning points and properly adjust step size. As a result the method fails to detect these important turning points at the right times, which results in misrepresented oscillation period after a few cycles, as shown on Figure 7. Note that this mistimed oscillation means that if someone was to measure a value at some specific time the answer could be off by multiple orders of magnitude. Nevertheless the nonstiff method can be used to find some (inaccurate) solution to a stiff problem, thous a more convenient casual definition of stiffens would be how hard a given problem is to solve using numerically in terms solution accuracy, stability and time

1 Unsolvable due to technical reasons.

requirement[2]. Similarly in the case of hydrofracturing problems there is a strong coupling between the tip region, and the rest of the solution which means that a small misrepresentation of this tip region behavior will have significant effect on the whole solution.

The stiffens of this problem problem will be measured as condition ratio κ_A [4]. This ratio in fact shows the disproportion between the effect on change in value of all solution components. High κ_A indicates that some solution components has much grater effect on the overall solution than the others. The Reynolds equations written in different dependent variables (32), (65) or (77) can be treated by spatial derivatives (using three point central finite difference Appendix A.4.3) as a system of equation . This system can be written in the following form:

$$\mathbf{F}' = \mathbf{A}^{(f)}\mathbf{F} + \mathbf{G}^{(f)}, \tag{91}$$

where $\mathbf{F} = \mathbf{F}(t)$ is a vector of unknown solution:

$$\mathbf{F} = [f(t, x_1), f(t, x_2), \ldots, f(t, x_N), L^2(t)], \tag{92}$$

of dimension $N + 1$. The system is non-linear, therefore matrix $\mathbf{A}^{(f)}$ is a linearized representation ($\mathbf{A}^{(f)}(\mathbf{F})$). while the vector $\mathbf{G}^{(f)}$ would generally be leak off dependent. Now the condition ratio κ_A can be calculated of the linearized matrix $\mathbf{A}^{(f)}(\mathbf{F})$:

$$\kappa_A^{(f)} = \frac{|\lambda_{max}|}{|\lambda_{min}|} \sim \varpi^{(f)} N^2, \quad N \to \infty. \tag{93}$$

Here $|\lambda_{max}|$, and $|\lambda_{min}|$ are the largest and smallest eigenvalues of linearized matrix[3]. $\mathbf{A}^{(f)}(\mathbf{F})$. For a discretized system that contains second derivative the quadratic stiffens behavior N^2 is an obvious result, however the parameter $\varpi^{(f)}$, which will be approximated numerically can be used as quantitative measure to select the less stiff variant of dynamic system.

The analysis should begin with approximation of $\varpi^{(f)}$ for all of the considered variants of dynamic systems. In case of Ω variable, alternative condition based on fluid balance can be used for $x = 0$ (74), additionally to Neumann type boundary condition based on q_0 (73). These two strategies should be referred as $\Omega_{(1)}$ and $\Omega_{(2)}$ respectively, and stiffness is measured for both of them. Since $\Omega_{(1)}$ leads to a slightly different form of $\mathbf{A}^{(f)}(\mathbf{F})$, different value of $\varpi^{(f)}$ should be expected, while $\Omega_{(2)}$ relies on a three point approximation similar to the used for w and U system.

2 Stiff method will need much less time steps on a stiff problem when compared a nonstiff method, which should result in faster computation time.

3 $\mathbf{A}^{(f)}$ is in fact the Jacobian explored later on in Section 3.6.4 and 4.5.2. Some methods of for solving systems use the linearized version directly, making this a relevant method for measuring stiffens

It is obvious that for all six variants of benchmark solutions under consideration (see Appendix A.2) one has different values of $\mathbf{A}^{(f)}$. Computations were carried out for two types of meshes (uniform (258) and non-uniform (259)). For each of the benchmark solutions, a constant condition ratio, independent of time, was obtained, despite the fact that $\mathbf{A}^{(f)}$ depends on time. Those values of condition ratio κ_A vary for different benchmarks and meshes.

Figure 8 shows values of κ_A for different values of N and three benchmarks and mesh choices. The least stiff formulation is U, and that result persist for all other possible test scenarios. However if w should be considered stiffer than Ω formulation depends on the benchmark type. The change of ratio from $1:1$ seems to have negative effect on w system in relation to effect on Ω. The boundary condition $\Omega_{(1)}$ (74) also has a negative effect on stiffness of Ω and should be replaced with $\Omega_{(2)}$ (and that change will have no impact on the accuracy of solutions).

As anticipated, the estimation (93) holds true only for sufficiently large N. The threshold value of N depends on the chosen ε, and the transition takes place at approximately $\varepsilon \approx \frac{1}{N^2}$. The Figure 9a shows two regimes, N^2 for $\varepsilon > \frac{1}{N^2}$, and another one, for $\varepsilon < \frac{1}{N^2}$. Thus for a fixed number of grid points N, there is a critical value of the regularization parameter $\varepsilon_s(N)$ for which the stiffness characteristics changes its behavior. By taking $\varepsilon < \varepsilon_s(N)$ one increases appreciably the system stiffness.

The choice of spacial discretization between uniform $x_m^{(1)}$ mesh (258) and $x_m^{(2)}$ mesh (259) has an effect of stiffness. As predicted in [65] the $x_m^{(2)}$ mesh improves system stiffness for about an order of magnitude compared to uniform mesh, when the optimal value of δ is chosen. On Figure 9b it is shown that indeed for $N \approx 10$ and $\varepsilon = 10^{-3}$ the $x_m^{(2)}$ mesh has lowest stiffness for the optimal value of $\delta = 2$. However for $N > 10$ the optimal value of δ changes, and the optimal value of $\delta \approx 2.5$ was experimentally obtained.

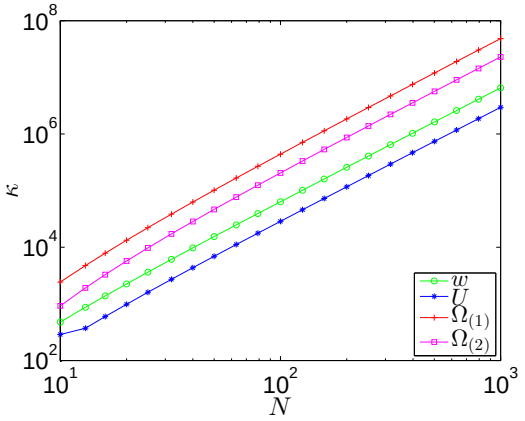

(a) ratio $Q_l/q_0 = 0.9$ on $x_m^{(1)}$ mesh

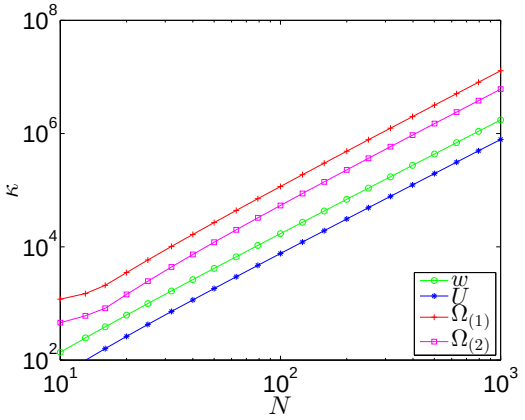

(b) ratio $Q_l/q_0 = 0.9$ on $x_m^{(2)}$ mesh

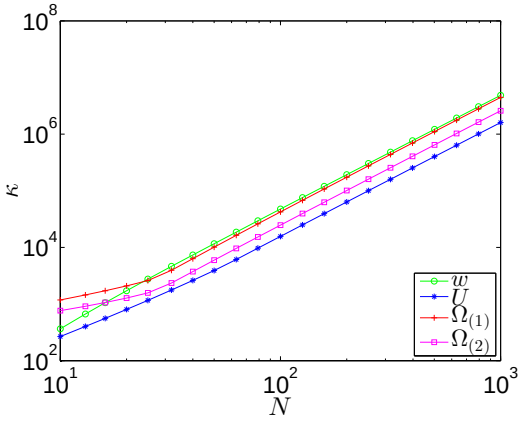

(c) ratio $Q_l/q_0 = 0.5$ on $x_m^{(2)}$ mesh

Figure 8: Stiffness in logarithmic scale defined as the ratio of smallest and largest eigenvalue in linearized matrix $\mathbf{A}^{(f)}(\mathbf{F})$ ($\epsilon = 10^{-3}$,$q_l^{(1)}$). Higher Q_l/q_0 ratio, indicating majority of the pumped in fluid leaks off, results in stiffer problems.

	$Q_l/q_0 = 0.9$			$Q_l/q_0 = 0.5$		
	$q_l^{(1)}$	$q_l^{(2)}$	$q_l^{(3)}$	$q_l^{(1)}$	$q_l^{(2)}$	$q_l^{(3)}$
	ϖ estimated for the system based on variable w					
$x_m^{(1)}$	6.5e+0	6.6e+0	6.8e+0	1.8e+1	1.8e+1	1.8e+1
$x_m^{(2)}$	1.7e+0	1.7e+0	1.7e+0	4.6e+0	4.7e+0	4.7e+0
	ϖ estimated for the system based on variable U					
$x_m^{(1)}$	3.0e+0	3.0e+0	3.2e+0	6.0e+0	6.1e+0	6.2e+0
$x_m^{(2)}$	7.5e-1	7.7e-1	8.1e-1	1.5e+0	1.5e+0	1.6e+0
	ϖ estimated for $\Omega_{(1)}$ based on condition (74)					
$x^{(I)}$	4.8e+1	4.8e+1	4.9e+1	1.7e+1	1.7e+1	1.7e+1
$x_m^{(2)}$	1.2e+1	1.2e+1	1.3e+1	4.3e+0	4.3e+0	4.3e+0
	ϖ estimated for $\Omega_{(2)}$ based on condition (73)					
$x_m^{(1)}$	2.3e+1	2.2e+1	1.9e+1	9.6e+0	1.0e+1	1.3e+1
$x_m^{(2)}$	5.8e+0	5.7e+0	4.7e+0	2.5e+0	2.6e+0	3.5e+0

Table 1: Values of $\varpi^{(f)}$ (93) for different variable formulations and benchmarks. ($\varepsilon = 10^{-3}$ was used with grids (258) and (259) $N = 1000$, the ratio Q_l/q_0 ratio, indicates how much of the fluid leaks off)

Table 1 shows values of $\varpi^{(f)}$, with a fairly large $N = 1000$ for Carter leak off type benchmarks (A.2). The values shown there prove that $x_m^{(2)}$ offers up to five times lower stiffness, for considered scenarios.

The results of the stiffness investigation are collected in the Table 1 and Fig. 9 The following conclusions can be drawn from this data:

1. The nonuniform mesh reduces the stiffness approximately up to five times regardless of the solution type (Table 1);
2. The most important parameter affecting the stiffness properties is the relation between the injection flux rate and the leak-off to the formation Q_l/q_0 as can be clearly seen in Table 1. The value of this parameter is more important than a particular distribution of the leak-off function (and its behavior near the crack tip);
3. When comparing systems for various dependent variables, the lowest condition ratio is obtained via U formulation (one order of magnitude lower than the others). The worst stiffness performance takes place for the system corresponding to the Ω variable. However, in some cases Ω may produce lower stiffness than w;
4. A value of the regularization parameter ε significantly affects the stiffness of a dynamic system.
5. The estimate (93) is valid for most values of N, if $\varepsilon > \frac{1}{N^2}$

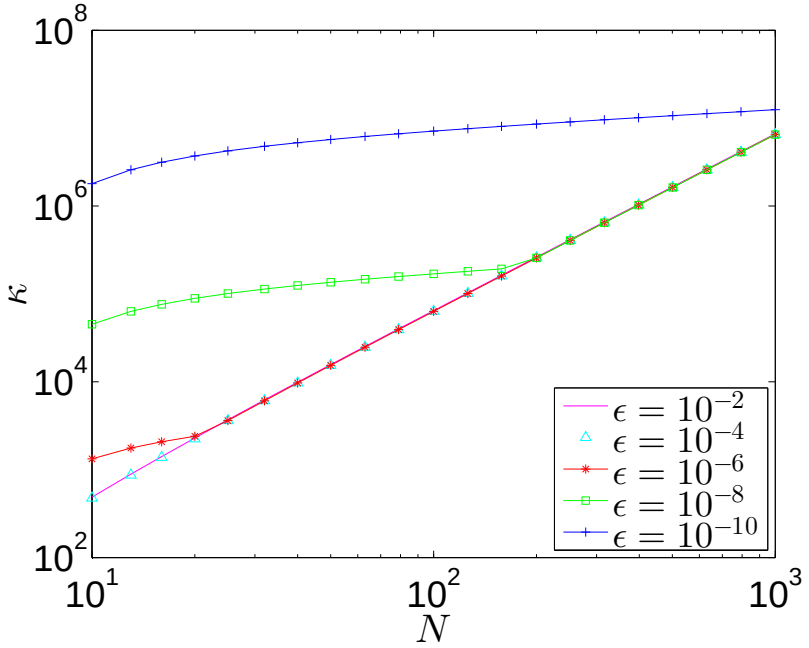

(a) Condition ratio $\kappa = \kappa^{(w)}(N)$ for w variable dynamic system and different values of the regularization parameter ε, with $x_m^{(1)}$ mesh.

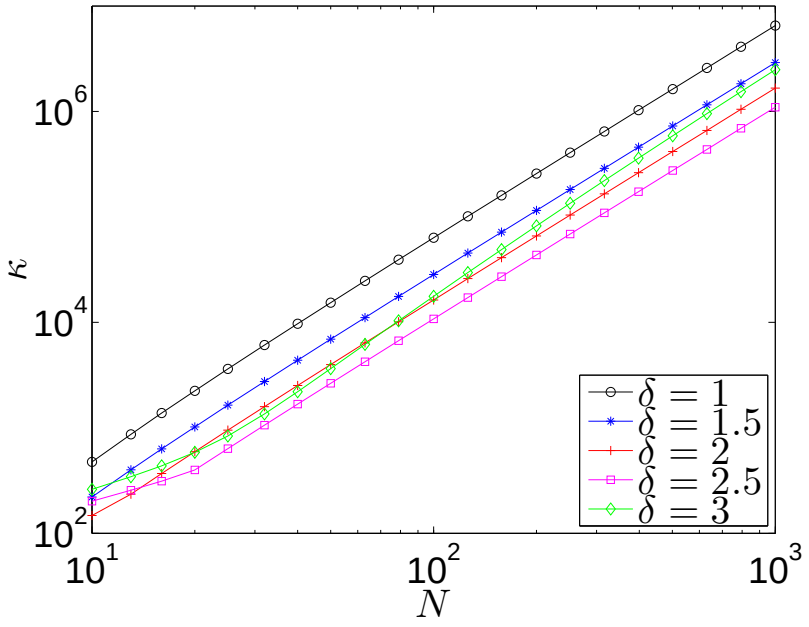

(b) Stiffness for w system with $x_m^{(2)}$ mesh (259) for various δ values, result obtained on uniform mesh (258) on Figure 8a overlap with $\delta = 1$

Figure 9: Effects of different values of ε and δ on the problem stiffness

3.2 DYNAMIC SYSTEMS WITH ODE15S

3.2.1 *BDF and ODE solvers*

Backward differentiation formulas is a set of implicit multistep methods designed to solve systems of stiff ordinary differential equations [96]. These formulas were originally developed by Gear [103] and are sometimes called Gear method.

BDFs can be used to solve initial value problem in form:

$$y' = f(t, y), \quad y(t_0) = y_0 \tag{94}$$

And the general formula for BDF is:

$$\sum_{k=0}^{s} a_k y_{n+k} = h\beta f(t_{n+s}, y_{n+s}) \tag{95}$$

Where h is the step size, while a_k and β are coefficient dependent on method order s. Although the general formula might not be very familiar, the 1^{st} order BDF is something that appears in all introductory numerical analysis courses:

$$y_{n+1} - y_n = hf(t_{n+1}, y_{n+1}) \tag{96}$$

Which is just the backward Euler method for differential equations. Such is not yet a multistep method as only one known point y_n is involved in the approximation of new solution point y_{n+1}. The 2^{nd} BDF formula is given as:

$$\frac{2}{3}hf(t_{n+2}, y_{n+2}) = y_{n+2} - \frac{4}{3}y_{n+1} + \frac{1}{3}y_n \tag{97}$$

Here the name multistep comes in as this approximation uses two known data points y_n and y_{n+1}. The further BDF up to 6^{th} order were derived by Gear [103]. The order of formula is the number of backward points used. Up to 6 points are used in 6^{th} order formula, and this is the last zero-stable[4] BDF [28].

BDF are most popular method in stiff solvers [68], and this should be probably attributed to several factors. Very good accuracy and stability can be obtained (as it will be shown later), and essentially the same algorithm can be used for each of the methods order. When using Euler method, the main challenge results from matrix inversion. Adjusting the solution vector such so it is a sum of several known previous points is a simple task, so higher order BDF are not really more difficult to use than Euler method. The constant coefficients a_k for each order, were derived by Lagrange Polynomial interpolation. The higher orders rely on more data points, so the approximation can

4 Further order formulas will not converge to a solution.

be more accurate, but at the same time method becomes less stable, as the approximation must much a more complex polynomial. Proper usage of this method requires balancing between high accuracy of higher orders, and better stability of lower orders.

The most important advantage of BDF methods in view of this work is how straightforward it is to apply these method to previously formulated PKN problem. For stiff BDF based solvers, as well as all other ODE solvers, one has to describe the problem as an IVP (94), that is specify at least these two constructs:

- initial value y_0, here it is a vector value of $N+1$ elements. Where N corresponds to grid size (Appendix A.1), the initial opening w_* (23) is evaluated at each of these points. This vector is amended by squared initial length l_*^2

$$\begin{aligned} y_0 &= \{w_*, l_*^2\} \\ &= \{w_*(x_1), w_*(x_2), \ldots, w_*(x_N), l_*^2\} \end{aligned} \tag{98}$$

- function y', the rate of change of this systems of ODE. This function takes a vector with $N+1$ elements as the value of $y(t)$, and then returns corresponding $y'(t, y(t))$ as another vector with $N+1$ elements. Operator $\mathcal{A}$ (32) is used to make N ODEs, one for each grid point, and $\mathcal{B}$ contributes one extra ODE.

$$\begin{aligned} y' &= \{\mathcal{A}(y), \mathcal{B}(y)\} \\ &= \{\mathcal{A}(y_{1\ldots N}, y_{N+1}), \mathcal{A}_2(y_{1\ldots N}, y_{N+1}), \ldots \\ &\qquad , \mathcal{A}_N(y_{1\ldots N}, y_{N+1}), \mathcal{B}(y_{1\ldots N})\} \end{aligned} \tag{99}$$

Finally having given value of y_0 and an expression for $y'(t, y)$, the solver is asked to perform integration from some initial time t_0 to final time t_{end}. A solution, a two dimensional array, will be produced that consists of all y values at initial, end, and a number if intermittent times:

$$\begin{aligned} y(t_0, \ldots, t_{end}) = \{&w(t_0, \ldots, t_{end}, x_1), w(t_0, \ldots, t_{end}, x_2), \ldots \\ &, w(t_0, \ldots, t_{end}, x_N), L^2(t_0, \ldots, t_{end})\} \end{aligned} \tag{100}$$

Although the above presents how w formulation (32) can be tackled with ODE solvers, other formulations U and Ω (65), (77) can be implemented in similar manner.

Having stated that the problem can be solved with common stiff ODE methods, the question that needs to be answered is: Should some existing solver be used, or own customized version be implemented? The answer is not trivial, as there are advantages and drawbacks associated with both choices. An attempt to develop own BDF solver was carried as well as another one based on alternative Cranck-Nicolson methods. This attempts however exposed various issues that

need to be resolved in order to make a properly working solver, even if it was to work only for this particular PKN formulation. Apart from integrating the function a good solver carries number of other tasks including: error approximation, time step handling, event detections and a number of performance and stability tunings. Writing a new solver would mean tackling these problems that were already attempted by someone else. These could pose a valid theoretical challenge, however lets remind ourselves of and an old software development principle:

Do not reinvent the wheel,

which in this case translates into: save time and effort by using existing well tested and understood solvers. Developing a solver could easily be a subject of another thesis on its own. This work will therefore first attempt to formulate a novel enough and solvable fracturing problem, and then seek in detail attempts to improve computational efforts.

The single fracture code will be approached with ODE15s, one of solvers available in MATLAB ode suite, that is specially designed to deal with stiff problems [62]. There are some very good readings [7] that clearly describe the inner mechanics of this solver that I would recommend anyone interested in the subject to have a glance at. As a brief summary it should be mentioned that ODE15s is based on two implicit sets of formulas: NDFs and BDFs. (which are the direct opposite to explicit Runge–Kutta methods that some authors insist to be involved [65]) Numerical differentiation formulas are a modification of BDF with better usage of predicted value.

An example simplified MATLAB script that obtains solution to self similar problem presented in Appendix A.4.1. Thanks to using well developed solver the implementation is very straightforward. Object orientated approach is used to divide tasks into separate modules. The main class is CrackSystemW (Appendix A.4.2), which holds general IVP made out off expressions (98), (99), (100).

3.2.2 *Building y' for ODE solvers*

This section should explain the details how w problem formulation is implemented into single fracture code (Appendix A.4).

The function representation y' (99) is dynamically passed *at runtime* (line 41 in A.4.2) to ODE15s, as a function reference (subroutine) with simple signature that directly translates to $y' = f(t, y)$ (line 47 in A.4.2), thous the ODE solver does not known anything about the behavior of these system upfront. The output value vector can be obtained in virtually any manner.

Multiple approaches to obtaining these are possible. An old school approach could treat the problem as

$$\mathbf{Y}' = \mathbf{AY} + \mathbf{G}, \tag{101}$$

With linearized mass matrix $\mathbf{A}$, and leak off dependent vector $\mathbf{G}$. The above would require multiple iterations, to finally produce the return value for y' function, as this problem is nonlinear.

The above approach is neither efficient (unnecessary iterations and sparse matrix creation) or straightforward. As the problem requires to find value of $\mathcal{A}_1, ..., \mathcal{A}_N$ at points $x_1, ...x_n$, the operator$\mathcal{A}$ for each of the three variables w (29), U (62), and Ω (72), is evaluated separately at each point:

$$y_i' = \mathcal{A}_i = \begin{cases} \mathcal{A}_{i\ w} = & \frac{1}{y_{N+1}} \left[\frac{1}{3} w_0^3 x_i \frac{\partial y_i}{\partial x_i} + 3 y_i^2 \left(\frac{\partial y_i}{\partial x_i} \right)^2 + y_i^3 \frac{\partial^2 y_i}{\partial x_i^2} \right] - q_l(x_i) \\ \mathcal{A}_{i\ U} = & \frac{1}{3 y_{N+1}} \left[w_0^3 x_i \frac{\partial y_i}{\partial x_i} + \left(\frac{\partial y_i}{\partial x_i} \right)^2 + 3 y_i \frac{\partial^2 y_i}{\partial x_i^2} \right] - 3 y_i^{\frac{2}{3}} q_l(x_i) \\ \mathcal{A}_{i\ \Omega} = & \frac{-1}{y_{N+1}} \left[\left(\frac{\partial y_i}{\partial x} \right)^3 \frac{\partial^2 y_i}{\partial x^2} + \frac{1}{3} w_0^3 \left(y_i - x \frac{\partial y_i}{\partial x} \right) \right] - Q_l(x_i). \\ & i = 1, \ldots, N \end{cases} \tag{102}$$

Since $y_{1...N} = w_{1...N}$ *or* $U_{1...N}$ *or* $\Omega_{1...N}$ and $y_{N+1} = L^2$. The value of asymptotic term w_0 is easily interchangeable with U_0 and Ω_0 since (59) and (69), furthermore the operator $\mathcal{B}$ also does not differ significantly between systems, so it is possible to interpret the problem as if only the first term w_0 is needed. Then the extra ODE governing $\mathcal{B}$ is just:

$$y_{N+1}' = \mathcal{B}_{w,U,\Omega} = \frac{2}{3} w_0^3 \tag{103}$$

Now it can be seen that for all the variable formulation the only actual unknowns when constructing y_i' are $\frac{\partial y_i}{\partial x_i}$, $\frac{\partial^2 y_i}{\partial x_i^2}$, w_0 and $q_l(x_i)$. This means one can threat all variables with essentially *one common algorithm* for building y' as presented as Algorithm 1.

The equation 102 can be directly translated to code for each grid point (line 76 in A.4.2), and so the additional equation (103) (line 81 in A.4.2). Values of $\frac{\partial y_i}{\partial x_i}$ and $\frac{\partial^2 y_i}{\partial x_i^2}$ should be computed before (102) is evaluated. For the interior of the grid $x_{2,...N-1}$ a numerical scheme, such as central finite difference can be used (details are outlined in Section (3.6)). The boundary values for grid point x_1 and x_N must treated specially with boundary conditions. So three subroutines are needed to evaluate:

$$\frac{\partial y_i}{\partial x_i}, \frac{\partial^2 y_i}{\partial x_i^2} = \begin{cases} left\ side\ BC & for\ x_1 \\ derivative\ approximation\ scheme & for\ x_{2,\dots N-1} \\ right\ side\ BC & for\ x_N \end{cases} \tag{104}$$

Leak off $q_l(x_i)$ requires usage of some additional code handle, the details on writing such are presented in Section 3.8.

In conclusion, the function (subroutine) for y' is designed here such so it uses four other functions (subroutines) left and right side BC, derivative approximation and leak off handle. This is shown in sample code at lines 64-73 A.4.2. The object representations of these are passed through constructor (line 14 A.4.2), and can be easily replaced by different implementations, allowing experimentation with many different ideas. Further Subsections 3.6.1 and 3.6.3 shows what happens when some different approximations of the derivatives are considered.

3.2.2.1 *Left BC*

Lets consider one variation of left side BC, derived explicitly for w.

$$\frac{\partial y_1}{\partial x_1} = -\frac{ML(t)}{k} q_0(t) \frac{1}{y_1^3} \tag{105}$$

$$\frac{\partial^2 y_1}{\partial x_1^2} \approx \left(-\frac{2}{x_2} a + \frac{4}{x_2} \frac{ML(t) q_0(t) y_1^{-4}}{k} - \frac{6}{x_2^{-2}} \right) y_1 + \left(-\frac{2}{x_2} b + \frac{6}{x_2^{-2}} \right) y_2 + \left(-\frac{2}{x_2} c \right) y_3 \tag{106}$$

Where:

$$a = -\frac{1}{2\,(x_2 - x_1)}, \quad b = \frac{1}{2} \left(\frac{1}{x_2 - x_1} - \frac{1}{x_3 - x_2} \right), \quad c = \frac{1}{2\,(x_3 - x_2)} \tag{107}$$

This left side BC relates first derivative (105) directly to fluid pumping q_0. The second derivative (106) is obtained by differentiating a cubic polynomial[5]. Similar expressions can be derived for U and Ω variables (but not if alternative form of Ω BC (74) is used) . Appendix A.4.8 shows example code.

5 A cubic polynomial $ax^3 + bx^2 + cx + d$ can be interpolated to match points (x_1, w_1), and (x_2, w_2), such so it first derivative and second derivative at x_1 matches 105 and 106. These are four conditions and four unknowns.

3.2.2.2 *Right BC*

The value of w_0 is best to be found as a byproduct of the right side BC. Several right side BC versions were tested, as (85), or (79), (80), (81), (82), (83) can be implemented in multiple ways, and the best found is to consider the following two equations:

$$\begin{aligned} w_0 &\approx A_1 y_{N-1} + A_2 y_N \\ w_1 &\approx B_1 y_{N-1} + B_2 y_N \end{aligned} \tag{108}$$

Where the constants $A_1,\ A_2,\ B_1,\ B_2$ are based on the last two grid points:

$$\begin{aligned} A_1 &= \left((1-x_{N-1})^{\frac{1}{3}} - \frac{(1-x_{N-1})^{\frac{1}{2}}}{(1-x_N)^{\frac{1}{6}}} \right)^{-1} \\ A_2 &= -\left(\frac{1-x_{N-1}}{1-x_N} \right)^{\frac{1}{2}} A_1 \\ B_1 &= -\frac{A_1}{(1-x_{N-1})^{\frac{1}{6}}} \\ B_2 &= \frac{1}{(1-x_{N-1})^{\frac{1}{2}}} - \frac{A_2}{(1-x_{N-1})^{\frac{1}{6}}} \end{aligned} \tag{109}$$

Again constants $A_1,\ A_2,\ B_1,\ B_2$ presented here were derived for w variable system, but it is possible to do the same for both U and Ω. Having found w_0 and w_1, these values can be used in (102) and the right end derivatives can be directly set as:

$$\begin{aligned} \frac{\partial y_N}{\partial x_N} &= -\frac{w_0}{3}(1-x_N)^{-\frac{2}{3}} - \frac{w_1}{2}(1-x_N)^{-\frac{1}{2}} \\ \frac{\partial^2 y_N}{\partial x_N} &= -\frac{2w_0}{9}(1-x_N)^{-\frac{5}{3}} - \frac{w_1}{4}(1-x_N)^{-\frac{3}{2}} \end{aligned} \tag{110}$$

Which corresponds to implementing (85) (or (88), or (88)). Appendix A.4.9 for example code.

input : $y(t)$ as a vector $\{y_1, y_2, ..., y_N, y_{N-1}\}$ equivalent of $\{w_1, w_2, ..., w_N, L^2\}$
output: $y'(t)$ as a vector $\{\mathcal{A}_1, \mathcal{A}_2, ..., \mathcal{A}_N, \mathcal{B}\}$

$q_l(t, x_i) \longleftarrow$ leak off handle $(y(t))$;
$\frac{\partial y_1}{\partial x_1}, \frac{\partial^2 y_1}{\partial x_1^2} \longleftarrow$ left BC $(y(t))$;
$w_0, \frac{\partial y_N}{\partial x_N}, \frac{\partial^2 y_N}{\partial x_N^2} \longleftarrow$ right BC $(y(t))$;
for $i \leftarrow 2$ **to** $N-1$ **do**
  $\frac{\partial y_i}{\partial x_i}, \frac{\partial^2 y_i}{\partial x_i^2} \longleftarrow$ derivative approximation scheme $(y(t))$;
end
for $i \leftarrow 1$ **to** N **do**
  $y'_i \leftarrow \mathcal{A}_i\left(y(t), w_0, \frac{\partial y_i}{\partial x_i}, \frac{\partial^2 y_i}{\partial x_i^2}, q_l(t, x_i)\right)$;
end
$y'_{N+1} \leftarrow \mathcal{B}(w_0)$;

Algorithm 1: The procedure for obtaining $y'(t)$

3.3 SENSITIVITY TO INITIAL CONDITIONS

Some works attempt to start from zero initial width and opening [106], others take some known non zero result and treat it as the initial condition [25, 65]. As it was shown in the problem formulation (23) this work assumes some existing non zero fracture aperture and length. In the work by [54] the self-similar zero leak off solution (see Appendix A.2.2) was used as this starting point, and this idea was continued in [65, 44]. The initial conditions were therefore based on a valid solution of existing hydraulic fracture. One can ask a question on what implications does the change of value of initial condition has on the solution, what happens if the initial fracture does not look like a casual hydraulic fracture?

To answer this question a set of test scenarios with modifications to the conventional initial conditions was prepared. The approach presented here uses the zero leak off self-similar solution (271) given by Linkov [54], to identify w_* and corresponding l_*. This values will be altered to show possible results of tempering with initial conditions. The outcome will be presented as plots with multiple possible trajectories of $L(t)$, each corresponding to different values of w_*,l_* and a (which is the initial time). As an example of such a plot consider Figure 10 where several possible trajectories of $L(t)$ are shown.

Different initial values will affect the stability of computations. The calculations which resulted in solver failures or incorrect fluid balance value (see Subsection 3.8.4), relative loss of over 5% of the fluid, will be shown as *doted lines*, or not shown at all. All the tests will be carried out with initial time values of:

$$a = \left\{10^{-8}, 10^{-6}, 10^{-4}, 10^{-2}, 1\right\},$$

and multiple values of some other parameters, a total of about 30-50 attempted fracture computations for each initial condition variation are attempted. Three variants of leak offs will be also considered for each of the tests scenarios: zero leak off, Carter law $q_l^{(1)}$ (4), and pressure proportional version $q_l^{(2)}$ of Carter law (4). Each of these leak offs can be associated with a known large time asymptote: (271), (274) or (275) to which the fracture length should eventually approach to. Zero leak off solution (271) is used both as modifiable starting point and large time asymptote for simulations with no leak off. The numerical simulations, if successful, will eventually tend to these large time solutions, but the transient regime will be shown to be difficult to obtain, but very interesting, in many considered cases. One of most deceptive aspects of this computation is the treatment of $\tau(x)$, two strategies (158) and (159) will be used. The first one essentially for-

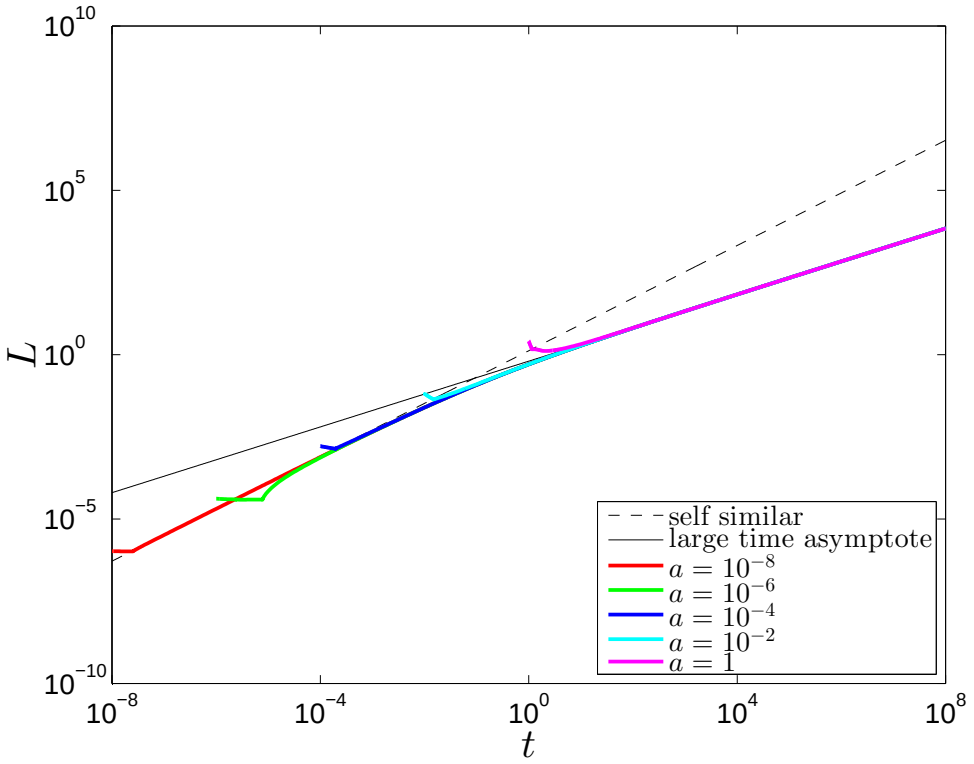

Figure 10: An example comparison of lengths $L(t)$ of five different fractures. Despite different starting times a and initial lengths all of the trajectories eventually converge to large time asymptote.

bids any leak off to the formation for the initial segment $xL(x) < l_*$, while the second strategy allows for leak off at this initial segment.

3.3.1 *Varying initial length*

Lets first examine effect of changing the initial length. To do so, the original initial crack length l_* will be multiplied by a factor B:

$$l_* := Bl_*, \tag{111}$$

where the considered values of B are:

$$B = \left\{10^{-5},\ 10^{-4},\ 10^{-3},\ 10^{-2},\ 10^{-1},\ 10^{0},\ 10^{1},\ 10^{2},\ 10^{3},\ 10^{4},\ 10^{5}\right\}. \tag{112}$$

So now one can observe effects of changing just the fracture length.

The most stable and predictable result is obtained with zero leak off. Figure 11 shows that trajectories either catch up immediately with the asymptote, if $B < 1$ hence shorter initial fracture, or wait for the asymptote if $B > 1$ and longer initial fracture.

Much more interesting results are obtained with leak offs $q_l^{(1)}$ and $q_l^{(2)}$ (4), as shown on Figure 12 and 13. Here the computations perform well if $B < 1$, but for $B > 1$ most of the attempts failed. This could be attributed to ODE15s loosing stability. Where there was no leak off at the initial length (158), these fractures, that were computed correctly, also waited for the asymptote, while if (159) was used, successfully computed fractures would shut down until meeting up with the asymptote 12. (The mechanics behind computing the shut down regime are shown in Subsection 3.8.3)

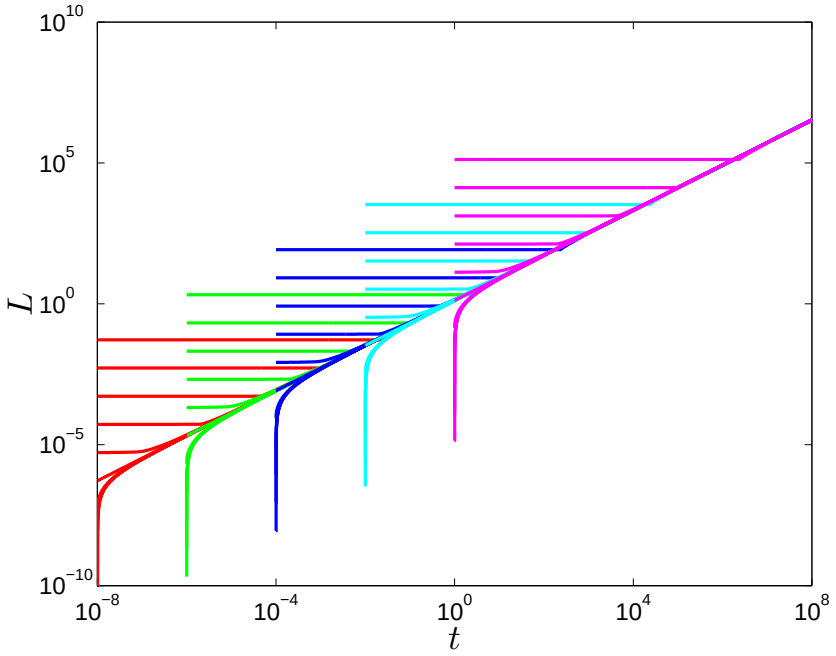

Figure 11: Varying initial length, zero leak off.

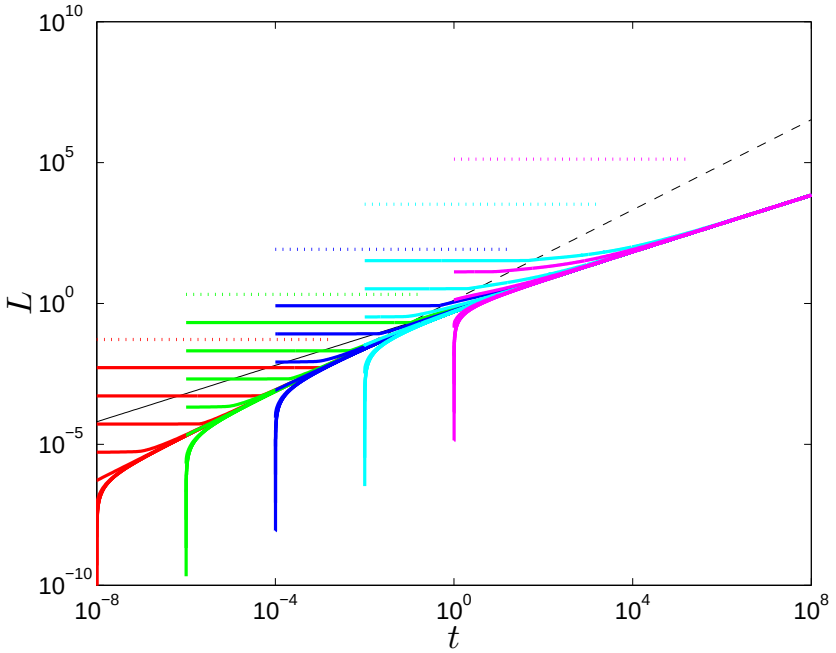

(a) No leak off at initial length (158)

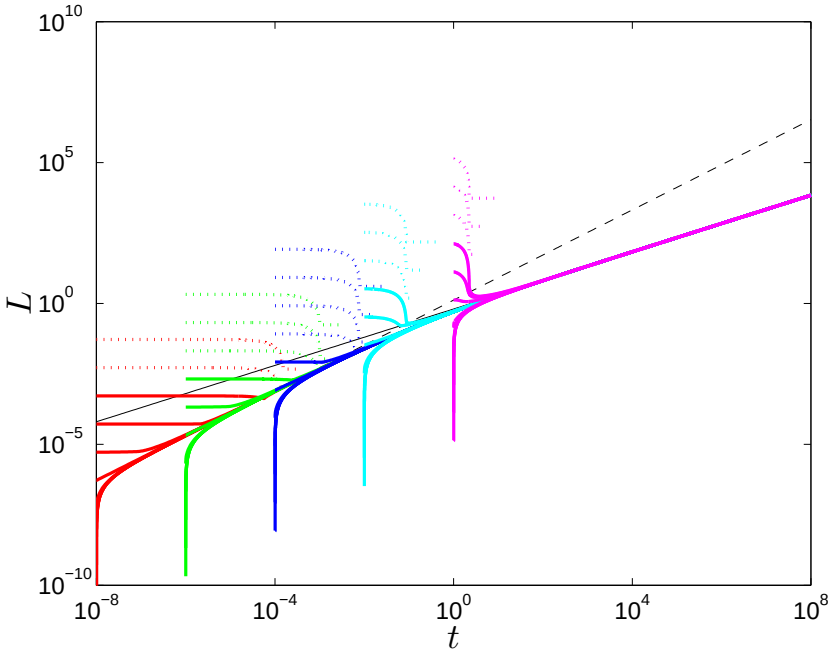

(b) Leak off allowed at initial length (159)

Figure 12: Varying initial length, Carter leak off $q_l^{(1)}$ (4).

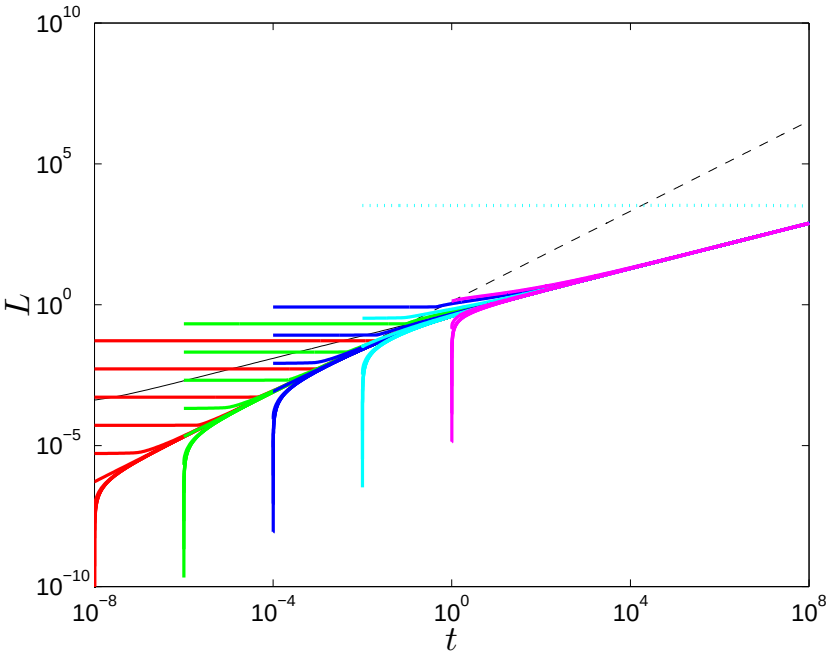

(a) No leak off at initial length (158)

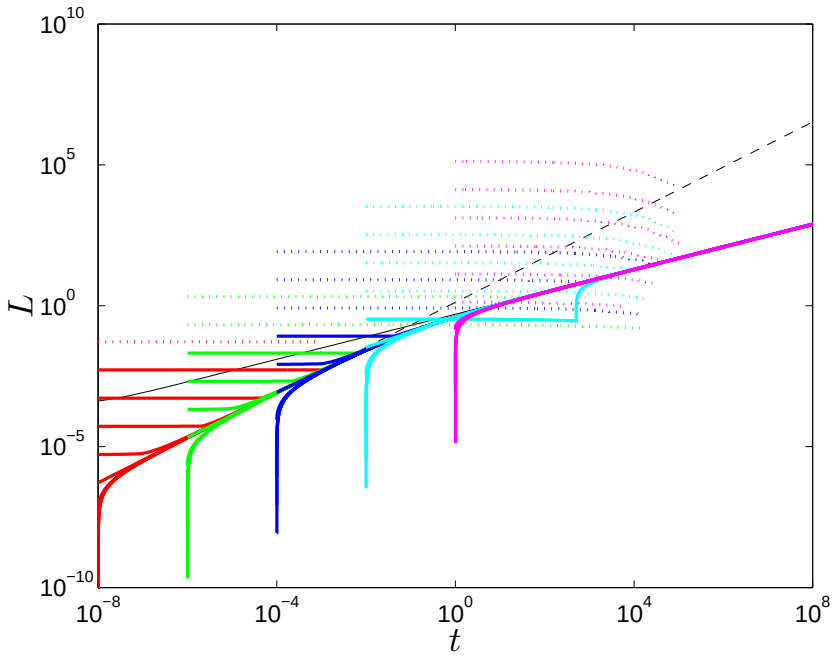

(b) Leak off allowed at initial length (159)

Figure 13: Varying initial length, pressure proportional Carter leak off $q_l^{(2)}$ (4).

3.3.2 *Varying the influx at crack mouth*

To analyze how perturbation of the influx at $x = 0$ affects problem solution , lets multiply the pump in rate q_0 [6] by a factor C:

$$q_0 := Cq_0, \tag{113}$$

considered range of C is:

$$C = \left\{10^{-5},\ 10^{-4},\ 10^{-3}, 10^{-2},\ 10^{-1},\ 10^{0},\ 10^{1},\ 10^{2},\ 10^{3},\ 10^{4},\ 10^{5}\right\}. \tag{114}$$

With the change of pump in rate, relevant large time asymptotes (271) (274) and (275) are also affected, solutions will eventually tend to asymptotes corresponding to the different values of fluid pump in rate.

The result for zero leak off is showed on Figure 14. Here no problems were encountered, there were smooth transitions from $q_0 = 1$ to other zero leak off solutions. The leak offs $q_0^{(1)}$ and $q_0^{(2)}$ (4), as shown on Figure (15) and (16) again proved to be much more of a challenge. The general tendency was again for each of the trajectories to tend to the corresponding asymptotes. For $C > 1$ all the attempted computations succeed. For $C < 1$ fractures would enter shut down regime, even if no leak off at initial length (158) was allowed. This shut down could take place on a newly opened fracture part (some blue trajectories on 15a). Interestingly the most reliable strategy with leak off is shown on 15b, where the effects of closing shut down regimes are most noticeable. Only two trajectories were terminated prematurely. On the remaining leak off enabled strategies more trajectories would not reach expected asymptotes, and the worst results were obtained for later start points. Starting at greater times means longer initial fractures, and so greater discrepancy between zero leak off initial fracture aperture and a solution with leak off.

6 Which in case of the aforementioned self-similar based initial condition has a constant value $q_0 = 1$ (see Appendix A.2.2)

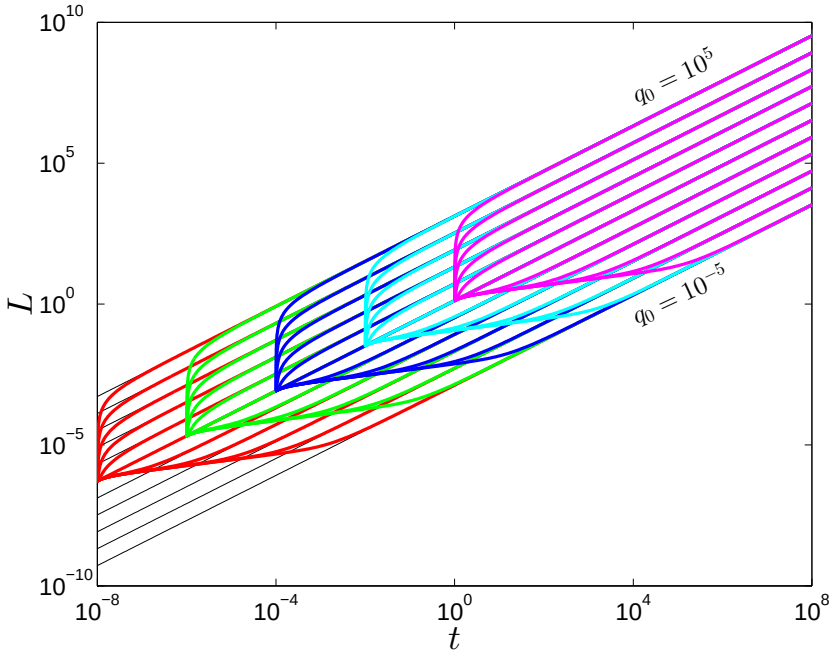

Figure 14: Varying pump in rate, zero leak off.

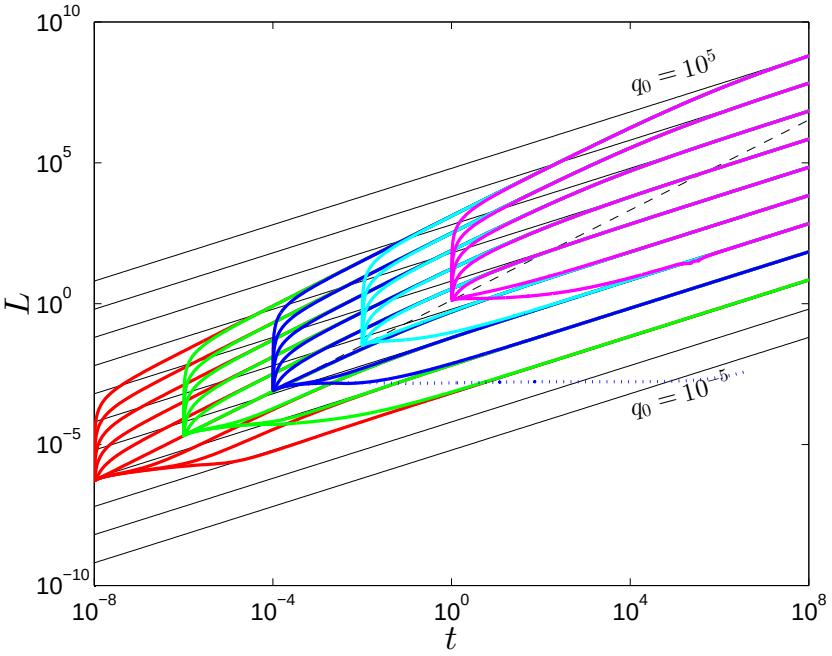

(a) No leak off at initial length (158)

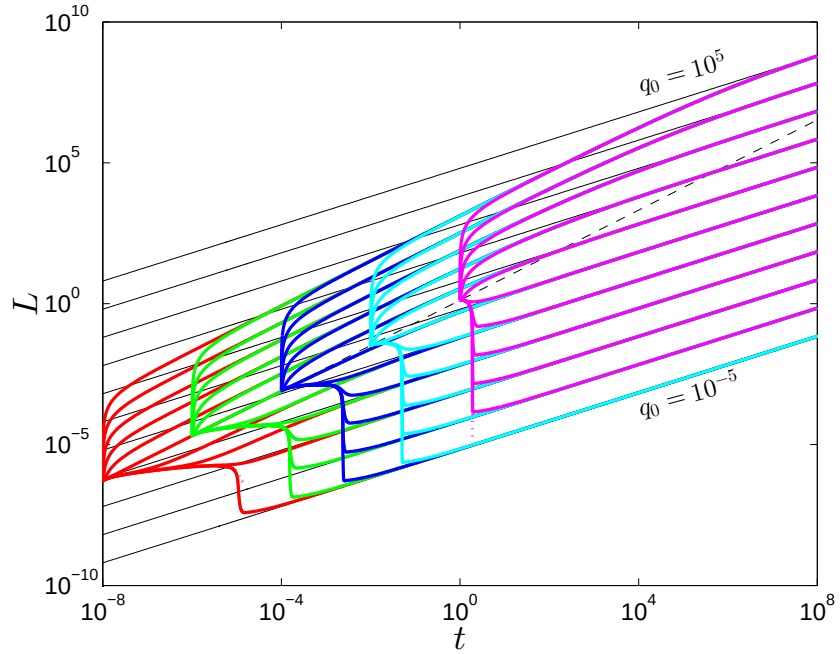

(b) Leak off allowed at initial length (159)

Figure 15: Varying pump in rate, Carter leak-off $q_0^{(1)}$ (4).

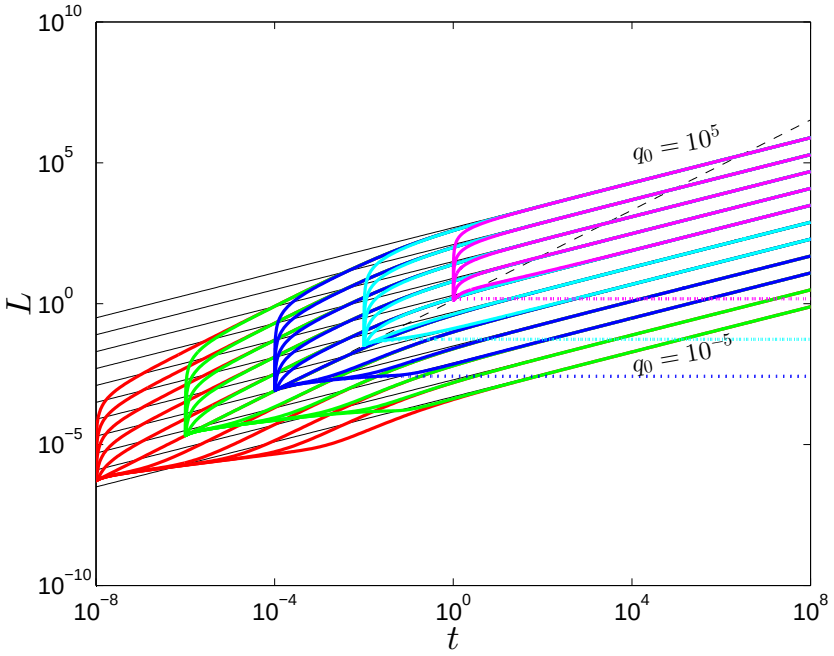

(a) No leak off at initial length (158)

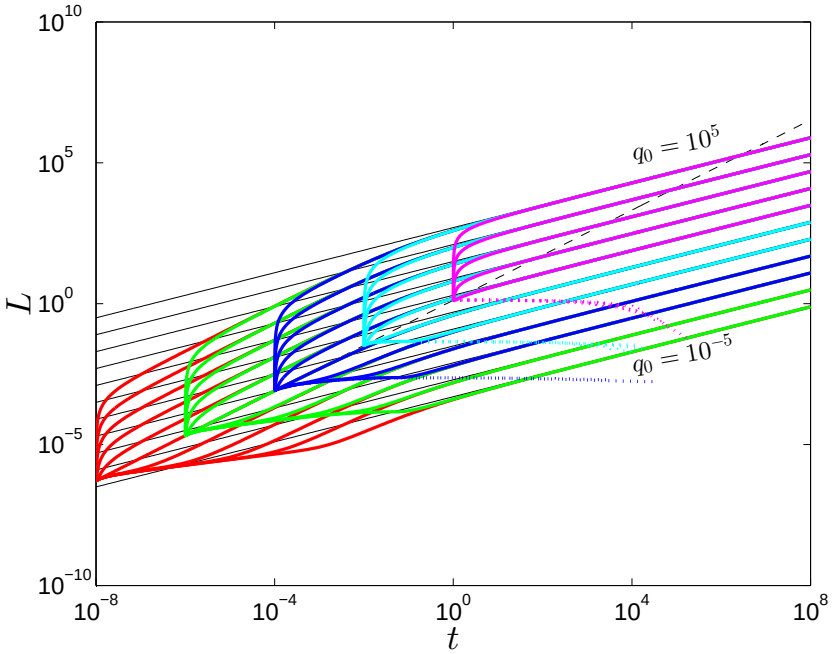

(b) Leak off allowed at initial length (159)

Figure 16: Varying pump in rate, pressure Carter leak-off $q_0^{(2)}$ (4).

3.3.3 *Varying the initial shape*

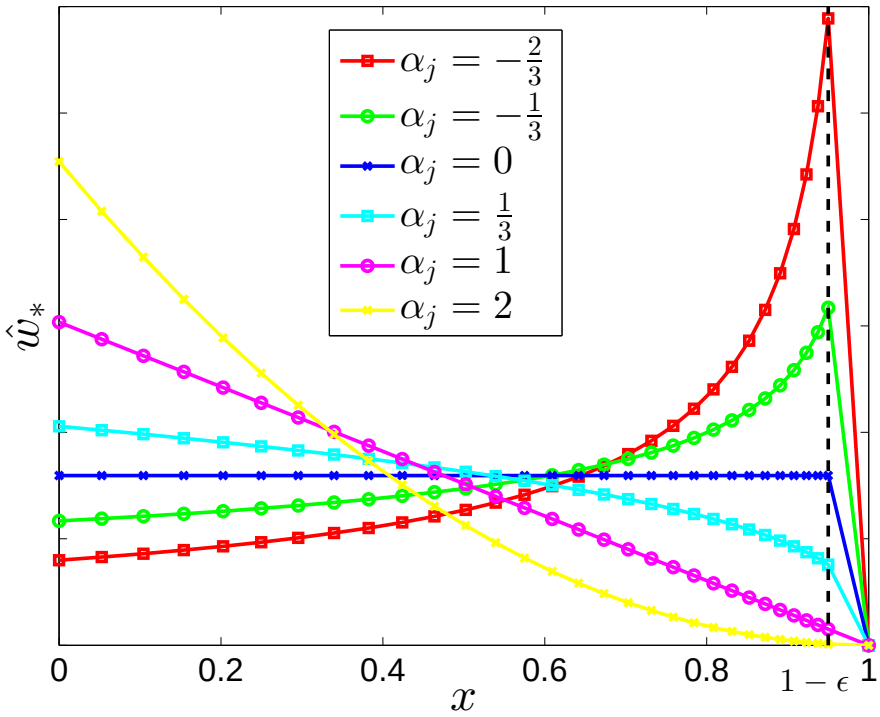

Figure 17: Initial opening $\hat{w_*}(x)$ obtained by changing power in $A_j(1-x)^{\alpha_j}$. Note that there are no grid points (markers) after $1-\epsilon$.

This time it will be investigated how the solution changes depending on the initial shape of the fracture opening $w_*(x)$. Lets use the following function:

$$\hat{w_*}(x) = A_j(1-x)^{\alpha_j},\ x \leq 1-\epsilon \tag{115}$$

where α_j defines the shape of the initial fracture and constant A_j is chosen so that the volume of the fracture is the same for each considered initial shapes.

The values of α_j are in range:

$$\alpha_j = \left\{-\frac{2}{3},\ -\frac{1}{3},\ 0,\ \frac{1}{3},\ 1,\ 2\right\}, \tag{116}$$

It can be argued that such conditions will create unnatural fractures. Indeed when taking a look Figure 17 it can be observed that for $\alpha_j < 0$ a singularity at the crack tip is being introduced. However, as the tip is already treated with the special boundary condition (84), zero value at crack the tip is implicitly build in the numerical procedure. Furthermore there is no actual grid point past $1-\epsilon$, so the produced initial opening has numerically valid values. There are numerous techniques for obtaining initial fractures [8], so it is not very

far fetched that under right circumstances unusual shapes, close to the results of $\alpha_j = -\frac{2}{3},\ -\frac{1}{3},\ 0$, might be produced. Testing negative α_j does add some interesting hypothetical scenario, and shows how the algorithm deals with some extreme input values.

The behavior of the solutions with zero leak off shown on Figure (18) was again the least interesting to analyze. The initial disturbance in fracture shape would initially contribute to different propagation speed. These differences would however be visible only at small times, thous some areas on Figure (18) are enlarged to show this subtle variations. The larger values of α_j would cause initial fracture to stop, while smaller α_j slightly accelerated initial propagation. For $\alpha_j = \frac{1}{3}$, the shape closest to zero leak off solution A.4.10, result was nearly identical.

For fractures with Carter type leak off ${q_l}^{(1)}$ (4) shown on Figure 19, similar results were observed, with an exception of initial time of $t = 1$. At this time start fractures with $\alpha_j < \frac{1}{3}$ would initially propagate faster, just to open more fresh fracture wall surface (not saturated by cake layer build up), and then recede due to large leak off value, and finally propagate again. For values of $\alpha_j > \frac{1}{3}$, the trajectories first show shut down regime, followed by propagation, another shutdown, and then yet more propagation. This result could not be obtained without sophisticated approach to $\tau(x)$ approximation 3.8. It is indeed a very interesting result, and should require some proper verification, but as for the testing of initial conditions it is enough to point out that such result might appear, and the single fracture procedure described in this work can handle such a result.

With Carter type leak off ${q_l}^{(2)}$ (4) shown on Figure (20), a similar issue of unexpected solution at $t = 1$ is present. Here fractures enter extended slow shut down period, which is terminated rapidly at $t \approx 10^4$. Note that this result was tested for conformance with fluid balance equation (Subsection 3.8.4).

The (158) interpretation of $\tau(x)$ is not shown here, as it was not possible to obtain any good solutions.

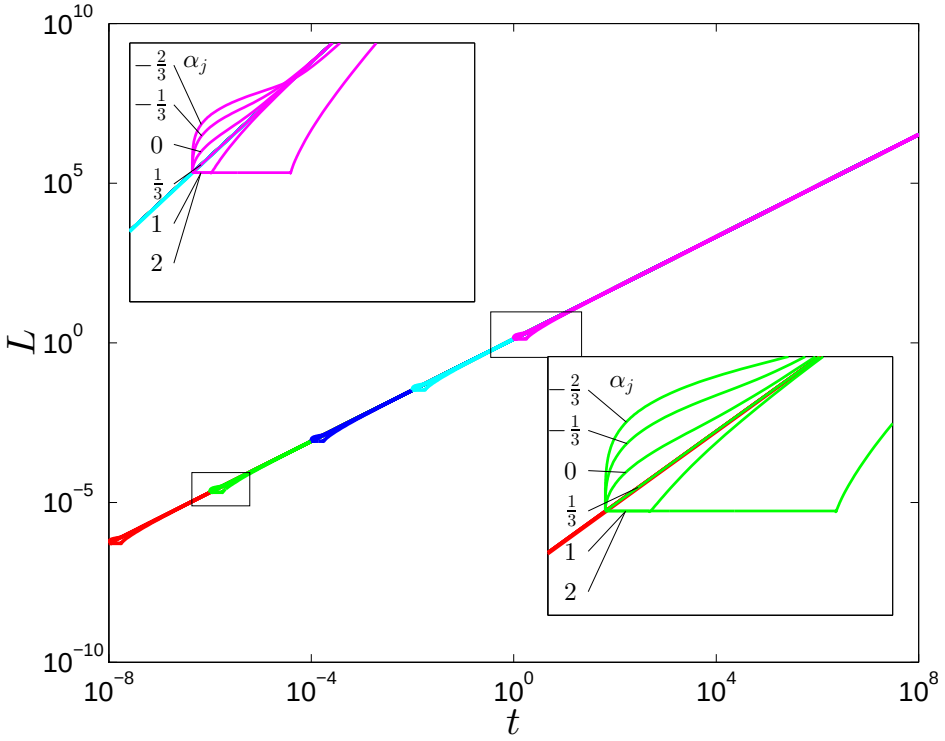

Figure 18: Varying initial shape, zero leak off.

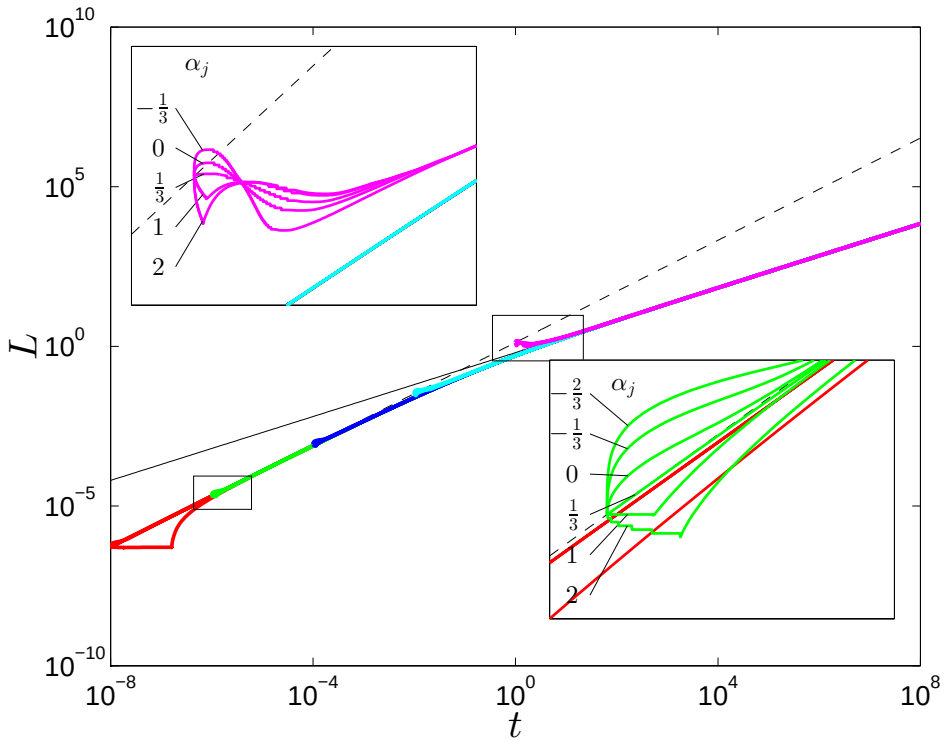

Figure 19: Varying initial shape, Carter leak off $q_l{}^{(1)}$ (4). Leak off allowed at initial length (159)

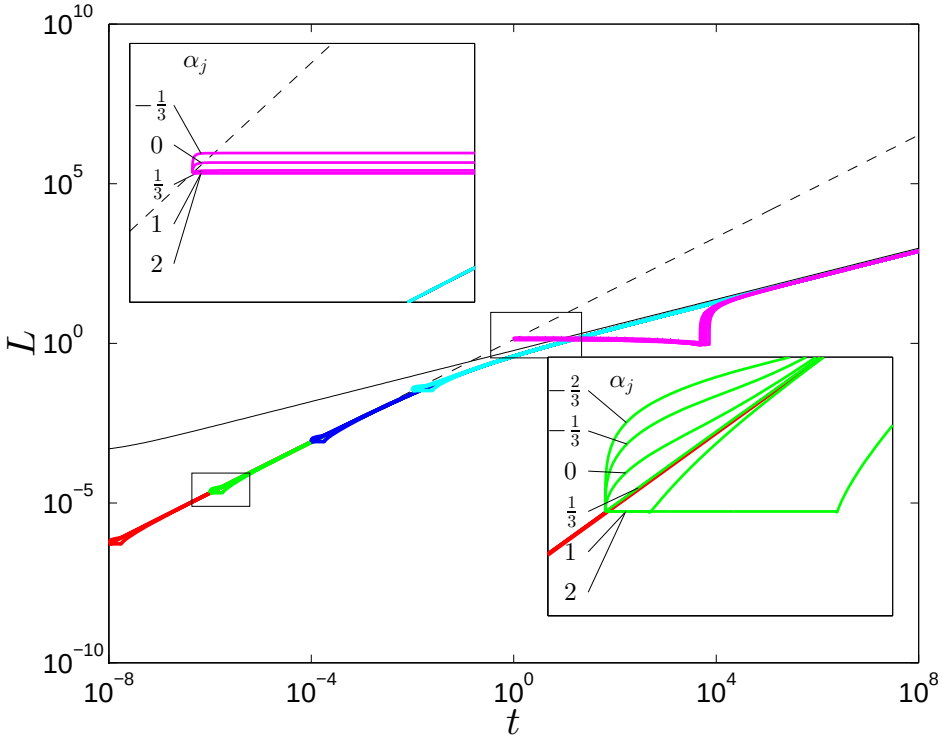

Figure 20: Varying initial shape, pressure Carter leak off $q_l{}^{(2)}$ (4). Leak off allowed at initial length (159)

3.3.4 *Fractures with added linear extension to the initial shape*

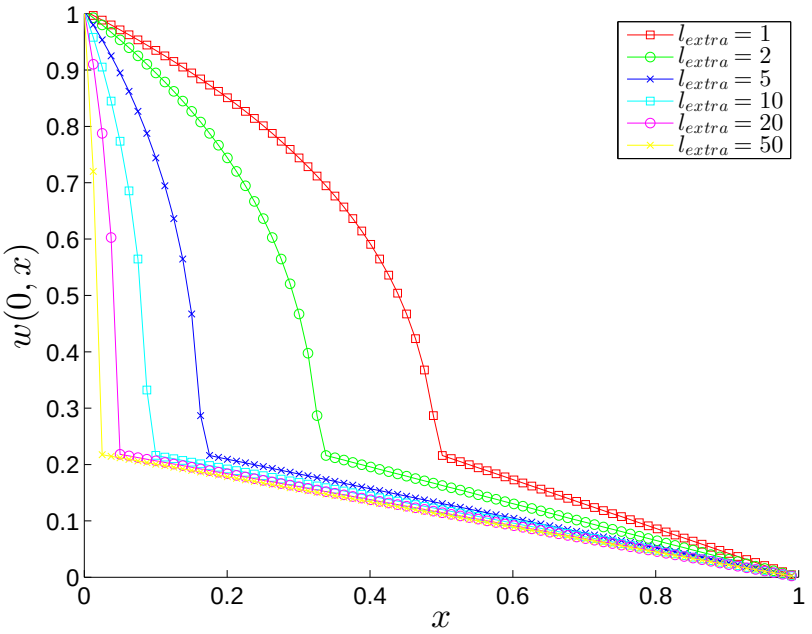

Figure 21: Aperture of fractures with added linear extension: $l_{extra} = 1, 2, 5, 10, 20, 50$

For the last test of initial condition modification lets consider if the initial shape can be enlarged by addition of a long and thin extension at the crack tip. After this modification the crack should have new initial length:

$$l_* := l_*(1 + l_{extra}), \tag{117}$$

with addition of extra quantity $l_{extra} > 0$, that is a multitude of original length. Initial fracture width changes as well, namely the old part obtained from self-similar solution is squeezed along x-direction, while linear function covers amount contributed by l_{extra}. This change in initial crack width can be written as:

$$w_*(x) := \begin{cases} w_*\left(x(1 + l_{extra})\right) & \text{if } 0 \le x \le x_* \\ w_*\left(x(1 + l_{extra})\right) \frac{1-x}{1-x_*} & \text{if } x_* < x \le 1, \end{cases} \tag{118}$$

and x_* is the connection point:

$$x_* = \frac{1 - \varepsilon}{1 + l_{extra}}, \tag{119}$$

where ε is a small value used in ε-regularisation. (see Subsection 2.5.1).

To account for the change in computation of opening times (158) and (159), the original used self-similar length inverse is changed to:

$$l^{-1} = l^{-1}\left(\frac{x}{1 + l_{extra}}\right). \tag{120}$$

which is later used to compute $\tau(x)$ in numerical leak off scheme (Subsection (3.8.2)). The considered values of l_{extra} are:

$$l_{extra} = \{1,\ 2,\ 5,\ 10,\ 20,\ 50,\ 100,\ 200\}.$$

As the following modification of initial solution is much easier to visualize, on Figure 21 a number of initial fracture openings is shown.

Yet again, with zero leak off the modification of initial condition contributed to no significant difference. Figure (22) shows how each extended fracture remains essential in storage regime, until merged with the asymptote.

With leak offs ${q_l}^{(1)}$ and $q_l^{(2)}$ (4) the added linear extensions closes, and the trajectories approach the asymptote. This behavior is much more rapid for pure Carter leak off ${q_l}^{(1)}$, Figure (23), than for pressure proportional variant ${q_l}^{(2)}$ shown on Figure (24). Furthermore for both of these leak offs, the addition of linear extensions does cause a great number of computations to fail. This could be used as a starting point if looking for a more reliable algorithm.

The (158) interpretation of $\tau(x)$ is also not shown here, as the computations failed in producing any good results.

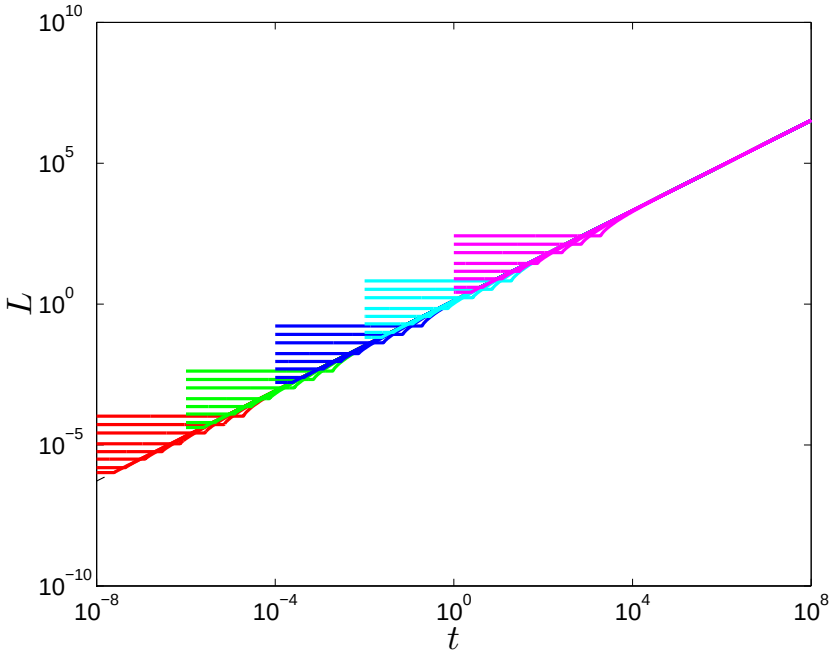

Figure 22: Adding linear extension, zero leak off.

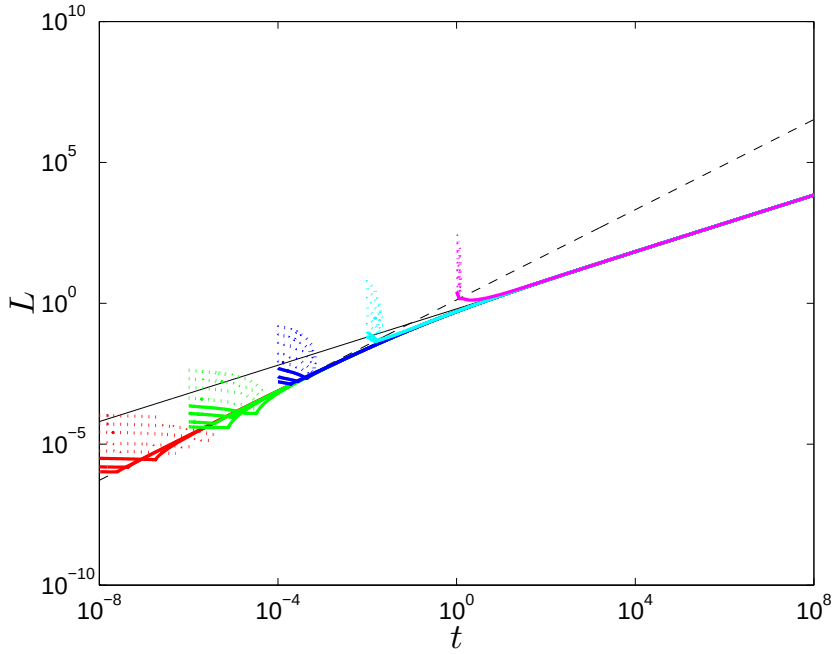

Figure 23: Adding linear extension, Carter leak off ${q_l}^{(1)}$ (4). Leak off allowed at initial length (159)

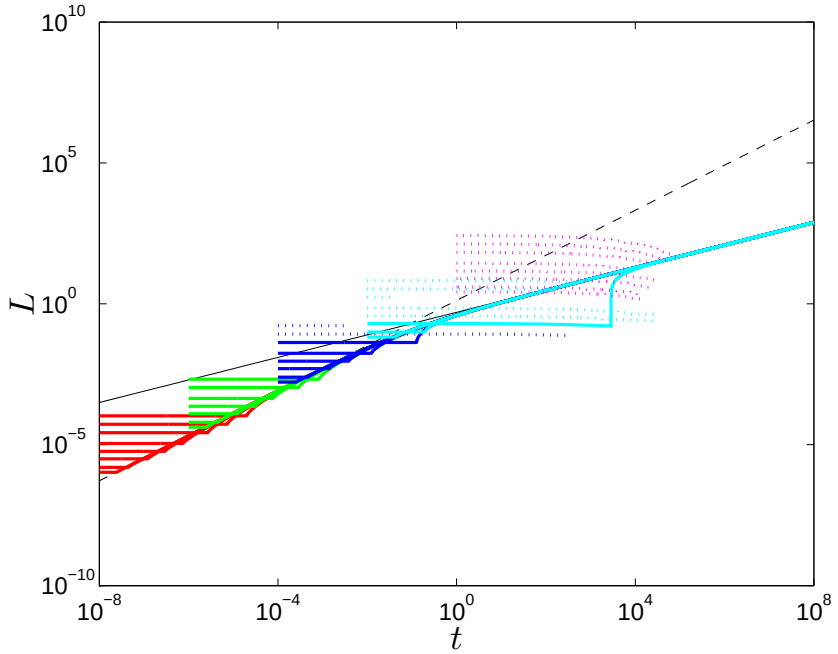

Figure 24: Adding linear extension, pressure Carter leak off ${q_l}^{(2)}$ (4). Leak off allowed at initial length (159)

3.3.5 *General conclusions from changing initial conditions.*

One can observe that in the vast majority of successful computation[7] the outcome tends to the expected large asymptote regardless of applied modifications to the initial conditions. This phenomena can be explained by taking a closer look at Figure 25a. Although the initial shape is much different than what forms in most fracture simulations, which generally closely resembles the lead asymptote $(1-x)^{\frac{1}{3}}$, it can be observed that these fractures profiles adjust to resemble this casual profile. Quite remarkably in both cases a new propagating front can be observed that appears as a fracture within the main background fracture. This inside fracture front itself propagates towards the tip $x = 1$, and should be governed by an equation similar to the speed equation (19) used for the main fracture front. Interestingly, as shown by initial conditions variants with increased fracture lengths, the fracture will not propagate significantly, that is remain in storage regime, until this inside propagating front joins with the tip. This process is however much more difficult to compute as the benefits of ε-regularization do not cover this additional in fracture propagating front.

Another general observation is, in case of leak off enabled simulations, that there seams to be a relation between the placement of the initial starting point relative to the starting self similar asymptote (271) and the large time asymptote (274) or (275) and the reliability of computational scheme. The locations of all starting points $(t, L(t))$ are shown on Figures 25b and 25c. If the initial condition places the start $(t, L(t))$ above the large time asymptote, the computations are apparently much more likely to fail. Also note that the less stable a computation is the longer it takes to finish. The systems that succeeded in producing results, would do so in just a few seconds, while the failed computations could run for minutes before an invalid solution was produced, or a solver exception was thrown. This means that proper choice of initial condition will have significant impact on computational performance.

Other observations can be summed up in the following points:

- Alerting initial conditions also indirectly changes interpretation of $\tau(x)$.
- Ability to handle closing fractures, being able to compute shut down regime, allows to carry simulations from a wider range of initial conditions.
- It appears that using zero leak off self similar solution is the most sensible choice.

7 A successful computation here means that a solution was obtained that ends at designated t_{end} and all the fluid volume can be accounted for (164).

- Small initial times and short fractures are preferable as initial conditions.
- Computations with zero leak off are much more reliable and predictable.
- Other leak off regimes produce less manageable results.

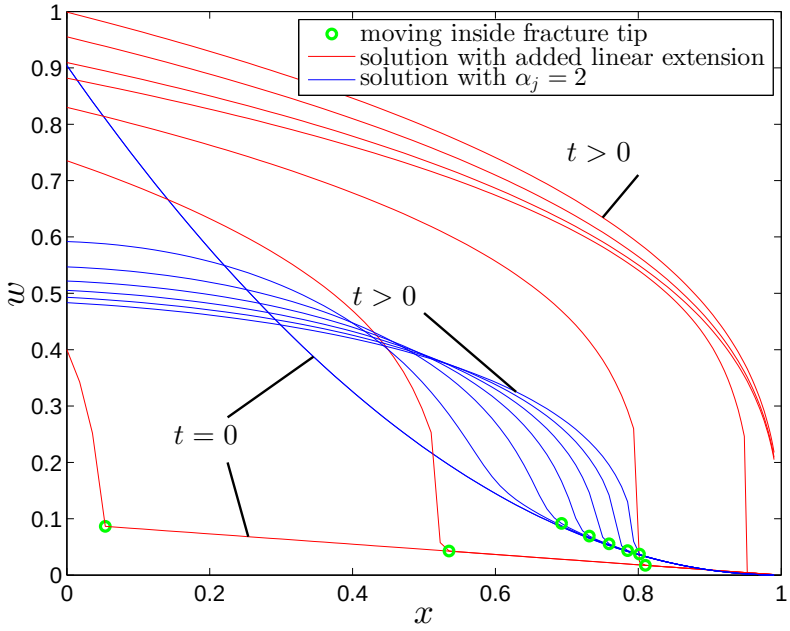

(a) Evolution of two modified fracture profiles. Both of these eventually converge to a more natural fracture shape. However it can be observed how another internal fracture shapes develops that overrides the initial condition.

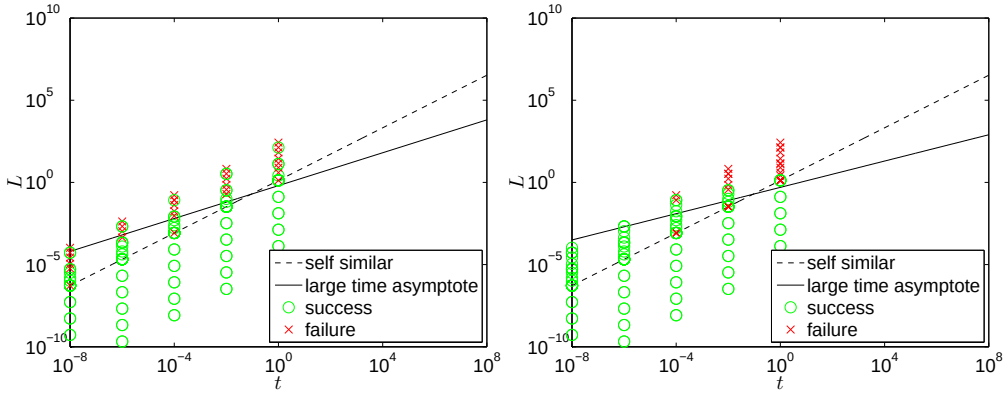

(b) Successful and failed starting points, Carter leak-off $q_l{}^{(1)}$ (4).

(c) Successful and failed starting points, pressure proportional Carter leak-off $q_l{}^{(2)}$ (4).

Figure 25: General observations on modified initial conditions.

3.4 COMPUTATION ACCURACY

3.4.1 *Effect of tip boundary condition.*

The presentation of computational accuracy should begin with comparison of the alternative approaches to defining the regularized boundary condition at the tip point $x = 1 - \varepsilon$.

The first approach is based on the ε-regularization technique, as it was defined in [54] and [65], and will be denoted as U_*(81). The second approach takes into account the two terms of asymptotics as described in Section 2.3 and Subsection 3.2.2.2. Additionally, for variable U, two different forms, linear U_l (88) and nonlinear U_n (89), will be considered here. Naturally a large range of tip conditions could be compared, but these three should be enough for the purpose of this test.

One can expect that the two term conditions would have a clear advantage, at least in cases when the solution smoothness near the crack tip deteriorates due to the singularity of the leak-off function. Table 2 shows accuracies obtained with U variable system and confirms such a prediction. Indeed, the relative errors of the solutions δU_l or δU_n are at least one order of magnitude lower than that in the case of δU_*. Interestingly for non-singular leak-off function, the improvement is even greater, especially on uniform mesh.

These computation was also repeated for the three different benchmarks reported in [65]. These correspond to leak-off functions vanishing near the crack tip. In these tests the accuracies of conditions based on two terms of asymptotics were always at least two orders of magnitude lower than that reported in the previous paper [65].

There is no observable difference between the solutions δU_l and δU_n in Table 2, at least for those two benchmarks and this particular choice of parameters ($N = 100$). However, it will be shown later, for larger N values or more leak-off dominant regime ($Q_l/q_0 \sim 1$), the nonlinear condition will show its advantage.

		Comparison of conditions (81), (88), (89)					
		$q_l^{(1)}$ $Q_l/q_0 = 0.9$			$q_l^{(3)}$ $Q_l/q_0 = 0.5$		
	$\epsilon =$	10^{-2}	10^{-4}	10^{-6}	10^{-2}	10^{-4}	10^{-6}
δU_*	$x_m^{(1)}$	1.6e-1	1.4e-1	1.3e-1	6.1e-3	3.7e-3	3.7e-3
	$x_m^{(2)}$	1.4e-1	7.6e-2	6.3e-2	4.5e-3	9.3e-5	8.9e-5
δU_l	$x_m^{(1)}$	5.0e-2	1.4e-2	1.7e-2	1.2e-5	1.1e-5	1.1e-5
	$x_m^{(2)}$	5.0e-2	1.7e-3	2.0e-3	4.9e-5	8.2e-5	8.7e-5
δU_n	$x_m^{(1)}$	4.4e-2	1.2e-2	1.3e-2	2.2e-5	1.3e-5	1.3e-5
	$x_m^{(2)}$	4.4e-2	9.9e-4	1.8e-3	4.2e-5	8.2e-5	8.7e-5

Table 2: Comparison accuracies obtained with different tip boundary conditions. U_* refers to one asymptotic term regularized boundary (81) , while U_l and U_n correspond to two terms approximation (linear (88) and nonlinear (89), respectively).

3.4.2 *Comparison of w, U and Ω variables.*

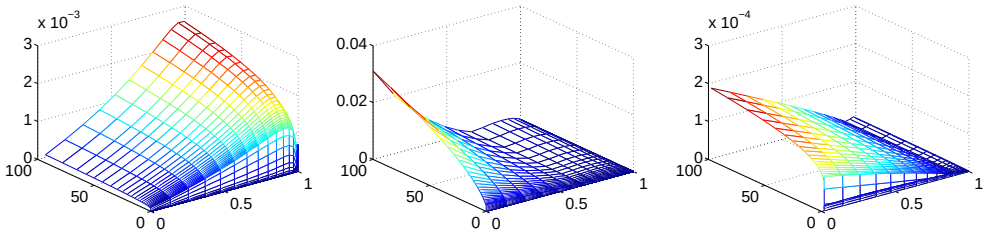

(a) Δw, $\varepsilon = 10^{-3}$ (b) ΔU_n system, $\varepsilon = 10^{-5}$ (c) $\Delta\Omega$ system, $\varepsilon = 5 \cdot 10^{-3}$

Figure 26: Absolute solution errors for benchmark $q_l^{(1)}$ with ratio $Q_l/q_0 = 0.9$ and nonuniform mesh $x_m^{(2)}$ ($\delta = 2$) with $N = 100$ nodal points.

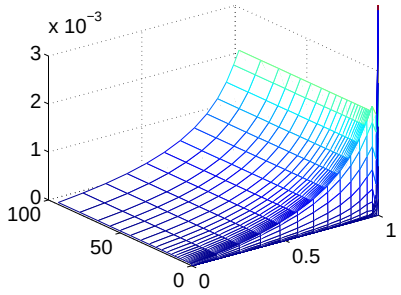

(a) ∂w, $\varepsilon = 10^{-3}$

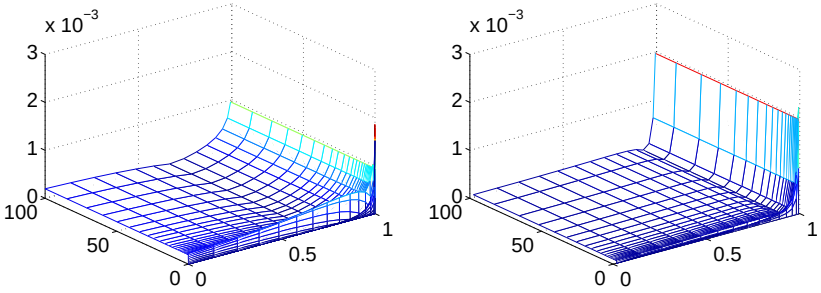

(b) ∂U_n system, $\varepsilon = 10^{-5}$ (c) $\partial\Omega$ system, $\varepsilon = 5 \cdot 10^{-3}$

Figure 27: Relative solution errors for benchmark $q_l^{(1)}$ with ratio $Q_l/q_0 = 0.9$ and nonuniform mesh $x_m^{(2)}$ ($\delta = 2$) with $N = 100$

The presented variable approaches w (32), U (65) and Ω (77), will be now compared against each other. The relative errors of respective dependent variables are difficult to compare directly in a sensible manner. Although the errors for w and U are interrelated via relationship $\delta U = 3\delta w$, their comparison with $\delta\Omega$ requires additional differentiation of Ω to obtain w. This conversion could introduce additional error. On the other hand, there exists a common component of the solutions, the crack length δL, which can be used for direct comparison.

To compute the accuracies of all three mentioned variable approaches, tests on all six benchmark solutions A.2 for each variable was performed. For each tests grids $x_m^{(1)}$ and $x_m^{(2)}$ with $N = 100$ were used. It turned out that the optimal ε differs slightly depending on the type of mesh chosen, benchmark variant, and variable choice. The values of ε were selected such so each system produced the best results.

The results of these computations are collected in Tables 3, 4, 5 and 6. The relative error of solution δf, the absolute error of solution Δf and the relative error of the crack length δL are presented. The results of all variable formulations are at least of order 10^{-3} accurate for all the choices of grids and benchmarks. However as it can be observed these accuracies improve even further, for some more specific benchmark and grids combinations. The $x_m^{(2)}$ grid allays offers better accuracy than $x_m^{(1)}$, by about one order of magnitude. By compering δL it can concluded that Ωvariable offers the best accuracy. Nevertheless the accuracy obtained with w and$U$ variables could be also accepted as good enough, and these approaches might come out as more straightforward to use. The time taken by ODE15s to obtain these solutions, was similar for all the variables, none appeared to offer significant advantage in computation time. Additionally Figures 27 and 26 show distribution of solution relative and absolute errors. These are stable in time, and quite similarly distributed if relative error is taken into account, thous could be potentially affected by the same source significant numerical error (this will be dealt with in Section 3.6).

		Dynamic system built on the variable w					
		$Q_l/q_0 = 0.9$			$Q_l/q_0 = 0.5$		
		$q_l^{(1)}$	$q_l^{(2)}$	$q_l^{(3)}$	$q_l^{(1)}$	$q_l^{(2)}$	$q_l^{(3)}$
δw	$x_m^{(1)}$	8.5e-3	5.4e-3	5.6e-3	5.2e-3	4.0e-3	3.5e-3
	$x_m^{(2)}$	2.2e-3	2.6e-3	2.9e-3	1.8e-3	1.9e-3	2.0e-3
Δw	$x_m^{(1)}$	7.4e-3	9.1e-3	8.8e-3	4.3e-3	4.6e-3	4.7e-3
	$x_m^{(2)}$	2.8e-3	3.0e-3	3.2e-3	2.1e-3	2.1e-3	2.2e-3
δL	$x_m^{(1)}$	1.2e-3	1.3e-3	1.1e-3	5.2e-3	5.3e-3	5.2e-3
	$x_m^{(2)}$	4.0e-4	3.8e-4	3.1e-4	1.8e-3	1.8e-3	1.8e-3

Table 3: Performance of the solver based on the dependent variable w for number of nodal points $N = 100$ and various benchmarks. Values of the regularized parameter are $\varepsilon = 5 \cdot 10^{-3}$ and $\varepsilon = 10^{-3}$ for the meshes for $x_m^{(1)}$ and $x_m^{(2)}$ respectively

		System built on U_l and condition (88)					
		$Q_l/q_0 = 0.9$			$Q_l/q_0 = 0.5$		
		$q_l^{(1)}$	$q_l^{(2)}$	$q_l^{(3)}$	$q_l^{(1)}$	$q_l^{(2)}$	$q_l^{(3)}$
δU	$x_m^{(1)}$	1.4e-2	1.0e-2	1.2e-4	2.0e-3	1.4e-3	1.1e-5
	$x_m^{(2)}$	1.2e-3	6.0e-4	2.5e-4	2.2e-4	1.7e-4	8.6e-5
ΔU	$x_m^{(1)}$	7.1e-2	4.4e-2	2.0e-3	6.6e-3	4.5e-3	3.9e-4
	$x_m^{(2)}$	3.1e-2	2.9e-2	7.9e-3	3.5e-3	3.2e-3	7.9e-4
δL	$x_m^{(1)}$	4.4e-4	2.8e-4	4.4e-6	4.3e-4	2.9e-4	5.6e-6
	$x_m^{(2)}$	2.6e-4	2.4e-4	1.2e-4	9.5e-5	8.3e-5	4.3e-5

Table 4: Numerical results for the system built on the dependent variable U with the linear regularized condition (88) for $N = 100$ and different ε for the uniform and nonuniform meshes ($\varepsilon = 10^{-4}$ and $\varepsilon = 10^{-5}$, respectively).

		System built on U_n and condition (89)					
		$Q_l/q_0 = 0.9$			$Q_l/q_0 = 0.5$		
		$q_l^{(1)}$	$q_l^{(2)}$	$q_l^{(3)}$	$q_l^{(1)}$	$q_l^{(2)}$	$q_l^{(3)}$
δU	$x_m^{(1)}$	1.2e-2	9.2e-3	4.3e-5	1.9e-3	1.4e-3	1.3e-5
	$x_m^{(2)}$	1.2e-3	6.0e-4	2.5e-4	2.0e-4	1.7e-4	8.6e-5
ΔU	$x_m^{(1)}$	6.4e-2	4.1e-2	1.7e-3	6.5e-3	4.4e-3	4.0e-4
	$x_m^{(2)}$	3.1e-2	2.9e-2	7.9e-3	3.5e-3	3.2e-3	7.9e-4
δL	$x_m^{(1)}$	4.1e-4	2.7e-4	1.5e-6	4.2e-4	2.9e-4	6.3e-6
	$x_m^{(2)}$	2.6e-4	2.4e-4	1.2e-4	9.5e-5	8.3e-5	4.3e-5

Table 5: Results for the solver based on the dependent variable U for nonlinear regularized condition for $N = 100$ and various benchmarks. Values of the regularized parameter are $\varepsilon = 10^{-4}$ and $\varepsilon = 10^{-5}$ for the meshes for $x_m^{(1)}$ and $x_m^{(2)}$, respectively

		Dynamic system built on variable Ω					
		$Q_l/q_0 = 0.9$			$Q_l/q_0 = 0.5$		
		$q_l^{(1)}$	$q_l^{(2)}$	$q_l^{(3)}$	$q_l^{(1)}$	$q_l^{(2)}$	$q_l^{(3)}$
$\delta\Omega$	$x_m^{(1)}$	2.5e-3	8.7e-4	3.0e-4	5.6e-4	3.3e-4	4.2e-4
	$x_m^{(2)}$	2.0e-3	7.3e-4	3.6e-4	4.4e-4	2.7e-4	3.1e-4
$\Delta\Omega$	$x_m^{(1)}$	9.4e-5	1.7e-5	5.9e-5	1.1e-4	1.3e-4	1.5e-4
	$x_m^{(2)}$	1.9e-4	2.1e-4	2.3e-4	1.3e-4	1.4e-4	1.4e-4
δL	$x_m^{(1)}$	2.7e-6	5.0e-7	1.7e-6	2.1e-5	2.5e-5	2.9e-5
	$x_m^{(2)}$	5.5e-6	6.2e-6	6.7e-6	2.6e-5	2.7e-5	2.8e-5

Table 6: Computation accuracy for the solver based on the dependent variable Ω for $N = 100$ and $\varepsilon = 10^{-2}$ for $x_m^{(1)}$ and $\varepsilon = 5 \cdot 10^{-3}$ for $x^{(II)}$.

3.4.3 *Accuracy vs N and ε*

Plots presented on Figure 28 and 29 present relative accuracies, the maximum δw, δU, $\partial\Omega$ and ∂L for all of the considered variable formulations, as functions of the number of the grid points N. The used benchmark assumes $Q_l/q_0 = 0.9$ (see Appendix A.2). Three different values of the regularization parameter $\varepsilon = 10^{-3}, 10^{-4}$ and 10^{-5} were chosen.

On Figure 28 two basic tendencies can be observed. The error decrease monotonicity with N, up to some saturation level. This level is different for all dependent variables and values of ε, and in some cases is reached for $N > 1000$ (and thus cannot be identified in the figure). The second trend is appears when comparing results for different values of ε. For each dependent variable there exists an optimal ε minimizing the solution error. This value however depends on N. It is not a surprise that the optimal stiffness properties and the maximal solution accuracy are not achieved for the same values of the regularization parameter ε. To increase computational accuracy one needs to decrease ε and increase number of the nodal points N. However, both of these leads to increase of the condition ratio.

Figure 29 compares the relative errors of the crack length δL . The values of the relative errors $\delta f = \{\delta w, \delta U, \partial\Omega\}$ and the respective $\delta L^{(f)}$ are directly related to each other. The following analysis identifies this relationship.

Using (84), after some algebra:

$$\delta f \approx \delta e_1^{(f)} + (\delta e_2^{(f)} - \delta e_1^{(f)}) \frac{e_2^{(f)}}{e_1^{(f)}} \varepsilon^{\alpha_2 - \alpha_1}. \tag{121}$$

For the benchmark $q_l^{(1)}$ and $Q_l/q_0 = 0.9$ which always provides the worst accuracy in our computations, one can conclude

$$\delta w \approx \frac{1}{3}\delta U \approx \delta w_0 + \frac{1}{10}(\delta w_1 - \delta w_0)\sqrt[6]{\varepsilon}, \tag{122}$$

$$\delta\Omega \approx \delta w_0 + \frac{8}{90}(\delta w_1 - \delta w_0)\sqrt[6]{\varepsilon}. \tag{123}$$

Finally, from (31) we can derive

$$\delta L \approx \frac{3}{2}\delta w_0. \tag{124}$$

It is clear from relations (122) and (123) that the relative errors of the respective dependent variables also depend on the quality of approximation of the second term in the regularized boundary condition (84).

Interestingly, the results presented on Figure 29 show that the value of ε which provides the lowest relative opening error δf, of the dependent variable f does not necessarily give the best accuracy of the crack length δL. Moreover, the relation $\varepsilon = \varepsilon_L(N)$ is much more sensitive to the variation of N than $\varepsilon = \varepsilon_f(N)$. Indeed, one can observe local minima (see Figure 29 a) and b)) while there is no such in the respective graphs for δf (Figure 28).

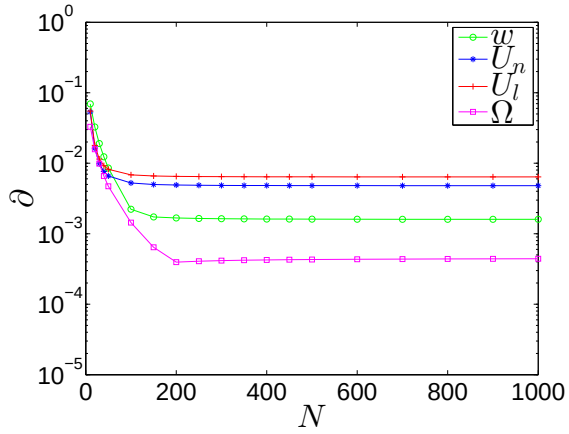

(a) $\varepsilon = 10^{-3}$

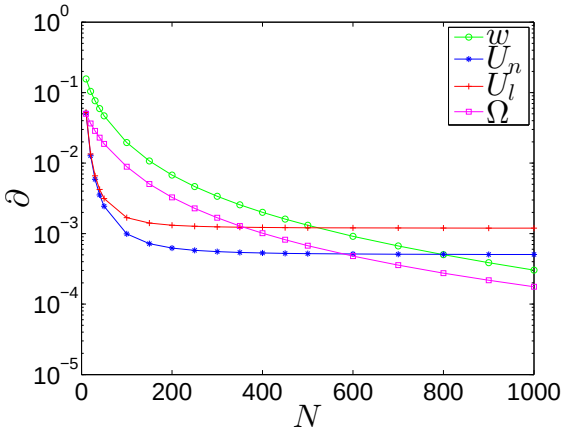

(b) $\varepsilon = 10^{-4}$

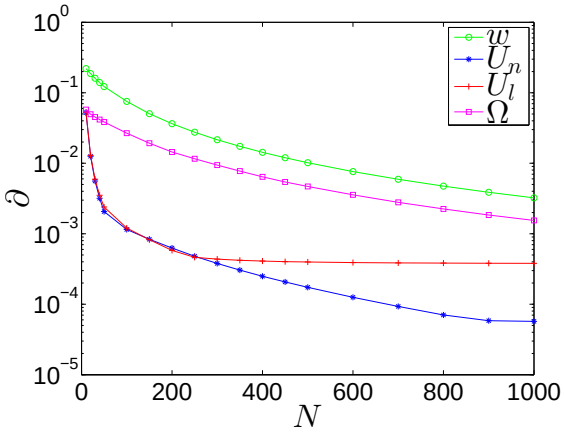

(c) $\varepsilon = 10^{-5}$

Figure 28: Maximum relative errors δw, δU and $\delta\Omega$, against different N of grid points, mesh $x_m^{(2)}$ ($\delta = 2$), benchmark with $q_l^{(1)}$ and $Q_l/q_0 = 0.9$. (U_l and U_n refers to (88) and (89))

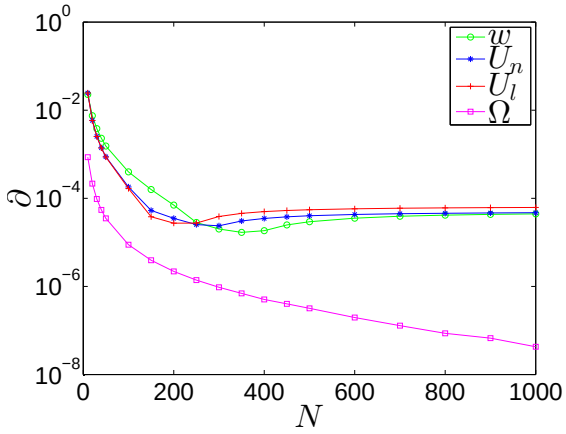

(a) $\varepsilon = 10^{-3}$

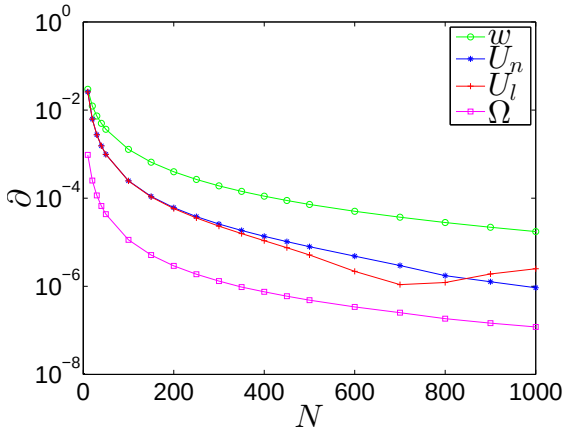

(b) $\varepsilon = 10^{-4}$

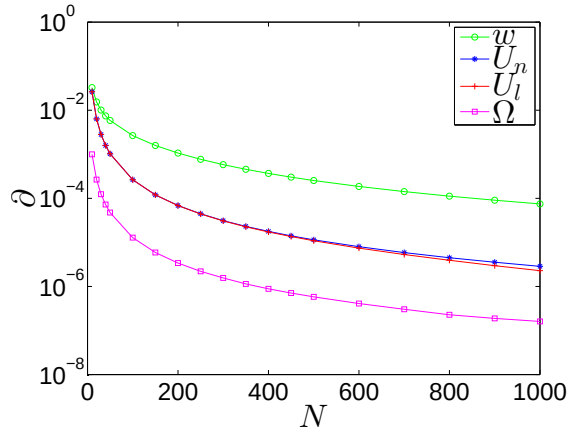

(c) $\varepsilon = 10^{-5}$

Figure 29: Maximum relative errors δL for systems build on w, U and Ω variables, against different N of grid points, mesh $x_m^{(2)}(\delta = 2)$, benchmark with $q_l^{(1)}$ and $Q_l/q_0 = 0.9$. (U_l and U_n refers to (88) and (89)

3.4.4 *Different benchmark γ*

The formulated benchmarks solutions (Appendix A.2.1) uses the parameter γ, which value can be linked with fracture propagation regime since $L(t) = (1+t)^{\frac{3\gamma+1}{2}}$ (267). By testing against different values of this parameter one can make prediction on accuracy if different propagation regimes are encountered.

As can be seen on Figure 30, for all dependent variables the crack length error rapidly decreases for $\gamma \to -1/3$. Indeed, this is the case when $L(t) \sim L_0$, and crack propagation is minimal, which corresponds to the storage regime, a stagnant static fracture. For w and U solvers, δL remains very stable over most of the analyzed interval. The solver based on Ω exhibits quite different behavior. For γ greater than about 1.4, the error decreases to achieve the level of its ultimate accuracy, the same as for $\gamma \to -1/3$. Depending on the crack propagation regime, this solver can give up to two orders of magnitude better accuracy of $L(t)$.

Figure 31 shows, that respective dependent variables openings are much less sensitive to the changes of γ that the crack length. In the considered interval each solver provides a relatively stable level of accuracy (within the same order of magnitude).This test proves that using the solver based on Ω is especially beneficial when dealing with the problems of fast propagating fractures (large values of γ), but again all of the considered variable formulations produce relatively good results.

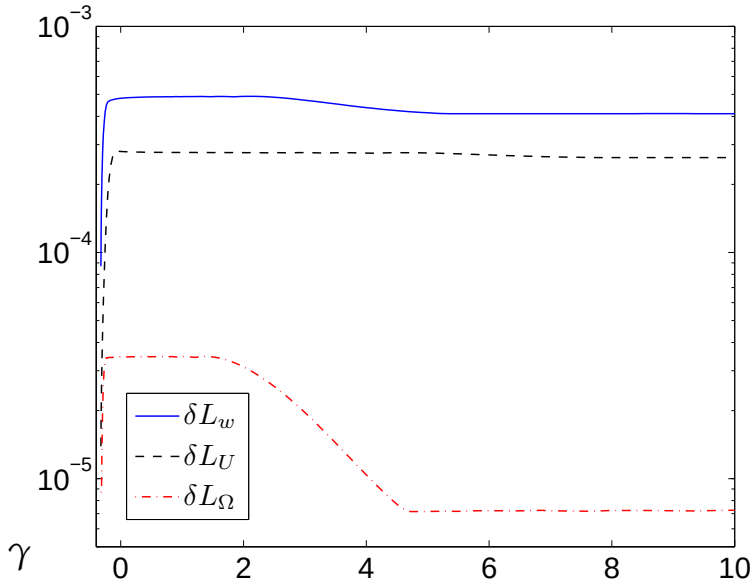

Figure 30: The relative errors of the crack length for different dependent variables as functions of γ.

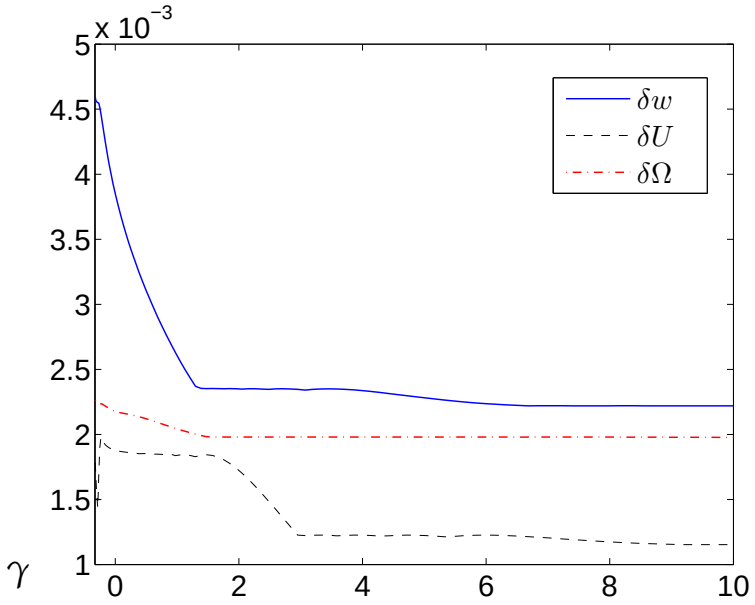

Figure 31: The maximal relative errors of respective dependent variables as functions of γ.

3.4.5 *Conclusions on numerical accuracy*

The general conclusions that sum up numerical accuracy analysis performed in this Section are:

- Similarly as in case of the stiffness analysis (Section 3.1), the solution accuracy is affected more by the value of Q_l/q_0 than by the leak-off function behavior near the crack tip. There is a trend of simultaneous increase of the ratio Q_l/q_0 and the relative errors of dependent variables δf. However this tendency is does not hold (or may be even reversed) when analyzing δL.
- In case of the dependent variable U, the non-linear (89) variation of the boundary condition achieves the best accuracies in terms of variable opening relative error.
- When comparing δL, the dynamic system for Ω gives the best results. The dynamic system for w is the worst performing scheme.
- Since Ω vanishes near the crack tip faster than other variables, one could expect the worst relative error in this case. Surprisingly, even when contrasting the relative (incomparable) errors of the respective dependent variables with each other, the system for Ω seems to be the best choice. The advantage of Ω over w and U is especially pronounced for the benchmarks variants with a higher ratio Q_l/q_0.
- Better solution accuracy is obtained for the non-uniform mesh in almost every case.

To complete the accuracy analysis, let consider some critical regime of crack propagation. Assume that the leak-off flux almost entirely balances the volume of fluid pump in rate. When taking the Carter type benchmark (266) with $b_1 = b_2 = 1$, one obtains the fluid balance ratio $Q_l/q_0 = 0.9857$. This gives very strong variation of the particle velocity function along the crack length, $\gamma_v = 2.07$ as defined by (270). Considering the previous conclusions on the influence of the ratio Q_l/q_0 on solution accuracy (which in fact confirms the observations from [65]), one can predict that the solution error will increase appreciably in comparison with the figures shown in Tables 3, 4, 5 and 6. In order to verify this assertion the computations were carried out. The results of are presented in Table 32. Here, the symbols δU_l and δU_n stand for the relative error of U obtained for the conditions (88) and (89), respectively. The subscript of δL informs us which dynamic system the corresponding result was obtained for.

	$\epsilon = 10^{-2}$		$\epsilon = 10^{-3}$		$\epsilon = 10^{-4}$		$\epsilon = 10^{-5}$	
	$x_m^{(1)}$	$x_m^{(2)}$	$x_m^{(1)}$	$x_m^{(2)}$	$x_m^{(1)}$	$x_m^{(2)}$	$x_m^{(1)}$	$x_m^{(2)}$
δw	1.6e-2	1.6e-2	3.4e-2	2.5e-3	6.8e-2	2.1e-2	–	8.2e-2
δU_l	1.9e-1	1.9e-1	8.2e-2	8.1e-2	1.0e-1	4.3e-2	1.5e-1	2.3e-2
δU_n	4.8e-2	4.8e-2	1.1e-2	6.3e-3	1.9e-2	3.2e-3	2.0e-2	9.1e-3
$\delta\Omega$	2.6e-3	5.0e-3	3.0e-3	1.7e-3	3.9e-3	9.9e-3	4.0e-3	3.0e-2
δL_w	2.0e-4	2.6e-4	2.0e-3	1.8e-4	3.4e-3	3.9e-4	–	6.2e-4
δL_l	1.2e-3	1.1e-3	2.7e-4	1.3e-4	7.5e-4	2.8e-4	1.0e-3	3.2e-4
δL_n	2.5e-4	1.2e-4	1.8e-4	2.6e-4	2.5e-4	3.0e-4	2.6e-4	3.2e-4
δL_Ω	8.1e-7	4.7e-7	1.1e-6	1.1e-6	1.2e-6	1.2e-6	1.2e-6	1.2e-6

Figure 32: Accuracies for limiting (critical) variant of the benchmark solution ($Q_l/q_0 = 0.9857$, $\gamma_v = 2.07$) . The blanks represents cases when ODE15s could not complete the computations.

3.5 COMPARISON WITH KNOWN RESULTS

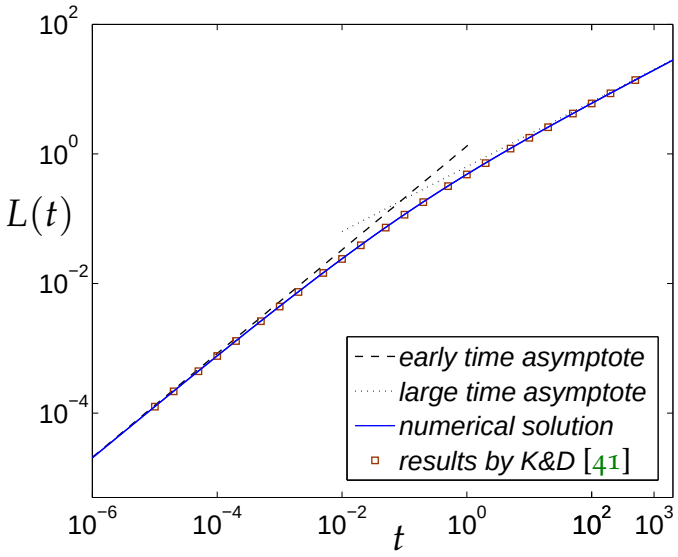

Figure 33: The crack length evolution in time.

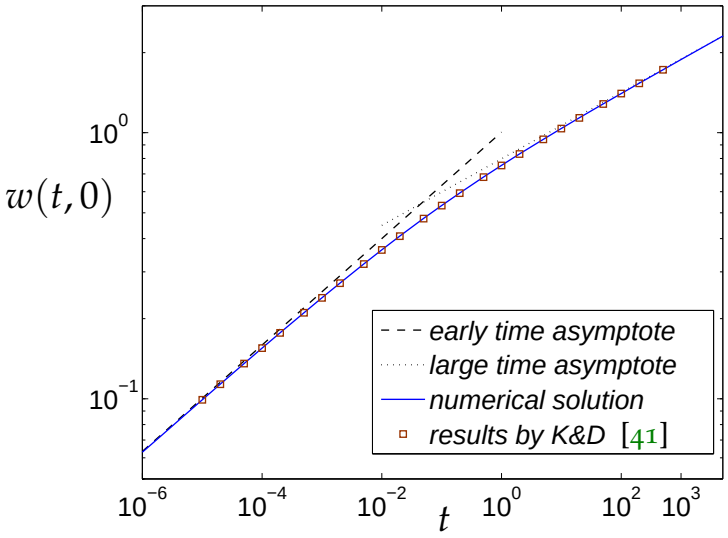

Figure 34: The evolution of crack opening at zero point, $w(t,0)$.

Although the benchmark solution used in this work (Appendix A.2), includes the leak-off term with a square root singularity, there is no analytical solution available in the literature for the Carter leak-off (4).

In [41] and [70], one can find the numerical results for this problem. However the original result by Nordgren [70] is presented as a low resolution figure, making it difficult to accurately interpret the

data. The more recent result by Kovalyshen will be used as a point of reference, as exact numerical values are given in [41] . Unfortunately the authors provided only some rough estimation of the solution error, but no direct comparison to a known solution, such as zero leak off result (271). The numerical method used in [41] is based on an implicit finite volume algorithm. The data collected in their Table 1 (p.332) describes the normalized values of the crack length, the crack propagation speed and the crack opening at $x = 0$, at a number of times steps in the interval $t \in [10^{-5}, 5 \cdot 10^{2}]$. Unfortunately the precise details on how this particular solution was obtained are not presented in great detail.

In Table 7, the results of using this work numerical scheme are presented in such a manner that these should correspond to those obtained by Kovalyshen [41]. Note that, due to different normalizations, the normalized crack length, L, is two times greater than respective value in that paper. This data was obtained by ODE15s using U variable on $N = 1000$ grid points, which should give the very best accuracy as shown by the analysis in Section 3.4. Additionally Figures 33 and 34 present the evolution of crack length $L(t)$, and crack aperture at inlet $w(t, 0)$. The data is presented against early time and large time asymptotic models (respective formula can be found also in[41]), and the numerical results for the transient regime given by Kovalyshen [41].

$\log(t)$	$L(t)$	$w(t,0)$	$u(t) \times 10$
-7	3.283747e-6	3.988347e-2	7.9701
-6	2.049209e-5	6.298786e-2	7.9355
-5	1.265786e-4	9.915967e-2	7.8716
-4	7.660018e-4	1.551088e-1	7.7536
-3	4.456291e-3	2.397462e-1	7.5185
-2	2.412817e-2	3.629593e-1	7.1173
-1	1.163591e-1	5.326638e-1	6.5267
0	4.849863e-1	7.541837e-1	5.8885
1	1.779508e0	1.037495e0	5.4408
2	6.035529e0	1.403522e0	5.1993
3	1.968511e1	1.883411e0	5.0847
4	6.308563e1	2.518338e0	5.0378
5	2.006370e2	3.362113e0	5.0146
6	6.360179e2	4.485636e0	5.0071
7	2.013373e3	5.982935e0	5.0029
8	6.369722e3	7.979082e0	5.0014

Table 7: Numerical solution of the PKN fracture with Carter leak off.

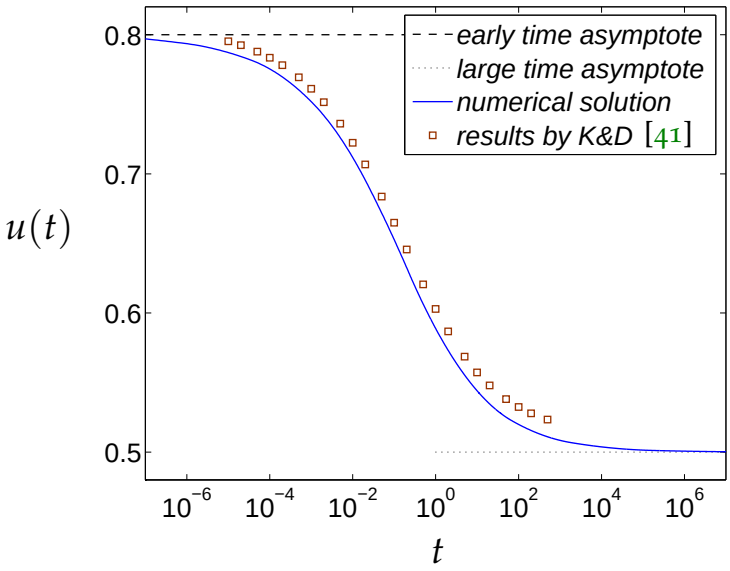

Figure 35: The evolution of the normalized crack propagation speed.

The analyzed time interval is $t \in [10^{-8}, 10^{8}]$ where the initial conditions correspond to the early time asymptote for $t = 10^{-8}$. The same initial time was used by [41] , but the authors presented their data starting from $t = 10^{-5}$. In order to increase the legibility of the graphs, the time axis is truncated to range $t \in [10^{-6}, 5 \cdot 10^{3}]$, while the complete data is presented in Table 7.

As can be seen in the Figure 33 and Figure 34, due to used scale, the solution is indistinguishable from that by [41]. But this type of graph was originally presented Nordgren [70], and it should be no surprise that a better presentation should be used to correctly compare the solutions. For this reason Figure 35 shows the normalized crack propagation speed, as defined by Kovalyshen in [41] .This shows that this work fits the asymptotes very well, which suggests its good quality. The solution by [41] approaches the asymptotic values much slower, and the interval it was presented on was caped to $t < 10^{-5}$ and $t > 5 \cdot 10^{3}$.

In the analyzed case, the value of the parameter $Q_l(t)/q_0(t)$ changes continuously with time from zero to unit. From the data presented in [65] and in this paper, one can conclude that for $N = 100$ nodal points, the relative error of the crack length changes from 10^{-6} to 10^{-4} with the increase of the parameter Q_l/q_0. On the other hand, analyzing the data from Figure 28 and 29 ($Q_l/q_0 = 0.9$), one can expect the achievable level of accuracy of the order 10^{-7} for $N = 1000$. This suggests that, the relative error of L varies between 10^{-4} and 10^{-6}.

In order to additionally assess the credibility of this work solution (computed for $N = 1000$ and presented in the Table 7), Figure 36

shows the relative deviations ∂L between this solution and other numerical solutions and the asymptotes:

- early and large time asymptotes;
- the solution by [41];
- a solution obtained for $N = 100$ grid points
- another solution obtained for $N = 1000$ grid points starting at $t_0 = 10^{-7}$.

When tracing the data from Figure 36 we can see that the deviations of L from the early and large time asymptotes at the ends of the considered interval are of the order 10^{-4}. Moreover, the relative deviation from the solution obtained for $N = 100$ points is of the same order over entire time interval. The discrepancy between the reference solution and the solution for $t_0 = 10^{-7}$ decreases rapidly with time. This observation confirms the credibility of the reference solution.

The relative discrepancies between the components of this work solution and the solution by [41] are shown on Figure 37. Here d_L, $d_{w(0,t)}$ and d_u refer to the deviations of the crack length, L, the crack opening, $w(t, 0)$ and the normalized crack velocity, u, respectively.

Considering the results presented in this Section, it is possible to believe that the data presented in Table 7 provide the accuracy **at least** of the order 10^{-4} for both, the crack length, L, and the crack opening at $x = 0$. Moreover, in the considerable time range ($10^{-6} < t < 10^{6}$), one can expect the error lower by up to two orders of magnitude. The normalized crack propagation speed u is computed with accuracy of one to two orders of magnitude lower. The level of accuracy for the results tabulated by[41] can be estimated as $10^{-3} \div 10^{-2}$ for L, $10^{-4} \div 10^{-3}$ for $w(t, 0)$ and of the order 10^{-2} for u.

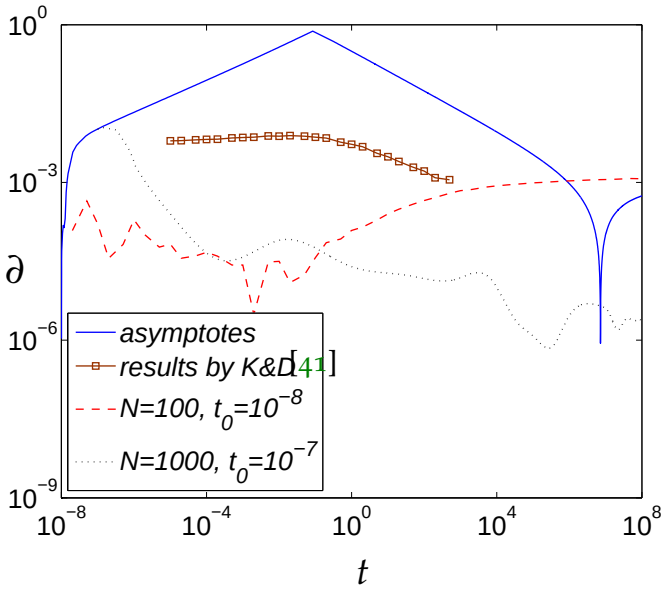

Figure 36: Relative deviations from the numerical solution for L.

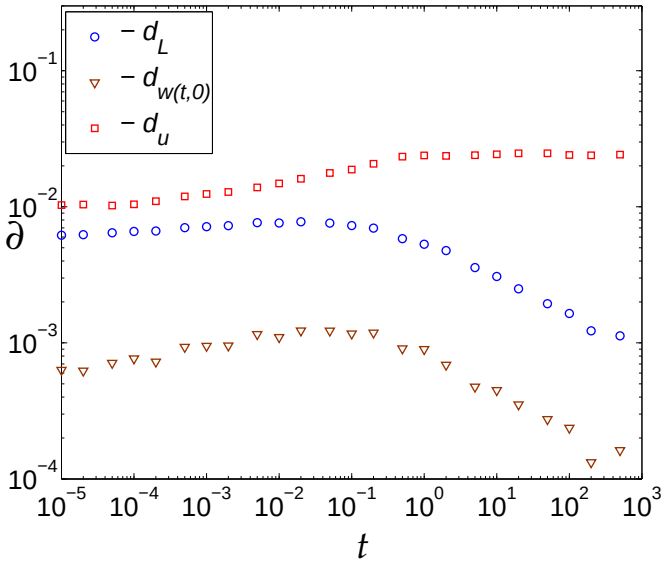

Figure 37: Relative deviations of the solution by [41], in terms of length d_l, inlet width $d_{w(t,0)}$ and normalized propagation velocity u, from the results reported in Table 7.

3.6 FURTHER IMPROVEMENTS TO DYNAMIC SYSTEMS

3.6.1 *Derivative approximation schemes*

For every numerical problem with numerical approximation of spatial derivatives one must make a choice of appropriate scheme for achieving this approximation. In this problem numerical approximation is used to compute $\frac{\partial}{\partial x}$ and $\frac{\partial^2}{\partial x^2}$, and the following numerical scheme for obtaining these were used.

3.6.1.1 *Central Finite Differences*

Probably the most casual approach to numerical approximation of derivatives are finite differences. In this work central scheme with variable interval length Δx_k is considered. It is already an odd choice as most casual sources present finite difference method derivation with fixed point spacing, the method used here is defined by:

$$\begin{aligned} \frac{\partial w}{\partial x}|_{x_k} &\approx \frac{1}{2}\left(\frac{\Delta w_{k+1}}{\Delta x_{k+1}} + \frac{\Delta w_k}{\Delta x_k}\right) \\ \frac{\partial^2 w}{\partial x^2}|_{x_k} &\approx \frac{1}{2}\left(\frac{1}{\Delta x_{k+1}} + \frac{1}{\Delta x_k}\right)\left(\frac{\Delta w_{k+1}}{\Delta x_{k+1}} - \frac{\Delta w_k}{\Delta x_k}\right), \end{aligned} \tag{125}$$

or in a computationally optimized and matrix representation friendly form:

$$\frac{\partial w}{\partial x}|_{x_k} \approx a_k w_{k-1} + b_k w_k + c_k w_{k+1} \tag{126}$$

$$a_k = -\frac{1}{2(x_k - x_{k-1})} \tag{127}$$

$$b_k = \frac{1}{2}\left(\frac{1}{x_k - x_{k-1}} - \frac{1}{x_{k+1} - x_k}\right) \tag{128}$$

$$c_k = \frac{1}{2(x_{k+1} - x_k)} \tag{129}$$

$$\frac{\partial^2 w}{\partial x^2}|_{x} \approx a_k w_{k-1} + b_k w_k + c_k w_{k+1} \tag{130}$$

$$a_k = \frac{1}{2}\left(\frac{1}{x_{k+1} - x_k} + \frac{1}{x_k - x_{k-1}}\right)\frac{1}{x_k - x_{k-1}} \tag{131}$$

$$b_k = -\frac{1}{2}\left(\frac{1}{x_{k+1} - x_k} + \frac{1}{x_k - x_{k-1}}\right)^2 \tag{132}$$

$$c_k = \frac{1}{2}\left(\frac{1}{x_{k+1}-x_k}+\frac{1}{x_k-x_{k-1}}\right)\frac{1}{x_{k+1}-x_k}. \tag{133}$$

See Appendix A.4.3 for example code.

3.6.1.2 *Quadratic Polynomial interpolation*

An alternative approach is to interpolate a quadratic polynomial $f(x) = a(x-x_k)^2 + b(x-x_k) + c$. Given three points: x_{k-1}, x_k, x_{k+1} this would give a system of two equations:

$$\begin{aligned} a(x_{k-1}-\tilde{x}_k)^2 + b(x_{k-1}-x_k) &= w_{k-1}-w_k \\ a(x_{k+1}-x_k)^2 + b(x_{k+1}-x_k) &= w_{k+1}-w_k. \end{aligned} \tag{134}$$

And such so is solved by

$$\begin{aligned} a =& \left(\frac{\Delta w_{k+1}}{\Delta x_{k+1}}\Delta x_k - \Delta w_k\right)\left(\Delta x_k\left(\Delta x_k + \Delta x_{k+1}\right)\right)^{-1} \\ b =& \frac{\Delta w_{k+1}}{\Delta x_{k+1}} - a\Delta x_{k+1}, \end{aligned} \tag{135}$$

As the last unknown is found automatically by setting $c = w_k$. So then the values of $f'(x_k)$ and $f''(\tilde{x}_k)$ can be found, and to find approximation for derivatives use:

$$\begin{aligned} \frac{\partial w}{\partial x}|_{x_k} \approx& \frac{1}{\Delta x_{k+1}+\Delta x_k}\left(\frac{\Delta w_{k+1}\Delta x_k}{\Delta x_{k+1}} + \frac{\Delta w_k \Delta x_{k+1}}{\Delta x_k}\right) \\ \frac{\partial^2 w}{\partial x^2}|_{x_k} \approx& \frac{2}{\Delta x_{k+1}+\Delta x_k}\left(\frac{\Delta w_{k+1}}{\Delta x_{k+1}} - \frac{\Delta w_k}{\Delta x_k}\right), \end{aligned} \tag{136}$$

or

$$\frac{\partial w}{\partial x}|_{x_k} \approx a_k w_{k-1} + b_k w_k + c_k w_{k+1} \tag{137}$$

$$a_k = -\frac{1}{x_{k+1}-x_{k-1}}\left(\frac{x_{k+1}-x_k}{x_k-x_{k-1}}\right) \tag{138}$$

$$b_k = -\frac{1}{x_{k+1}-x_{k-1}}\left(\frac{x_{k+1}-x_k}{x_k-x_{k-1}} - \frac{x_k-x_{k-1}}{x_{k+1}-x_k}\right) \tag{139}$$

$$c_k = - = \frac{1}{x_{k+1}-x_{k-1}}\left(\frac{x_k-x_{k-1}}{x_{k+1}-x_k}\right), \tag{140}$$

and

$$\frac{\partial^2 w}{\partial x^2}|_{x_k} \approx a_k w_{k-1} + b_k w_k + c_k w_{k+1} \tag{141}$$

$$a_k = \frac{2}{x_{k+1} - x_{k-1}} \left(\frac{1}{x_k - x_{k-1}} \right) \tag{142}$$

$$b_k = -\frac{2}{x_{k+1} - x_{k-1}} \left(\frac{1}{x_{k+1} - x_k} + \frac{1}{x_k - x_{k-1}} \right) \tag{143}$$

$$c_k = \frac{2}{x_{k+1} - x_{k-1}} \left(\frac{1}{x_{k+1} - x_k} \right). \tag{144}$$

See Appendix A.4.4 for example code.

3.6.1.3 *Cubic spline interpolation*

As another alternative approach one could build a spline and differentiate it to abstain derivative approximation. One way of achieving this is to use MATLAB build in function spline(), to compute cubic spline, and ppval() plus fnder() to get $\frac{\partial}{\partial x}$ and $\frac{\partial^2}{\partial x^2}$ values of such a construct. This could potentially be a very good approximations, but has a high cost burden as requires a solution of separate traditional problem to obtain spline coefficients. Nevertheless it can be used as an exotic comparison point. Appendix A.4.5 for example code.

3.6.1.4 *Finite difference with asymptotic approximation*

Suppose that we have already computed the first and second asymptotic term w_0, and w_1 from tip boundary (85). Now we can differentiate the two term asymptotic approximation (26) to obtain:

$$\begin{aligned} \frac{\partial w}{\partial x} =& \alpha_1 w_0 (1-x)^{\alpha_1 - 1} \\ &+ \alpha_2 w_1 (1-x)^{\alpha_2 - 1} + o\left((1-x)^{\alpha_3 - 1}\right) \\ \frac{\partial^2 w}{\partial x^2} =& \alpha_1(\alpha_1 - 1) w_0 (1-x)^{\alpha_1 - 2} \\ &+ \alpha_2(\alpha_2 - 1) w_1 (1-x)^{\alpha_2 - 2} + o\left((1-x)^{\alpha_3 - 3}\right) \end{aligned} \qquad x \to 1. \tag{145}$$

This would be very accurate in crack tip region $x \to 1$, but should not be used on its own for the whole interval. However it is possible to combine this with the standard FD scheme:

$$w = w - asymptotics + asymptotics \tag{146}$$

$$\frac{\partial w}{\partial x} = \frac{\partial}{\partial x_{FD}} (w - asymptotics) + \frac{\partial}{\partial x_{analytical}} asymptotics \tag{147}$$

$$\frac{\partial^2 w}{\partial x^2} = \frac{\partial^2}{\partial x_{FD}^2}\left(w - asymptotic\right) + \frac{\partial^2}{\partial x_{analytical}^2} asymptotics, \tag{148}$$

where the result of subtraction $(w - asymptotics)$ is treated with FD scheme (125) to approximate $\frac{\partial}{\partial x_{FD}}$ and $\frac{\partial^2}{\partial x_{FD}^2}$, while $\frac{\partial}{\partial x_{analytical}}$ and $\frac{\partial^2}{\partial x_{analytical}^2}$ are exact analytical expressions (145). To be more precise this method results in:

$$\begin{aligned}
\frac{\partial w}{\partial x} \approx & \frac{\partial}{\partial x}\left(w - w_0(1-x)^{\alpha_1} - w_1(1-x)^{\alpha_2}\right) \\
& + \alpha_1 w_0 (1-x)^{\alpha_1 - 1} + \alpha_2 w_1 (1-x)^{\alpha_2 - 1} \\
\frac{\partial^2 w}{\partial x^2} \approx & \frac{\partial^2}{\partial x^2}\left(w - w_0(1-x)x^{\alpha_1} - w_1(1-x)^{\alpha_2}\right) \\
& + \alpha_1(\alpha_1 - 1) w_0 (1-x)^{\alpha_1 - 2} + \alpha_2(\alpha_2 - 1) w_1 (1-x)^{\alpha_2 - 2}
\end{aligned} \tag{149}$$

The motivation behind this procedure is that fracture width $w(x)$ is going to very similar to its asymptotic expansion at the tip region. The difference of these two should produce less error when differentiated with numerical methods, which can be observed on Figure 40c. Appendix A.4.6 for shows example code implementation of this idea.

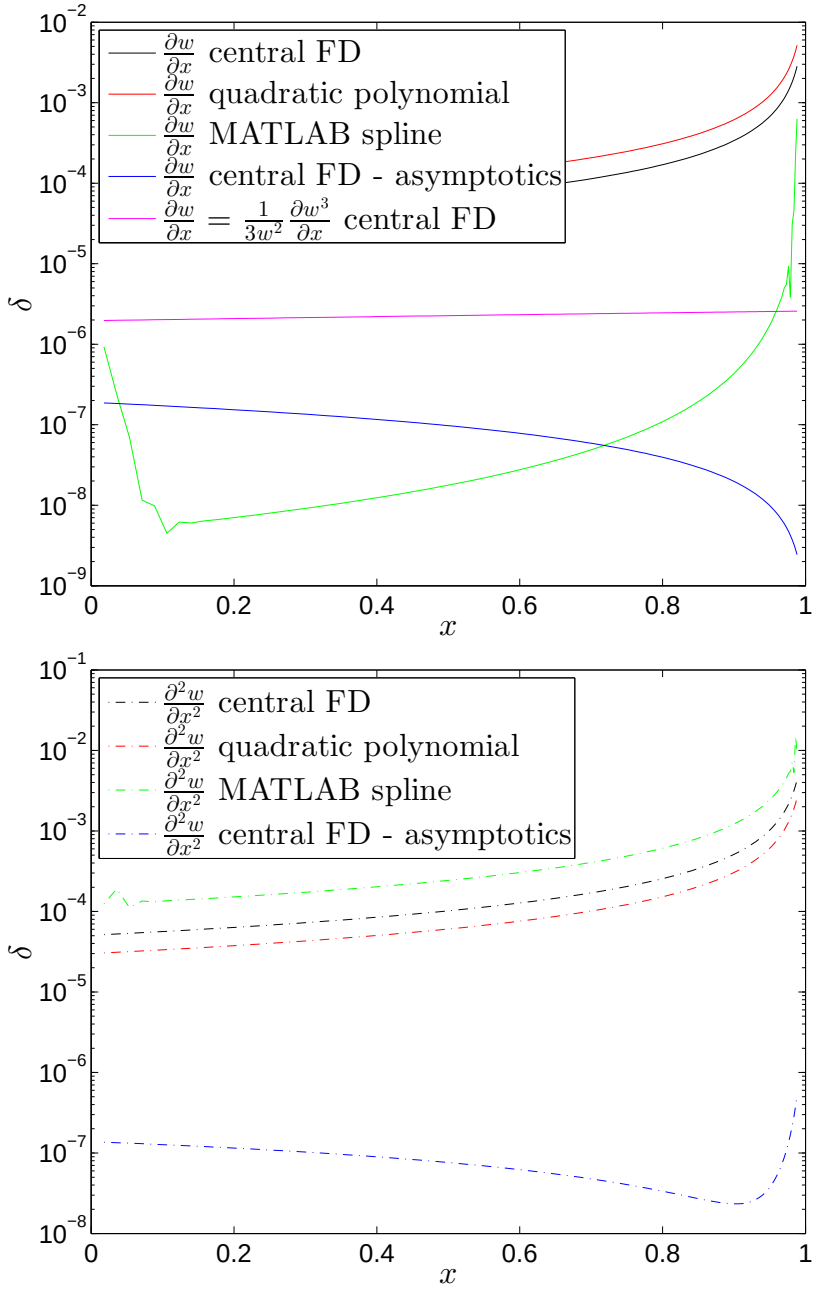

Figure 38: Comparisons of relative errors in approximation of $\frac{\partial}{\partial x}$ and $\frac{\partial^2}{\partial x^2}$ against zero leak off benchmark (271) The FD method with utilized asymptotics clearly outperforms other methods, particularly in most susceptible to numerical error tip region. ($x_m^{(2)}$ grid, $N = 100$)

3.6.2 *"Hybrid" $\frac{1}{3w^2}\frac{\partial U}{\partial t}$ system*

In hydrofracturing problems the discretization is much more difficult than integration[8]. Indeed the three mentioned formulations differ in spatial discretization, while the same integrating algorithm is used. The U formulation was derived because it offers linear first term of asymptotic (58) which can be much better approximated with finite differences method [54, 65]. The Ω formulation on the other hand has the property of $\frac{\partial \Omega}{\partial x}|_{x=1} = 0$ which also makes finite difference approximation much easier. The question here might arise if the gain in numerical accuracy is attributed to some improvement in integration, or do these formulations just offer much more accurate representation of $\frac{\partial}{\partial x}$ and $\frac{\partial^2}{\partial x^2}$, thus the variable under integration makes no noticeable difference.

This question can be relatively easily answered, since w and U formulations are in fact very similar, and a "hybrid" mixture of these two systems can be easily constructed by:

$$\frac{\partial w}{\partial t} = \frac{1}{3w^2}\frac{\partial U}{\partial t} \tag{150}$$

It can be alternatively written in terms of operators (32) (65) as:

$$\mathcal{A}_w(w, L^2) = \frac{1}{3w^2}\mathcal{A}_U(w^3, L^2) \tag{151}$$

The implementation of such a system is quite straightforward, the same function as in case of U system is used, except inputs and outputs are multiplied. *What is important is that the numerical performance and accuracy of such a system can not be distinguished from the original U formulation.* The results produced by this mixture are within solvers accuracy, and appear as could only be contributed to insignificant double precisions disturbances caused by a few extra multiplications. Thus presenting any numerical results comparison of these here would show nothing, but the machine epsilon effects. This "hybrid" mix gets the benefit of improved differentiation (38) with respect to spatial variable x, thus has the same advantage as U system.

8 Or at least as generally observed for PKN model in this work. Nevertheless the problem includes moving boundary in a form of the crack tip, hence the discretization is much harder, especially if multiple fractures are involved. On the other hand many problems, such as 1D heat transfer in an uniform rod, pose much less challenge when choosing the right discretization method.

Integration is however still performed on w variable instead of U, but this makes no difference as the output of modified $\mathcal{A}_w$ has the same accuracy as $\mathcal{A}_U$, and *the significant amount of numerical error is introduced at the spatial discretization not integration.* A similar mixed formulation could be considered where the U is worsened by reversing (151) to form:

$$\mathcal{A}_U(U, L^2) = 3w^2\mathcal{A}_w(U^{\frac{1}{3}}, L^2) \tag{152}$$

Such formulation would loose benefits of improved differentiation and consequently should be as accurate as w system.

3.6.3 *Better FD formulation*

When constructing operator $\mathcal{A}$ one needs to make a choice of how to differentiate with respect to spatial variable x. As showed in derivative approximation schemes Section 3.6.1 a proper choice can result in several orders of magnitude in improvement. When an ODE solver is used, such as ODE15s, it is relativity easy to make differentiation scheme changeable inside the operator $\mathcal{A}$, as shown in Section 3.2.2. Thus one can test performance of the same system, with using different differentiation formulas or schemes. This means that for each of the versions of differentiation scheme described in Subsection 3.6.1 a version of $\mathcal{A}$ build with respective differentiation scheme can be made.

The results of using this four approaches: (136), (125) (149) and MATLAB spline, are shown on Figure 39. Here it can be clearly seen the numerical error inherited form spatial discretization, as shown on Figure 38, affects the accuracy of the solution. The Finite difference with asymptotic approximation (149) remains the most accurate choice. Note that the gain compared to the worst scheme in this particular case is *three orders of magnitude*, which is a huge improvement as the best scheme does not requires a considerable amount of extra computation (and the solver might actuality decide to use less time steps due to better relative accuracies, thus effectively reduce the computation time).

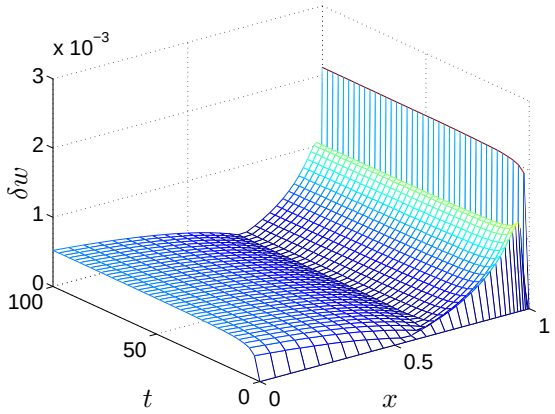

(a) Central FD (125)

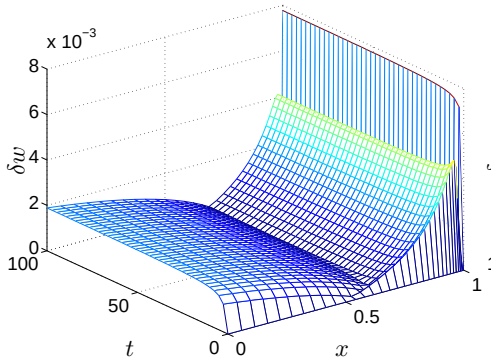

(b) Quadratic polynomial (136)

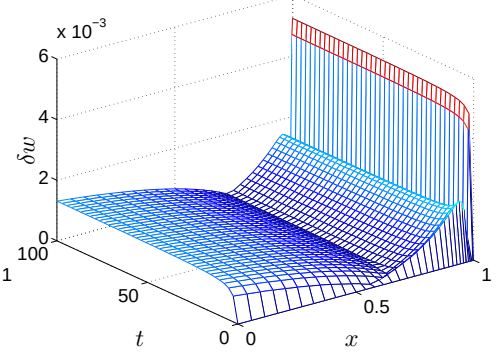

(c) Spline (MATLAB funciton)

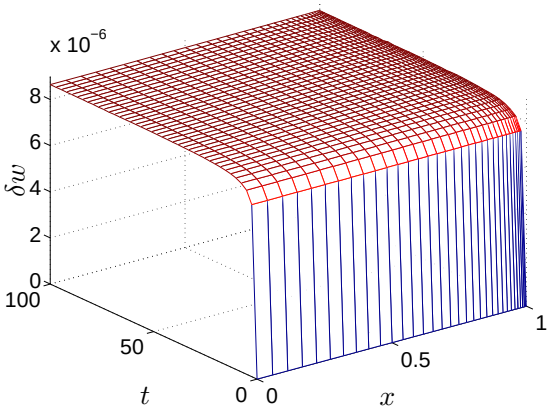

(d) FD - asymptotics (149)

Figure 39: Comparison of relative error opening ∂w for w systems using various differentiation scheme. Testing against zero leak off benchmark (271), on $x_m^{(2)}$ grid, $N = 100$.

3.6.4 *Jacobian Matrix pattern*

Jacobian matrix [98] is the matrix of all first-order partial derivatives of a vector-valued function (such as (99)). Here the Jacobian matrix J of y' is an n-by-n matrix, where n is the length of y'. Column element j is the partial derivative of y' with respect to component i of x:

$$J = \begin{pmatrix} \frac{\partial y'_1}{\partial x_1} & \cdots & \frac{\partial y'_1}{\partial x_n} \\ \vdots & \ddots & \vdots \\ \frac{\partial y'_m}{\partial x_1} & \cdots & \frac{\partial y'_m}{\partial x_n} \end{pmatrix} \tag{153}$$

This matrix is of particular interest for the problem as a number of ODE solvers use it internally to perform Newton iterations and obtain the next time step [7, 47]. This iterations are therefore repeated a number of times, at least once for each time step. As an example a simple implementation of BDF method would have a number of vector operations, an inversion of a product of mentioned Jacobean and its numerical approximation. In a system of N ODEs, if implemented properly the simple vector operations should have no more than $O(n)$ time complexity. Inversion and numerical approximation of Jacobian on the other side are $O(n^3)$ if naive dense matrix algorithms are used. However the Jacobian of this problem is not dense, in fact it has a well defined close to tridiagonal pattern:

$$J_{pattern} = \begin{pmatrix} 1 & 1 & 1 & & & & & 1 & 1 & 1 \\ 1 & 1 & 1 & & & & & 1 & 1 & 1 \\ & 1 & 1 & 1 & & & & 1 & 1 & 1 \\ & & \ddots & \ddots & \ddots & & & \vdots & \vdots & \vdots \\ & & & \ddots & \ddots & \ddots & & \vdots & \vdots & \vdots \\ & & & & \ddots & \ddots & \ddots & \vdots & \vdots & \vdots \\ & & & & & 1 & 1 & 1 & 1 & 1 \\ & & & & & & 1 & 1 & 1 & 1 \\ & & & & & & & 1 & 1 & 1 \\ & & & & & & & 1 & 1 & 1 \end{pmatrix} \tag{154}$$

This pattern can be obtained by analyzing operators $\mathcal{A}$ and $\mathcal{B}$. First the usage of approximated spatial derivatives, (125) or (149), means that there is dependence of each term y'_i on terms y'_{i-1},y'_i, and y'_{i+1}. This forms the tridiagonal middle pattern. Operator $\mathcal{A}$ dependents on L^2, which here is the last element in y', thus each y'_i is additionally depended on y'_n. Furthermore each element of $\mathcal{A}$ is multiplied by the first term of asymptotic which is found using (85), and depends

on two last points $y'_{n-1}$and y'_{n-2}, thus the crack tip BC (A.4.9) and normalization over L (18) adds three right columns to the overall pattern. Operator B also utilizes first asymptotic term produced by tip BC (A.4.9) so these three right columns include the last row. Finally the BC (24) at crack inlet is implemented using three points, hence additionally $J_{patern\ (1,3)} = 1$.

The tridiagonal structure with three right side columns (154) prevails for all variable formulations w, U and Ω. It is common for all three previously considered spatial discretization (136), (125) and (149) (all are dependent on tip asymptotes by tip condition, only (149) uses them fully). In fact it is yet another argument for superiority of (149), as it means that the big $O(h)$ cost is not increased. Unfortunately spline formulation would yield a full Jacobian matrix, as a consequence of spline interpolation algorithm, thus no further benefit of patterning Jacobian would follow.

This binary Jacobian pattern (154), when supplied to ODE15s solver [62] alone, *allows to save at least a half, if not a vast majority, of the computation time* needed for most of the problems tackled by this work. If this pattern is not provided a solver must assume dense structure and compute an approximation for each matrix entry, thus consider n^2 elements. If the pattern is used roughly $6n$ elements, three diagonals and three columns are in question. Therefore from the algorithmic point of view one could reduce $O(n^3)$ complexity to $O(n)$ when evaluating Jacobian matrix with pattern (154). For ODE15s solver this theoretical speedup can be tested by timing computation for different system sizes N, with both provided $J_{pattern}$ and default dense option. Results of this test are presented in Table 8 , where benefits of using this pattern are made obvious. Thus if an ODE solver is to be used efficiently for fracturing problem, the Jacobian *must* be provided.

Further improvements could be obtained if problem sparseness is to used at the inversion stage of integrating algorithm . Here the pattern $J_{pattern}$ could be used to develop a custom made matrix inversion, that first by Gaussian elimination would reduces the matrix to pure tridiagonal form, and then perform standard Tridiagonal matrix sweep. Such algorithm would have $O(n)$ time complexity, which is far better than any generic dense system solving algorithm could ever achieve, (which generally are $O(n^3)$). This will not be unfortunately developed in this work because of both deadline constrains and the fact that future considered problems will disturb this neat $J_{pattern}$, and consequently would make this algorithm improvement obsolete.

N	default dense J	optional sparse J
10	0.09s	0.05s
20	0.10s	0.05s
50	0.11s	0.05s
100	0.15s	0.05s
200	0.26s	0.06s
500	0.81s	0.08s
1000	2.38s	0.14s
2000	8.41s	0.26s
5000	37.90s	0.79s
10000	211.50s	2.43s

Table 8: Example times needed to compute solution for a propagating fracture with ODE15s, with and without using optional $J_{pattern}$. The speed up obtained with pattern varies from a factor of two for small systems, to a hundred and over for very large N

3.7 EXTRA TESTS ON CARTER LAW

3.7.1 *Test with known q_j^**

An additional test can be performed using the general analytical benchmark A.2.1, which mimics the behavior of the problem with Carter Law leak off type. The leak off (3) can be split in to two terms: $q_l^{(j)}(t,x)$ based on Carter law and supplementary $q_j^*(t,x)$. Since in the benchmarks the exact value of $q(t,x)$ (269), and $\tau(x) = L^{-1}(x)$ required for $q_l^{(j)}(t,x)$, is know, the term q_j^* can also be found as:

$$q_j^*(t,x) = q_l(t,x) - q_l^{(j)}(t,x) \tag{155}$$

So if the analytical benchmark A.2.1 is limited in to the two terms its components (265)-(269) it can be worked out that $q_l^{(1)}(t,x)$ (4) can be substituted in to (155) to obtain:

$$\begin{aligned} q_1^*(t,x) =& W_0(a+t)^{\gamma-1}\Bigg[(3\gamma+1)\Big(\frac{7}{8}W_1(1-x)^{-\frac{1}{2}} + \frac{5}{2}W_1^2(1-x)^{-\frac{1}{3}} \\ &+ \frac{55}{24}W_1^3(1-x)^{-\frac{1}{6}} + \frac{3}{4}W_1^4(1-x)^0\Big) + \frac{1}{6}(1-3\gamma)(1-x)^{\frac{1}{3}} + \\ &+ \frac{1}{4}(1-\gamma)W_1(1-x)^{\frac{1}{2}}\Bigg] - \frac{1}{\sqrt{t-L^{-1}(x)}}, \end{aligned} \tag{156}$$

The term $q_l^{(j)}(t,x) = \frac{1}{\sqrt{t-L^{-1}(x)}}$ can also be supplied analytically, by inverting the known fracture length L from benchmark (267), or found numerically using a numerical procedure for $\tau(x) = L^{-1}(x)$ described in Subsection 3.8.2 ($C(t)$ is set to one). This means a test that measures the effect of numerical leak off approximation can be constructed. While no analytical solution for transient regime for Cartel Law leak off exist, the benchmark solution can serve as a relatively close counterpart.

The w variable system can be slightly modified such so the known q_l^* term is provided and only the remaining $q_l^{(1)}$ term is to be found numerical. In other words the operator $\mathcal{A}$ (32) is slightly modified to include two leak off terms:

$$\frac{\partial w}{\partial t} = \frac{1}{L^2(t)}\left[\frac{1}{3}w_0^3 x\frac{\partial w}{\partial x} + 3x^2\left(\frac{\partial w}{\partial x}\right)^2 + w^3\frac{\partial^2 w}{\partial x^2}\right] - q_l^{(1)} - q_1^*. \tag{157}$$

This gives us some settings to test the accuracy of the method for computing leak off itself, and indirectly the accuracy of the transient

solution. Lets use the leak off numerical τ approximation as proposed in Subsection 3.8.2 and compute the system two times, one time with analytical and fully known leak off, and one time with numerical approximation of $q_l^{(1)}$ added to the known analytical part q_j^*. In other words, the idea is construct a specific example which serves as a middle ground between testing against known analytical and the unknown transient solution.

The results are shown on Figure 40. Interestingly regardless of the method used to compute leak off function the accuracy remains unchanged. The computation time, and number of time steps required is affected. Numerical approximation triggers the solver to make more time steps. Note that this essential binds the maximum time step to the propagation speed. While the fracture opening w and fracture length L apparently become predictable after a number of successful time steps, the numerical approximation of $\tau(x)$ for each grid point prevents the solver from increasing the time steps infinitely. Numerical inversion of L^{-1} based on an interpolation of previously computed time steps will eventually produce less accurate result if the time step becomes too large, that is $\tau(x)$ is guesstimated on history points that are too far away. This means that the strategy shown in [106], and any publication that follows, where the time step grows *exponentially*, will require a new time step strategy or much more sophisticated leak off computation algorithm than the one presented here, if the leak off is to be computed as a part of the unknown solution rather than simply artificially analytically provided. On the other hand the test shown here was relatively straightforward to set up, as conventional ODE solvers are capable of effectively managing the time step themselves.

Nevertheless this tests proves that Carter leak off can be accurately computed numerically, and suggests that the numerical accuracy is unaffected by the leak off approximation used in this work.

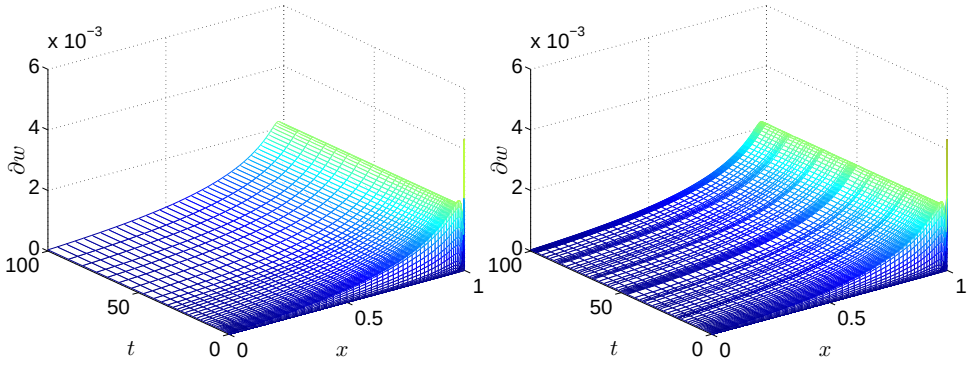

(a) δw_{max} for full analytical leak off

(b) δw_{max} for partially numerical leak off

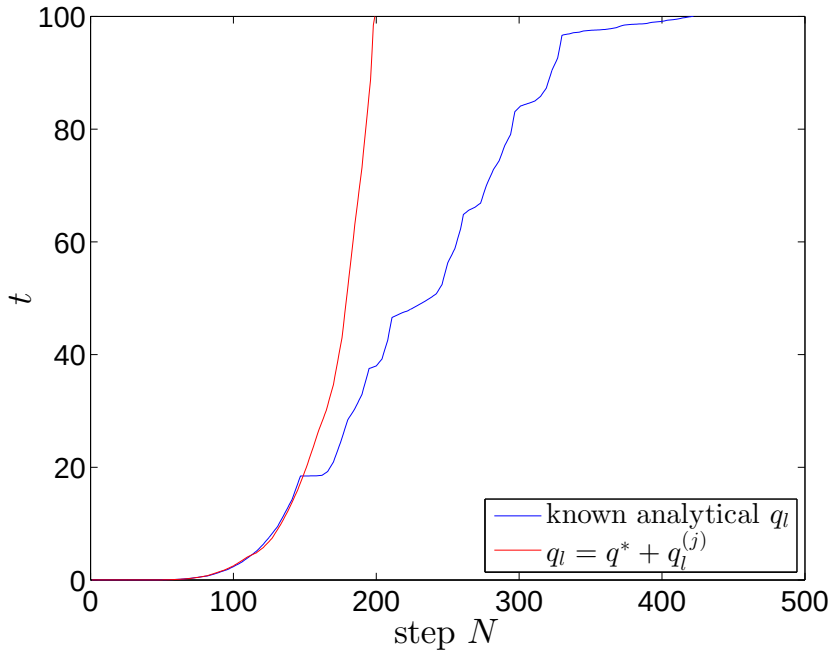

(c) Solver time step result

Figure 40: Results of using numerically approximated Carter type leak off on w variable system.

3.7.2 *Remarks on the sensitivity of the Carter leak-off model.*

It is well known that applicability of the empirical Carter law (4) in the vicinity of the fracture tip is questionable [25, 40, 66] Moreover, when combining Carter leak off with some non-local variants of elasticity models (for example, KGD model of hydrofracturing), one obtains an infinite particle velocity at the crack tip. As a result, the speed equation (12) cannot be applied in such a case. One way to eliminate this unwanted behavior is to assume that the Carter law becomes valid only at some distance away from the fracture tip (see for example [66]).

The PKN model, which does not exhibit such a drawback, gives an opportunity to assess how the solution is affected by a modification of the classical Carter law in the neighborhood of the fracture tip.

Thus, lets consider two modifications. The first assumes that leak-off function equals zero over some distance from the crack front ($d > \varepsilon$). The second uses a constant value of q_l in the same interval. This value is chosen to maintain continuity of the leak-off function. Note, that both of these modifications change the volume of fluid loss to the rock formation.

The relative deviations of the crack lengths for these modifications from the original one are shown in Figure 41. Results for two values of d: $d = \varepsilon$, $d = 10\varepsilon$ (for $\varepsilon = 10^{-5}$) are displayed. The symbol q_{ld} in the legend refers to the cases when the leak-off function is complimented by the constant value over $1 - d \leq x \leq 1$. One can deduce that the maximal relative discrepancies (up to 1%) appear at the initial and large times. To explain this phenomenon, lets evaluate the additional volume of fluid retained in the fracture as a result of the modification to Carter law . Taking into account (34), these values are $\Delta Q_l(t) = 2D(t)\sqrt{d}$ and $\Delta Q_l(t) = D(t)\sqrt{d}$, for the respective modifications (see (22) for $D(t)$). Note that $D(t) = \sqrt{u(t)/t}$ represents deviation for the small time. For large time, the effect of accumulation of the difference of the fluid loss, $\int_0^t \Delta Q_l(\tau)d\tau = O(\sqrt{td})$, plays the crucial role.

The above test proves that the application of Carter law modified in the aforementioned ways, is fully justified when one considers the accuracies required in the practical applications.

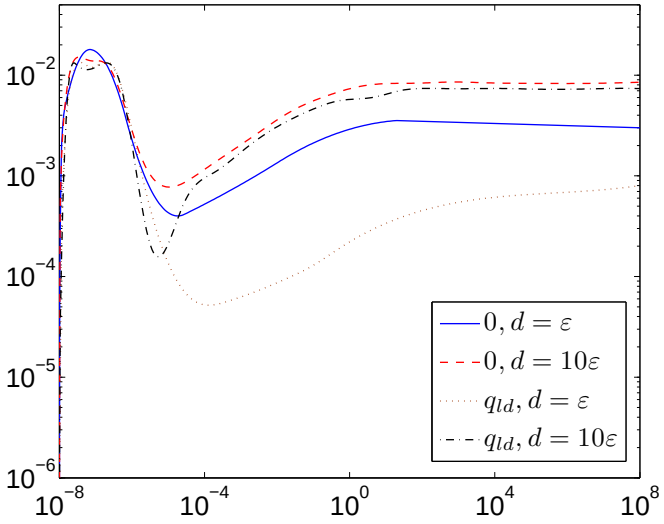

Figure 41: Relative deviations of the crack lengths for different variants of truncated Carter law.

3.8 EXTRA COMPUTATIONAL CHALLENGES

3.8.1 $\tau(x)$ *computation interpretations*

To compute $\tau(x)$ it is necessary to find the inverse length function over the entire interval $x \in (0,1)$. The initial condition gives a non-zero positive value l_* (8), however the information about the history of the process, including the inverse length function, is not given in the original formulation. It could be understood that the crack was previously opened and filled with fluid for some large unknown time, or have just been opened and well defined $l^{-1}(x)$ is available. The physical justification for Carter law is that a cake filter layer is being formed on exposed crack surfaces [14]. Hence one could expect an impermeable layer to already exist on the initial opening, or try to use some reference values for early $\tau(x)$ of some known solution. To address those issues two approaches will be considered:

- If the initial fracture was opened for a long time, the initial opening is fully saturated:

$$\tau_a^{(1,2)}(x) = \begin{cases} -\infty & \text{if } 0 \le l(t)x \le l_*, \\ \tau_{num}^{(1,2)}(x) & \text{if } l_* < l(t)x \le l(t); \end{cases} \tag{158}$$

- If the initial fracture developed similarly to the zero leak-off self-similar solution [65] (for small time it is reasonable that $\int_0^1 q_l(x)dx \to 0$):

$$\tau_b^{(1,2)}(x) = \begin{cases} \left(x\xi_* x_n\right)^{5/4} - t_0; & \text{if } 0 \le l(t)x \le l_*, \\ \tau_{num}^{(1,2)}(x) & \text{if } l_* < l(t)x \le l(t); \end{cases} \tag{159}$$

where $\tau_{num}^{(1,2)}(x)$ refers to (160) or (161) outputs of the numerical exposure time calculation scheme described in Subsection 3.8.2 below. The effects on q_l of both of these approaches are presented in Figure 42. The comparison of these two cannot be however completed without understanding the effect of such on fracture solution. The τ_a strategy essentially means that $q_l = 0$ for $xL(x) < l_*$.

On Figure 43 it is shown how a fracture with sufficiently large leak off can recede at initial times instead propagating as expected. Furthermore next two interpretations could be considered:

- $\tau_{(a,b)}^{(1)}$ - only recent fracture history is taken into account, reopened segments are treated as if no cake layer existed

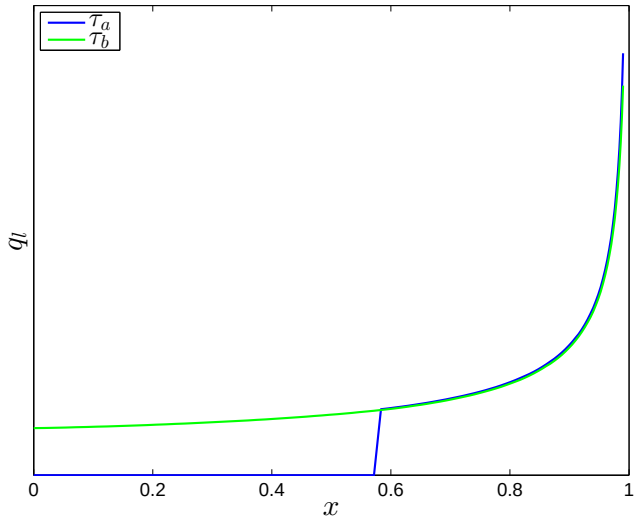

Figure 42: Comparison of effect on leak off volume between approaches τ_a and τ_b on a fracture with $\frac{l_*}{L(t)} \approx 0.6$

- $\tau^{(2)}_{(a,b)}$- fracture history is traced form the beginning, reopened segments are taken into account, thous $\tau^{(2)}_{(a,b)}(x)$ might return multiple opening times.

This adds up to a total of four combinations of strategies for obtaining τ.

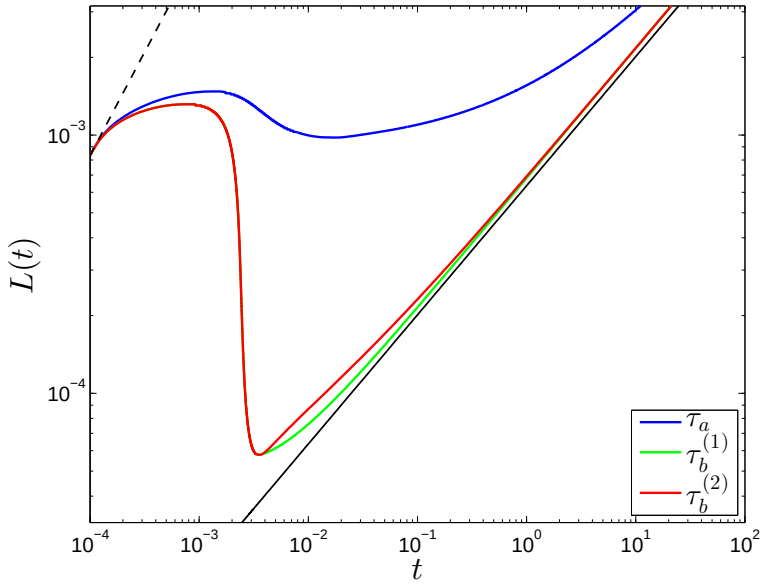

(a) Initial fracture closes for both τ_b and τ_a. Zero leak off at initial opening (158) only prevents the initial part of fracture from closure.

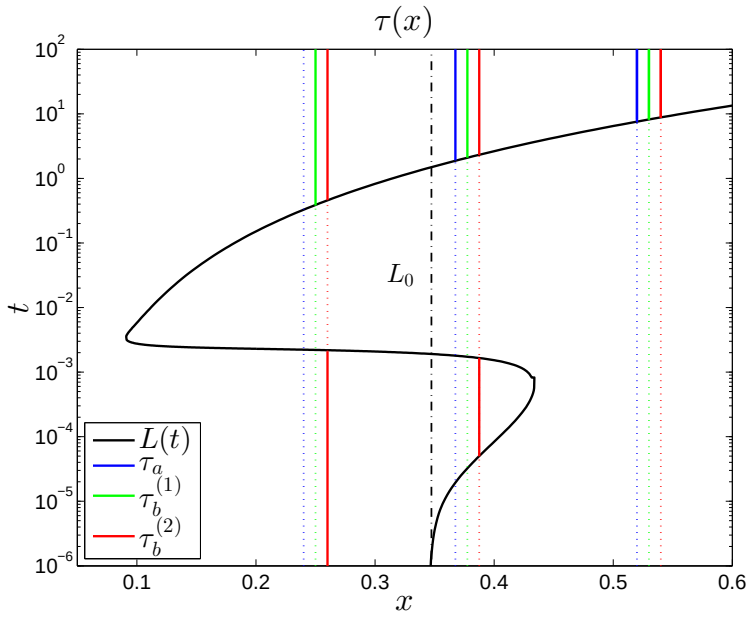

(b) Depending on the choice of $\tau_{(a,b)}^{(1,2)}$ different times when fracture was opened are taken into account. Only $\tau_b^{(2)}$ finds all times when a point x was exposed, as marked by the solid red line. τ_a ignores most of the information. Dashed lines indicate ignored exposure time.

Figure 43: Comparison of effects of various interpretations of initial fracture history and $\tau(x)$ calculation. This particular result was obtained while testing initial conditions shown on Figure 15a. (negligible difference for $\tau_a^{(1,2)}$)

3.8.2 *Exposure time computation*

For the both variants of Carter leak-off (4) it is necessary to perform additional computation of exposure time $t - \tau(x)$ for each grid point x_i. This can however be a separate challenge on its own, especially if it is to be performed within the derivative function supplied to an arbitrary ODE solver.

If only recent fracture opening time is taken into account:

$$\tau^{(1)}_{num}(x) = \tau_{2N_\tau+1}(x) \tag{160}$$

Furthermore if a point on fracture was previously opened and closed several times the exposure time $t - \tau(x)$ account for some historical opening periods:

$$\begin{aligned}\tau^{(2)}_{num}(x) = -\tau_1(x) + \tau_2(x) - \tau_3(x) + \tau_4(x) \ - \dots \\ \dots - \tau_{2N_\tau-1}(x) + \tau_{2N_\tau}(x) + \tau_{2N_\tau+1}(x)\end{aligned} \tag{161}$$

Where odd terms refer to opening times and even times to closure times, and N_τ is the number of times a single point on fracture was opened (or reopened).

As the solution is integrated the function (99) is called, and values of $L(t_i)$, t_i, and $V_0(t_i)$ as calculated at each call are stored in a dynamic array, sorted by t_i. Values are filtered before insertion so that each value of L_i and t_i is greater than the previous one, with the exception of closing fracture events (162). Then when $t - \tau(x)$ is to be found, the formed array is iterated over to form the trajectory of the crack tip (black line on Figure 43). As this iteration is made, for each grid point on x-axis the number of times the crack tip passed through that point is accounted for, as shown by intersections of vertical lines with black line in Figure 43. Cubic polynomial is interpolated to approximate this intersections, on two points $(L(t_i),\ t_i)$ and $(L(t_{i+1}),\ t_{i+1})$, such so $L(t_i) < xL(t_i) < L(t_{i+1})$ or $L(t_{i+1}) < xL(t_i) < L(t_i)$ for closing segments, with derivative conditions from $V_0(t_i)$ and $V_0(t_{i+1})$. Finally these times are combined to obtain total exposure time for each grid point (161). By taking into account all N_τ times $\tau^{(2)}$ is calculated, if only the most recent opening time $\tau_{2N_\tau+1}$ is used $\tau^{(1)}$ is obtained.

3.8.3 *Shut down regime handing*

This work was so far focused on propagating regime. However there are two other possible regimes: storage and shut down. Storage regime refers to a situation when large toughness K_C value prohibits any fracture growth [93]. This scenario is not accounted by PKN model, as it does not include formation toughness. On the other hand, the shut

input : vectors with $L(t_i)$, t_i and $V_0(t_i)$, arranged by their appearance time t_i, N grid points x_k
output: $\tau_{num}(x_k)$ as a vector of size N

$\tau_n(x_k) \longleftarrow$ array length N of empty dynamic arrays;
$k \longleftarrow 1$;
for $i \leftarrow 1$ **to** *length of* $t_i - 1$ **do**
  if $L(t_{i+1}) \geq L(t_i)$ **then**
    repeat
      $\tau_{n+1}(x_k) \longleftarrow$ output of interpolating $L(t), V_0(t)$ at t_i, t_{i+1};
      $k \longleftarrow k + 1$;
    until $x_k > L(t_i)$;
  end
  if $L(t_{i+1}) < L(t_i)$ **then**
    repeat
      $\tau_{n+1}(x_k) \longleftarrow$ output of interpolating $L(t), V_0(t)$ at t_i, t_{i+1};
      $k \longleftarrow k - 1$;
    until $x_k < L(t_i)$;
  end
end
for $i \leftarrow 1$ **to** N **do**
  $\tau_{num}(x_k) \longleftarrow \tau_1(x_k)$;
  for $j \leftarrow 2$ **to** *length of* $\tau_n(x_k)$ **do**
    if j *even* **then**
      $\tau_{num}(x_k) \longleftarrow \tau_{num}(x_k) + \tau_j(x_k)$;
    else
      $\tau_{num}(x_k) \longleftarrow \tau_{num}(x_k) - \tau_j(x_k)$;
  end
end

Algorithm 2: Scheme for numerically approximating $\tau(x)$ in a propagating or closing fracture

down regime, which corresponds to receding fracture is possible to obtain in PKN model by alerting fluid injection or allowing for high leak off values.

The underlying assumptions were that the crack propagation speed is positive ($V(1) > 0$) and the crack width is greater than zero ($w(t,x) > 0$), except for the crack tip where $w(t,1) = 0$. These could however become invalid under specific conditions. Fracture remains open as long as the fluid flux inside the fracture is greater than the leak off, so propose a simple observation that: *if the fracture width is monotonically decreasing from mouth to tip, and the value of leak-off monotonically increases up to the crack tip, then the first possible non-tip point x where $w(t,x) = 0$ can occur is $1 - \varepsilon$ for an infinitely small ε*. The first point on fracture to close, should be the last grid point, closest to the tip.

Noting that MATLAB ODE15s solver provides an option to include events, detection of zero values crossings for additional arbitrary provided functions, lets supply a simple event function:

$$f_{event}(t) = w_N. \tag{162}$$

Then when the value of the crack width at the last grid point reaches $w_N = 0$, ODE15s is going to hold integration. Now it is possible to resume after a small modification of the solution at the time the event occurred:

$$l_{end} := (1 - \varepsilon) l_{end}, \qquad w_{end}(x) := (w_{end}(x(1 - \varepsilon)), \tag{163}$$

where l_{end} and w_{end} refer to the values at the last time step. The discretized value w_{end} needs to be extrapolated, this is done using spline interpolation and asymptotic terms w_0 and w_1 for "good enough" accuracy (Appendix A.3). The fluid balance is satisfied (see Subsection 3.8.4). This operation essentially chops off closed fracture segment off length εl, thus it is a discontinuous step, however the change is relatively small and insignificant. If fracture is to recede significantly, this operation needs to be repeated multiple times, which might lead to high computational cost, as each backward step is εl. For this reason to compute possibly closing fractures it would be unwise to use $\varepsilon < 10^{-2}$ for shut down regime, but it is possible to use smaller ε in propagating regime, and switch to a larger value if change of propagation regime is detected. Note that this approach should not be treated as a proper closing regime solution, it is a simplified extension to propagating fracture model. An example of closing fracture is presented in Figure 44.

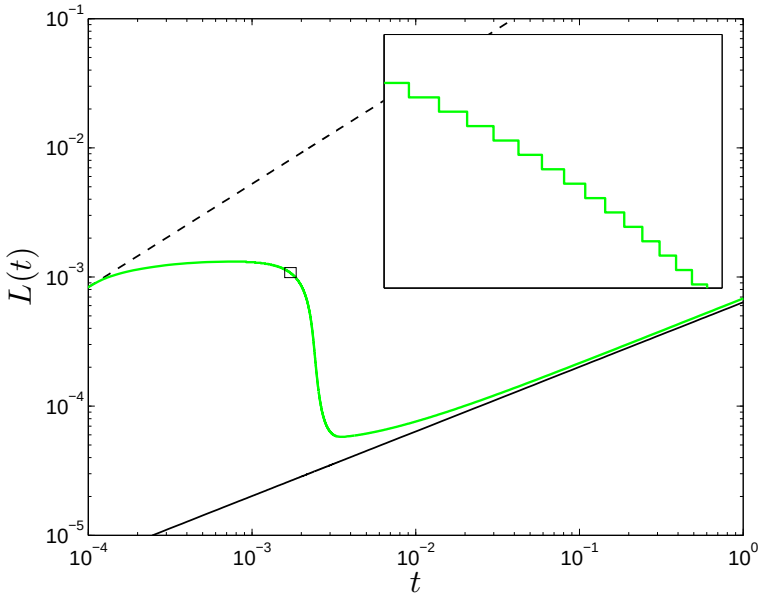

Figure 44: Close up view on closing fracture length. Fracture is allowed to close by εl, thus staircase pattern is formed. Smaller ε would result in even smother trajectory, but would dramatically increase number of steps.

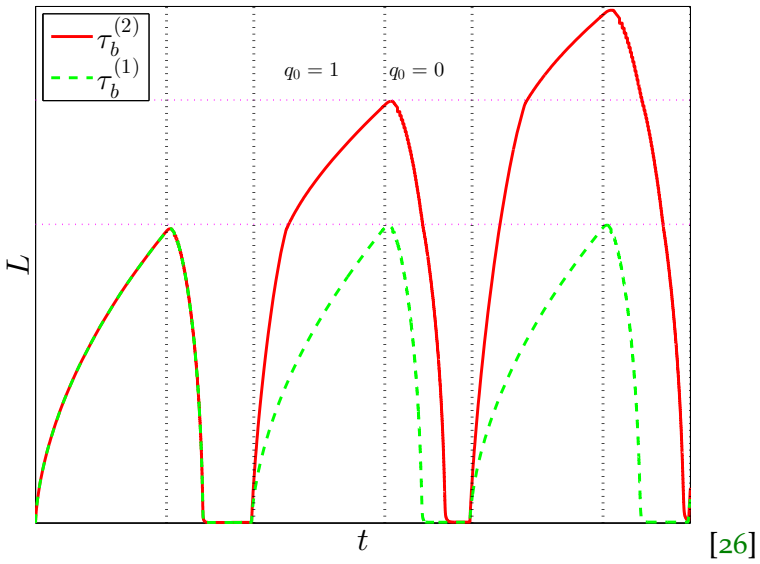

[26]

Figure 45: Testing $\tau_b^{(1,2)}$ with periodic pumping function (alternating $q_0 = 0$ *or* 1). Cycles of propagation and shut down regimes appear (as expected from other results, example [26], [93]). The choice of τ interpretation affects second and third cycle, this result however refers to fracture L, not net inlet pressure, possibly making it original (as it is hard to find such an example in the literature). Note relation between old peeks and change in propagation speed marked by dotted horizontal lines.

3.8.4 *Fluid balance check*

Fluid balance equation is used to verify if solver output is valid:

$$\int_0^t q_0(t)dt = \int_0^1 w_*(x)dx + \int_0^t \int_0^1 w(t,x)dxdt + \int_0^t \int_0^1 q_l(t,x)dxdt. \tag{164}$$

A good way to integrate leak off function $\int_0^t \int_0^1 q_l(t,x)dxdt$ is to add an extra ODE, lets make in an operator and call it:

$$\mathcal{C} = \int_0^1 q_l(t,x)dx, \tag{165}$$

so then the derivative function (99) can be extended by attaching $\mathcal{C}$:

$$y' = \{\mathcal{A}, \mathcal{B}, \mathcal{C}\}. \tag{166}$$

This is a relatively small modification, that does not significantly affect the computations in any manner. It should be rather treated as a good optional addition. To keep things simple this operator $\mathcal{C}$ will stay hidden for the remainder of this work, as it presence is not essential. However all the mentions of fluid balance checking in this work are based on this additional operation.

3.9 TEST ON REAL LIFE DATA

An opportunity raised to test the single fracture model against some actual field data. A post frac job report was made available by a friendly third party gas company. This contained summary of three fracturing operation performed in porous sandstone formations, thus calculation of fluid leak off was needed. Unfortunately exact value of Carter leak off constant C_L was not provided. Instead a formula similar to pressure proportional Carter type variation (4) as used by Kresse in [42] was utilized:

$$q_l = \frac{2hC_{vc}}{\sqrt{t - \tau(x)}} \tag{167}$$

$$C_{vc} = \frac{2C_vC_c}{C_v + \sqrt{C_v^2 + 4C_c^2}}, \quad C_v = \sqrt{\frac{k_r\phi_r p}{2\mu_f}}, \quad C_c = \sqrt{\frac{k_r\phi_r c_T}{\pi\mu_f}}p \tag{168}$$

Where a number of physical constants is used:

- ϕ_r - reservoir porosity,
- C_T - total compressibility of reservoir,
- k_r - permeability of rock matrix,
- μ_r - reservoir fluid viscosity in the porous media,
- μ_f - filtrate fluid viscosity.

The fracturing job was performed with ThermaFrac fracturing fluid designed for operations at significant depths and high temperatures [84]. It is significantly more viscous than other fracturing fluids to allow for greater width of created fractures. The underground temperature during this operation was well over 100^oC, at these conditions the viscosity of reservoir fluids (natural gas) and filtrate fluids (sandstone filtrated ThermaFrac, witch is assumed to be water) were adjusted to account for the higher temperatures. To simplify calculations constant q_0 was assumed to be constant over the entire treatment time. The remaining parameters were provided by the third party gas company as presented in Table 9. Results of running these simulations are shown on Figures: 47, 48 and 49.

These absolutely can not be treated as final and accurate. The model does note take into account various physical processes. Proppant transportation was ignored to name one example, which is a subject of research on its own [45]. Nevertheless to say the formed fracture does not even need to be of PKN type. Furthermore the collaboration with the gas company involved frequent changes to both value and

	well 1	well 2	well 3	
ν	0.25	0.295	0.26	–
E	$5.0 * 10^6$	$5.87 * 10^6$	$5.69 * 10^6$	psi
μ	0.3			$Pa.s$
q_0	0.010	0.025	0.014	$\frac{m^3}{s}$
h	5.2	7.2	6.0	m
t_{end}	56	46	53	min
ϕ_r	0.0848		0.07241	–
C_T	$6.492 * 10^{-4}$			Pa^{-1}
k_r	$3.8606 * 10^{-9}$		$1.1143 * 10^{-9}$	m^2
μ_r	$2 * 10^{-4}$			$Pa.s$
μ_r	$1 * 10^{-5}$			$Pa.s$

Table 9: Physical parameters used in simulations of well 1, well 2 and well 3, based on a third party gas company reports

interpretation of physical parameters. These were measured in laboratories, and these measurements could vary significantly even for the same parameter, between each measurements.

The purpose was to verify if the one fracture model behaves in a predictable manner and gives reasonable results. These results are within the same order as those presented in confidential reports, the gas company had ordered from a professional source. Furthermore the reports also included pre and post fracturing gas flow from the wells. Interestingly well 1 produced no gas after fracturing, while well 2 and well 3 outputs were quadrupled. One could seek connection with end time fracture length, as well 1 resulted in much sorter fracture, but this might be a coincidence as well.

Nevertheless, as far from good industry practice as this example might be, by comparing numerical predictions obtained by the model developed here, it is reasonable to use it to forecast which fracturing scenarios are more likely to result in favorable outcomes. The sand stone reservoir does appear to soak most of fracturing fluid, a reasonable result given sandstone high porosity. The hypothetical fractures length are not very long, but neither the reports suggested considerably better outcomes. Given that the alternative providers demand significant price for such simulations, the program developed here, available online, shown on Figure 46, is at least a free alternative.

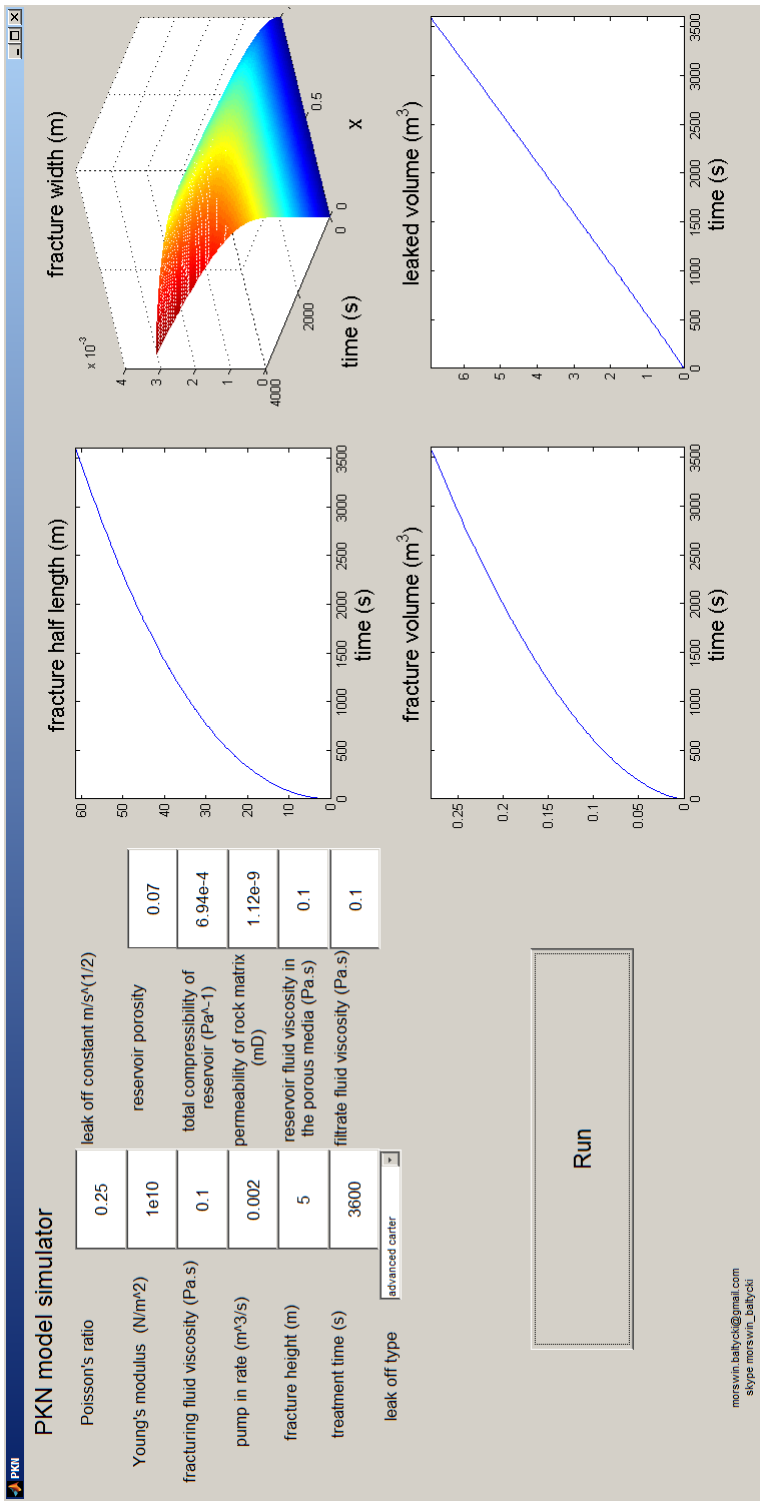

Figure 46: Screenshot of MATLAB based program developed while testing on real life data. Available for download at http://morswin.co.nf/

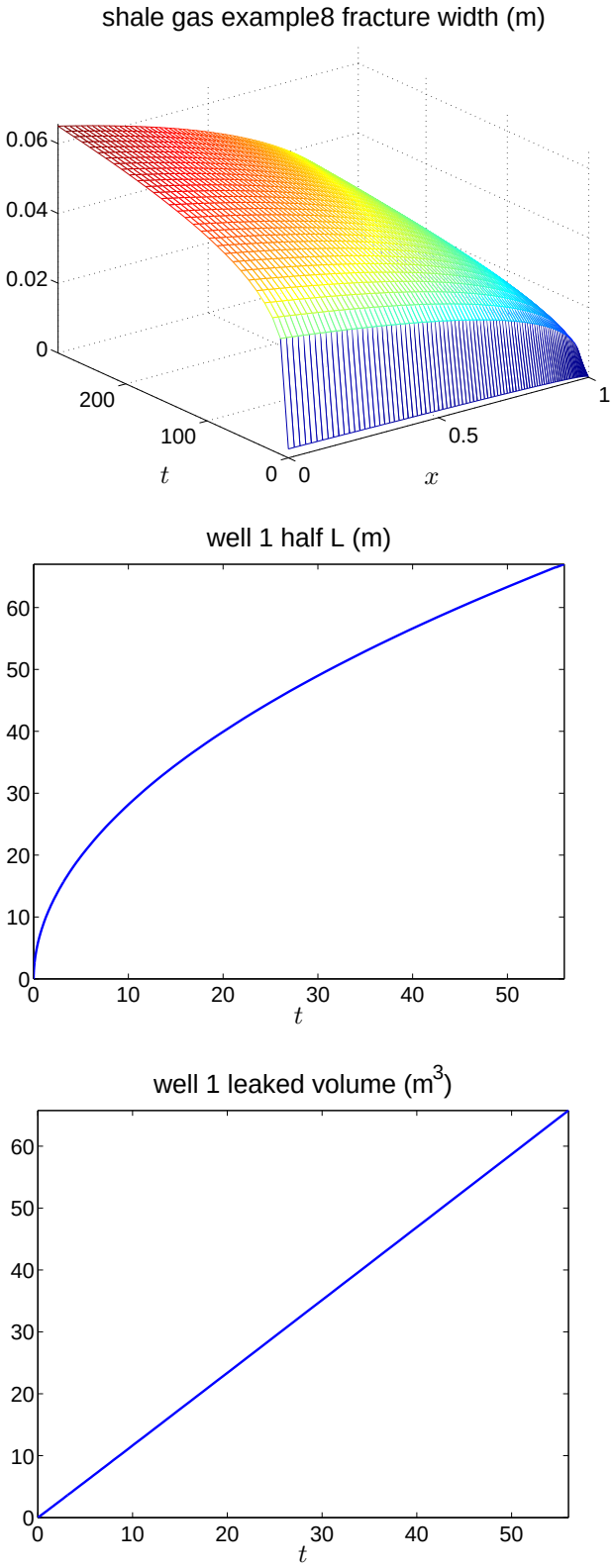

Figure 47: PKN fracture simulation for well 1

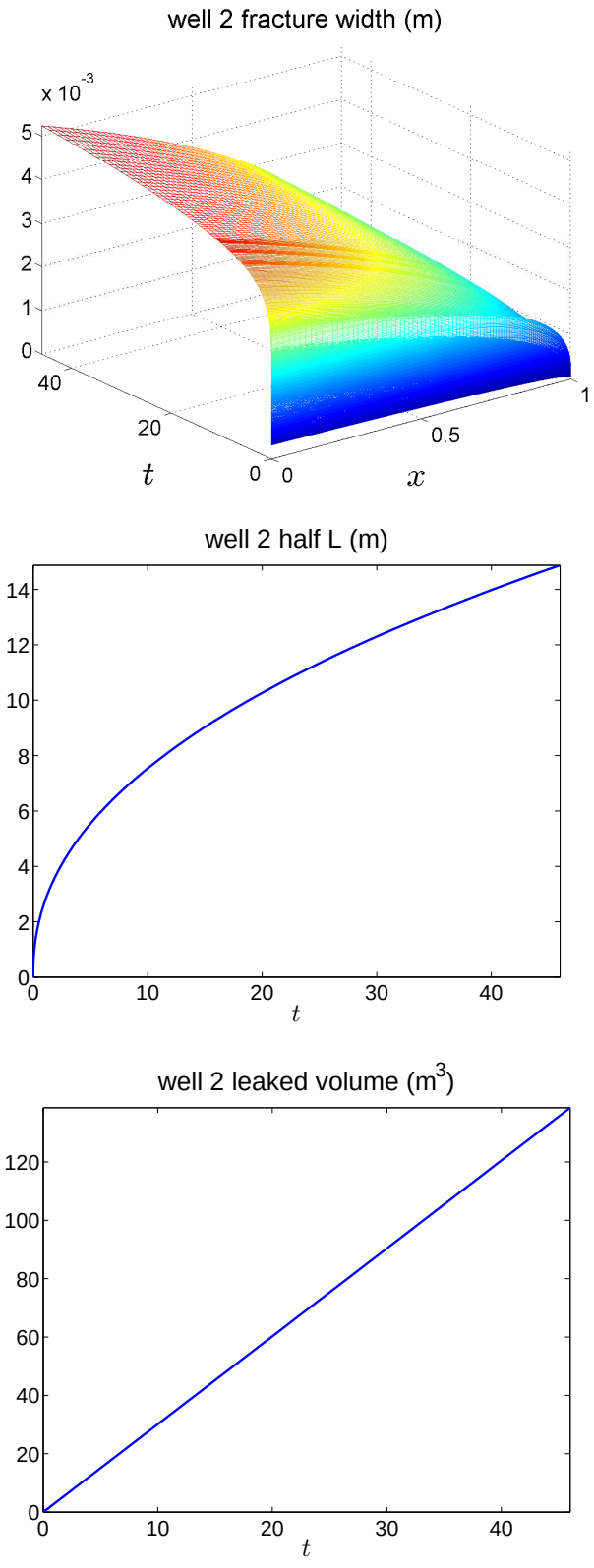

Figure 48: PKN fracture simulation for well 2

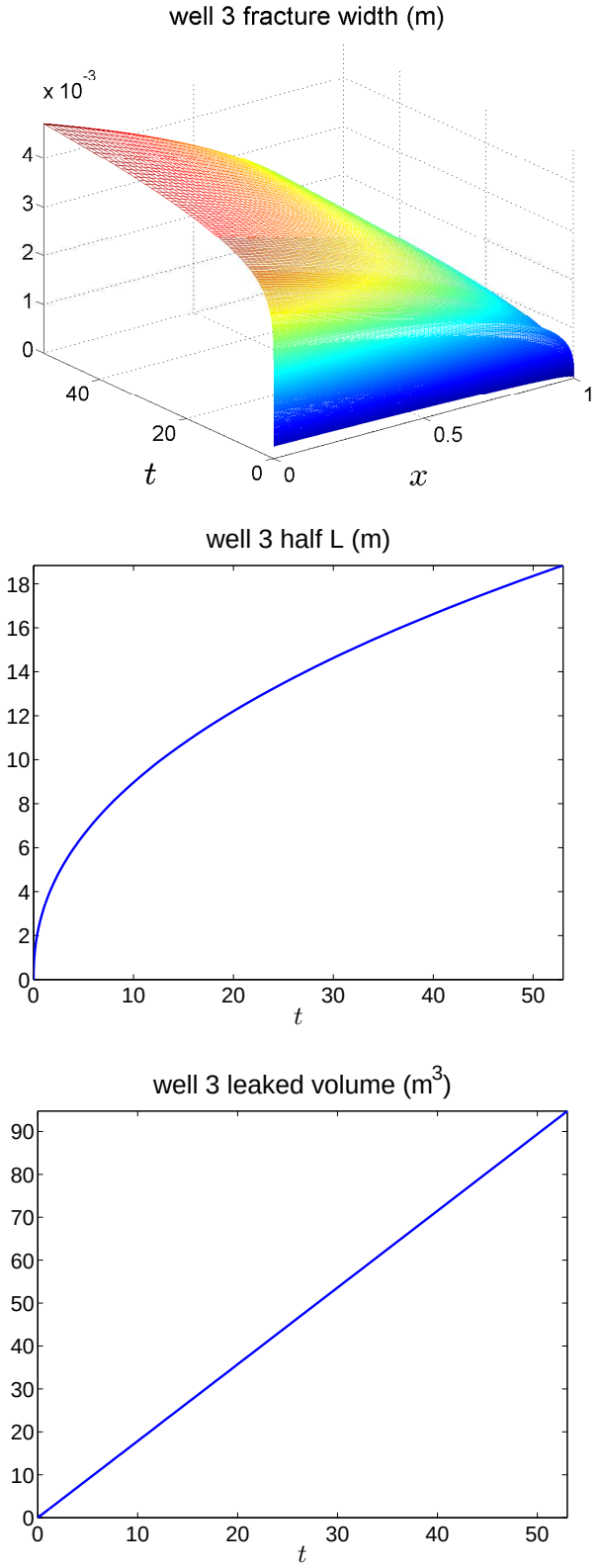

Figure 49: PKN fracture simulation for well 3

4

MULTIFRACTURE MODEL THEORY

Having developed good and accurate methods for a single fracture, as derived in Chapter 2, tested in Chapter 3, and published in [44], knowledge of the single fracture model will be now applied to simulate complex structures composed of multiple fractures. The PKN model used as a basis for this challenge requires a few significant modifications, the first one being the replacement of simple linear elasticity relation (6) with:

$$kw = p_{net} = p_{fluid} - \sigma_o - \sigma_l \tag{169}$$

This was used by Bunger[10], and is identical to original Nordgren [70] formulation except for the term $\sigma_l(x,t)$ with refers to the influence of other neighboring fractures.

Poiseulle equation (1) with these modified elasticity (169) will be updated:

$$q = -\frac{1}{M}w^3\frac{\partial p_{fluid}}{\partial x} = -\frac{1}{M}w^3\frac{\partial(p_{net}+\sigma_o+\sigma_l)}{\partial x}, \tag{170}$$

The term σ_o is assumed to be uniform along propagation direction and disappears with differentiation. The term σ_l on the other hand remains in the new continuity equation (2), and contributes to new updated Reynolds equation:

$$\frac{\partial w}{\partial t} - \frac{1}{M}\frac{\partial}{\partial x}\left(w^3\frac{\partial(kw+\sigma_l)}{\partial x}\right) + q_l = 0. \tag{171}$$

Now note that this small decision to include σ_l leads huge modification to the single fracture formulation, not to mention the additional work required to combine them into a functional system of multiple fractures.

The description of this theoretical multifracturing model will be divided into five sections.

- Section 4.1 explains a new mathematical formulation for multifracturing, introduces a number of components and a general idea on how to combine them.
- Section 4.2 presents an approach to joining fractures together and outlines an algorithm for calculating common junction pressure.

[September 10, 2015 at 14:04 – classicthesis version 1.0]

- Section 4.3 presents an algorithm for resolving fracture *visibility*, and as the result calculating σ_l efficiently.
- Section 4.4 theorizes simple approaches to resolving fracture collisions.
- Section 4.5 explains how this whole multifracturing formulation can be assembled together in a computer model, outlining some performance bottlenecks.

4.1 FORMULATION OF 2D MULTIFRACTURING PROBLEM

4.1.1 *Graph like structure*

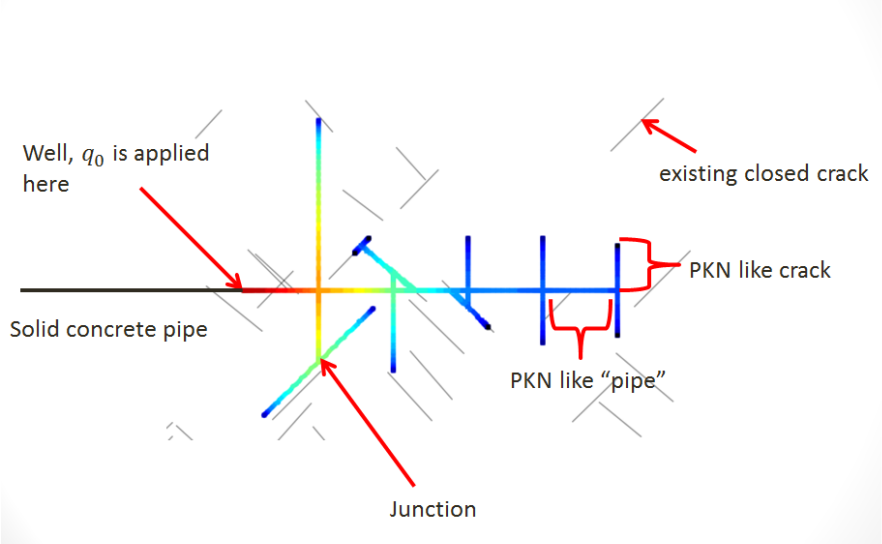

Figure 50: A sample 2D multifracturing geometry visualized

Lets assume that the multifracturing model is a collection of some smaller constructs. It exists in some horizontal rock layer, that when viewed form the top can be interpreted as a two dimensional plane. Consequently a number 2D points, *vertices*, can be specified. Each two *vertices* can be connected by an *edge*, consequently making the entire structure a *graph*. Edges and vertices are abstractions of various physical structures.

Edge can be interpreted as:

- *PKN crack*
- *PKN pipe*
- *solid pipe*
- *closed crack*

Vertex can be thought as:

- *junction* connection points, distributes fluid among connected edges, can act as a pump in location (wellbore)
- *propagating cracks tip* a movable *crack* tip location
- *closed cracks tip*, indicates *crack closed* start or end location

With this abstraction it follows that :

- each vertex can be located by its unique (x, y) coordinates (not to be confused with the normalized $\tilde{x}$)
- every vertex is connected to at least one edge
- every edge must connect two vertices
- normal vector $\hat{n}$ to each edge can be obtained.
- length L for edge is the distance between these two connected vertices
- each edge has different orientation, which results in different net backstress σ_o value
- *crack* and *crack pipe* store additional information about the distribution of fluid, and spatial discretization (grid type and N), while *crack pipe* and *crack closed* have no such data.
- locations of each edge local 1D grid point i in global 2D coordinate system can be then consequently derived as:

$$(x_i, y_i) = (x_1 + L_x L\tilde{x},\ y_1 + L_y L\tilde{x}) \tag{172}$$

Where unit vector $\hat{L} = (L_x, L_y)$ shows propagation direction and is perpendicular to edge normal $\hat{n}$.

Representing model as a graph structure is not necessary from mathematical, but highly beneficial form practical computational point of view (some other works also suggest this abstract structure interpretation [16]). This representation allows to couple 1D formulation, into 2D problem, while still effectively using 1D to describe each fracture. The added dimension is dealt with at a higher level, while the single fracture solution is reused locally for each edge. Additionally several issues, such as fracture interactions, rendering or actual code quality, will be shown later to be elegantly addressed with such structure representation. Note that if only one *junction* and *propagating crack tip* are connected by a *crack* edge this formulation is equivalent to standard half wing PKN model fracture.

4.1.2 *Backstress* σ_0

The backstress experienced by each fracture should be based on that fracture orientation relative to horizontal stresses in the underground formation. It is a common assumption in hydrofracturing problems, as showed by [43, 75, 105] to simply split this experienced stress into two parallel components, this should be denoted in this work as σ_x

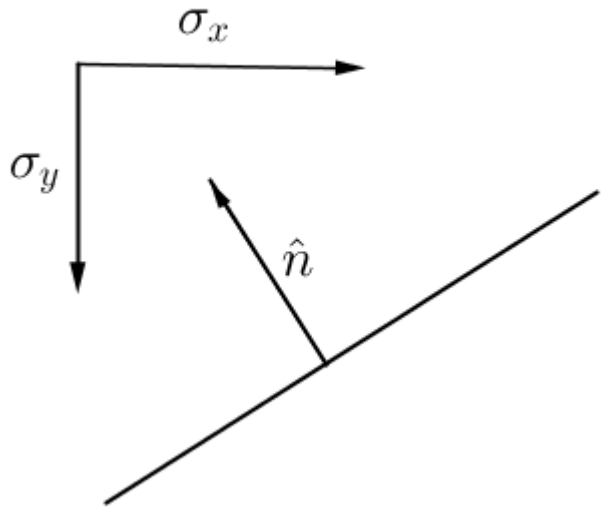

Figure 51: Edge normal $\hat{n}$ in relation to σ_x and σ_y.

and σ_y. The third component σ_z , acting in vertical direction, is ignored as has little influence on existing PKN like fractures. This assumes uniform stress experienced all over the underground formation.

The following relation will be used to find σ_0 for each edge:

$$\sigma_0 = |\hat{n} \cdot \sigma_x| + |\hat{n} \cdot \sigma_y|. \tag{173}$$

Where $\hat{n}$ is unit normal to that edge. As it can be observed from (170), if σ_0 is constant along fracture length this term would eventually vanish in computations. However if σ_0 is different for interconnected fractures, then this term must be taken into account if the fluid pressure (169) is to be properly compared between these fractures.

4.1.3 *PKN crack*

The conventional PKN like fracture, as described in Section 2.2, is used with a number of changes. Such a crack is attached to a *junction* by its inlet and has a *propagating tip*, that moves away from its the inlet. The computation for PKN crack needs to be slightly updated. The old governing equation for PKN model (29) is replaced by:

$$\begin{aligned} \mathcal{A}^w_{crack} = \frac{\partial w}{\partial t} = & \frac{k}{ML^2}\left[\frac{1}{3}w_0^3 x\frac{\partial w}{\partial x} + 3w^2\left(\frac{\partial w}{\partial x}\right)^2 + w^3\frac{\partial^2 w}{\partial x^2}\right] \\ & \frac{1}{ML^2}\left[3w^2\frac{\partial w}{\partial x}\frac{\partial \sigma_l}{\partial x} + w^3\frac{\partial^2 \sigma_l}{\partial x^2}\right] - q_l, \end{aligned} \tag{174}$$

to add the stress influence from nearby fractures σ_l. Furthermore the boundary at the inlet (24) should be modified to:

$$w(0,t) = \frac{1}{k}\left[p_{fluid}^{(x=0)} - \sigma_0 - \sigma_l(0,t)\right], \tag{175}$$

where p_{fluid} is the fluid pressure the *junction* this *crack* propagates away from. This formulation does not affect L computation, defined by operator $\mathcal{B}_w$ (32). The change applied to operator $\mathcal{A}$ still allows to use previously defined proper variable U with relative ease:

$$\begin{aligned}\mathcal{A}_{crack}^{U} = \frac{\partial U}{\partial t} =& \frac{k}{ML^2}\left[xU_0\frac{\partial U}{\partial x} + \left(\frac{\partial U}{\partial x}\right)^2 + 3U\frac{\partial^2 U}{\partial x^2}\right] \\ &+ 3U^{\frac{2}{3}}\left\{\frac{1}{ML^2}\left[\frac{\partial U}{\partial x}\frac{\partial \sigma_l}{\partial x} + U\frac{\partial^2 \sigma_l}{\partial x^2}\right] - q_l\right\}\end{aligned} \tag{176}$$

Therefore formulation (65) is still available. Although Ω formulation (77) could also be used, it carries an inherited problem with conversion form the width integral to actual width of the fracture. While this could be managed, it would considerably increase the time needed to develop the whole model, thus it should be left for future development.

4.1.4 *PKN pipe*

Within the boundaries of PKN model, described in Subsection 4.1.3, it is possible to consider some fixed length of fracture as a separate flow channel. Consequently this would results in a new system where we seek to find pipe width $w(x,t)$ with initial conditions

$$w(0,x) = w_*(x), \quad x \in (0,1), \tag{177}$$

and boundary conditions:

$$w(0,t) = \frac{1}{k}\left[p_{fulid}^{(x=0)} - \sigma_0 - \sigma_l(0,t)\right] \tag{178}$$

$$w(1,t) = \frac{1}{k}\left[p_{fulid}^{(x=1)} - \sigma_0 - \sigma_l(1,t)\right], \tag{179}$$

where $p_{fulid}^{(x=0)}$ and $p_{fulid}^{(x=1)}$ refers to fluid pressure at two connected *junctions*. This condition at $w(1,t)$ is much easier to deal with than the previous zero opening at crack tip condition (24), thus there will be no need for special BC conditions or ϵ-regularization.

The governing equation is similar to result obtained in normal PKN crack (29) with one significant difference; the propagation related term is removed:

$$\mathcal{A}^{w}_{pipe} = \frac{\partial w}{\partial t} = \frac{k}{ML^2}\left[3w^2\left(\frac{\partial w}{\partial x}\right)^2 + w^3\frac{\partial^2 w}{\partial x^2}\right] - q_l \tag{180}$$

Now $L = constant$ is the length of this channel, and the distance between two connected *junctions*. This governing equation has much smoother behavior than the previous for crack segment (174) , as the fracture tip and its singularity is no longer exist. Just like in previous case the proper dependent variable U can be introduced:

$$\mathcal{A}^{U}_{pipe} = \frac{\partial U}{\partial t} = \frac{k}{3ML^2}\left[\left(\frac{\partial U}{\partial x}\right)^2 + 3U\frac{\partial^2 U}{\partial x^2}\right] - 3U^{\frac{2}{3}}q_l. \tag{181}$$

Finally when the effect of neighboring fractures σ_l is included the governing equation becomes:

$$\begin{aligned}\mathcal{A}^{w}_{pipe} = \frac{\partial w}{\partial t} =& \frac{k}{ML^2(t)}\left[3w^2\left(\frac{\partial w}{\partial x}\right)^2 + w^3\frac{\partial^2 w}{\partial x^2}\right] \\ &+ \frac{1}{ML^2(t)}\left[3w^2\frac{\partial w}{\partial x}\frac{\partial \sigma_l}{\partial x} + w^3\frac{\partial^2 \sigma_l}{\partial x^2}\right] - q_l.\end{aligned} \tag{182}$$

4.1.5 *Solid pipe and Closed Crack*

It is reasonable to assume that there might be some fixed flow channels, such as man made horizontal concrete pipes. These *solid pipe* segments are assumed to have circular cross-section. Direct application of Poiseuille's Law in the simplest form can be made:

$$Q = \frac{\Delta p_{fluid}\pi R^4}{8\mu L}. \tag{183}$$

Where variable Q is the flow rate, and length L and radios R are constant. The term Δp_{fluid} is the difference between fluid pressure at the two junctions this *solid pipe* connects. Thus the flow rate might take negative or positive values, depending on the direction of the flow. This assumes laminar flow in these solid pipe connections, but the PKN model itself is based on a non turbulent flow assumption.

Closed cracks are preexisting fractures. This type of fractures is assumed to be closed by the confining pressure, but might be opened by the fracturing fluid. These have zero width, and exist as "markers" that may change the path of propagation of existing fractures. Each closed crack spams between two *closed cracks tips*, or if it was reached, but not opened by the fracturing fluid, between a *closed tip* and a *closed cracks tip*.

It could be assumed, as it follows (169), that this fracture will remain closed as long as:

$$p_{fluid} \leq \sigma_o + \sigma_l \tag{184}$$

There can be a number of other factors that should be taken into account. However ensuring that $p_{net} > 0$ for a fracture to open is necessary for the computations, as well as can be logically explained.

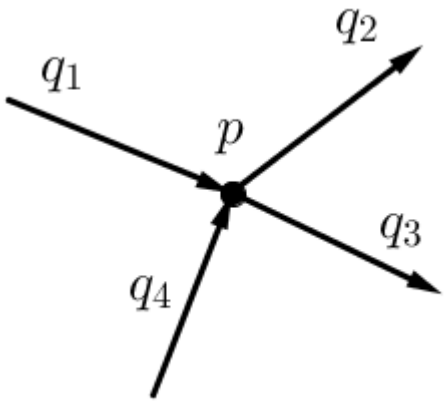

Figure 52: Junction condition visualized

4.2 JUNCTION STRATEGY

4.2.1 *General concept*

Each *junction* connects a number m of edges: *crack*s, *pipes, concrete pipes* or *closed cracks.* At least one edge should be connected, but there should be no restriction made on the maximum number (or at least there is no need to impose such limits). If we assume that the size of a *junction* itself is small enough, compared to the dimensions of connected edges, and these openings are relatively small compered to their lengths, it is plausible to modeled *junctions* as point size connections. For such point one would expect a single value of fluid pressure p_{fluid}, and fluid balance of flow through that point to be zero. Therefore within one *junction* it is assumed that:

Fluid pressure is exactly the same across all connected edges at the point of connection

$$p^{(1)}_{fluid} = p^{(2)}_{fluid} = ... = p^{(m)}_{fluid}. \tag{185}$$

Zero flux sum, all the flow in and out adds up to zero

$$q_1 + q_2 + ... + q_m = 0. \tag{186}$$

The above is similar to the one used by Kresse [42], but the idea can be traced back to simple pipe network problems [95]. However, the further derivation of the method presented here was not found in the considered bibliography.

4.2.2 *Newton method for junction fluid pressure*

Now lets say there is a *junction* with a number *m cracks, crack pipes* and *solid pipes* connected to it. Flow components of these connected

segments q_i (PKN pipe 4.2.4 or PKN crack 4.2.3) should added up to zero as required by flux sum (186). thus:

$$\sum_i^m q_i + q_0 = 0, \tag{187}$$

where additional q_0 can be added to account for fluid pumping at that *junction*, essentially turning it into wellbore.

To find the pressure value $\mathcal{J}$, for a *junction* one would need to find the root of:

$$F_{\mathcal{J}}(\mathcal{J}, \mathcal{J}_{other}) = \sum_i^m q_i + q_0 \tag{188}$$

Root of the above can be found using newton method. Note that the iterations must be performed together for all clusters of $\mathcal{J}$ connected by solid pipe segments, to pass the value of $\mathcal{J}_{other}$ (as required by solid pipe segments (195)) between concurrent iteration.

$$\mathcal{J}_{n+1} = \mathcal{J}_n - \frac{F_{\mathcal{J}}(\mathcal{J}_n, \mathcal{J}_{other\,n})}{F'_{\mathcal{J}}(\mathcal{J})}. \tag{189}$$

In other words before concluding step $n+2$, the step $n+1$ of all the other *junctions* must be found. The derivative of $F'_{\mathcal{J}}(\mathcal{J})$ is simply:

$$F'_{\mathcal{J}}(\mathcal{J}, \mathcal{J}_{other}) = \sum_i^m \frac{dq_i}{d\mathcal{J}}, \tag{190}$$

thus to implement this scheme we must define a way to obtain flow rates of each connected *cracks*, *crack pipes* and *solid pipes*, the function $q(\mathcal{J}, \mathcal{J}_{other})$, and it derivative $\frac{dq}{d\mathcal{J}}$. The expressions for these are given in later Subsections 4.2.3 and 4.2.4. Note that this strategy for obtaining junction pressure is not dependent on the type of connected edges, instead each edge should contain a generic function to calculate this values, which can be later used in a object orientated code design.

4.2.3 *Flow components for* cracks *and* crack pipes

In contradiction to the previously used Neumann type boundary condition in PKN model (24), where fluid injection rate q_0 was related to the first derivative at the crack inlet, the junction formulation results in Dirichlet boundary condition. The volumetric flow rate given by (1) can be rewritten in just the terms of fluid pressure using (169) as:

$$q = -\frac{1}{ML} w^3 \frac{\partial p_{fluid}}{\partial x} = \frac{1}{MLk^3} (p_{fluid} - \sigma_o - \sigma_l)^3 \frac{\partial p_{fluid}}{\partial x}. \tag{191}$$

If there are *cracks* or *pipe cracks* attached to a *junction* some numerical approximation of $\frac{\partial p_{fluid}}{\partial x}$ measured at these can be derived. If this approximation is based on a polynomial, then we can then find some parameters α and β to replace $\frac{\partial p_{fluid}}{\partial x}$, thus find $q(0,t)$, and write junction component flow $q(\mathcal{J}, \mathcal{J}_{other})$ as the following nonlinear relationship:

$$q(\mathcal{J}, \mathcal{J}_{other}) = \frac{\lambda}{MLk^3}(\mathcal{J} - \sigma_o - \sigma_l)^3 (\alpha\mathcal{J} + \beta)\,. \tag{192}$$

And consequently:

$$\frac{dq}{d\mathcal{J}} = \frac{\lambda}{MLk^3}\left[3(\mathcal{J} - \sigma_o - \sigma_l)^2 (\alpha\mathcal{J} + \beta) + (\mathcal{J} - \sigma_o - \sigma_l)^3\alpha\right]. \tag{193}$$

The parameters α and β are dependent on $w(x,t)$, σ_0, $\sigma_l(x,t)$, the discretization of x and type of polynomial used for the approximation, $\lambda = \pm 1$ depends on the direction of flow. Two versions of these polynomial approximations are shown in Subsection 5.1.1.

4.2.4 *Flow components for* solid pipes

Lets use the following parameter γ to replace fixed length L and radius R of a *solid pipe*:

$$\gamma = \frac{3\pi R^4}{2ML}. \tag{194}$$

Solid pipe has to be connected to two distinct *junction*s, and the difference in pressure between these is given by $\Delta p = (\mathcal{J} - \mathcal{J}_{other})$, where the fluid pressure given at the other junction connected by a solid pipe is given by $\mathcal{J}_{other}$. Therefore a solid pipe attached to a junction would result in the following component of flow sum (188):

$$q(\mathcal{J}, \mathcal{J}_{other}) = \gamma\mathcal{J} - \gamma\mathcal{J}_{other}. \tag{195}$$

And consequently:

$$\frac{dq}{d\mathcal{J}} = \gamma. \tag{196}$$

4.3 METHOD FOR ELASTICITY INTERACTIONS

4.3.1 *Calculating σ_l value*

This section will describe a method for approximation of neighboring fracture influence σ_l.

Some previous work by Bunger [10] presented analytical methods for far field influence witch can be interpreted as:

$$\sigma_l^{(1)} = \frac{3}{8} p \frac{h^2}{H^2}, \tag{197}$$

$$\sigma_l^{(2)} = \frac{kLh \int_0^1 w dx}{H^3}, \tag{198}$$

where H is fracture spacing in an array of parallel PKN fractures, the distance between two fractures. The approximations $\sigma_l^{(1)}$ and $\sigma_l^{(2)}$ were derived from the full theoretical formulation for elastic response in an uniform isotropic medium. The new method proposed here should be constructed such so it obtains comparable results, yet allows for calculation of σ_l for any placement of edges (fractures) in the model. The assumption is that for every point x_i on target fracture the influence projected by point x_j, and the region near the point x_j, on the influencing neighboring edge is:

$$\sigma_l^{(j)} = \frac{gkhw_j \Delta x_j L}{min(d^3, 1)} |(\hat{n}_j \cdot \hat{\sigma})(\hat{n}_i \cdot \hat{\sigma})|, \tag{199}$$

where:

- $\hat{n_j}$- normal unit vector to source edge
- $\hat{n_i}$- normal unit vector to destination edge
- $\hat{\sigma}$- unit vector in the direction of calculated σ_l, the direction from x_i to x_j on a two dimensional plane
- w_j- width of edge at x_j
- Δx_j - half the distances to next and previous points on source edge grid
- d_j - the distance between x_i and x_j
- L - length of influencing edge
- h - height of the influencing edge
- g - an elasticity constant (value approximated in Subsection 5.2.1)

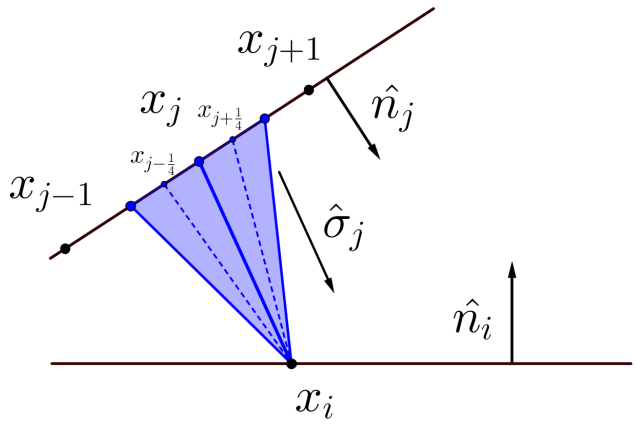

Figure 53: Graphical reference to calculation of pseudoelastic influence between two edges.

Figure 53 provides a graphical description of this formulation. The term $min(d^3, 1)$ is not present in (198), but is added here to make simulations possible, as explained further in Subsection 5.2.2. Furthermore the equation (199) is in fact very similar to the far field approximation, (198) both compute the integral, but (199) does take the orientation of fractures into account. Adding up (199) for each point, in a case of two close parallel fractures will add up to (197), as shown in Subsection 5.2.1. Therefore the presented approximation is close to the one suggested by Bunger [10], however some details for computation of this method must be provided.

Although Δx_j value could be fixed on already existing grid discretization, doing so could result in significant inaccuracy if $d_j << \Delta x_j$. Therefore additional subdivision of source grid will be needed until relative and absolute change in $\sigma_l^{(j)}$ between each subsequent subdivisions is less than some tolerance values σ_l^{abstol} and σ_l^{reltol}, which will be found later.

For edge with N points lets define:

$$\Delta x_{j-1/4} = \frac{x_j - x_{j-1}}{2}, \quad \frac{3}{2} \leq j - 1/4 \leq N, \tag{200}$$

$$\Delta x_{j+1/4} = \frac{x_{j+1} - x_j}{2}, \quad 1 \leq j + 1/4 \leq N - \frac{3}{2}, \tag{201}$$

$$\Delta x_{1+1/4} = 0, \quad , \Delta x_{N-1/4} = 0, \tag{202}$$

$$\Delta x_{2-1/4} = x_2, \quad \Delta x_{N-1+1/4} = 1 - x_{N-1}. \tag{203}$$

This includes connected *vertexes*[1] at $x_1 = 0$ and $x_N = 1$, therefore initially for *crack pipes* $N := N$, but for *cracks* $N := N + 1$. The subdivision of this interval is done such each point is assigned two segments $j - 1/4$ and $j + 1/4$, which are quaters of the distance to each other neighboring points. The most outer points are given zero Δx value, as it is chosen that *vertexes* are point size and therefore should project no σ_l value. The crack opening at these outer points would either be zero value (if crack tip), hence no projected influence, or tied to pressure at the junction. As the value of pressure at the junction is already depends on σ_l this would create recursive dependence between *junction* fluid pressure and σ_l perceived by connected edges. To avoid this zero values at points $x_{1+1/4}$ and $x_{N-1/4}$ are set.

This process should then recursively continue dividing the original Δx_j interval:

$$\begin{aligned} \sigma_l^{(j)} &= \sigma_l^{(j-1/4)} + \sigma_l^{(j+1/4)} \\ &= \sigma_l^{(j-3/8)} + \sigma_l^{(j-1/8)} + \sigma_l^{(j+1/8)} + \sigma_l^{(j+3/8)}, \\ &= \dots \end{aligned} \tag{204}$$

$$\begin{aligned} \sigma_l^{(j)} &= \sigma_l^{(j-c)} + \sigma_l^{(j+c)} \\ &= \sigma_l^{(j-c-c/2)} + \sigma_l^{(j-c+c/2)} + \sigma_l^{(j+c-c/2)} + \sigma_l^{(j+c+c/2)}, \\ &= \dots \end{aligned} \tag{205}$$

Where $c = \left\{\frac{1}{4}, \frac{1}{8}, \frac{1}{16}, \dots\right\}$ is a fraction that depends on the depth of recursion. This process is repeated until tolerances σ_l^{abstol} and σ_l^{reltol} are met:

$$\begin{aligned} \sigma_l^{abstol} &> |\sigma_l^{(j\pm c)} - \sigma_l^{(j\pm c-c/2)} - \sigma_l^{(j\pm c+c/2)}| \\ \sigma_l^{reltol} &> \frac{|\sigma_l^{(j\pm c)} - \sigma_l^{(j\pm c-c/2)} - \sigma_l^{(j\pm c+c/2)}|}{\sigma_l^{(j\pm c)}}. \end{aligned} \tag{206}$$

For each new point $x_{j\pm c}$ resulting from this interval division extra values of $w_{j\pm c}$ must be extrapolated. This can be achieved by linear extrapolation:

$$w_{j\pm c} = a_{j\pm 1/4} x_{j\pm c} + w_{j-1/4}, \tag{207}$$

where the value of $a_{j\pm 1/4}$ is calculated initially and carried over to each further recursive step:

1 Junctions or crack tips. Again abstracting the whole structure to a graph simplifies the calculation.

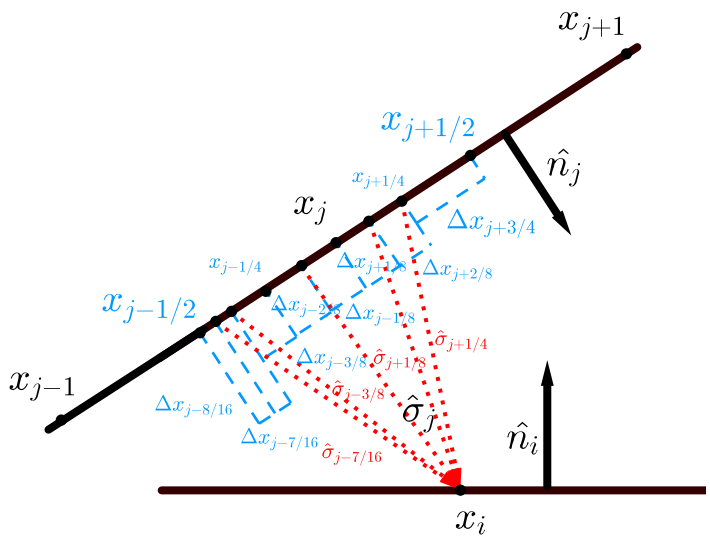

Figure 54: Recursive subdivision of Δx_j. The vector $\hat{\sigma}_l$ is changed with every division, thus the process is repeated until desired accuracy is obtained

$$a_{j-1/4} = \frac{x_j - x_{j-1}}{2}, \quad a_{j+1/4} = \frac{x_{j+1} - x_j}{2}. \tag{208}$$

The length for each subdivision of $\Delta x_{j\pm c}$ is also defined recursively by dividing in half:

$$\Delta x_{j\pm c} = \frac{\Delta x_{j\pm 4c}}{2}, \tag{209}$$

and finally to find the distance $d_{j\pm c}$ one must find $x_{j\pm c}$, this is preferably also done recursively with each step:

$$x_{j\pm c/2} = x_{j\pm c} + \Delta x_{j\pm c/2}. \tag{210}$$

So then $d_{j\pm c}$ can be found by distance between two points (172), $x_{j\pm c} = \tilde{x}$ to find their coordinates in 2D plane. A graphical explanation of this subdivision is shown on Figure 54. This method could be replaced by some integral, as this recursive subdivision does essentially do numerical integration, where distance function d is rewritten in terms of one variable $\tilde{x}$. Unfortunately such integral, although exists, does not considerably reduces the amount of operations that must be performed, and the complexity of σ_l computation does not change significantly. Furthermore this method does allow to change $min(d^3, 1)$ term to any other function, without the need to again evaluate the integral, thus this method is much better for initial prototyping.

4.3.2 *Resolving edge visibility*

Further question arises from finding which fractures are visible to each other, and therefore project stress influence σ_l on to each other. The approximations of σ_l were derived for uniform continuous medium. Fractures effectively split this medium making it much harder to for formulating sensible interpretation. Here it is assumed that the force of σ_l is projected in straight lines from the source. If this straight lines meet another fracture, the medium ends and the force is projected no further, but applied to the flow inside that fracture. In this simplified approach there must be a *straight line of sight*, the calculation requires to know which edges are visible, and which are obstructed.

This is trivial if only parallel fractures of equal length are considered [10], yet if some more advanced geometries are to be allowed it is required to implement some generic algorithm. Existing solution for 2D visibility problem is adopted [72]. This is a combination of ray casting and wall tracking techniques, common in 2D graphics applications. PKN crack and pipe edges are treated as impermeable walls for casted visibility rays, and these rays are treated as projections of $\sigma_l^{(j)}$ force. If a grid point on *crack pipe* or *crack* can see a grid point on the other edge then a ray can be cast, and calculation of σ_l follows. (see Figure 55). This Algorithm 3 needs to be effectively performed on each grid point on each edge, in order to determinate its visibility to the other points.

The Algorithm 3 results in an representation of 360 degrees view around each grid point as an interval from 0 to 2π with marked visible slices of edges (check Figure 55). These slices are created by intersections of cast rays and edges, and only the one closest to the projection source are kept. Slices have their start and end positions specified relative to parent edges , and so the specific range of all grid points in that edge can be determined. This means that situations when entire edge or just a part of it are visible can be handled.

The detailed code can be found in Section A.5.

Finally having dealt with finding collection of all visible grid points with respect to one grid point the formula (199) should be carried over all of those to get the total neighboring fracture influence on that grid point.

$$\sigma_l = \sum_{k=1}^{all\ visible} \sigma_l^{(k)}. \tag{211}$$

Then it is possible to numerically approximate $\frac{\partial \sigma_l}{\partial x}$ and $\frac{\partial^2 \sigma_l}{\partial x^2}$ which appeared in (174) and (182), preferably with central finite difference scheme (125). These approximation can then be used in Reynolds equations (174), (176) and (182), or in junction strategy shown in Section 4.2.

```
input  : a collection of edges, and a collection of vertexes
output : resolved grid point to grid point visibility
for each grid point in every edge do
    pick one random vertex and cast a ray to that vertex;
    cast rays to all the other vertexes;
    sort other vertexes by the angle between that one vertex ray,
    and other vertexes rays;
    prepare an array to hold a slice of an edge, same size as
    number of vertexes;
    for each non transparent edge, but the one the grid point belongs to
    do
        find its end vertexes positions in the sorted array, loop
        around if necessary (the two vertexes this edge connects);
        divide the edge into edge slices using rays between this
        edge end vertexes, as determined by vertexes index in the
        sorted array;
        for for each sliced edge piece do
            if array is empty at slicing ray vertex index or this edge
            slice is closer to grid point than the one already occupying
            the array then
                put edge slice in the structure at slicing ray vertex
                index;
            end
        end
    end
    for each edge slice in the array do
        mark all corresponding points as visible by the grid point
        considered in the outer loop;
    end
end
```

Algorithm 3: Simplified visibility determining algorithm (informal pseudocode)

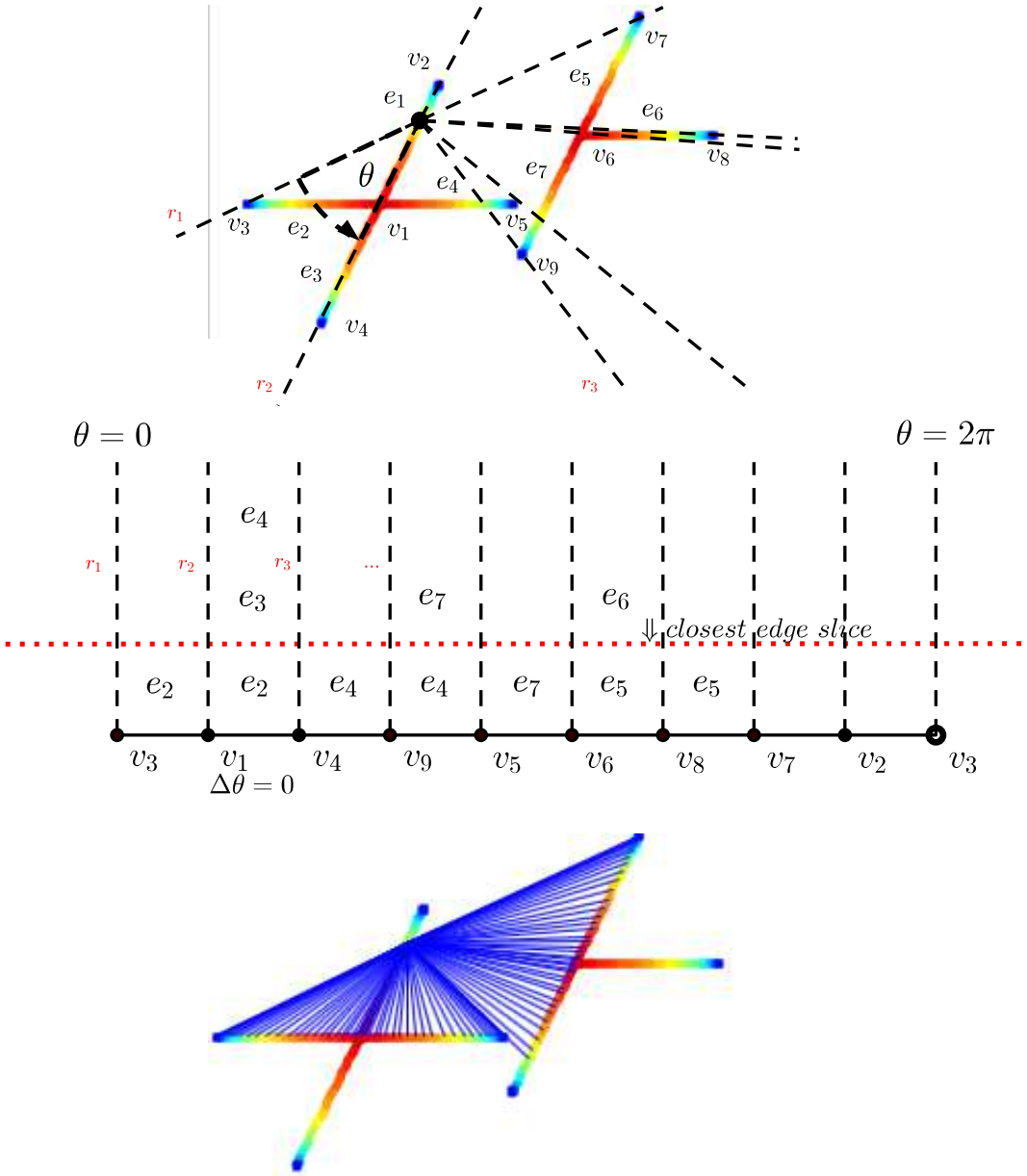

Figure 55: Details of visibility resolving algorithm. First rays r_i are projected form source point to all vertexes v_i. Then edges e_i are sliced by these rays and stored in a structure, sorted by θ. Closest slice on each interval is marked as visible.

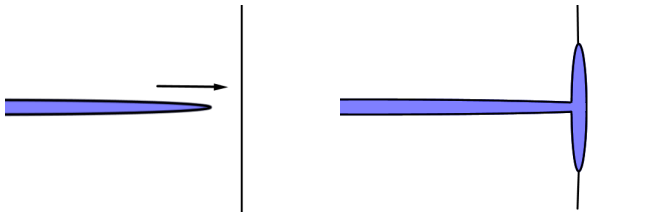

(a) Propagating fracture approaches closed fracture

(b) Closed fracture is opened

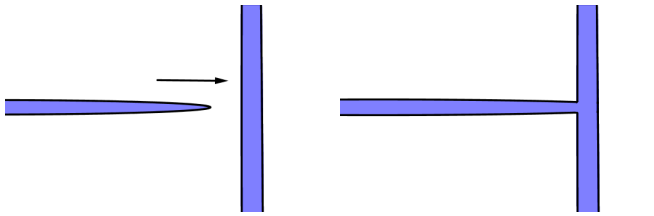

(c) Propagating fracture approaches existing opening

(d) Openings are joined together.

Figure 56: Interpretation of some possible fracture collision scenarios.

4.4 FRACTURE COLLISIONS

So far the presented formulation offered no restrictions on geometry of the model. Each edge representing fracture object could be placed anywhere in the 2D plane, without any particular rules about its position with respect to other objects. This should be changed in order to obtain more physical meaning. The most urgent restriction to the placement of fractures should be accounting for possible edge intersections. As a general rule there *should be no fracture grid intersection*, if two edges intersect that indicates a junction should rather be placed instead at the intersection point, and the grid points should be relocated. Otherwise two separate flow channels would overlap, resulting in obviously highly unrealistic formulation. While this still might have some reason behind it, if one of the edges in question is an *concrete pipe* object this intersection should be ignored, for intersections of other type of edges a possibility of fluid flowing in and out of intersecting edges must be taken into account. There are two ways intersection of edges might be introduced in the model:

- The initial placement of edges contains intersections. Such initial condition for the model would be considered invalid, one should provide proper initial problem geometry or fix the initial condition such so junctions replace the intersection points..
- When the solution is computed, propagating fracture front runs into other edge. This event could have its consequences in cre-

ation of new fractures and propagating in new directions, thus rapidly increase complexity of the model geometry.

While the first type is a trivial problem that should be resolved before computation is started, the collisions of propagating fractures must be detected during computation, as well as their outcome must be decided.

To detect these collisions any simple line intersection algorithm can be used, when each edge is treated as a line segment between the two vertexes it connects. This requires the number of edges squared intersection tests to be performed, but compared to the complexity of the whole problem is not a significant number.

When collisions are detected, they can be of one of this types:

- crack to closed fracture, interaction with natural fracture
- crack to other crack or pipe, interaction with another hydraulic fracture
- crack to other junction of crack tip

The third type is a rare scenario since vertexes considered here are of point size, nevertheless one can assume that some collisions are of this type by assuming some proximity threshold. Similar specification of collision types, but for a different multifracturing model, was done by Kresse [42].

The strategy used here is to pause if these collisions are detected, apply changes to the model to transform intersecting edges into some new meaningful structures and then continue computation. For all the changes made, there are two practical criteria that arise if this model is to be consistent.

The total amount of fluid in the system before and after collision must remain constant:

$$Vol_{before} = Vol_{after} \tag{212}$$

Which can be calculated by integrating all openings of all affected edges $\sum L \int_0^1 w(x)dx$. This will allow for fluid balance (164) to remain unaffected by the collision.

The second criteria comes from junction condition (185). The strategy used to compute fluid pressure at junctions ensures the same value across connected edges, but does not guarantee valid nor relatively smooth transition in this value. To maintain relatively smooth and continuous p_f (reasonable differences over discretized grid), lets assume the value at next closest grid points ($x_2 > 0$ or $x_{N-1} < 1$) is similar:

$$p^{(1)}_{fluid}|_{x_2 \text{ or } x_{N-1}} \approx p^{(2)}_{fluid}|_{x_2 \text{ or } x_{N-1}} \approx ... \approx p^{(j)}_{fluid}|_{x_2 \text{ or } x_{N-1}} \tag{213}$$

As collisions in this work are expected to force some fluid transfer to achieve (212), balancing out pressure at the same time (213) provides a reasonable way of managing this transfer.

4.4.1 *Crack to Natural Fracture (closed crack)*

A good study of interaction between propagating fracture and natural closed fracture was presented by Chuprakov in [17] and Kresse in [42]. Both formulations show well the complexity of the problem, the involved parameters include toughness and natural fracture permeability, that are not considered in this model. Hence developing an extensive model for this type of interactions would be a inferior redoing of work that was already done, and the result could be easily invalidated by introduction of some new variable or physical phenomena. A very simplified model should be presented here, that is not meant to properly describe the entire physical process, but to rather acts a reliable solution for the whole multifracturing model, that produces a meaningful result.

As it is well shown in [17], there is a finite number of possible outcomes of fracture to natural fracture collision. The propagating fracture might open natural closed fractures or continue propagating, or both. The approach presented here should allow for all of these theoretical outcomes, thous add new fracture segments depending of the choice of action.

First lets define when an intersection of fracture and closed fracture triggers this strategy. The collision is considered *if intersection of line segment representation of fracture and closed fracture exist and the distance d between the point of intersection and crack tip is $T_C < d < 2T_C$*. The parameter T_C will represent here some small collision distance detection threshold. Under this definition the collision is in fact accepted after propagating fracture crosses the natural fracture. If this cross distance is greater than $2T_C$ the computation proceeded to far, and should revert to previous time step. Consequently it can be predicted when a fracture will hit some closed NF (natural fracture):

$$\textit{time to collision} \approx \frac{\textit{distance to intersection } + \frac{3}{2}T_C}{V_0}, \tag{214}$$

which gives yet another usage for speed equation V_0 term (30). This criteria for prediction and detection, should be used to adjust time steps. Once the tip reaches right position, the length of propagating hydraulic fracture (HF) d that makes past the natural fracture (NF) should be cut of and removed. This removed amount counts as before volume in (212):

$$Vol_{before} = L_{crack} \int_{1-\frac{d}{L}}^{1} w_{crack} dx. \tag{215}$$

Now the reminder of initial crack should be translated into a pipe segment. The new width of this new pipe would be:

$$w_{pipe}(x) = w_{crack} \left(x \frac{L_{crack} - d}{L_{pipe}} \right) \; x \in (0,1). \tag{216}$$

Since new pipe segment will be shorter by d. This translation will require some extrapolation, as w comes as discretized over some points. The process of finding intermittent data points in described in Appendix A.3. Then the old crack segment is removed from the model and three new segments originating from new junction are considered (Figure 58). These have respective lengths L_1, L_2, L_3 and are under influence of stresses $\sigma_1, \sigma_2, \sigma_3$. For a fracture to remain opened net fluid pressure must be greater than experienced stress, thus the condition (184) is used to verify that for each considered fracture:

$$p_{net} > 0 \;\rightarrow\; p_{fluid} - \sigma_o^{(i)} - \sigma_l^{(i)} > 0, \; i = 1,2,3, \tag{217}$$

where the value of p_{fluid}, fluid pressure[2], is determinate by the value of the old fracture at intersection. Since for each considered new fractures $\sigma_o^{(i)}$, $\sigma_l^{(i)}$ will have different values, it is possible that all considered new fractures can remain, or the fluid pressure might not be enough to open any of these new segments, and all of them should be discarded. It is possible that a fracture with negative net pressure p_{net} might shield other considered fracture, therefore the condition must be checked again if one of the new fractures was discarded. Once the number of allowed new segments is found, the width at x_2 is set

$$w^{(i)}(x_2) := \frac{p_{fluid} - \sigma_o^{(i)} - \sigma_l^{(i)}}{k}, \; i = 1,2,3, \tag{218}$$

for each of the newly opened fractures. Therefore the initial width of these segments might be different, while p_{fluid} remains at relatively the same levels. Finally the remaining data points $w(x_3 ... x_N)$ can be delivered from self similar solution (271), as argued in Subsection A.4.11, scaled by a constant factor to obtain the same value at x_2. The remaining values of L_1, L_2, L_3 can be found such so

2 Note again that the fluid pressure is different than the net pressure, as the later is affected by the fracture orientation.

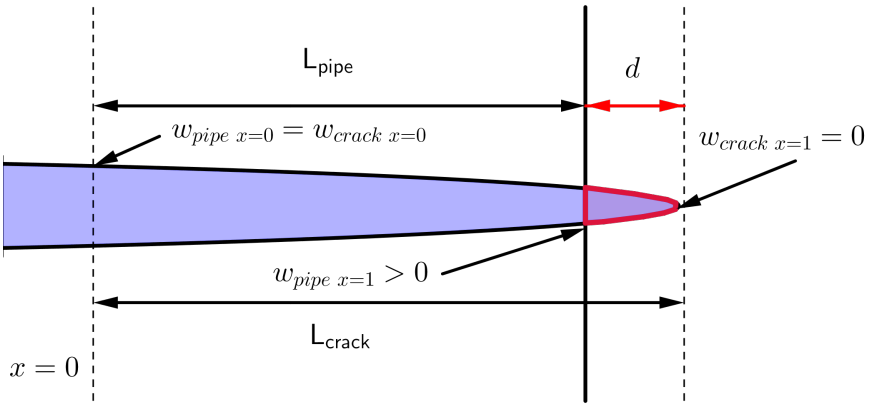

Figure 57: Obtaining w_{pipe} by taking a part of existing w_{crack}, visualization of conversion (218).

$$Vol_{after} = L_1 \int_0^1 w^{(1)}_{new\ crack} dx + L_2 \int_0^1 w^{(2)}_{new\ crack} dx + L_3 \int_0^1 w^{(3)}_{new\ crack} dx \quad , \tag{219}$$

has the same volume as originally removed part (215). This can be achieved by assuming some simple proportion of volume split among opened fractures, say proportional to their relative width $\frac{w^{(i)}}{w^{(1)}+w^{(2)}+w^{(3)}}$, and bisection method used on function:

$$f(L_{(i)}) = L_{(i)} \int_0^1 w^{(i)}_{new\ crack} dx - \frac{w^{(i)}}{w^{(1)} + w^{(2)} + w^{(3)}} Vol_{before}. \tag{220}$$

The procedure described here will produce an outcome that can be then further integrated in time by the model described in this work. The only guaranteed property is that it aligns with all the other assumptions already made, and does not significantly influences stability or accuracy of computation. In fact this strategy is designed to fit the best with the rest of the model. Alternatively it is possible to arbitrary force removal, or addition of other segments, as long as non negative net fluid pressure is maintained (217). The method could potentially be replaced by other, more sophisticated solutions by [17, 42], however the outcome should still have to agree with (212) and (213). Regardless of strategy used, the process of interaction with natural closed fractures is considered as an instant time event, and as long as all possible outcomes can theoretically by handled by this model, this method for collisions can be used at least as a simplified test procedure.

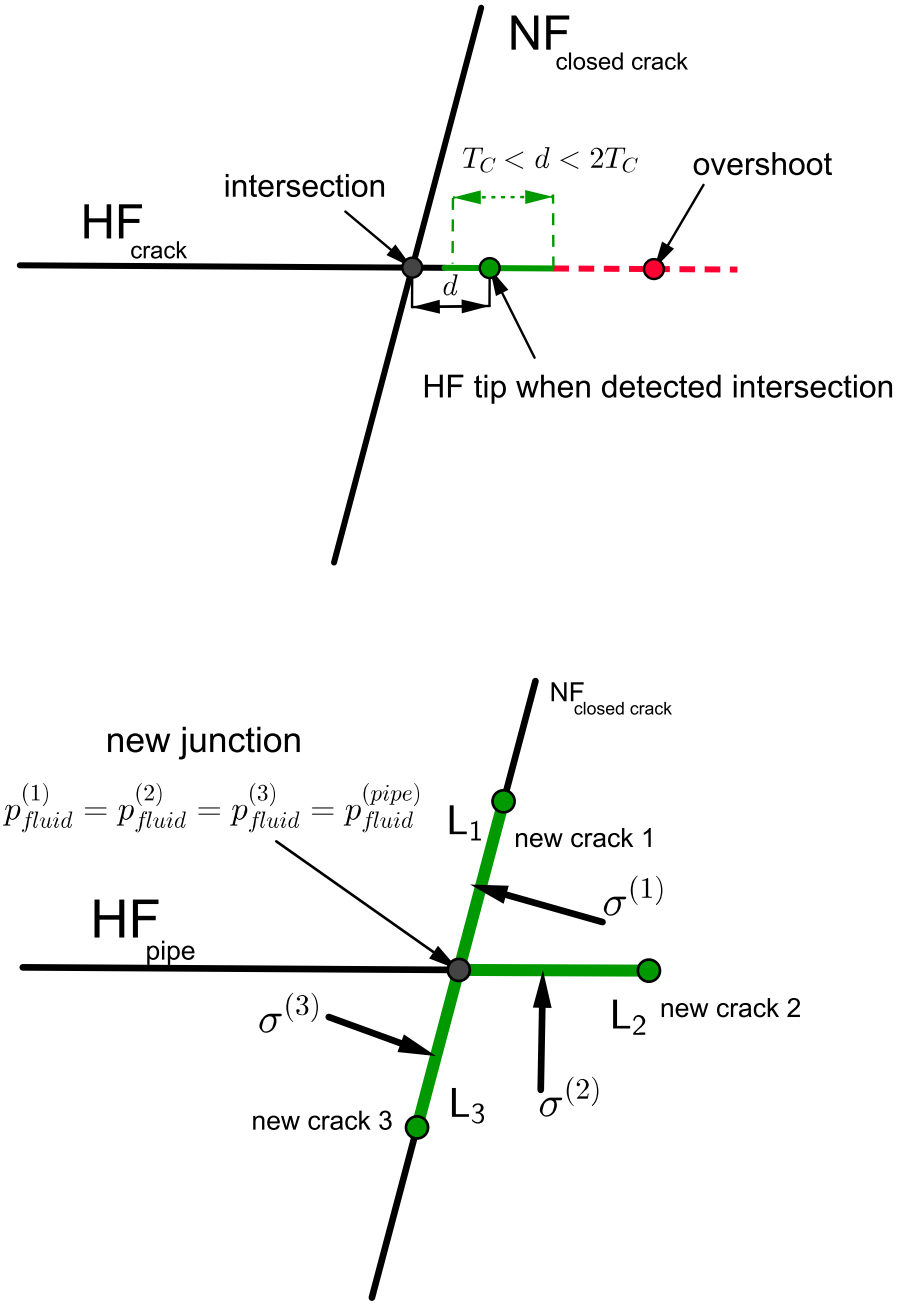

Figure 58: Detection criteria and possible outcome of crack to NF collision.

4.4.2 *Crack to Hydraulic Fracture (crack or pipe crack)*

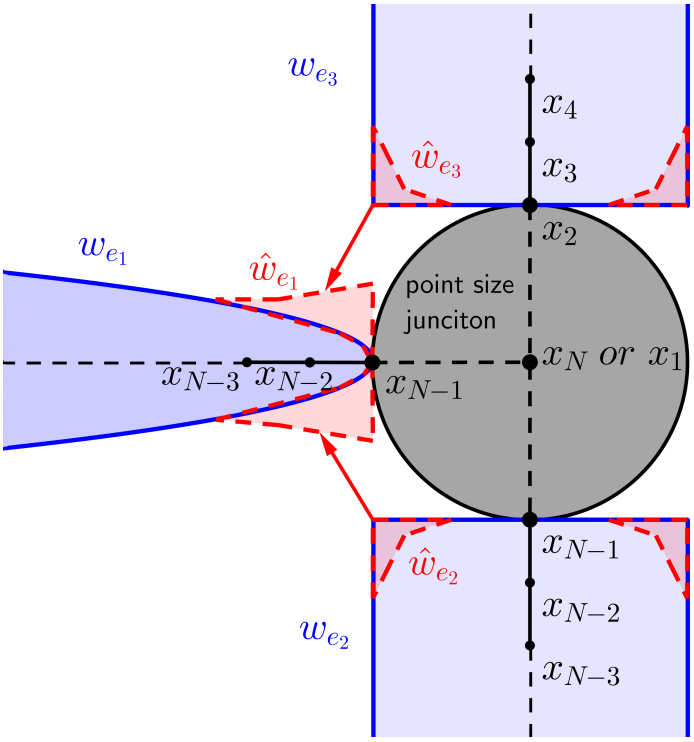

Figure 59: When two fractures collide some fluid transfer is allowed in the close proximity of newly connected junction point. The volume added by $\hat{w}_{e_1}$ should correspond to the volume removed by $\hat{w}_{e_2}$ and $\hat{w}_{e_3}$. This crates nice smooth starting point for further simulations. Not to scale.

The second probable type of collisions are intersections of propagating fracture with another fracture or PKN pipe segment. Unfortunately attempts to find any explanation of this phenomena in the literature were unsuccessful and no good existing example was found. Here again some simplified method that does the task for the purpose of simulating the whole model is used. The detection of this intersections will be again based on some collision acceptance threshold T_C. If the distance form fracture tip, to the intersection with opened hydraulic fracture d is less than threshold $|d| < T_C$ the collision is detected (extended projection of crack is used). If the fracture collides but, the $d > T_C$, overshoot happens, and smaller time step should be used. The time to intersection can, again, be predicted using fluid velocity :

$$\textit{time to collision} \approx \frac{\textit{distance to intersection}}{V_0} \tag{221}$$

When intersection is detected, new junction is created in its place. The old crack, and hit pipe or crack are removed form the model, and

replaced with two new pipe segments and a new crack segment (if hit a crack), or three new pipe segments (if hit a pipe). The procedure is the same, regardless of what type of object was hit, as all are being treated as generic edges. The crack will be transformed into new edge e_1, and the hit edge will be split in two new edges e_2 and e_3.

The volume before is:

$$Vol_{before} = L_{old\ crack} \int_0^1 w_{old\ crack} dx + L_{hit\ edge} \int_0^1 w_{hit\ edge} dx, \tag{222}$$

while the volume after would be

$$Vol_{before} = L_{e_1} \int_0^1 w_{e_1} dx + L_{e_2} \int_0^1 w_{e_2} dx + L_{e_3} \int_0^1 w_{e_3} dx. \tag{223}$$

The openings w_e of new edges are given by:

$$w_{e_1}(x) = w_{old\ crack}(x) \quad x \in (0,1), \tag{224}$$

$$w_{e_2}(x) = w_{hit\ edge}(s_1 x) \quad x \in (0,1), \tag{225}$$

$$w_{e_3}(x) = w_{hit\ edge}(s_2 x + s_1) \quad x \in (0,1), \tag{226}$$

where parameters $s_1 = \frac{L_{e_1}}{L_{e_1}+L_{e_2}}$ and $s_2 = \frac{L_{e_2}}{L_{e_1}+L_{e_2}}$ are proportional to new edges lengths share in old hit edge $s_1 + s_2 = 1$. This assignment of crack opening will require some extrapolation of values, similarly as needed in NF case. This is done with techniques shown in Appendix A.3.

So far the volume has changed, as e_1 is a result of snapping old crack to attach it at the new intersection. Moreover the inherited value of $p_{net\ e_1}(x_{N-1}) \approx 0$, as this is the proximity of old crack tip, does not match with $p_{net\ e_2}(x_{N-1}) \approx p_{net\ e_3}(x_2) > 0$. This creates a jump in fluid pressure value that is likely to destabilize either junction strategy, via disturbing Newton iterations in (189), or significantly increase problem stiffness. To fix this problem, while maintaining the same fluid volume a scheme is constructed that attempts to transfer some of the volume to meet both conditions (212) and (213). First lets define ϖ as "weights" for each of the grid points.

$$\varpi_i^{(e_1)} = x_i^p, \tag{227}$$

$$\varpi_i^{(e_2)} = s_2 x_i^p, \tag{228}$$

$$\varpi_i^{(e_3)} = s_1 (1 - x_i)^p. \tag{229}$$

These are chosen such so most of the fluid volume is transferred near the junction, as idealized on Figure 59. Now lets seek values of a and b used in:

$$\hat{w_{e_1}}(x) = (1 + b\omega_i^{(e_1)})w_{e_1}, \tag{230}$$

$$\hat{w_{e_2}}(x) = (1 + a\omega_i^{(e_2)})w_{e_2}, \tag{231}$$

$$\hat{w_{e_3}}(x) = (1 + a\omega_i^{(e_3)})w_{e_3}, \tag{232}$$

such so (212) (213) are satisfied by finding zeros of:

$$f_1(a,b) = Vol_{before} - L_{e_1}\int_0^1 \hat{w_{e_1}}dx - L_{e_2}\int_0^1 \hat{w_{e_2}}dx - L_{e_3}\int_0^1 \hat{w_{e_3}}dx, \tag{233}$$

$$f_2(a,b) = p_{fluid}^{(e_1)}(x_{N-2}) - \frac{p_{fluid}^{(e_2)}(x_{N-1}) + p_{fluid}^{(e_3)}(x_2)}{2}. \tag{234}$$

Chained bisection method, one bisection algorithm inscribed into another, can be used to first find the value of b that matches a for volume f_1, and then check for solution of pressure f_2.

The following scheme handles a relatively small volume transfer, compared to the volume of involved edges. With $p > 1$ used for weights (227), (228) and (229) , the majority of volume is displaced locally, near the junction. It can have a physical interpretation of pressure jump in system resolving relatively fast, compared to the other processes. However, this modification does not resolve entire pressure drop problem, which must be later resolved by the ODE solver.

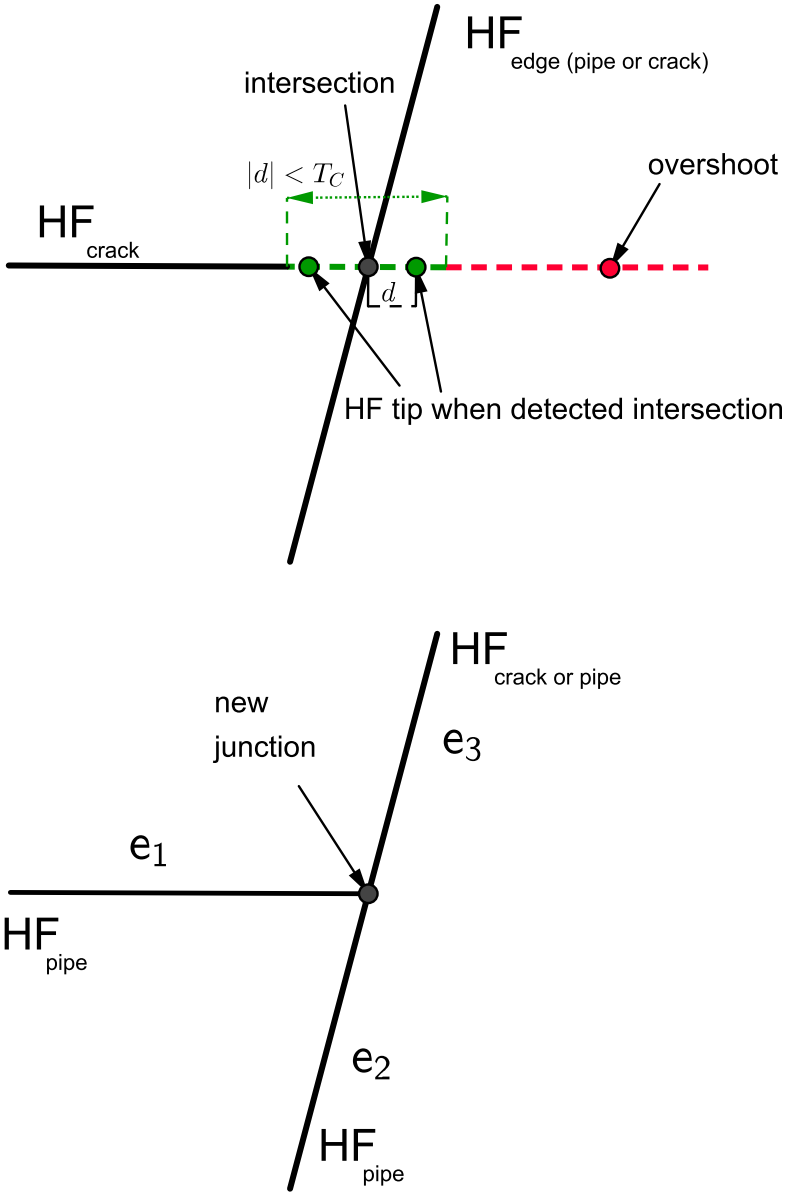

Figure 60: Detection criteria and outcome of crack to HF collision.

4.5 LARGE COUPLED DYNAMIC SYSTEM FOR MULTIFRACTURING

4.5.1 *Main algorithm*

4.5.1.1 *Model object concept*

So far the basis for the multifracturing model was derived, that covers multiple types of connected edges and their interactions, now it should be combined into a single working model. The approach presented here is an evolution of previous single fracture solution shown in Section 3.2. The problem will again be solved as an initial value problem, where the value of $y(t) = \mathcal{M}(t)$ is sought, as the problem changes over some time from initial state $y_0 = \mathcal{M}_0$. Here $\mathcal{M}$ should denote the whole model, which is however more than just a value vector as compared to the single fracture case. Instead $\mathcal{M}$ should be treated as a higher level abstract object that includes:

- expression for the change in time $y'(t) = \mathcal{M}'(t, \mathcal{M})$.
- collection of edges (cracks or pipes) connected with vertexes into a graph fracture structure.
- 1D discretization for each edge with a mesh $x \in < 0, 1 >$, and a set of edge specific properties ($k,\ L,\ \epsilon,\ ,\ q_l, ...$).
- 2D discretization of the entire model and other properties, such as volume and placement of fluid pumping q_0.

In case of the one dimensional single fracture problem the solution was effectively a two dimensional array, the value of w and L for each considered x_i and time step. However since in the multifracturing scenario the number of fractures and the structure they create changes over time, the solution should be expressed as a collection of $\mathcal{M}$ states at different times, which encapsulates both numerical values and the changes in fracture structure:

$$multifracture\ solution = \{\mathcal{M}_0,\ \mathcal{M}_1,\ \dots\ ,\ \mathcal{M}_{t_{end}}\}. \tag{235}$$

It is a step away from the simple numerical value array solution interpretation. Moreover it means that the algorithm must be able to produce a more complex output, which size must be adjusted dynamically as it is impossible to predict the number of fractures. The total number of discretization points will change. The underlying graph structure will be modified. If the solution is to remember all these events it must hold a separate $\mathcal{M}$ state for each of these. On top of that some intermediate $\mathcal{M}$ states should be stored to accurately represent widths and lengths of fractures in between these events. Consider Figure 61.

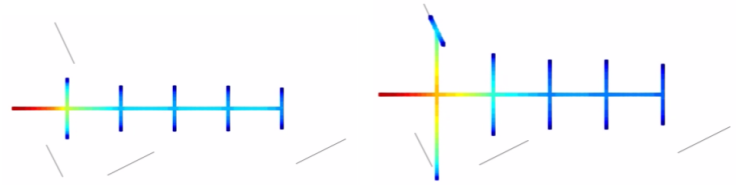

(a) Initial state $\mathcal{M}_0$, 10 cracks and 5 pipes, and one injection point.

(b) Some intermittent $\mathcal{M}_i$, two newly opened fractures are added.

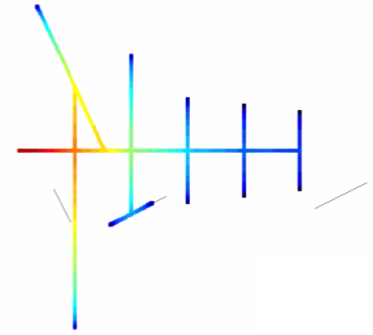

(c) Further $\mathcal{M}_i$ state, extra openings were activated, when should $\mathcal{M}_{t_{end}}$ be reached ?

Figure 61: A solution to the multifracturing problem should consist of model states $\mathcal{M}$ at multiple times, to accurately represent the whole process dynamics (red color indicates high pressure originating from the pumping point).

4.5.1.2 *Indexing elements*

As it should be possible to change the size of $\mathcal{M}$, all measurements of its size should be adjusted dynamically, rather than predefined at start. This calls for a well defined method for counting and indexing its components. The size can be measured by three different quantities:

- N_V - the number of vertexes, this includes junctions and crack tips.
- N_E - the number of edges, fractures and solid pipes.
- N_{ODE} - the total number of ODEs, and the total number grid points.

Lets recall that PKN crack formulation used its own size N to define the number of grid points on the normalized one dimensional grid (see Appendix A.1). Unfortunately the introduction of the operator $\mathcal{B}$ (32) added one extra ODE that was not associated with any grid point. Furthermore the connection points for PKN pipes and PKN

cracks, that are to be used here, rely on grid points of $x_1 = 0$ or $x_N = 1$, but do not produce any ODE to be associated with those. This creates a situation where the number of introduced grid points is very close, but not identical to the number of N_{ODE}. To simplify the process it is possible to add a few extra grid points or extra ODE to match these two values:

- PKN *crack* grid can be set to account for N points $x_m = \{0, ..., 1 - \epsilon, 1\}$, a simple modification that includes $x_N = 1$ as the last grid point. The vale at $x_1 = 0$ is obtained via connected junction. Hence operator $\mathcal{A}_{crack}$ ((174) or (176)) can be used for $x_2, ..., x_{N-1}$, while $\mathcal{B}$ (32) produces the last ODE and the first ODE is either a dummy or added extra operator $\mathcal{C}$ (165) for leak off integration.
- PKN *pipe* grid already accounts for exactly N points $x_m = \{0, ..., 1\}$, and $\mathcal{A}_{pipe}$ ((181) or (182)) works for $x_2, ..., x_{N-1}$. The vale at $x_1 = 0$ and $x_N = 1$ comes from the two connected junction segments, meaning there are two more points than ODEs. The operator $\mathcal{C}$ (165) or a dummy zero ODE can be added to match grid point number with the amount of produced ODEs.
- Other type of edges, closed cracks or concrete pipes contribute no grid points nor ODEs.

So it is fairly easy to makes sure that:

$$N_{ODE} = \sum_{j=1}^{N_E} N_j, \tag{236}$$

where N_j is the number of grid points and ODEs associated with each edge. *The total number of ODEs is the same as the sum of all edge grid points.*

Up to this point indexing of grid points x_i was concluded locally, with local index i ranging from 1 to grid N. However with the introduction of junction condition and elasticity interactions (Section 4.2 and 4.3) it is important to introduce a higher level global indexing :

$$i_{global}(i^{(j)}_{local}) = \sum_{j=1}^{j-1} N_j + i^{(j)}_{local}, \tag{237}$$

here $i^{(j)}_{local}$ refers to indexing in the reference frame of an edge j, while i_{global} refers to index in the whole model $\mathcal{M}$. For an example consider an system with 2 fractures each of $N = 10$. The first grid point $i_{local} = 1$ in the second fracture would correspond to $i_{gloabal} = 11$. The maximum $i_{gloabal} = 20$ would refer to the last grid point $i_{local} = 10$ in the second fracture. Note that this dynamic indexing allows for *unique grid size for each edge.*

The main point of this indexing scheme is to be able to present $\mathcal{M}$ as a single vector, and be able to identify which element corresponds to which edge, and what value it carries. This is necessary for the next step, which builds an ODE system. Furthermore the global indexing allows for building, and interpreting additional utility matrices described in Subsection 4.5.2.

4.5.1.3 *Model as ODE system*

Having written down a method for indexing grid points and associated ODEs (237), lets declare y_0 and $y'(t, y)$ for a given $\mathcal{M}$. As

$$y_0 = \mathcal{M}_0 = \{\mathcal{F}_1^*, \mathcal{F}_2^*, ..., \mathcal{F}_{N_E}{}^*\}, \tag{238}$$

$$y'(t, y) = \mathcal{M}'(t, \mathcal{M}) = \{\mathcal{F}_1(t, \mathcal{M}), \mathcal{F}_2(t, \mathcal{M}), ...\mathcal{F}_{N_E}(t, \mathcal{M})\}, \tag{239}$$

where $\mathcal{F}_j^*$is the initial value, and $\mathcal{F}_i$ is a generic ODE operator for each edge in the model. $\mathcal{F}_i$ should be made of operators $\mathcal{A}$, $\mathcal{B}$, $\mathcal{C}$ as given by: (32), (65), (174), (182), (176), (165), for example:

$$\mathcal{F}_{crack} = \{\mathcal{C}, \mathcal{A}_1, ..., \mathcal{A}_{N-1}, \mathcal{B}\} \tag{240}$$

$$\mathcal{F}_{pipe} = \{\mathcal{C}, \mathcal{A}_1, ..., \mathcal{A}_{N-1}, 0\} \tag{241}$$

Where 0 indicated a dummy zero ODE, and the usage of C is optional. The initial values of $\mathcal{F}^*$ should be similarity combined, meaning when the initial value for model $\mathcal{M}_0$ is needed, all the vector values of discretization edges are combined together in a single vector. Similarly when the derivative $\mathcal{M}'(t, \mathcal{M})$ is needed the vector values of derivatives for each *crack pipe* or *crack* are put together in to one vector.

4.5.1.4 *Multifracturing algorithm*

This formulation leaves the task of integrating equations to some unspecified ODE *solver*. Similarly to single fracture case, the used *solver* is unaware of the whole formulation, it is merely a tool to perform numerical integration from initial time t_0 to final time t_{end}. The *solver* will be encapsulated as an abstract object to advance the model $\mathcal{M}$ by some time step Δt. Its instance will be provided with a function constructed to appear as a simple generic $y'(t, y)$, though the inside of that function will perform a whole set of operations to calculate the whole $\mathcal{M}'(t, \mathcal{M})$ (check Algorithm 4). On top of this there is another quasi integrating algorithm, that runs the provided abstracted *solver*, tracks fluid balance and checks for fracture collisions (check

Algorithm 4 and 5). The state of $\mathcal{M}$ at each steps made by this upper algorithm is recorded. Any required re-meshing is done separately from the encapsulated ODE *solver*, since such operations are not a part of casual integrating methods.

There are two significant advantages of this approach:

- The integration, discretization, and fracture collisions are well divided between different parts of code.
- The utilized integration code/ODE solver *can be changed at will*, switched to any other method of preference (a search for best solvers is presented in Subsection 5.3.2)

The result of computation is stored as a collection of $\mathcal{M}(t)$ states at different times $t \in (t_0, t_{end})$. These might be different in size, due to collisions or other events. Processing the solution is a challenge on its own, but will not be shown in this work, except for some interesting results.

input : model instance $\mathcal{M}$, at time t
output: $\mathcal{M}'(t, \mathcal{M})$

for $i \leftarrow 1$ **to** N_{ODE} **do**
  calculate $\sigma_l^{(i)}$;
end
for $k \leftarrow 1$ **to** N_V **do**
  approximate initial junction fluid pressure $\mathcal{J}$;
end
while $\left|\sum_1^{N_V} \left(\mathcal{J}_{n+1}^k - \mathcal{J}_n^k\right)\right| >$ *some tolerance* **do**
  for $k \leftarrow 1$ **to** V **do**
    $\mathcal{J}_{n+1}^k \leftarrow$ newton method for junctions with $\mathcal{J}_n^k$;
  end
end
for $i \leftarrow 1$ **to** N_E **do**
  $j \leftarrow$index of first ODEs in E_i ;
  $\mathcal{M}'_{j+1,\ldots,j+N_i} \leftarrow \mathcal{F}_i(t, \mathcal{M}_{j+1,\ldots,j+N_i})$;
end

Algorithm 4: Algorithm for computing $\mathcal{M}'(t, \mathcal{M})$

input : initial time t_0, end time t_{end}, initial model state $\mathcal{M}_0$, inner *solver* instance
output: colection of model states $\mathcal{M}_0, ..., \mathcal{M}_{t_{end}}$

$Vol_0 \longleftarrow$ initial fracture volume;
$\mathcal{M}_{list} \longleftarrow$ new model collection;
add $\mathcal{M}_0$ to $\mathcal{M}_{list}$;
$\mathcal{M}_i \longleftarrow \mathcal{M}_0$;
$t \longleftarrow t_0$;
$\Delta t \longleftarrow$ default time step;
while $t < t_{end}$ **do**
  $\mathcal{M}_j \longleftarrow \mathcal{M}_i$;
  $\mathcal{M}_i \longleftarrow$ deep copy of $\mathcal{M}_i$;
  update $\mathcal{M}_i$ visibility and jacobian pattern matrices;
  use *solver* to advance $\mathcal{M}_i$ by Δt;
  $Vol \longleftarrow$ total volume of $\mathcal{M}_i$;
  $Q_0 \longleftarrow$ sum of $\int_t^{t+\Delta t} q_0 \, dt$ for all vertecis ;
  $Q_l \longleftarrow$ sum of $\int_t^{t+\Delta t} \int_0^1 q_l \, dx \, dt$ for all edges ;
  store relative fluid balance for $\mathcal{M}_i$ as $\frac{Vol - Vol_0 - Q_l}{Q_0}$
  if $\mathcal{M}_i$ *has overshoots* **then**
    $\mathcal{M}_i \longleftarrow \mathcal{M}_j$;
    $\Delta t \longleftarrow$ time to soonest overshot in $\mathcal{M}_i$;
  else if $\mathcal{M}_i$ *has valid collisions* **then**
    add $\mathcal{M}_i$ to $\mathcal{M}_{list}$;
    $\mathcal{M}_i \longleftarrow$ deep copy of $\mathcal{M}_i$;
    resolve collisions for $\mathcal{M}_i$;
  else
    $\Delta t \longleftarrow 2\Delta t$;
    $t_{col} \longleftarrow$ soonest forecasted time to collision for $\mathcal{M}_i$;
    if $t_{col} < \Delta t$ **then**
      $\Delta t \longleftarrow t_{col}$;
    end
    add $\mathcal{M}_i$ to $\mathcal{M}_{list}$;
end

Algorithm 5: Algorithm for processing multifracturing problem.

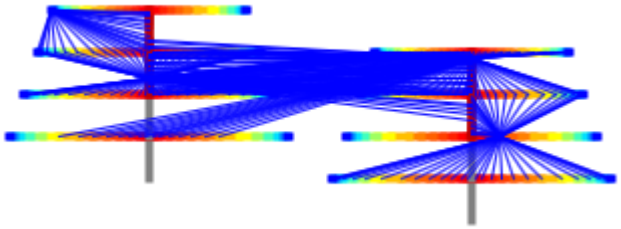

Figure 62: Example multifracturing scenario. Two arrays of PKN fractures, connected by some PKN pipes, and concrete pipes. Edge visibility shown for some grid points (but not all).

4.5.2 *Jacobian and "utility" matrices*

Lets recall the benefits that were achieved by properly utilizing Jacobian matrix pattern J_{patter} shown in Subsection 3.6.4. It would be worthwhile to make some attempts to use similar techniques in multifracturing formulation. Similar speedup could be achieved as the presented multifracturing problem will also produce sparse J_{patter}. The sparseness pattern will however be now much more complex to derive. To deal with this problem, lets divide J_{patter} into three matrices, each introduced by a different part of this problem, all of then N_{ODE} by N_{ODE} in size that when added together form the full J_{patter} of this problem. Instead of presenting exact formulas for obtaining these, generalized means of obtaining and sample results for an arrangement of fractures, as shown on Figure 62, are presented here. The exact code used for calculating these can be is shown in Appendix A.5.

Additionally it is worth considering that J_{patter} could be generalized by a much smaller matrix that shows edge to edge dependence. The number of N_{ODE} will be of at least one order more than used N_E edges, thous such would allow to save a lot of time by giving some possible shortcuts in further computations.

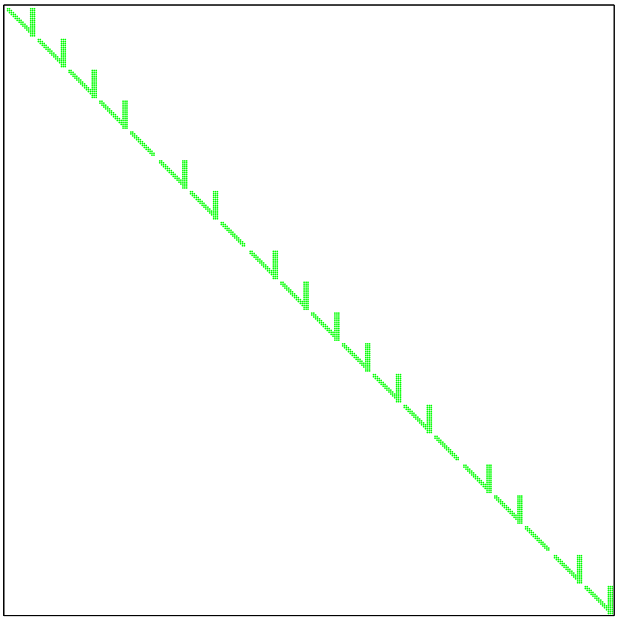

Figure 63: Discretization Matrix for example shown on Figure 62, formed by FD approximation ((125) or as shown in sample code Appendix A.4.6) and normalization over L , close to tridiagonal in structure.

4.5.2.1 *Discretization Matrix*

The first source of J_{patter} is the tridiagonal like discretization. It is formed by operator $\mathcal{A}$ and $\mathcal{B}$, in a similar manner as described in Subsection 3.6.4 for a single fracture. With multiple fractures each fracture will add this almost tridiagonal structure. Here an example of such a matrix is shown in Figure 63. All N_E edges in the problem form a piece of this diagonal pattern, and the indexes of associated grid points are given by (237). Each repeated \| shape represents a PKN *crack*, while single \ stands for a PKN *pipe* element.

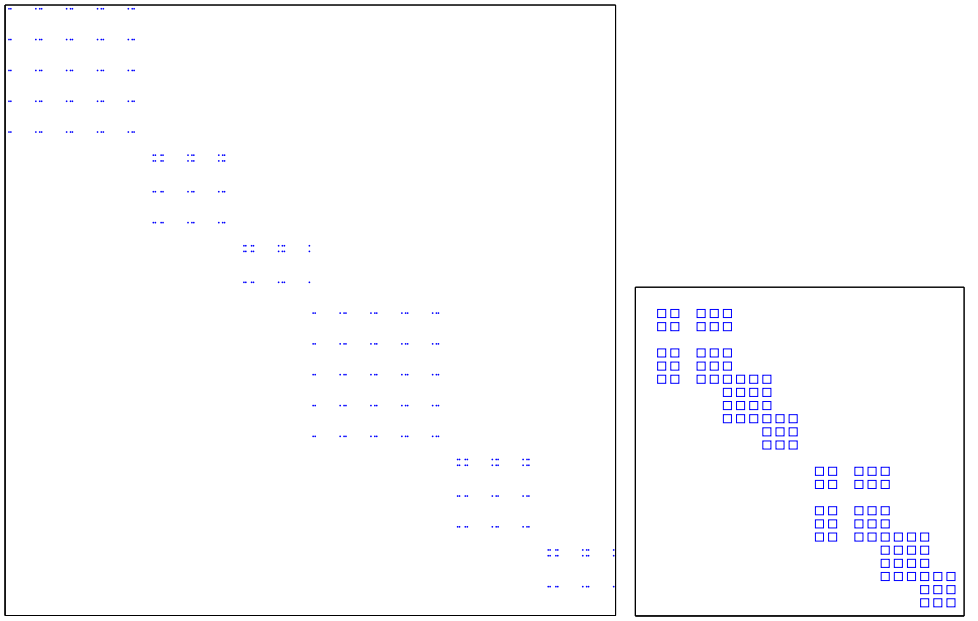

(a) Full point to point joint matrix.

(b) Generalized edge to edge version.

Figure 64: Junction Matrix for example shown on Figure 62, indicates which points are dependent on another by junction condition (Section 4.2).

4.5.2.2 *Junction Matrix*

The boundary condition at $x = 0$, calculated by junction strategy (Section 4.2) adds dependence of each boundary point (x_2 and x_{N_i-1}) involved in fluid pressure approximation on all the other points contributed by connected edges. These in case of PKN *cracks* and *pipes* this points are local x_2 and x_3 or x_{N_i-2} and x_{N_i-3}. Furthermore all interconnected concrete pipe segments share pressure, thus all other attached edges are connected by this pressure dependence. If an edge shares a junction with concrete pipe, then the edges connected to the other end of that concrete pipe are also affected. To find these interactions a graph traversal must be done, to mark all clusters of junctions traversable by concrete pipe connections. The outcome of these operation is converted into a very sparse matrix, marking all of these connections, as shown on Figure 64a.

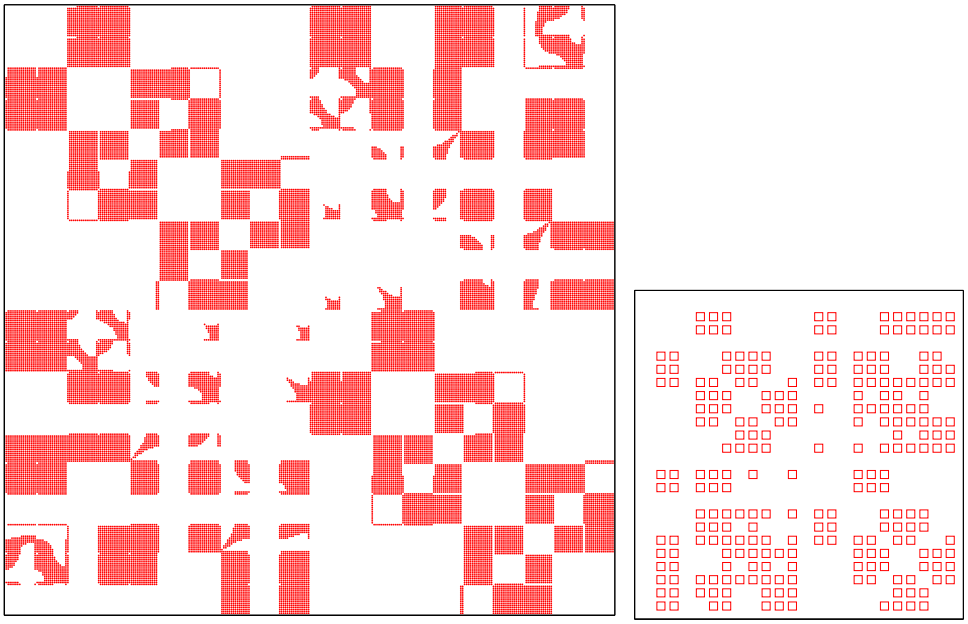

(a) Full elasticity matrix, shows point to point visibility.

(b) Edge to edge visibility matrix, generalization of the above with much less entries to work on.

Figure 65: Pseudo elasticity visibility matrices, for example shown on Figure 62.

4.5.2.3 *Pseudo elasticity Visibility Matrix*

Finally the matrix formed by resolving edge visibility (Subsection 4.3.2). It is a symmetric matrix, that has non-zero entries where two points are visible to each other, hence σ_l is projected. The structure itself is unfortunately very dependent on location of edges in relation to each other. Furthermore while in case of a single fracture, or some other specific placement, this matrix will be empty, for some geometries this matrix might be full, or very close to being a full dense matrix. In fact comparing this to Discretization 4.5.2.1 and Junction 4.5.2.2 matrices, in can be clearly observed how the introduction of σ_l increases the overall effort required to solve a multifracturing problem.

4.5.2.4 *Utilization of sparseness pattern*

A common feature for many ODE solver is that custom Jacobian function can be optionally supplemented. If not some naive dense approximation function is used. The dense approximation would however have a very high computational cost, especially in this multifracturing scenario. To naively compute the Jacobian, one needs to compute (239) for a small change of each solution vector element (238). This itself is N_{ODE} number of operations, but when σ_l is present, the function (239), if not handled properly will check for visibility of all the other grid points (211), effectively making (239) perform $O\left(N_{ODE}^2\right)$ operations. Thus ignoring the overall structure will force $O\left(N_{ODE}^3\right)$ time complexity.

Although this could indicate that the computation of Jacobian would take somehow comparable amount of time to that consumed by matrix inversion inside integrating solver, the real cost could be much higher as (239) requires in fact much more operations a than simple matrix reduction (as proven in Subsection 5.3.3). On the other hand if simplified edge to edge versions visibility (Figure 65b) and junction (Figure 64b) matrices are used, the function (239) can cost much less. Knowing which edges depend on each other reduces the number of calculations needed in (211) from N_{ODE}, to possibly even 0 if no edges are visible, as knowing whereabouts of non zero entries of visibility allows to skip unnecessary calculations. Similarly knowing which edges are connected to each other through junction connection allows to skip unnecessary operations when computing the Jacobian.

For the best case scenario, such as a single fracture, the cost of (239) and calculating Jacobian is $O\left(N_{ODE}\right)$, if the information about sparseness is used. Excluding fracture length L effect, all points depend on two neighbors, thus $O\left(N_{ODE}\right)$ additional cost of Jacobian. In the worst case scenario, all grid points are visible to each other and computing (239) will require $O\left(N_{ODE}^2\right)$, so Jacobian would cost $O\left(N_{ODE}^3\right)$. It is impossible to make an accurate prediction of what average time complexity would be, but it is clear that for many geometries that result in much sparser J_{patter} the improvement gained by taking problem sparseness into account can be of a time order, or greater (again computationally proven in Subsection 5.3.3).

To conclude the above monologue, it will be very beneficial to exploit sparseness effects appearing in the multifracturing system. The computational ideas described here are best shown by the actual code in Appendix A.5.

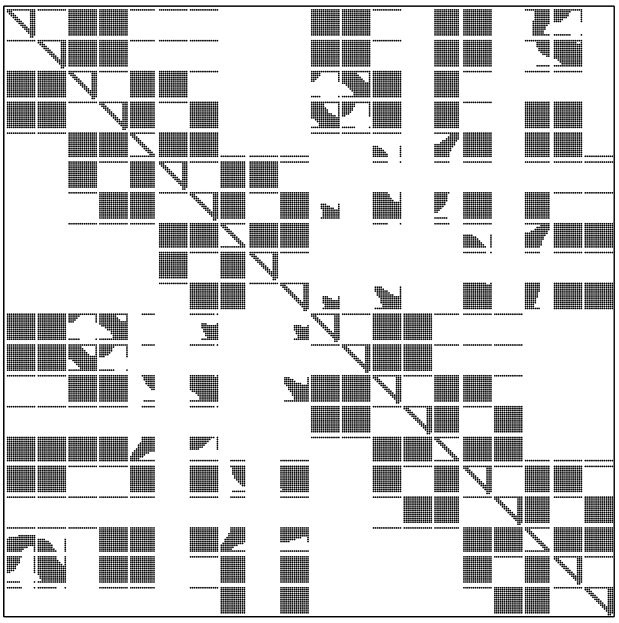

(a) Naively, always $O\left(N_{ODE}^3\right)$, computed Jacobian, can be used to verify results.

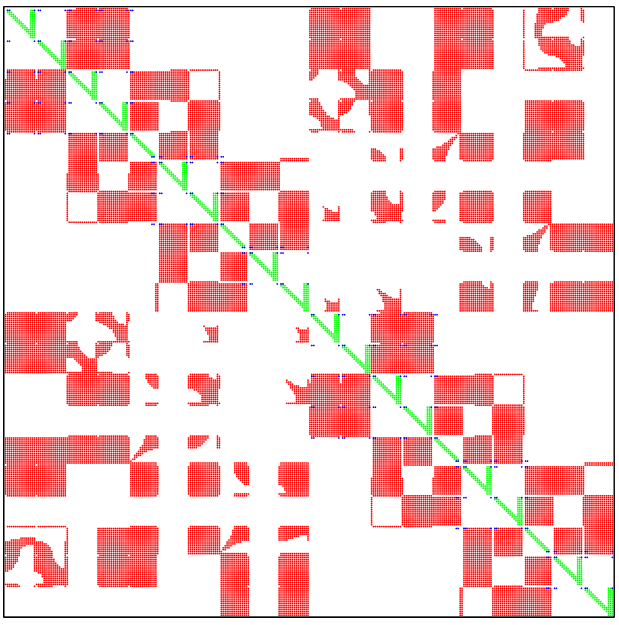

(b) Sum of Discretization, Junction and Visibility matrices, may lead to $O\left(N_{ODE}\right)$ in the best case if no visibility.

Figure 66: Full J_{patter} for of an example multifracturing scenario shown on Figure 62.

5

MULTIFRACTURE NUMERICAL TESTING AND IMPLEMENTATION

This Chapter covers specific numerical and computational details, and present a series of various test scenarios developed for the multifracturing case. As many tests were already performed in Chapter 3 on a single fracture, the focus here is to confirm that the different, multifracturing capable implementation, performs identically to the single fracture code, and show its capabilities when dealing with multiple fractures.

- Section 5.1 confirms that both single fracture and multifracture code produce identical results under right conditions.
- Section 5.2 tests elasticity computation scheme with various possible fracture structures, and proves that it produces reasonable results when compered to other counterparts.
- Section 5.3 focuses on practical implementation aspects, including object orientated design, parallelization, and multiple ODE solvers comparison.
- Section 5.4 shows some tests scenarios, to proof that the whole formulation is working.

The Appendix A.5 points to the location of developed source code.

[September 10, 2015 at 14:04 – classicthesis version 1.0]

5.1 TESTING MULTIFRACTURE VS SINGLE FRACTURE.

Here the implementation and some basic testing of the junction strategy proposed in Section 4.2 will be described. If multifracturing formulation consists of a straight chain of pipe segments, ended by a crack piece, this is in fact equivalent to having a single fracture. Thus the effect of dividing a single pipe with junction boundary condition can be measured against known results.

5.1.1 *Numerical details for junction boundary condition*

First the numerical details for obtaining polynomial approximation of pressure value at junction should be outlined. These approximations are used in (189) to obtain flow value q and its derivative as outlined in $\frac{dq}{d\mathcal{J}}$ Subsection 4.2.3. Two types of approximation are considered, linear and quadratic. These approximations are valid for both PKN like crack and pipe edges. The $Left$ version refers to application at $x = 0$ boundary, which is the only case for all crack segments. Pipe segments have two junctions attached, hence $Right$ version will refer to boundary at $x = 1$.

5.1.1.1 *Linear*

Simpler version, that is derived from linear function, based on two points is:

$$\begin{aligned} Right\ x = 1 \qquad & Left\ x = 0 \\ x^{(1)} = x_{N-1} \qquad & x^{(1)} = x_2 \\ p^{(1)}_{fluid} = p_{fluid}(x_{N-1}) \qquad & p^{(1)}_{fluid} = p_{fluid}(x_2) \\ \lambda = -1 \qquad & \lambda = 1 \end{aligned}$$

$$\alpha = -\frac{1}{x^{(1)}} \tag{242}$$

$$\beta = \frac{p^{(1)}_{fluid}}{x^{(2)}} \tag{243}$$

5.1.1.2 *Quadratic*

Another approach is to use quadratic polynomial that interpolates the three edge points:

$$
\begin{aligned}
Right\ x = 1 \qquad & Left\ x = 0 \\
x^{(1)} = x_{N-1} \qquad & x^{(1)} = x_2 \\
x^{(2)} = x_{N-2} \qquad & x^{(2)} = x_3 \\
p^{(1)}_{fluid} = p_{fluid}(x_{N-1}) \qquad & p^{(1)}_{fluid} = p_{fluid}(x_2) \\
p^{(2)}_{fluid} = p_{fluid}(x_{N-2}) \qquad & p^{(2)}_{fluid} = p_{fluid}(x_3) \\
\lambda = -1 \qquad & \lambda = 1
\end{aligned}
$$

$$\Gamma = x^{(2)}\left(x^{(2)} - x^{(1)}\right)$$

$$\alpha = -\frac{1}{x^{(1)}} - \frac{x^{(2)} - x^{(1)}}{\Gamma} \tag{244}$$

$$\beta = p^{(1)}_{fluid}\left(\frac{1}{x^{(1)}} + \frac{x^{(2)}}{\Gamma}\right) + p^{(2)}_{fluid}\frac{x^{(1)}}{\Gamma} \tag{245}$$

5.1.2 *Testing simple split of PKN fracture*

A simple way to test if the split mechanism proposed in Section 4.2 produces adequate results is to split a single fracture into one pipe and crack segment, as shown on Figure 67a. As previously single fracture would be compared against some analytical benchmark A.2 , new pipe and crack segments will be compared against the subsection of fracture they represent. Initially lets assume some split ratio, between 0 and 1, named L_{split} that divides original crack length l_* into crack and pipe length L_{crack} and L_{pipe} such so:

$$L_{crack} = (1 - L_{split})l_*, \tag{246}$$

$$L_{pipe} = L_{split}l_*, \tag{247}$$

$$l_* = L_{crack} + L_{pipe}. \tag{248}$$

Naturally as the fracture propagates this will be valid only at initial time.

In the first test lets use $L_{split} = 0.9$, so the resulting crack pipe will have the constant length of $0.9l_*$, and the initial length of propagating crack segment will be of $0.1l_*$. Both crack pipe and pipe should be given grid of $N = 100$ points, however crack should grid that gets denser at the crack tip $x^{(ii)}$ while crack pipe will use uniform grid $x^{(i)}$. The outcomes of this tests are shown on Figures 67 and 68.

It can be observed that the linear fracture split condition works, as the result is within 10^{-3} order of accuracy, but the obtained result is less accurate when compared to original single fracture computation.

The quadratic polynomial approach is however very close to producing identical error as the undivided solution. In fact the difference in δw with quadratic split is so little that is likely that it does not affected the solution. Conclusion: junction BC strategy 4.2 with quadratic flow components approximation allows to split fracture into two segments without noticeably affecting computation accuracy.

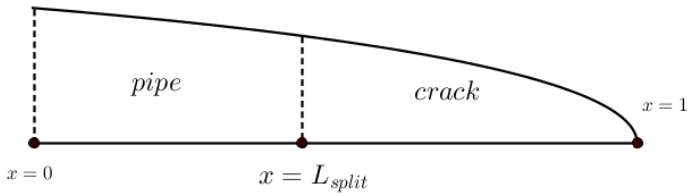

(a) Single fracture can be split into pipe and crack segment, without alternating the solution.

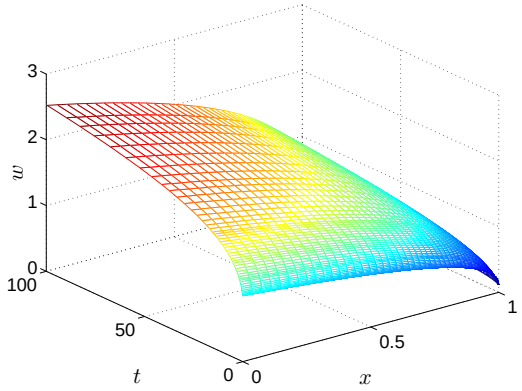

(b) Single fracture opening.

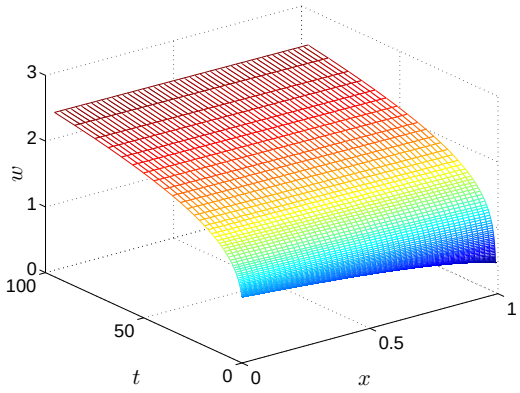

(c) Left pipe segment.

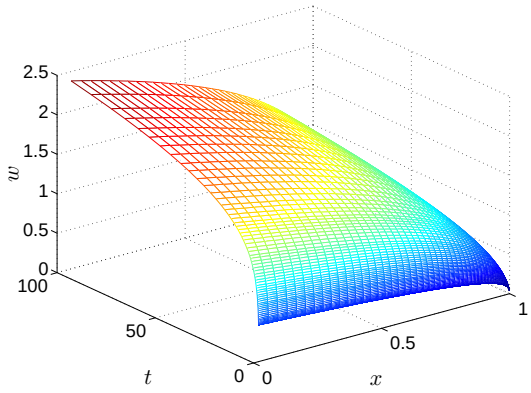

(d) Right crack segment.

Figure 67: An explanation of single fracture spiting, left pipe and right crack segments add up to the whole fracture.

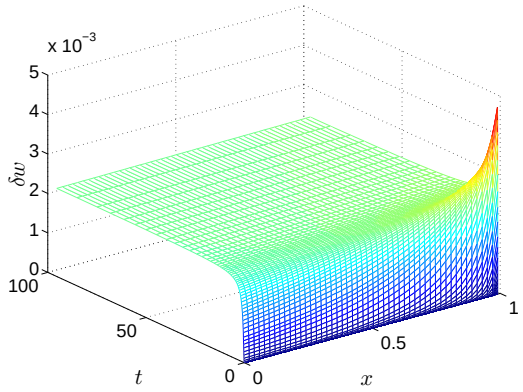

(a) Pipe segment relative opening error δw under linear split.

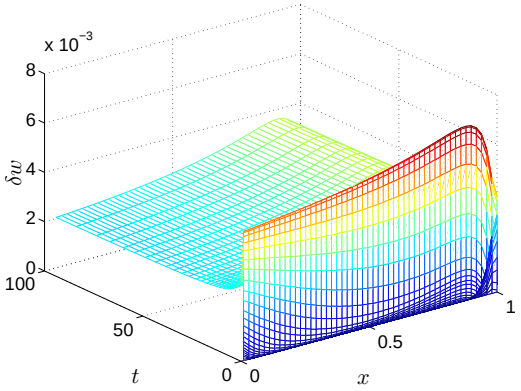

(b) Crack segment relative opening error δw under linear split.

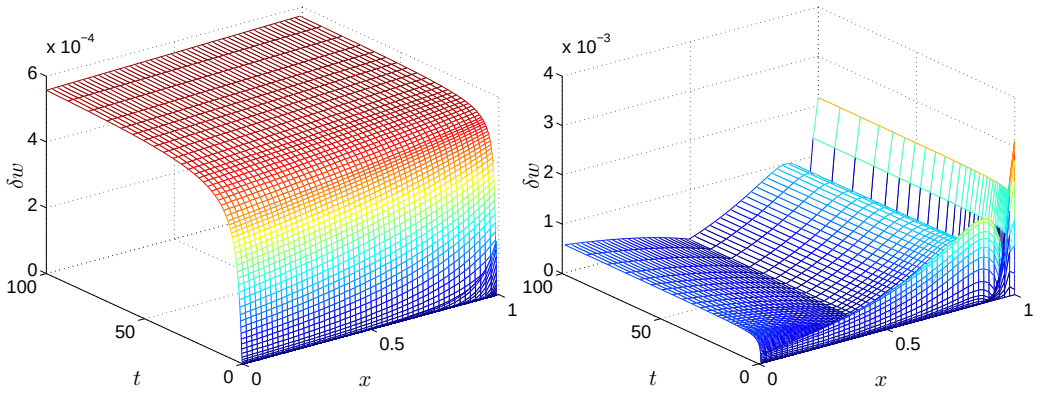

(c) Pipe segment under relative opening error δw quadratic split.

(d) Crack segment under relative opening error δw quadratic split.

Figure 68: Comparison of crack opening relative error δw on connected pipe and crack segments, using linear (242), (243) and quadratic (244), (245) split methods.

5.1.3 *Finding acceptable split proportions*

Lets make a test to find out what values of L_{split} are acceptable. Consider all values of $L_{split} \in (0, 1)$. Figure 69 shows the maximum relative errors obtained when computing connected pipe and crack segment. For the majority of L_{split} values, up to 0.8 the difference in accuracy is negligible. This indicated that long crack segments attached to shorter pipe segments do not present any challenge to compute. For the values of $L_{split} > 0.8$, when initial crack segments are much shorter than connected pipe significant relative accuracy discrepancies can be observed, that may appear as an singularity at $x = 1$. This issue is shown in more detail on Figure 70 where much smaller values of L_{split} are presented. Here it can be observed that although initially introduced error is quite high, it does eventually vanishes at larger times. Even for $L_{split} = 10^{-9}$, which indicates initial pipe segment 10 orders of magnitude longer than the crack segment the computation eventual produces accurate result. However for real fracturing applications such difference in lengths might be a huge exaggeration, the $L_{split} = 10^{-5}$ factor which is probably already over the upper limit of possible disproportions[1] takes relatively short time to converge to acceptable accuracies. As shown previously in Section 4.4 and Appendix A.4.11 the initial condition (8) could have l_* a few orders lower than attached fractures, which in relation to the test done here, is a plausible combination.

1 $L_{split} = 10^{-5}$ would indicate a one centimeter crack connected to a 10 kilometer long pipe.

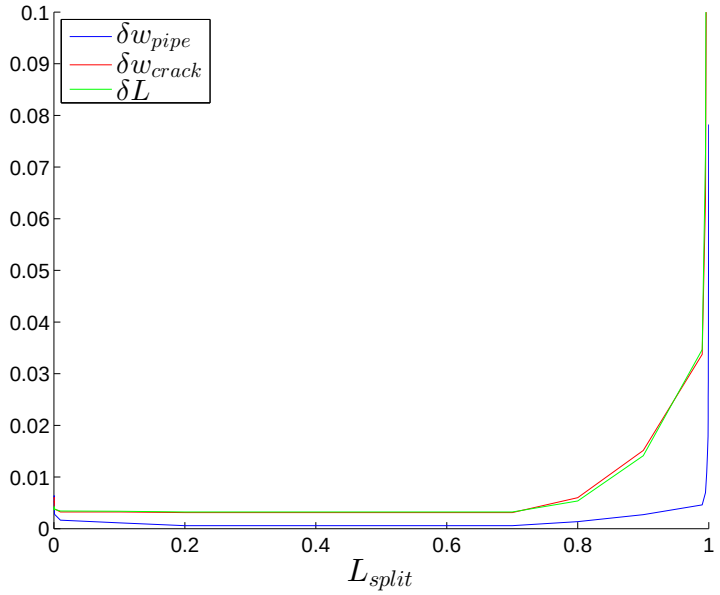

Figure 69: Testing how the different values of L_{split} affects maximum relative error, in terms of fracture length, and pipe and crack segments widths. Close to 1 values of L_{split} generate large maximum error, however these values might be deceptive.

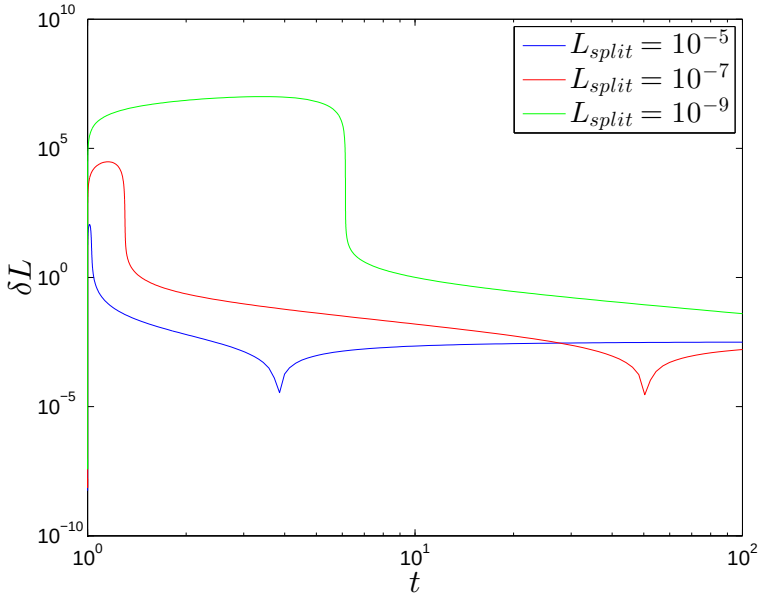

Figure 70: Testing how the different values of L_{split} affects accuracy of relative fracture length error δL with respect to time. Even with $L_{split} = 1 - 10^{-9}$ solver eventually returns to normal accuracy at larger times, as showed by relative error in fracture length. L_{split} values close to zero were however not possible to compute in feasible run time

5.1.4 *Testing a multiply divided PKN fracture.*

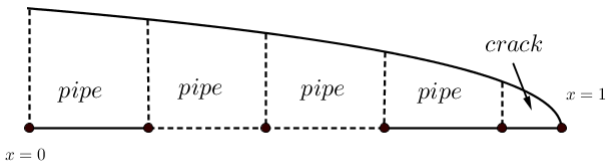

Figure 71: A single crack can be modeled as a chain of connected pipe segments with short crack segment at the tip.

So far testing was done to investigate numerical details of joining pipe and crack segments, and how these affect two connected segments. But this test can be extended to an arbitrary number of pipe segments connected by each other, in one sequence, ended with a crack segment at the tip (see Figure 71). Interestingly, while doing such, this multifracturing formulation begins to reassembly FV formulation used by Kovalyshen [40], and others whose problem formulations do not include speed equation (12). Each pipe segment controls its in and out flow by junction BC 4.2, as FV formulation of this would in fact do, while crack segment at the tip acts as a special element. Naturally this similarity is just an outcome of different assumptions and techniques in just this particular test scenario.

Figure 72 presents outcomes of combining various numbers of pipe segments, with different number of grid points used, per each of these segments. Introduction of additional pipe segments *improves* the accuracy. This agrees with previous result, that quadratic split (244) (245) does not affects the accuracy. The improvement should be attributed to a higher number of overall grid points used. The first result $N_c = 100$ is nearly identical to $N_p + N_c = 100$, yet worse than $N_p + N_c = 200$, but more grid points make no more difference. This is consistent saturation at around $N \approx 200$ observed on Figure 28.

The most important conclusion from this observation is that the number of pipe segments be can be increased freely without any negative impact, at least if dividing one fracture.

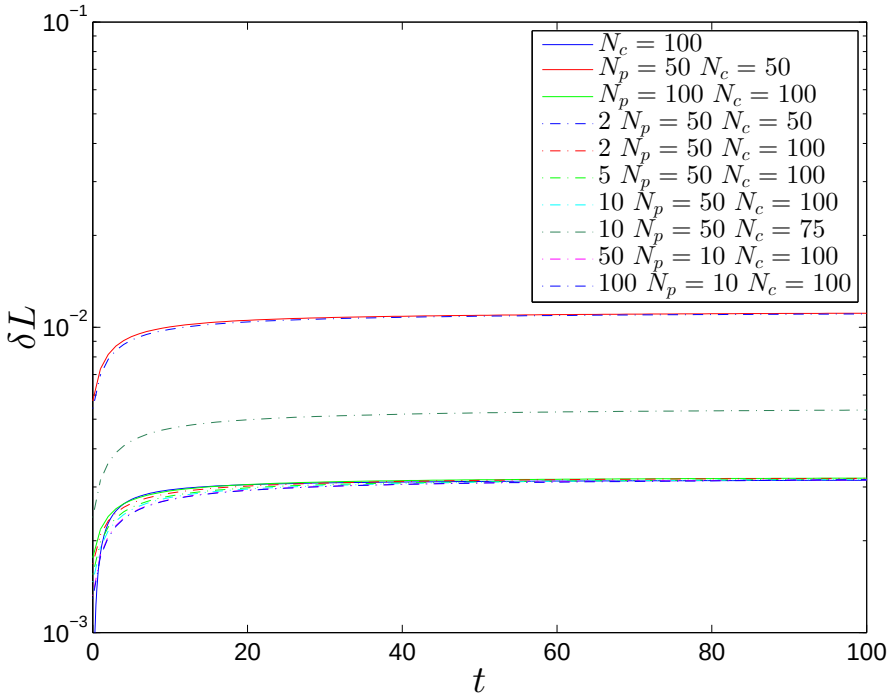

Figure 72: Relative crack length errorδL for various numbers off segments splits with different points N_p for pipe and N_c for crack. Up to 100 pipe segments are used. Extra segments initially increase the accuracy, but saturation at $N \approx 200$ is reached.

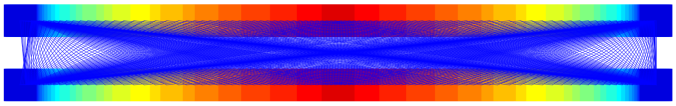

Figure 73: Two close parallel fractures, with all point to point interactions drawn.

5.2 ELASTIC INFLUENCE TESTING AND IMPLEMENTATION

5.2.1 *Two nearby parallel fractures*

As the first test for the pseudo elastic influence procedure (Section 4.3), lets consider a relatively simple case where two fractures are placed parallel to each other, and aligned as if there were mirror images of each other. This is similar to the case described by Bunger [10], except for the fact that only two fractures are present, hence σ_l value should be half of the expected value form relation (197). Given that the both fracture height and spacing are set to 1, one should expect this elastic scheme to produce a result that follows:

$$\sigma_l(x) = \frac{3}{16} p_{net}(x). \tag{249}$$

From the above one can work out the value of g in (199), as this is the only unknown parameter. The approximate value proposed here is:

$$g = 0.1413. \tag{250}$$

This value of g allows the pseudo elastic influence used here to match the value one would expect from Bunger scheme [10], at the crack inlet $x = 0$. The comparison of the two schemes is shown on Figure (74). However, Bungers method [10] was derived for very long fractures, thus the effect of tip region where width decreases to zero, and consequently the region with no opened fracture that follows, was not included, the whole fracture aperture was essential treated as flat surface. Therefore to find matching value of g, approximation was made for a case where fracture half length $L = 100$. This produces a nearly perfect match as L is indeed much larger than the spacing (accuracy grater than the internal relative tolerance set to 10^{-3}, see Subsection below 5.2.3). In cases when shorter fractures are considered, namely $L = 10$ and $L = 1$, greater discrepancy can be observed especially for $x > 0.9$ where a switch form underestimation to overestimation of σ_l value takes place. When fracture length is lesser than the distance, as for example $L = \frac{1}{4}$, shape of σ_l changes to a constant line, which represents switch to the far field approximation (198).

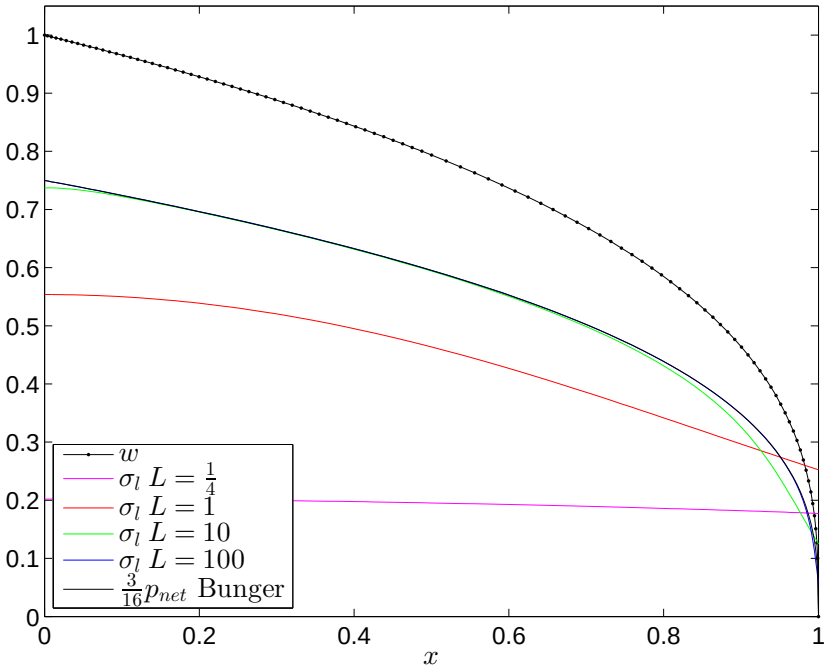

(a) Values of σ_l for different half fracture lengths.

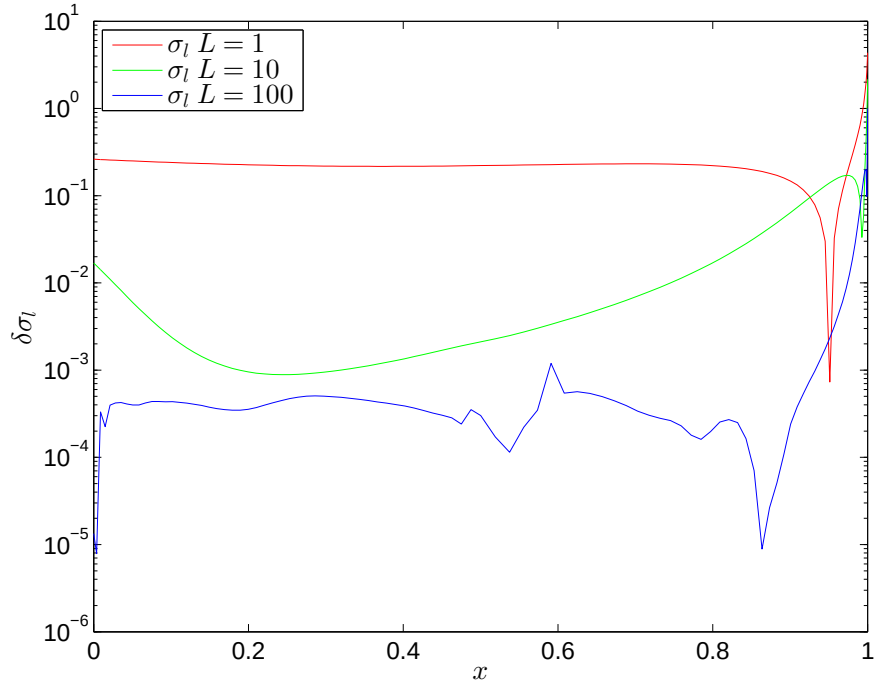

(b) Relative discrepancies of $\delta\sigma_l$ from close approximation 249 for different half fracture lengths.

Figure 74: Elasticity effect of two close parallel fractures. Values of σ_l depending on the half fracture length.

5.2.2 *Two fractures from common junction*

Here the calculation of σ_l for two connected fractures will be tested. Suppose that there are two fractures originating form the same point (wellbore), that for this particular test scenario are placed at some angle α between them, as shown on Figure (75). This setting gives a good opportunity to test the effect of distance term $\frac{1}{min(d^3,1)}$ in (199). If strict $\frac{1}{d^3}$ was to be used a singularity would appear when $x \to 0$. This would be disastrous. Furthermore note that the single fracture formulation (6) already effectively normalized fracture height to 1, hence when $d = 1$ the term $\frac{1}{d^3}$, which is valid in three dimensions, could be switched to $\frac{1}{d^2}$, as the problem now is closer to describing two parallel planes.

Furthermore there is a much more significant problem with distance calculation for two connected fractures. Lets remind ourselves that vector $\hat{\sigma}$ is computed by (199) as originating from the fracture propagation axis x, that is in the middle of the fracture, but not from the fracture surface. Under most conditions $w << L$, thus the slight deviation from location on crack surface and middle should not matter, but here as these fractures are interconnected a small overlapping region appears near the connecting junction. Properly modeling this region is beyond the current problem formulation, thus $\frac{1}{max(d^3,1)}$ is used here again as a convenient approximation.

The effects of using $\frac{1}{min(d^3,1)}$ in (199) as opposed to $\frac{1}{d^3}$ are shown on Figure 75b. It is expected that under most circumstances the over all difference in the value of σ_l should be indistinguishable, for both of these strategies. Here it can be observed for all considered angles, the singularity at $x \to 0$ is removed, but the whole influence σ_l is mostly affected at shallow angles. This particular example uses $L = 10$, thus with much longer fractures less difference should be observed.

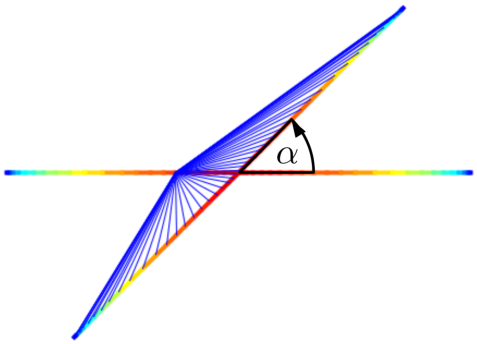

(a) Two fractures attached at an angle α in relation to each other.

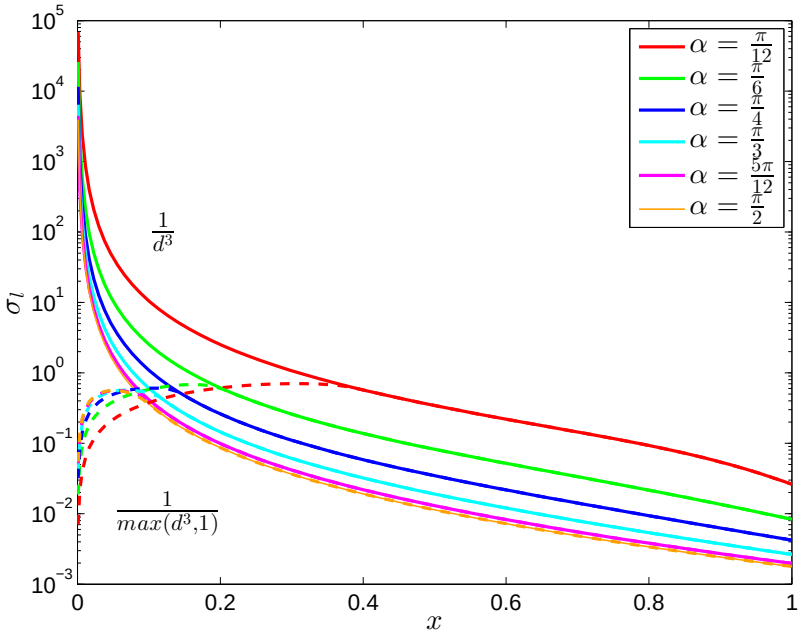

(b) Value of $\sigma_l(x)$ for different α, compares $\frac{1}{min(d^3,1)}$ to $\frac{1}{d^3}$

Figure 75: Two connected fractures from common junction.

5.2.3 *Approximation tolerances, and fast square root*

The recursive method for approximation of (199) described in Section 4.3 uses tolerance thresholds σ_l^{reltol} and σ_l^{abstol} to decide when to stop recursion (206). The previously considered case of two close parallel fractures, as shown on Figure 73 can be used to measure the effects of different tolerances on the final value of σ_l. The spacing is set to 1 while $L = 100$ to increase number the divisions needed to achieve desired accuracies. Results of such measurements for three pairs of tolerance values are shown on Figure 76. The baseline comparison is a result obtained with $\sigma_l^{reltol} = \sigma_l^{abstol} = 10^{-12}$. Increasing the tolerances to $\sigma_l^{reltol} = 10^{-4}$, $\sigma_l^{reltol} = 10^{-8}$ reduces the accuracy but to a level comparable with $\sigma_l^{reltol} = 10^{-3}$, $\sigma_l^{reltol} = 10^{-6}$ when considering the proximity of end interval points $x = 0$ and $x = 1$. However further increase to $\sigma_l^{reltol} = 10^{-2}$, $\sigma_l^{reltol} = 10^{-4}$ results in unsafe relative values of $\delta\sigma_l$, that exceed 10^{-2}, thus less strict tolerances should not be used.

The reason for seeking optimal values σ_l^{reltol} and σ_l^{abstol}, is that the lower the tolerances are, the more recursive steps are needed to find (199), and thus more time is consumed. Since the general accuracies of this multifracturing model are unlikely to be greater than 10^{-5} (see Subsection 5.3.2), using methods of higher accuracies will be somehow a waste of resources. Meanwhile finding other means off speeding up this elasticity calculation may prove to be very beneficial for overall performance.

An additional improvement can be achieved by tweaking the inverse square root included in (199):

$$\frac{1}{d^3} \xrightarrow[d=\sqrt{\dots}]{} \frac{1}{\sqrt{x}}. \tag{251}$$

Interestingly so far the majority of this work could be implemented only as numerical additions, subtractions, multiplications and divisions. The whole pseudo-elasticity scheme shown in Section 4.3 does not require any complex arithmetic operations, except for $\sqrt{x}$ required to calculate the distance d. The simplest approach is to use the existing native sqrt() function, available in all programing languages. This function however has one significant disadvantage: its accuracy is extremely high, while the time cost can be in hundreds of CPU cycles. Unfortunately, $\sqrt{x}$ will be used a lot in this multifracturing problem, but there are other great works where the issue of native sqrt() performance was fixed.

A number of 3D graphics problems requires massive repeated calculations of surface normals, which can be speedup by the fast approximation of inverse square root, a method which is very well described in a blog by Hansen [32]. This fast inverse square root approxi-

	t
$\sigma_l^{reltol} = 10^{-2}, \sigma_l^{reltol} = 10^{-4}$	1.00
$\sigma_l^{reltol} = 10^{-3}, \sigma_l^{reltol} = 10^{-6}$	1.09
$\sigma_l^{reltol} = 10^{-4}, \sigma_l^{reltol} = 10^{-8}$	1.31
one iteration fast $\frac{1}{\sqrt{x}}$	0.82
two iterations fast $\frac{1}{\sqrt{x}}$	1.01

Table 10: Relative time consumed when computing σ_l. The alternative calculations with fast $\frac{1}{\sqrt{x}}$ uses $\sigma_l^{reltol} = 10^{-3}$ and $\sigma_l^{abstol} = 10^{-6}$

mation is based on bitwise operations with the "magic " hexadecimal number $0x5F3759DF$, an exploitation of floating point notation bit properties, which is then followed by one or more newton iterations. The most influential code implementation of this algorithm would be the one attributed to Cormack found in Quake III source code [36], but unfortunately the original source appears to be unknown. Nevertheless the fast inverse square root, is of interest here as it can be used in (199) to replace the native sqrt() function. The almost endlessly repeated calculation of inverse distance (251), makes this problem somehow similar to a 3D graphics engine.

In Table 10 the relative time differences resulting from different tolerances, and square root methods are shown. With one newton iteration fast $\frac{1}{\sqrt{x}}$ the approximation of whole σ_l needs about 20% less time, than less accurate native sqrt() with $\sigma_l^{reltol} = 10^{-2}, \sigma_l^{reltol} = 10^{-4}$. Furthermore two newton iterations in the fast square root, are enough to achieve the same results as native sqrt() function, but still save about 10% of computation time. Although these improvements are not large performance gains, these are given for *free* and offer straightforward improvement for the whole scheme. Naturally many similar numerical tweaks exist, but this one was chosen in particular as it adds an interesting transferable flavor.

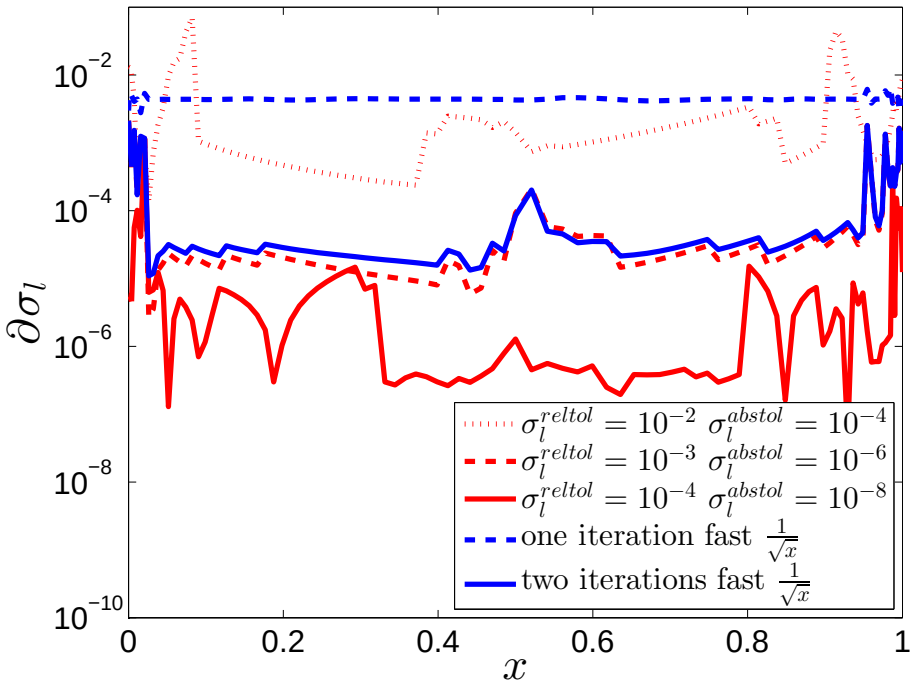

Figure 76: Relative discrepancies in σ_l, depending on the desired accuracies, baseline $\sigma_l^{reltol} = 10^{-8}$ and $\sigma_l^{abstol} = 10^{-12}$. The alternative calculations with fast $\frac{1}{\sqrt{x}}$ uses $\sigma_l^{reltol} = 10^{-3}$ and $\sigma_l^{abstol} = 10^{-6}$

5.2.4 *Pseudo elastic influence σ_l, in some sample geometries*

The method for resolving fracture visibility shown in Algorithm 3, is rather complex and deserves a few extra tests to verify if the produced results agree with expectations. On Figures 77, 78 and 79 some relatively simple to analyze structures are presented. One can have a look on the arrangements of edges, and deduce what the pattern of corresponding visibility matrix would be. Consequently the output of algorithm 3 can be check against these empirical expectations.

First lets have a look at Figure 77. Here six cracks are placed in such a way that e_3, e_4 are in the center, and e_1, e_2, e_5, e_6 are on the outer edges of a short array of fractures. This placement makes e_3, e_4 visible to all e_1, e_2, e_5, e_6, which can be confirmed by the presented visibility pattern. Furthermore the end tips of e_1, e_2 are long enough to extend beyond the shadow of center fractures, and are visible to end tips of e_5, e_6 respectively. The value of σ_l for the middle e_3, e_4 at $x = 0$ is double of that for outer e_1, e_2, e_5, e_6, as the middle is influenced by the two outer fractures, while outer segments only by the single middle fracture. As the pair e_1, e_2 is the longest, the end tips $x = 1$ are furthermost away form the rest of σ_l sources, thus the value of σ_l is the lowest at these points. However having a closer look at σ_l for e_1, e_2 one can notice that the rate of change slightly decreases near the tip, which should be associated with these tips being also exposed to influence from parts of e_5, e_6.

On the next Figure 78, a number of PKN segments are connected to each other directly. The visibility matrix shows only full squares, as all the fractures are fully visible to each other, or not visible at all. The effect of $min(d^3, 1)$ in (199) on σ_l can be well observed here. For the relatively long e_1, the reduction of σ_l occurs at relatively close proximity of the crack tip $x = 1$. The distribution of σ_l is most affected for the shortest e_4. Whether this is a serious issue or not, is a hard question to answer.

Finally Figure 79 consist of a mixture of partially and fully visible interconnected PKN cracks and pipes. Pipe segment e_1, as expected is seen by all the other edges, with the exception of e_5 and parts of e_7, which is well reflected in the visibility matrix . The presence of e_4, e_5 affects σ_l for e_7 as a local maxima near $x \approx 0.5$ can be observed. Even in such a case of relatively small test scenario, much more observations could be made. However as complex as the pattern of visibility matrix and distribution of σ_l might be, the generic formulation for obtaining σ_l presented in this work produces valid and consistent results, which is an achievement in its own. Having verified the procedure for this examples, it is reasonable to assume that other possible arrangements of fractures will also be properly handled.

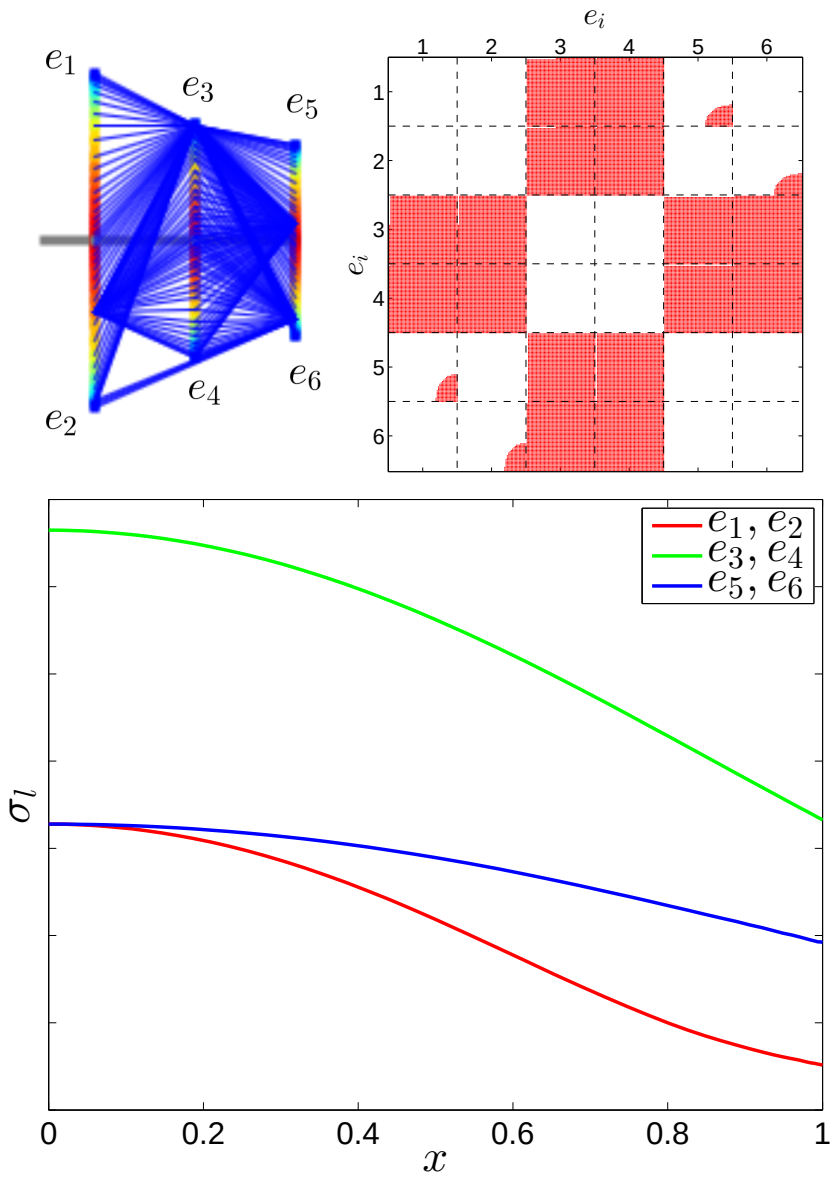

Figure 77: Example visibility matrix and σ_l, array of PKN fractures connected by solid pipes.

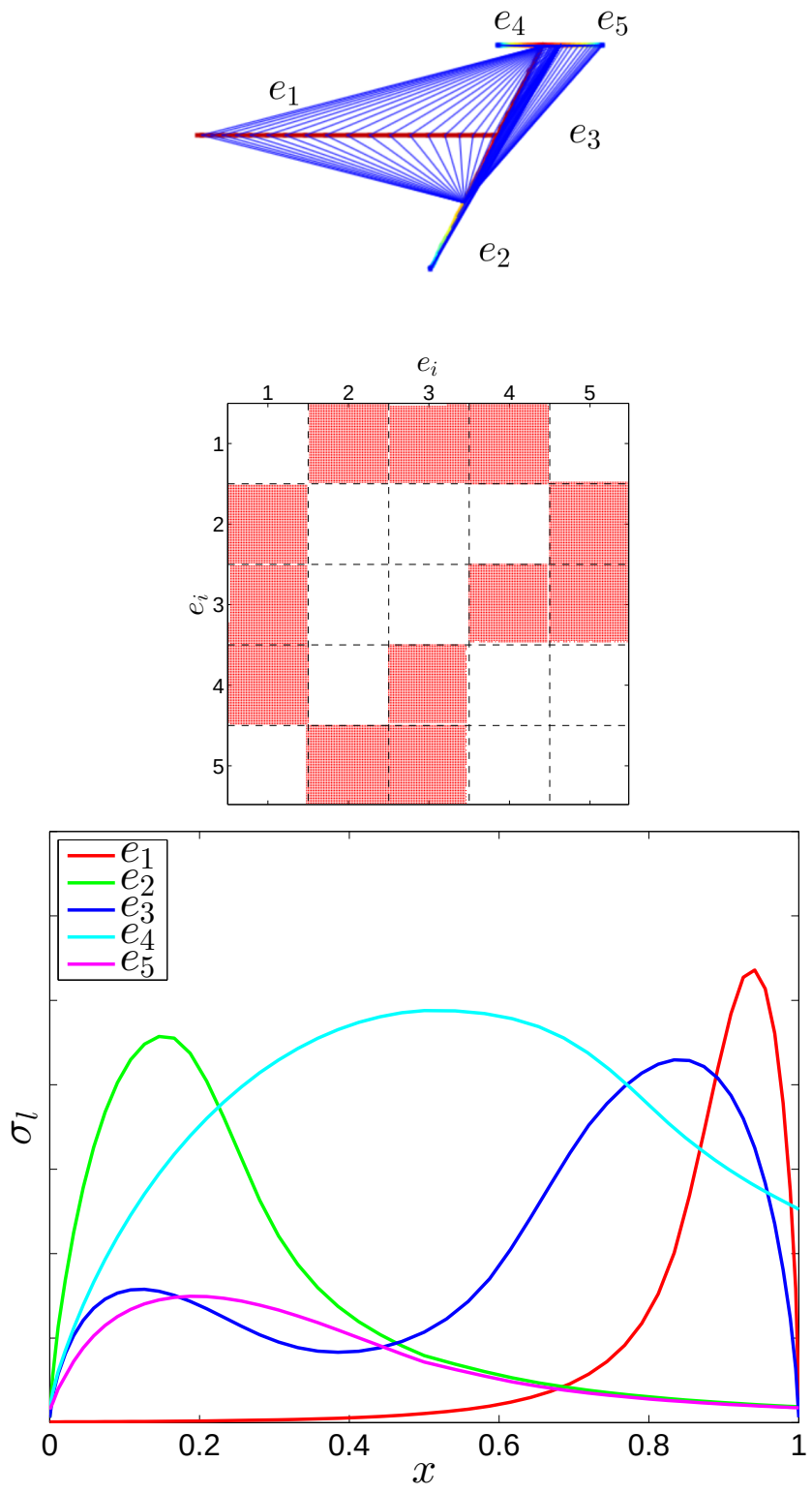

Figure 78: Example visibility matrix and σ_l, a set of connected PKN cracks and pipes.

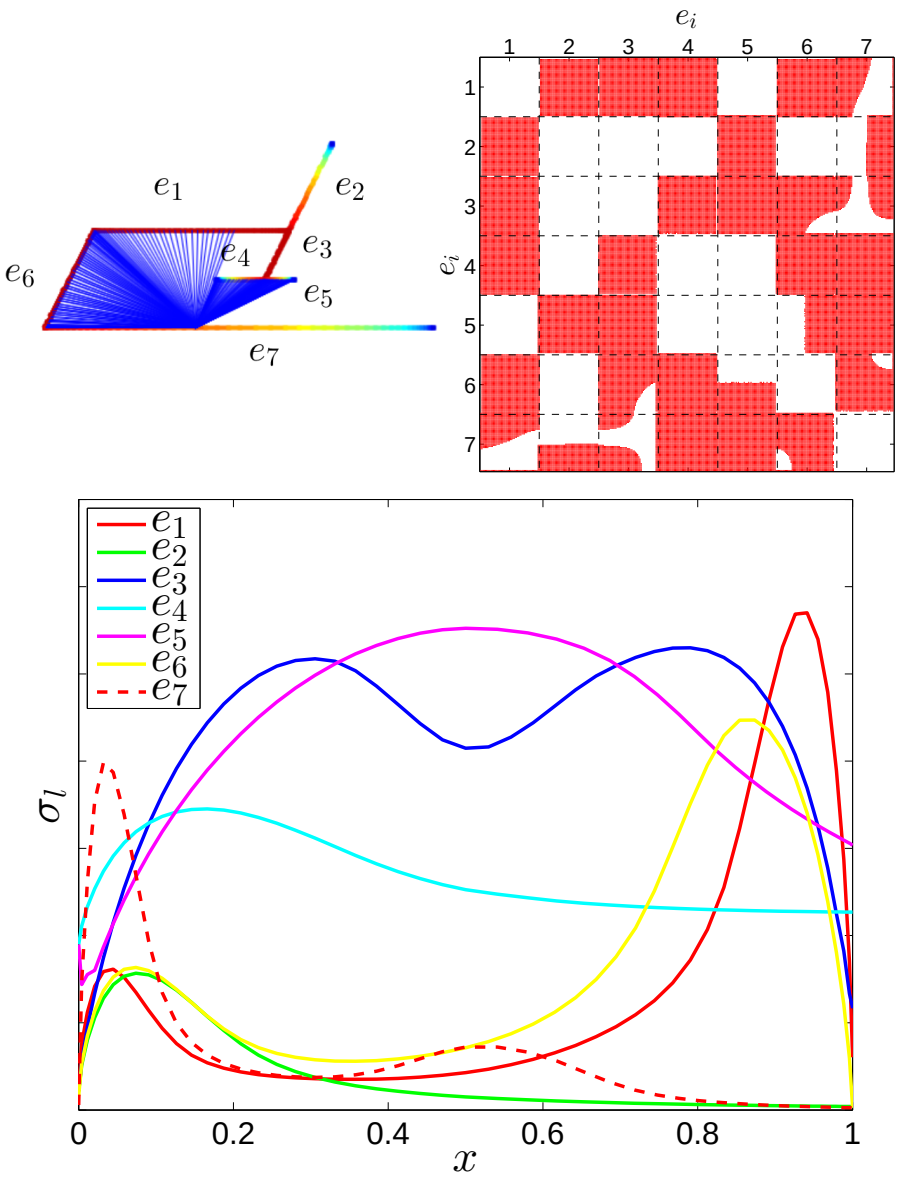

Figure 79: Example visibility matrix and σ_l, a set of connected PKN cracks and pipes with some partial visibilities.

5.2.5 *Power input in an array of fractures*

In the work by Bunger [10] as mentioned before in Subsection 5.2.1, a specific scenario was considered. A number $N_{fracture}$ of double wing fractures are placed in a parallel array at some interval with fixed width Z . The work was conducted on Radial, KGD and PKN geometry, and one of its goals was to approximate the number of placed fractures that minimizes power input required to maintain constant pump in rate over time. That analytical work test can be reproduced for PKN model using numerical methods introduced in this work. First lets write the spacing of fractures H, and $\hat{q}$ the individual pumping rate for each half fracture wing:

$$H = \frac{Z}{N_{fracture}}, \quad \hat{q} = \frac{q_0}{N_{fracture}}, \tag{252}$$

which follow the test scenario proposed by Bunger [10], thus in this case flow is assumed to disperse evenly to each fracture resulting in the same value of pumping $\hat{q}$ for each fracture. The total array power input in watts $P(t)$ is approximated by:

$$P(t) = \sum_{j=1}^{N_{fracture}} \hat{q} p^j_{fluid}(t, 0). \tag{253}$$

Where $p^j_{fluid}(t, 0)$ is the net fluid pressure at the inlet of each fracture (it has to be evaluated through junction pressure scheme as showed in Section 4.2), so the total power input is proportional to the sum of fracture opening widths and effective σ_l. The other parameter values used in this scenario are:

$$\begin{array}{rclrcl} \nu & = & 0.25 & \mu & = & 1 \\ E & = & 10^{10} & q_0 & = & 0.1 \\ h & = & 20 & \sigma_x & = & 7 * 10^7 \end{array} \tag{254}$$

where all these values are taken form the original paper [10] , except for Poisson's ratio which was set to a reasonable value. The results of these test are shown on Figure 80a, and compared against the original Bungers result on Figure 80b. It is impossible to make direct comparison of these two, as the value of ν is not known. Furthermore this work does not include formation toughness K_{IC}, hence the energy required to break rock structure is not included. However the general result, minimization of power input for some number of fractures, prevails. Fluid balance was maintained at least 10^{-4}, no leak off was used.

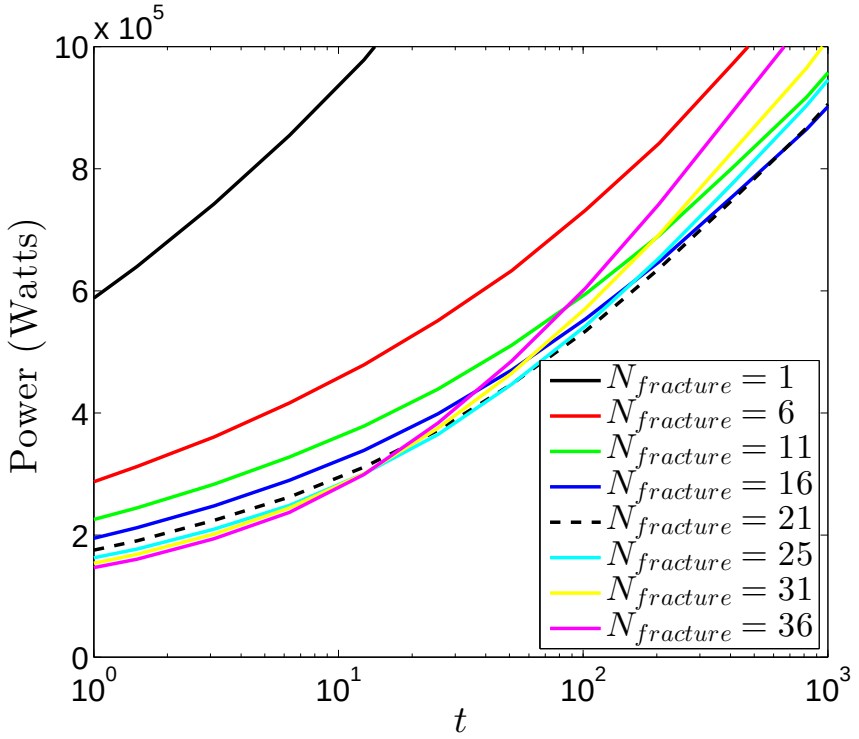

(a) With the proper choice of the elasticity constant g (250), a very similar result is obtained. The optimal value of $N_{fracture}$ can be found.

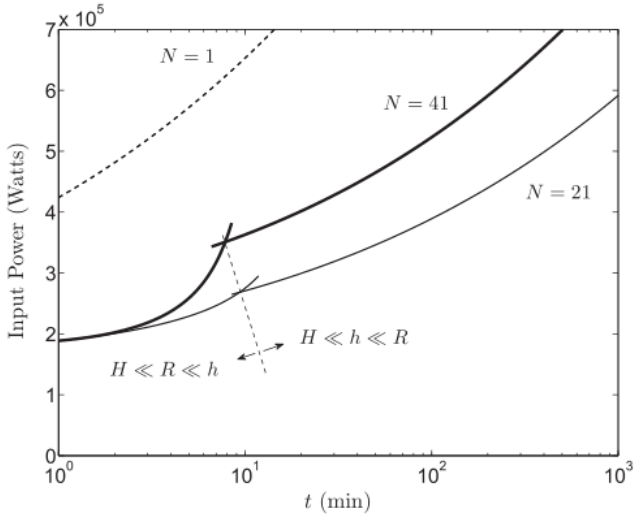

(b) The original analytical result by Bunger [10]

Figure 80: Power input in parallel array of fractures, vs number of fractures. Although the exact value of output was not matched, the saturation at some critical $N_{fracture}$ was reproduced.

5.3 NOTES ON IMPLEMENTATION

5.3.1 *Java and OO design*

So far the formulation of the multifracturing problem was made with Object Oriented approach in mind. This programing paradigm is not much newer than the more conventional procedural style used by C and FORTRAN languages. In fact the first appearance of OO can be traced back to 1960s [63]. The widespread of OO as the dominant paradigm took place in the mid 1990s [100], as languages supporting this paradigm, C++ and Java become available. Interestingly, as observed by the author, quite a large number of academics, who were educated before OO became dominant, do not use, nor attempt to use any of OO features in their work. On the other hand a number of courses from top universities, or researchers from recognized institutions, do mix OO methods with numerical models [73, 82, 53], not to mention numerous other sources ([**?**] is a good book on this topic). The multifracturing problem in its very roots does call for usage of some objects to represent abstract data. All mentioned cracks, pipes, injection points and other abstract structures are well addressed if treated as objects, and the multitude of other applicable functionalities: rendering, collisions, data operations can be well handled with this paradigm.

It appears as the most practical choice to use at least a few features of OO design, but the other remaining question is to what programing language this work should be implemented in. There are two main challenges in this problem, maintaining sufficient performance and obtaining accurate and reliable solution. The single fracture formulation was done in MATLAB, which although performed good enough for the single fracture case, has significant drawbacks when facing more complex problems. A good practical discussion on usefulness of MATLAB for any larger project can be found on stack overflow [88]. The dominant opinion stated there is that, although MATLAB is good for small quick tasks, it is a bad choice as a general purpose programing language and offers slow performance. Additional, MATLAB is not freely available, which would mean releasing any results as open source would mean additional complications.

Having crossed out MATLAB as a feasible language for multifracturing problems the other choices of languages should be outlined. Traditionally the heaviest numerical projects have been developed in C/C++ or FORTRAN[2]. However over the past decade the most popular language was Java [90], which has only recently given up the lead due to appearance of other similar competing languages (Python, C#,

2 In fact FORTRAN is probably the oldest programing language one can still expect to find in usage.

D). Despite many myths about Java performance, there is a large number of publications that prove that in numerical application, *including matrix operations*, Java performs at the same levels, *or even better* than C/C++ and FORTRAN based libraries [71, 6, 5, 9]. A very well written study of this phenomena was done by Lewis [50], which highlights, pointers garbage collection and run-time compilation as some technical explanation why Java can perform better than C/C++. Nevertheless the performance gap between these languages should not be the main factor affecting the decision.

Writing well written and maintainable code is at least as important as its numerical performance[3]. Some languages are naturally better at this task than others. One cannot however expect someone with experience in one language to produce quality code from day one after switch to another language. If most of the experience is Java related, than sticking with this language would be the most consistent choice. Furthermore Java has unquestionably superior capabilities (stack trace, portability, exceptions) when it comes to code stability and reliability. Thus the final choice was to solve the main part of this multifracturing problem in Java. This decision was outlined here as a brief overview, and could be in fact carried further into much more detail, but the general reasoning should be made clear at this point. There are some drawbacks of this choice, but none of them appeared to be significant enough to get mentioned here.

The constructed object orientated structure should also be mentioned. Figure 81 represents, somehow simplified UML diagram. The design principles flowed here are:

- The ODE Interface states methods that would be expected from a set of ODEs to be operated by an arbitrary ODE solver. These include getting initial value (98), the integrated derivative (99) and setting solution (100). It is implemented by Edge that ultimately handles a single fracture, and Model that combines all fractures outputs (Algorithm 4). The result is feed to Solver, turning this part into Builder pattern.

- Abstract Solver is used by Multifracturing, which is the main class that logically advances the whole model in time (Algorithm5). The numerical work of integration is however done by extensions of Solver, which serve as Bridges. Multiple versions of ODEs solvers can be used here, as shown in the next Subsection 5.3.2.

- Model acts as a Facade, that decouples most of the detail away from main Multifracturing class. A separate instance of Model for each State corresponding to multiple $t = \{t_0, ..., t_{end}\}$ is held. (or at least an attempt to compute these is made).

3 Basic Computer Science principle.

- There are N_V number of Vertexes and N_E number of Edges held by Model. Each Edge has two Vertexes, while each Vertex can have many, or none Edges. This represents a graph.
- Edge is extended by multiple classes, that represent the actual physical objects. These eventually properly implement Interface ODE methods. These can ultimately rely on different implementation of operator $\mathcal{A}$ (32), (65) and (77) , and combinations of derivative approximation techniques (125), (136), (149) or (125). The assignment of these could be done by a Factory, but for keep some simplicity this pattern is omitted on Figure 81 and only a few possibilities are shown. An important advantage of this solution here is that further implementations of Edge can be integrated with the rest of this structure. Other fracturing geometries, especially KGD model that can abstracted as line connection between two points, if made compatible with junction strategy (Section 4.2) and described as a system of ODEs, should fit without the need to alert any other of the code.
- Additional Classes used by Multifracturing hold specific functionality for collisions (Section 4.4), global and configuration variables, and do other tasks such as data handling and rendering.
- The Utility Matrices specified in Subsection 4.5.2 are also decoupled from the Model, to spread out the functionality over even more classes.

The code for some of the classes presented here is available in Appendix A.5

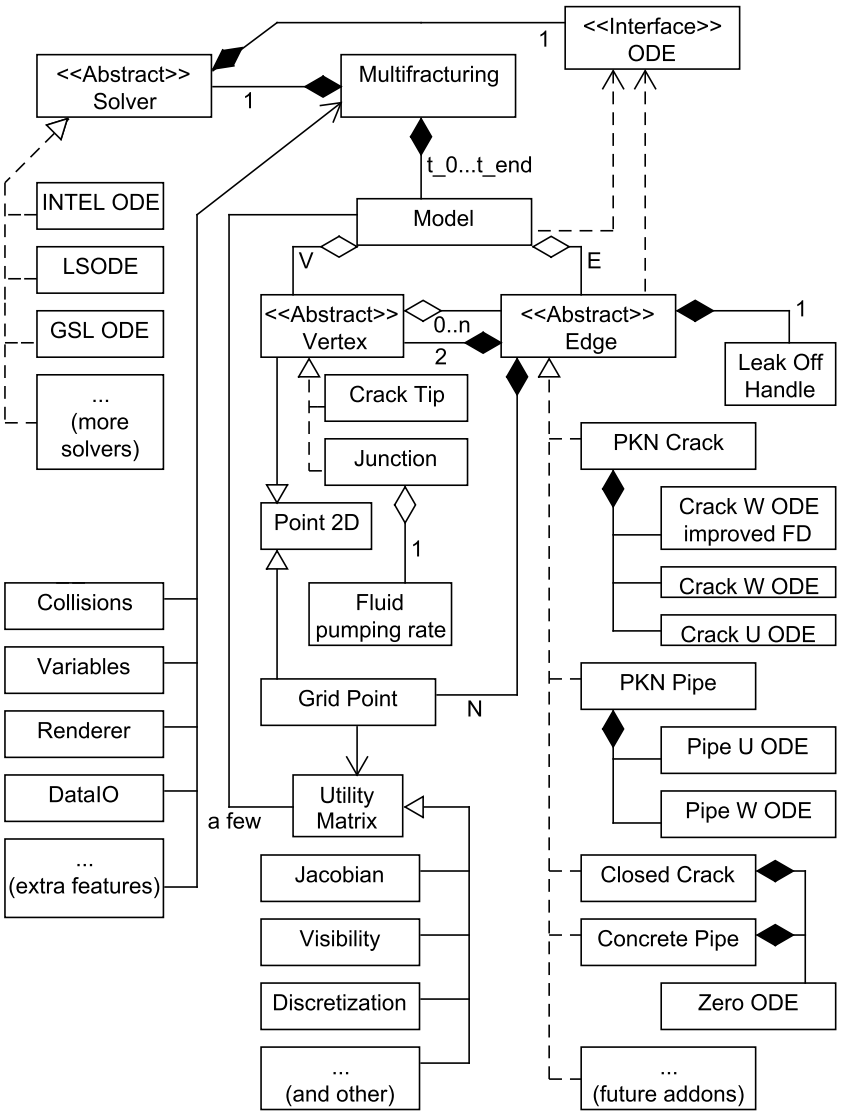

Figure 81: Simplified UML design diagram, general class structure of multifracturing code.

5.3.2 *Comparison of ODE solvers*

Having formulated the design in such a manner that the underlying solver is in fact just an abstraction, it is possible to switch utilized integration code with a single command. A separate bridge is prepared to deal with each method. Most of these rely on JNI[4] to access native C code.

5.3.2.1 *GLS (GNU Scientific Library) ODE Solver*

GNU Scientific Library [89] is a collection of numerous numerical libraries available under GNU public license. These libraries cover all major numerical tools, which include solving initial value problems. The particular function used here is gsl_odeiv2, which can make a choice of type of method used. These include a range of Runge-Kutta, Adams and BDF (95) methods.

5.3.2.2 *LSODE*

LSODE was developed by NASA [79] and released as a publicly available ODE solver based on BDF (95) methods. The solver has a long history and is available in different versions. The particular variation used here is borrowed from [51], as this particular C based implementation is very well packed into one file, containing all needed additional BLAS functions.

5.3.2.3 *Intel ODE Solver Library*

The newest solver among considered in this work. Developed by Laevsky [47] at Intel. Although the project is discontinued, the solver is still available for usage. This solver combines both explicit method for non-stiff problems, and implicit method for stiff solver, and can switch between each method depending on the difficulty of given problem.

5.3.2.4 *ODE15s*

At the earlier state of development of this software, a successful attempt to use MATLAB ODE15s solver was made. Unfortunately the process of calling MATLAB from Java is not straightforward. Despite the reverse type of call, accessing Java code from MATLAB is made extremely easy with build in features, the only way to access ODE15s that was found, was through some open source bindings [22]. This did worked, but exposed several flaws in MATLAB. The biggest is the reliance on its own internal JVM, which in case of used bindings

4 Java Native Access

meant all send objects needed to be serialized and transferred between two running JVMs. This alone would not be a huge issue, but the MATLAB R2013a version of Java was 1.6, but the developed code already relied on Java 1.8 functionality. This means keeping backward compatibility with ODE15s was not feasible at later stages. The accuracy and performance of ODE15s, when the code was still compatible with Java 1.6, was at the same levels to what was obtained by LSODE or GLS solvers.

TEST ON ZERO LEAK OFF SELF SIMILAR SOLUTION. Now a comparison of several available solvers can be made. These solvers were tested on the same test based on zero leak off self similar solution, Appendix A.2.2. The test was done with $N_c = 11$, which is *a very small* number of grid points, w system formulation (32) with improved spatial discretization scheme (149) and Junction strategy BC 4.2 was supplied to the solvers. Double power grid $x_m^{(4)}$ (264) with $\delta_a = \delta_b = 2.5$ was used. The test proved that abstraction of solver implementation works, and allows to easily interchange integrating algorithm. This opens future possibility of switching solvers on the fly, depending on their performance or even to try another algorithm if one fails at some stage of multifracturing simulation. Comparing results (Figure 82 and 83) one can conclude that Intel ODE solver and LSODE obtained nearly identical results in terms of accuracy for crack opening w, and Intel ODE performed about and order off accuracy[5]. better when computing fracture length L. However the time needed to obtain the solution was about 5 times longer for Intel ODE solver, when compared to LSODE. The third shown solver GSL ODE did performed worse by and up to two orders of magnitude, which can be associated with visible struggle (sharp edge on 83a) to keep up near the crack tip. The time needed by GLS was about 30 times grater compared to the time used by LSODE in this test. This is a very significant difference, but similar discrepancy, 10-30 times more iterations, was observed in comparison made in [51] between LSODE and GSL solvers. This results suggest LSODE should be the default solver for most of the scenarios, as it offers the best performance, but the other solvers can still be used if any difficulties were encountered.

5.3.3 *Code optimization and parallelization*

Lets recall from the definition of an initial value problem (94), the y' used in multifracturing problem (239) is :

5 Yet these accuracies are about two orders better than these presented in Mishuris at [64] for dynamic systems and can compete with integral solver and straightforward algorithm

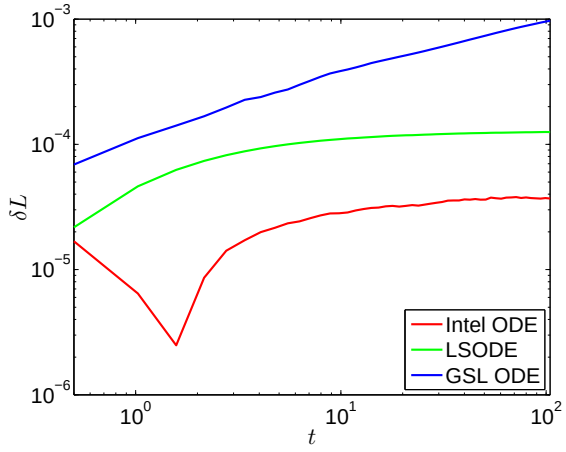

Figure 82: Relative crack length error ∂L for zero leak off solution obtained with various ODE solvers.

$$y'_{1..N_E}(t,y) = \{\mathcal{F}'_1(t,\mathcal{M}), \mathcal{F}'_2(t,\mathcal{M}), ...\mathcal{F}'_{N_E}(t,\mathcal{M})\}. \tag{255}$$

Since all $\mathcal{F}'_i$ here are independent of each other, the function y' is data parallel, and can be trivially split into any number of threads, each working on a piece of the whole y'. A convenient approach is to allow for each edge $\mathcal{F}'_i$ to be assigned to one thread. Hence a problem with N_E edges could be effectively split into N_E threads:

$$y'_{1..N_E}(t,y) = \left\{ \underbrace{\mathcal{F}'_1(t,\mathcal{M})}_{thread\ 1}, \underbrace{\mathcal{F}'_2(t,\mathcal{M})}_{thread\ 2}, ..., \underbrace{\mathcal{F}'_{N_E}(t,\mathcal{M})}_{thread\ N_E} \right\} \tag{256}$$

Since the current implementation is Java based, and executes commands on the local CPU, a simple for each loop that assigns edge to one local worker is used. With Lambda expressions introduced in Java 1.8, the task is even easier perform. A multifracturing problem is likely to have tens, if not a few hundreds of edges involved, which should be grater than available hardware threads, so this simple work division is likely to achieve fair balance without adding too much parallel overhead.

But the above simple parallelization of y' does not solve the problem of optimizing Jacobian pattern. Previously in Subsection 4.5.2 it was shown how the matrix for Jacobian pattern can be constructed, which should be used in a proper custom Jacobian function. First lets make another version of (239) that operates on global grid point index i_{global} ranging from 1 to N_{ode}:

$$y'_{1..N_{ODE}}(t,y) = \{\mathcal{F}'_1(t,\mathcal{M}), \mathcal{F}'_2(t,\mathcal{M}), ...\mathcal{F}'_{N_{ODE}}(t,\mathcal{M})\}. \tag{257}$$

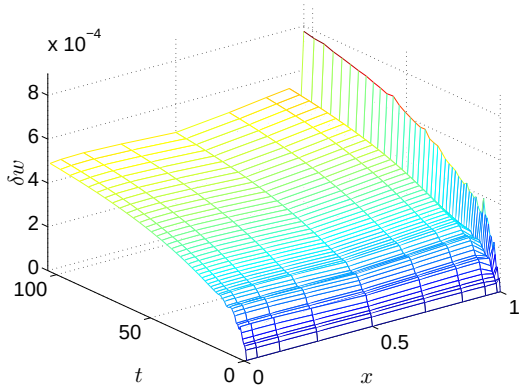

(a) GNU Scientific Library ODE solver

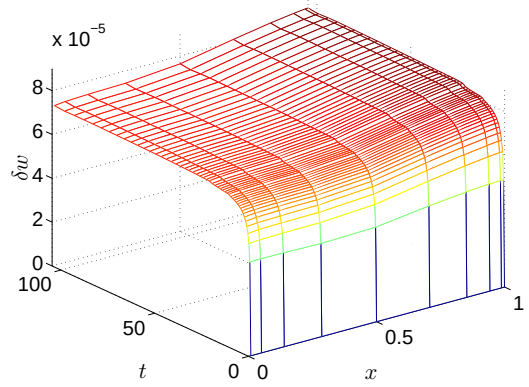

(b) LSODE

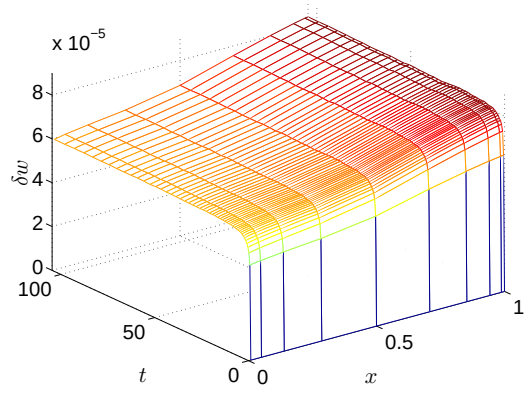

(c) Intel ODE Solver Library

Figure 83: Relative crack opening error δw for zero leak off solution obtained with various ODE solvers.

Where $\mathcal{F}'_{i_{global}}$ translates to $\mathcal{F}'_{i_{local}}$ by (237). So now $\mathcal{F}'_{i_{global}}$ returns a single point, as opposed to vector value. So now when calculating the Jacobian it is possible to make the approximation for only the non zero values:

$$J_{m,n} = \begin{cases} \frac{\mathcal{F}'_m(t,\mathcal{M}),-\mathcal{F}'_m(t,\mathcal{M}+\Delta_n)}{\Delta_n}, & if\ J_{pattern\ m,n} = 1 \\ 0 & if\ J_{pattern\ m,n} = 0 \end{cases}$$

The above is also a data parallel operation that can split into a number of threads. The term Δ_n refers to a small change to a single element in vector, so vector $\mathcal{M} + \Delta_n$ is different from $\mathcal{M}$ by a small change in one element. This change can be done in a single thread, so $J_{m,n}$ is split into N_{ODE} number of streams, one for each column n.

Figure 84 shows the computation time gains on a sample multi-fracturing system achieved with code parallelization and Jacobian matrix patternization. The speed up can be over 2 orders of magnitude, which in practice means that a problem that would take an hour to solve, with proper code implementation would take less than a minute. The main goal of this section is to show that these relatively simple techniques can make a difference between a solution that gives a result, and a one that is still running. Indeed even though the ODE solver code remains serial, the whole code achieves over 80% CPU usage on a quad core i7 (8 threads) which translates to at least 5 times less running time.

Although this improvements are very specific to this implementation, similar gains could be achieved on other problems. Some of the previous tests done in this work, could not be finished in a sensible time if no computational optimization of any kind was made (see Section 3.3 and Subsection 5.2.5)

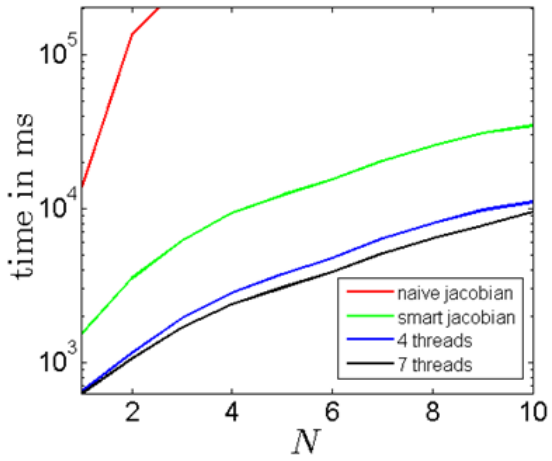

Figure 84: Performance gains with various computational techniques. Achieving orders of magnitude difference can save hours of real life time.

5.4 TEST SCENARIOS

5.4.1 *Collision: crack to natural fracture, uniform σ_0s*

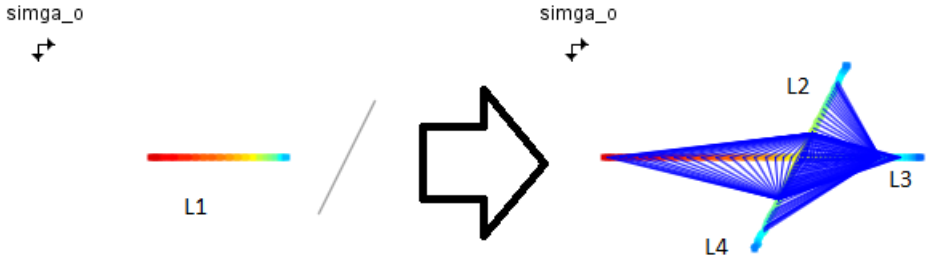

(a) A fracture collides with natural fracture and produces three new openings.

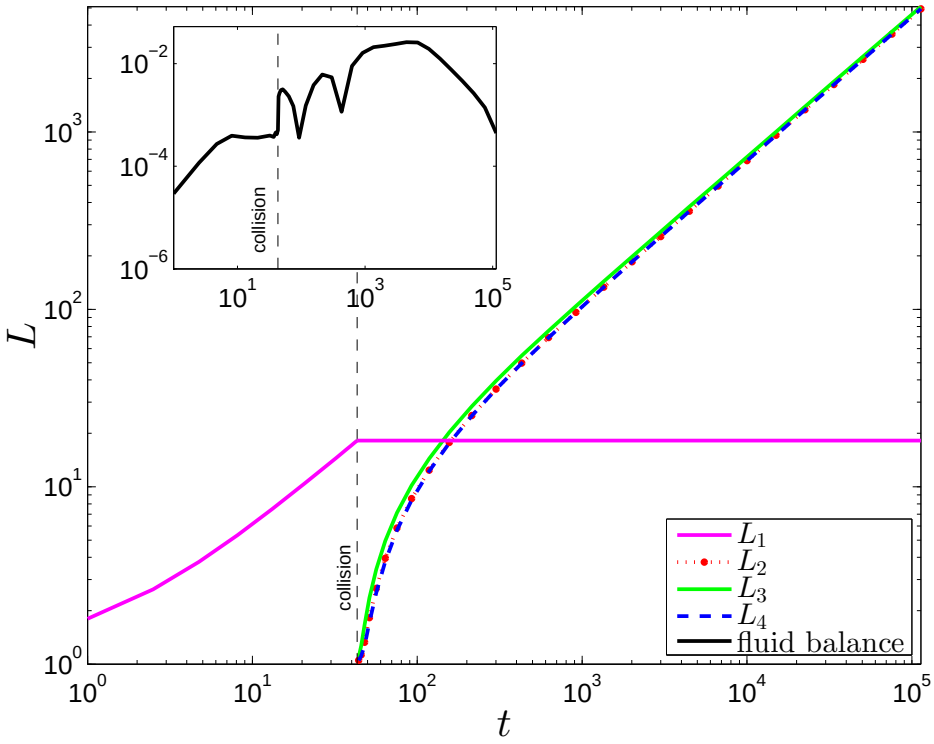

(b) Lengths of fractures and relative fluid balance in respect of time.

Figure 85: NF collision $g = 0.143$, $k = 4$, $m = 1$, $q_0 = .5$, $\sigma_x = 1$, $\sigma_y = 1$

5.4.2 *Collision: crack to natural fracture, uneven σ_0*

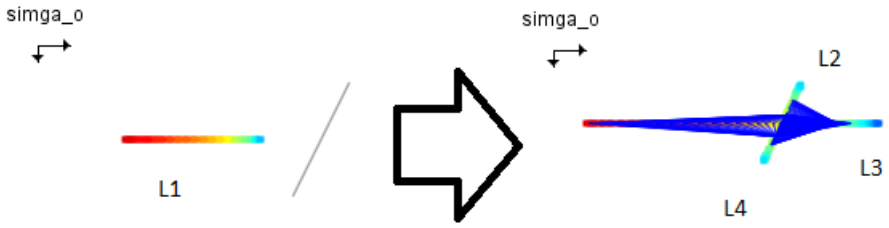

(a) A fracture collides with natural fracture and produces three new openings. The difference in backstress σ_0 creates differences in produced fracture lengths.

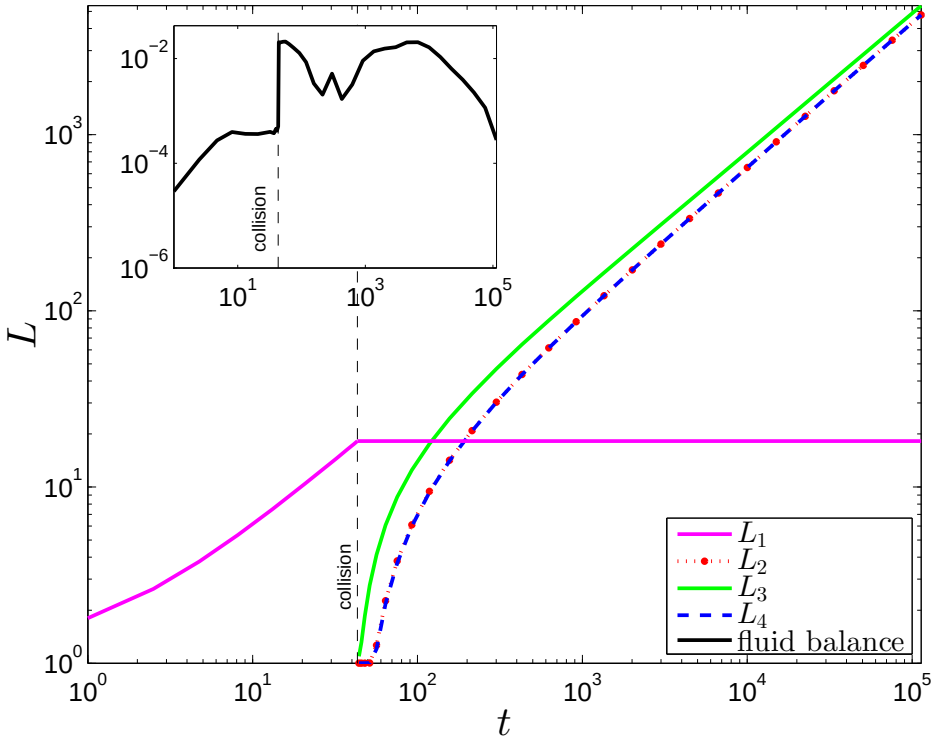

(b) Lengths of fractures and relative fluid balance in respect of time.

Figure 86: NF collision $g = 0.143,\ k = 4,\ m = 1,\ q_0 = .5,\ \sigma_x = 2.2,\ \sigma_y = 1$

5.4.3 *Collision: crack to other hydraulic fracture*

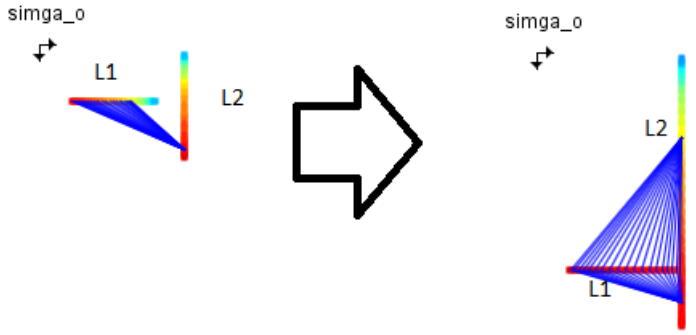

(a) A fracture merges together with another one.

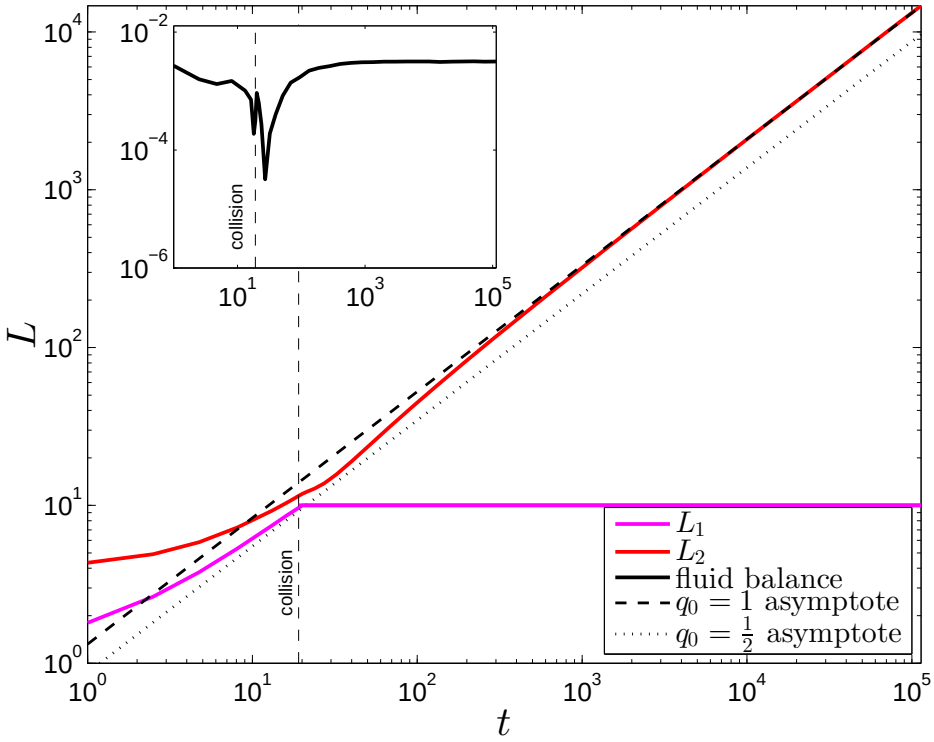

(b) Lengths of fractures and relative fluid balance in respect of time., note the convergence to different asymptotes.

Figure 87: NF collision $g = 0.143$, $k = 4$, $m = 1$, $q_0 = .5$, $\sigma_x = 1$, $\sigma_y = 1$

5.4.4 *Tree like fracture structure*

Consider the following example geometry organized in a binary tree shape as shown on Figure 88. The top node is a junction (Section 4.2) with pump in rate $q_0 = 1$. Then there are four consequent depth levels. The first three levels split the flow through connected PKN pipe segments (Subsection 4.1.4), and the deepest level represents an array

of PKN cracks (Subsection 4.1.3). For the purpose of this test the crack stress influence is ignored, $\sigma_l = 0$, and back stress components are set equal $\sigma_x = \sigma_y$, so there should be no preference in flow direction introduced by stress differences. Therefore the structure is constructed in such a manner that the flow should be equally distributed to all end PKN crack segments. The initial opening w_* and length l_* for each of used crack segments is set to match zero leak off benchmark solution , Appendix A.4.10, and to have $w_* = 1$ at $x = 0$. The pipe segments are set up such so $w_*(x) = 1$ for all values of x. This distribution of initial $w_*$is not chosen as a natural state, and should introduce some extra initial error, however the multifracturing scheme should be able to deal with it, which adds additional challenge to this problem. This test should be run with zero leak off $q_l = 0$.

The result of running computation on this structure is shown on Figure 88. Here two effects can be observed.

First, the behavior of end crack segments, at large times, can be characterized by the large time asymptote for the zero leak off solution. This is a trivial result by itself, but it verifies that the pump rate $q_0 = 1$ at the first junction is distributed evenly to all end cracks segments, so each effectively receives $q_0 = \frac{1}{8}$, as there are eight end crack segments it this scenario. This proper distribution of fluid is achieved once length of end fracture segments is much grater than combined length of distributing pipe segments.

The accuracy is most significantly affected by the choice of grid type (Appendix A.1) and number of grid points N per crack and pipe segments. In this scenario four combinations of grid points per crack segments N_c, pipe segments N_p and the density parameter γ in the double power grid $x_m^{(4)}$ (264) are used. The value of γ which is refereed here affects points density near junction segments, not in the proximity of crack tip. Therefore the test with $\gamma = 1$ refers to actually using uniform grid $x_m^{(1)}$ over majority of the structure, while other three tests with $\gamma = \frac{3}{2}$ have denser mesh near junctions. The number of crack grid points is set to $N_c = 11$, as it does not appear to have most effect on the accuracy (as observed for fractures in Section 5.3.2).

It is an early experimental result, however the general observation proves that using $x_m^{(4)}$ with $\gamma > 1$ allows better accuracies, than when uniform mesh $x_m^{(1)}$ is used for pipe segments. The number of pipe grid points N_p can be decreased after time, when the length of pipe segment becomes insignificant.

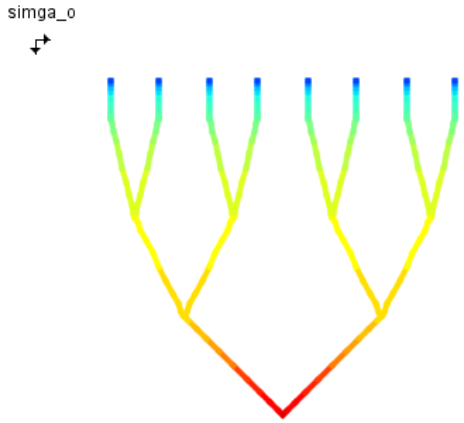

(a) Pipe segments arranged in a binary tree pattern, equally dividing flow to end Crack segments.

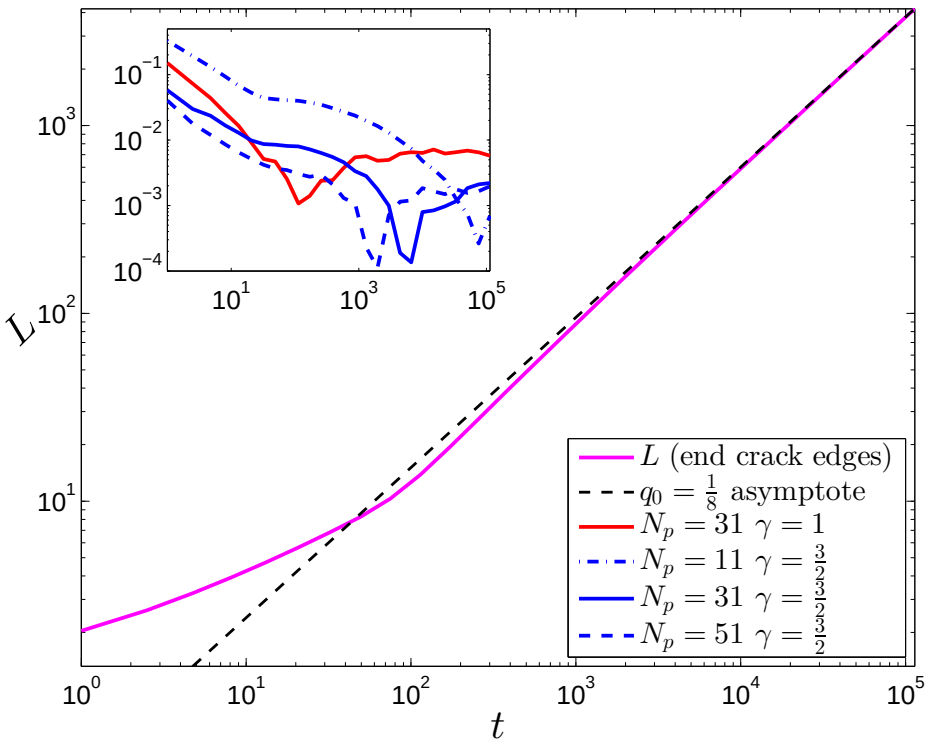

(b) Length of end cracks segments converges to the large time asymptote. Fluid balance accuracies for various combinations of pipe grid type and point number N_p.

Figure 88: Test on a tree like structure, $q_0 = 1$, $q_l = 0$, $\sigma_x = \sigma_y$, $\sigma_l = 0$, $k = 4$, $M = 1$

6

CONCLUSIONS

[September 10, 2015 at 14:04 – classicthesis version 1.0]

6.1 GENERAL SUMMARY

There were two main goals in this work. The first goal was to study and improve the existing PKN model, the second was to develop a working multifracturing solution based on this model.

Using a mixture of recent improvements, forgotten computational techniques, and some own additions it was possible to construct and implement an improved formulation for this classical model. The overall accuracies were always of at least 10^{-3}, up to 10^{-6} in some more specific cases. Additionally the computation time needed for these single fractures was always kept at reasonably low levels. The two term asymptotics boundary condition proved to be especially beneficial in this single fracture formulation, as it not only allowed to adequately tackle degenerative PDE at the crack tip, but also gave accurately approximated first term, later used for fracture velocity, finite differences and integration. It was shown that the proper choice of dependent variable offers substantial improvements, although even better improvements could be achieved with proper discretization: derivative approximation and spatial mesh choices.

The obtained procedure for single fracture was tested on a wide range of initial conditions: different leak off types, storage, receding and propagating regimes, various pump in rates and initial shapes. It was proven that it is possible to obtain accurate numerical solution for a great majority of possible combinations of these conditions, although in some cases it was necessary to do some extra extensions to the original formulation, to properly account for previously unforeseen circumstances.

The second task of building multifracturing model proved to be much more challenging. Although the PKN model neatly serves its purpose, it is, just like other theoretical fracturing models, very limited in its scope and grossly oversimplified. If a single fracture model is to be called a multiphisics formulation, then a combination of these should be treated as a "grand" multiphisics problem. Not all the possible issues were addressed or resolved here, rock toughness, propane transportation or thermal effects were skipped all along. The achieved primary task was to build a multifracturing model with open 2D geometry and fracture interactions, both pseudo elastic and derived from presence of natural fractures. This required derivation of new governing equations and boundary conditions that could handle multiple fractures adequately. The algorithms developed for obtaining numerical solutions of single fractures were also eventually superseded to deal with growing size and complexity. Furthermore it was necessity to consciously design software capable of dealing with multiple fracture hydraulic simulation, using appropriate programing techniques as well as the derived mathematical formulation.

The final result of this work is a study that formulated theoretical and practical basis for construction of relatively simple but powerful hydraulic fracture simulation program, that can handle a wide range of possible hydraulic fracturing treatment scenarios. The task is by no means complete yet, but rather works as a prof of concept that using one dimensional formulation it is eventually possible to build a comprehensive solution that could compete with its commercial counterparts. A variety of mathematical techniques ranging from asymptotics analysis, through numerical integrations, and ending up on computer graphics and vision algorithms were utilized, making this thesis covering several fields, but all of these were applied to solve strict hydraulic fracture problems.

6.2 FUTURE WORK

There is a large number off possible future projects that could follow after this work. The following concepts should include the most manageable and interesting ones.

- The newly introduced Ω variable was show to be very beneficial in a number of specific cases. However as it requires extra handling it was dropped from multifracturing formulation. Nevertheless some improvements tested on w and U variables, could be done on Ω, and the multifracture formulation could be modified to use it as well. This could bring even further accuracy improvements.

- The speed equation formulation was constructed with strictly propagating fractures in mind. Another formulation could be developed that would be designed for closing fracture. This should have different expressions for tip asymptotics, and use a sort of reversed speed equation.

- More physical properties could be included in the formulation such as rock toughness, thermal expansion or viscosity effects and proppant transportation.

- A more dynamic approach to mesh sizes could be considered. Currently the mesh sizes are fixed, but each fracture could be assigned a different number of grid points. This could increase local accuracy in a few crucial fractures, or improve overall performance by decreasing grid density in some less important areas.

- So far only one dimensional leak off models were considered. In reality the fluid flow around the hydraulic fractures should be modeled independently by 2D or even 3D porous flow simulations. This could be achieved by some coupling of Darcy law flow solutions with the developed multifracturing model.

- Proper testing on real life hydraulic fracturing data should be carried on. This would require access to actual drilling logs, including microcosmic data which would allow attempts to match the theoretical model with some real outputs.

- And finally a larger project should exploit the fact that, as observed from initial condition and multifracturing tests, all fractures eventualy converge to large time asymptotes. Furthermore the computations are rather very repetitive. Having computed a solution for a single fracture in a set of specific conditions, it would be reasonable to assume that this solution can be copied

for other fractures developing in similar conditions. Thus for a multifracturing model it could be possible to create a precomputed table containing a range of sample solutions, for different q_0 values, and then just use the closest matching solution instead of repeating another computation for each new slightly perturbed fracture in multifracturing problem. Such an approach would allow for huge problems to be computed instantaneously. This could produce fairy accurate result, with fine table resolution and some error corrections techniques, which could be used in treatment optimization algorithms, where placements of multiple wheels must be checked in order to find most profitable solution.

APPENDIX

[September 10, 2015 at 14:04 – classicthesis version 1.0]

A.1 GRIDS

All grids assume spacing of N number of points in an interval of $\tilde{x} \in [0, 1-\epsilon]$ with some small value of ϵ.

UNIFORM GRID

$$x_m^{(1)} = (1-\epsilon)k/N, \quad k = 0, 1, ..., N. \tag{258}$$

The simplest possible grid, divides the interval into N equally spaced points.

POWER GRID

$$x_m^{(2)}(\delta) = 1 - \left(1 - \left(1 - \varepsilon^{\frac{1}{\delta}}\right)\frac{m}{N}\right)^{\delta}, \quad m = 1, ..., N. \tag{259}$$

Such grid has a benefit of being denser in the proximity of crack tip where the solution for the problem is harder to obtain, therefore allows for greater accuracy [1]. The value of parameter δ should be chosen such so problem stiffens is minimized. In the Section 3.1 it is shown that the optimal value is somewhere close to $\delta = 2.5$

EXPONENTIAL GRID

$$x_m^{(3)} = tanh(ak), \quad k = 0, 1, ..., N. \tag{260}$$

Modification of the exponential law, where parameter a is given by:

$$a = \frac{tanh(1-\epsilon)}{N}. \tag{261}$$

Again such grid has a benefit of being denser in the proximity of crack tip where the solution for the problem is harder to obtain, therefore allows for greater accuracy.

DOUBLE POWER GRID Specially designed grid that will be used in the case of multifracturing. It is a composition of two power grids, that has the same advantage as power grid when it comes to extra accuracy in the tip region, and adds extra accuracy at the crack inlet:

$$x_a(\delta_a) = 1 - \left(1 - \left(1 - (2\varepsilon)^{\frac{1}{\delta_a}}\right)\frac{m}{\lfloor\frac{N}{2}\rfloor}\right)^{\delta_a}, \quad m = 1, ..., \lfloor\frac{N}{2}\rfloor + 1, \tag{262}$$

1 As proved by countless tests with non regular meshes

$$x_b(\delta_b) = 1 - \left(1 - \frac{m}{\lfloor \frac{N}{2} \rfloor}\right)^{\delta_b}, \quad m = 1, ..., \lfloor \frac{N}{2} \rfloor + 1, \tag{263}$$

$$x_m^{(4)} = \begin{cases} \frac{1-x_b}{2} & m < \lfloor \frac{N}{2} \rfloor + 1 \\ \frac{1}{2} + \frac{x_a}{2} & m > \lfloor \frac{N}{2} \rfloor + 1 \end{cases} \quad m = 0, ..., N. \tag{264}$$

The values of parameters are $\delta_a = 2.25$ and $\delta_b = 1.5$. This mesh has one disadvantage of working only for odd values of N (though this is not a real problem).

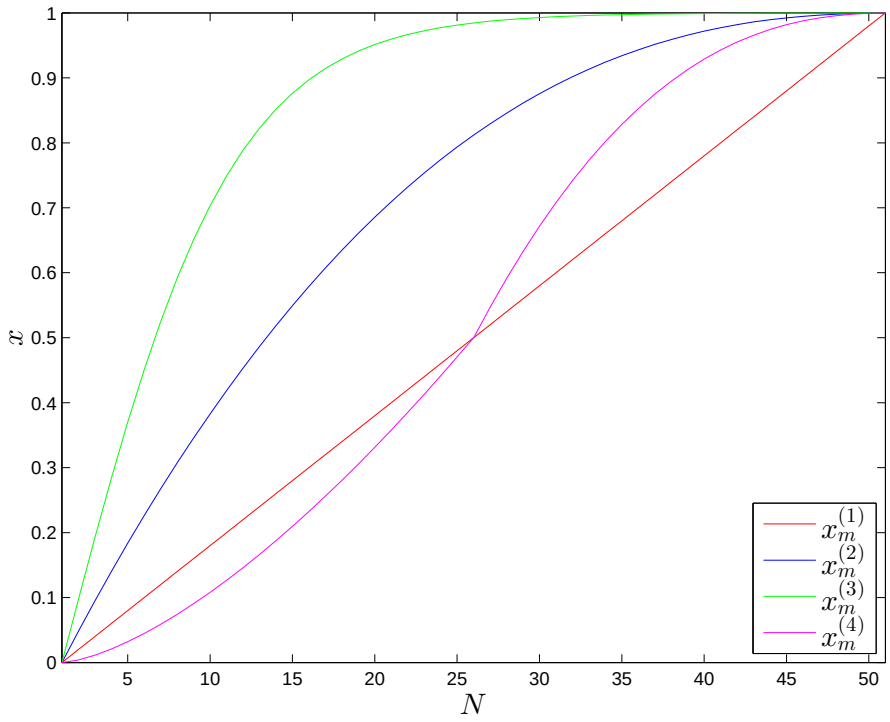

Figure 89: Comparison of used grids.

A.2 BENCHMARK SOLUTIONS

There are several benchmarks available in the literature that can be used in investigation of numerical algorithms. Benchmark solutions for impermeable rock have been constructed in [38, 54], while whose corresponding to the non-zero leak-off model with q_l vanishing at a crack tip has been analyzed in [65]. The large time asymptote for Carter problem was given by Nordgren in [70]. This work is tested against three types of solutions.

A.2.1 *General benchmark*

To simulate three types of leak off a procedure for obtaining analytical benchmarks solutions representing each one of the behaviors (21) was obtained. Moreover, for each of the leak-off functions two different proportion of injection flux rate q_0 and leak-off to formation q_l was considered. This added up to a total of six distinct analytical benchmarks.

The procedure for obtaining these starts by assuming the following form of crack opening function:

$$w(t,x) = W_0(1+t)^{\gamma}h(x), \quad W_0 = \sqrt[3]{\frac{3}{2}(3\gamma+1)}, \tag{265}$$

where γ is an arbitrary parameter, and the function $h(x)$ $(0 < x < 1)$ is given by:

$$h(x) = (1-x)^{\frac{1}{3}} + b_1(1-x)^{\lambda_1} + b_2(1-x)^{\lambda_2}. \tag{266}$$

The choice of the next powers $1/3 < \lambda_1 < \lambda_2$ will depend on the leak-off variant from (4). On consecutive substitutions of (265) (266) into the relations (19), (24), (29) and (31) one obtains the remaining benchmark quantities:

$$L(t) = (1+t)^{\frac{3\gamma+1}{2}}, \quad V(t,x) = -W_0^3(1+t)^{\frac{3\gamma-1}{2}}h^2(x)\frac{\partial h}{\partial x}. \tag{267}$$

$$q_0(t) = -W_0^4(1+t)^{\frac{5\gamma-1}{2}}\left(h^3\frac{\partial h}{\partial x}\right)|_{x=0}. \tag{268}$$

$$q_l(t,x) = W_0(1+t)^{\gamma-1}\times \tag{269}$$

$$\left(\frac{3}{2}(3\gamma+1)\left[\frac{1}{3}x\frac{\partial h}{\partial x} + 3h^2\left(\frac{\partial h}{\partial x}\right)^2 + h^3\frac{\partial^2 h}{\partial x^2}\right] - \gamma h\right).$$

It can be easily checked that for $\lambda_1 = 1/2$ and $\lambda_2 = 4/3$ the leak-off function incorporates a square root singular term of type $(21)^{(1)}$. By setting $\lambda_1 = 5/6$ and $\lambda_2 = 4/3$ it complies with representation

(21)$^{(2)}$. Although in both cases $q^*_{(1,2)}$ exhibits a singular behavior at the crack tip, it does not affect the applicability of this benchmarks. Finally, when using $\lambda_1 = 4/3$ and $\lambda_2 = 7/3$, this benchmark gives a non-singular leak-off function (21)$^{(3)}$.

Note , that by manipulating the value of γ one can simulate different crack propagation regimes. For example $\gamma = 1/5$ corresponds to constant injection rate, while $\gamma = 1/3$ results in constant crack propagation speed. For this work $\gamma = 1/5$ should be used.

Choosing appropriate values b_1 and b_2 affects proportion between fluid loss and injection rate. This ratio is be defined by Q_l/q_0, where Q_l is the total volume of leak-off $\int_0^1 q_l dx$. This measure decreases in time, from its maximum value to zero, for all chosen benchmarks. Thus, taking the maximum value and tracing the solution accuracy in time, one can analyze the algorithms performance for all probable values of this ratio. The first considered value of Q_l/q_0 corresponds to fluid injection double the size of total fluid loss, the second to total fluid loss being close to injection rate. The values of corresponding parameters b_1, b_2 are presented in Table 11.

	$Q_l/q_0 = 0.9$			$Q_l/q_0 = 0.5$		
	$q_l^{(1)}$	$q_l^{(2)}$	$q_l^{(3)}$	$q_l^{(1)}$	$q_l^{(2)}$	$q_l^{(3)}$
	0.1	0.19	0.74	0.02	0.03	0.15
	0.5	0.41	−0.13	0.1	0.08	−0.02
γ_v	1.69	1.70	1.65	0.55	0.56	0.55

Table 11: The values of parameters b_1 and b_2 for different benchmark solutions corresponding to desired leak-off to fluid injection ratios.

Additionally an additional parameter γ_v, defined in [65], which measures uniformity of fluid velocity distribution, can be computed as:

$$\gamma_v = [\max(V(t,x)) - \min(V(t,x))] \left[\int_0^1 V(t,\xi)d\xi\right]^{-1}. \tag{270}$$

Interestingly, this measure is directly related to leak-off ratio Q_l/q_0.

On Figure 90 the distributions of leak-off functions and corresponding particle velocities for respective benchmarks are presented. Velocities near the crack tip differ depending on the benchmark variant. To highlight this phenomena a close up view is shown on Figure 90 (c).

Note that the benchmark $q_l^{(1)}$ appears to be more difficult, than the original Carter's model as it contains additional singular terms of the leak-off function. These terms are absent in the normalized Carter's law as it follows from Subsection 2.2.1.

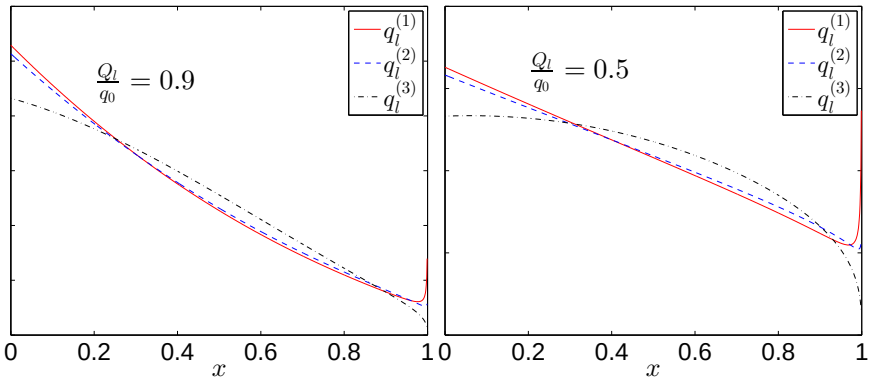

(a) a

(b) b

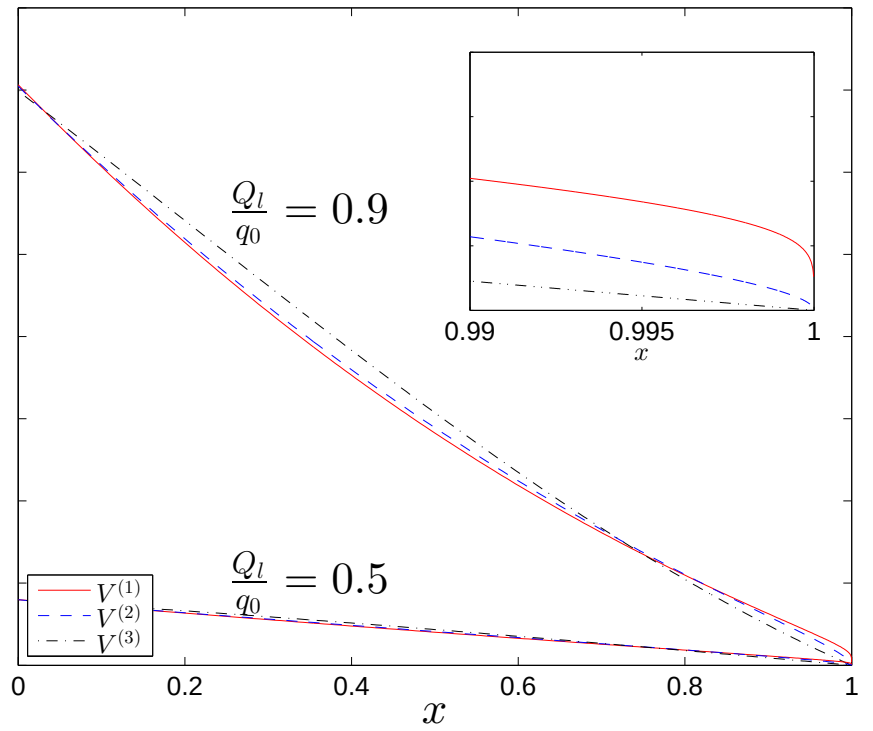

(c) c

Figure 90: Distributions of the leak-off functions $q_l(t,x)$ and the respective particle velocity $V(t,x)$ over $x \in (0,1)$ at initial time $t = 0$.

A.2.2 *Zero leak off Self Similar solution*

In the paper by Linkov [54] the following self similar solution is presented:

$$w(t,x) = w_n h(x)^{1/3}(a+t)^{1/5}, \quad l(t) = \xi_* x_n (a+t)^{4/5}. \tag{271}$$

Where function $h(x)$ is given by:

$$h(x) = 0.6\xi_*^2 \sum_{j=1}^{j=\infty} \frac{b_{j-1}}{j}(1-x)^j, \tag{272}$$

This expansion converges rapidly, thus only first five terms shall be considered:

$$\begin{aligned} b_0 &= 1 \\ b_1 &= -\frac{1}{16} \\ b_2 &= -\frac{15}{224}b_1 \\ b_3 &= -\frac{3}{80}b_2 \\ b_4 &= -\frac{11}{5824}b_3 \end{aligned} \tag{273}$$

The remaining parameters are given values:

$$\begin{aligned} \xi_* &= 1.3208446(q_0/q_n)^{0.6} \\ w_n &= 1 \\ x_n &= 1 \\ q_n &= 1 \end{aligned}$$

Which corresponds to $k = 4$ and $M = 1$.

This benchmark is particularly useful if testing without leak off function properly implemented. Since five terms are used it is in fact not necessary easier to compute than the three term general benchmark shown in the previous Appendix (A.2.1).

A.2.3 *Large Time asymptotes*

The large time asymptote for Carter Law $q_l^{(1)}$ (4) was given by [70]:

$$L(t) \approx \frac{2q_0}{\pi}\sqrt{t}, \quad t \to \infty \tag{274}$$

By assuming variable separable form, the large time asymptote for pressure proportional Carter Law $q_l^{(2)}$ (4), can be numerically approximated, by correctly guessing that exponential functions are involved. The apparently exact approximation is:

$$L(t) \approx \frac{q_0^{0.6}}{2} t^{0.4}, \quad t \to \infty \tag{275}$$

A.3 INTERPOLATING AND INTEGRATING FRACTURES

For the problem of multifracturing it is necessary to have a procedure for both integrating and interpolating the crack and pipe segments. These need arises form two reasons.

- First, when computing the fluid balance equation the volume of fractures needs to be found.
- Second, various events of crack collisions and splits require unknown intermediate width values that must be found by interpolation the known width data on discredited grid.

Three strategies for interpolation are considered: linear, cubic and cubic Hermite splines. All of these however result in construction of a piecewise polynomial. Such a polynomial for grid of N points divides it into $N-1$ intervals, and for each of these such values of a_i, b_i, c_i, d_i are found that:

$$S_i(x) = d_i(x - x_i)^3 + c_i(x - x_i)^2 + b_i(x - x_i) + a_i \tag{276}$$

Where $S_i(x)$ is a polynomial piece for each of $N-1$ segments. In case of linear formulation for all i $c_i = 0$ and $d_i = 0$. To find a_i, b_i, c_i, d_i some numerical work needs to be done. This is trivial for linear. For cubic polynomial construction some well known interpolation algorithm can be used (such as [46]). The Hermite version of cubic is obtained via MATLAB spline() function. Yet another variation to this is clamping. Cubic spline can be constructed with natural boundary, that is the first derivative at beginning and end of interval is set to zero, or with some desired value, which refers to a clamped spline.

To obtain the value of piecewise polynomial at some arbitrary point $x \in (0, 1)$, that is to extrapolate a value, the interval $x_i < x \leq x_{i+i}$ which contains $S_i(x)$ polynomial piece to must be found. Since the values of x_i are sorted the index i of the next lesser value than given x can be found using binary search method. Doing so $O(\log_2 N)$ search time is obtained, so the need to find the right piece of polynomial when evaluating is not a burden on computation time.

Knowing which segment i to use, to compute the value of $S_i(x)$ the following form is optimal to use:

$$S_i(x) = a_i + (x - x_i)\left(b_i + (x - x_i)\left(c_i + (x - x_i)\, d_i\right)\right)), \quad x_i < x \leq x_{i+i} \tag{277}$$

Having a segment of a pipe or crack interpolated, it is easy to find the integral of a cross section by integrating the piecewise polynomi-

als. Given integration start point a and end point b the integral of $S_i(x)$ is:

$$\int_a^b S_i(x)dx = \\ (x - x_i)\left(\frac{a_i}{2} + (x - x_i)\left(\frac{b_i}{3} + (x - x_i)\left(\frac{c_i}{4} + (x - x_i)\frac{d_i}{4}\right)\right)\right) \tag{278}$$

We can apply this to the whole piecewise spline:

$$\int_a^b w dx = \int_a^{x_k} S_{k-1}(x)dx + \sum_0^j \int_{x_{k+j}}^{x_{k+j+1}} S_{k+j}(x)dx + \int_{x_{k+j}}^b S_{k+j+1}(x)dx \tag{279}$$

Where w is the width of pipe or crack under integration. The values of j and k are searched such so $a < x_k$ and $x_{k+j} < b$.

ANOTHER TRICK WITH ASYMPTOTICS When dealing with crack and its width w_{crack}, it is possible to obtain much better accuracy when interpolating. The two terms asymptotic representation of PKN model fracture (15) can improve the process:

$$f(x) = A(1 - x)^\alpha + B(1 - x)^\beta \tag{280}$$

With the powers α, β and parameters A, B obtained through crack tip handling strategies (Subsection 3.2.2.2). Now when interpolating polynomial $S(x)$, it can be interpolated over $w_{crack} - f(x)$ instead. Then the value of $w(x)$ after interpolation for some point x can be found as:

$$w(x) = S(x) + A(1 - x)^\alpha + B(1 - x)^\beta \tag{281}$$

This improves accuracy of $\int_a^b w_{crack}dx$, that is accuracy of finding cross section volume of a fracture:

$$\int_a^b w_{crack}dx = \int_a^b (w_{crack} - f)dx + \int_a^b f(x)dx \tag{282}$$

and since $f(x)$ can be easily integrated:

$$\int_a^b f(x)dx = (b - a)\left(\frac{A}{\alpha + 1} + \frac{B}{\beta + 1}\right) \tag{283}$$

Subtracting $f(x)$ from w_{crack} allows major part of the integral is done analytically, leaving much lesser part to be computed by numerical approximation. This allows for less error when obtaining volume and extrapolating width values.

	$\int_0^1 w_{crack} dx$	$\int_0^1 (w_{crack} - f) dx + F$	$\int_0^1 w_{pipe} dx$
linear	3.17e-03	3.34e-05	1.13e-04
cubic	1.24e-04	2.22e-06	8.53e-06
cubic clamped	2.48e-04	1.22e-04	5.57e-06
Hermite	2.64e-04	4.44e-08	1.17e-07
Hermite clamped	3.24e-04	1.34e-04	5.84e-08

Table 12: Accuracy of integration of pipe and crack sections on $N = 10$ point quadratic (for crack) and regular grid (for pipe). Clearly with as little as $N = 10$ points it is possible to achieve integration accuracy of a few orders better than the expected accuracy of numerically computed w.

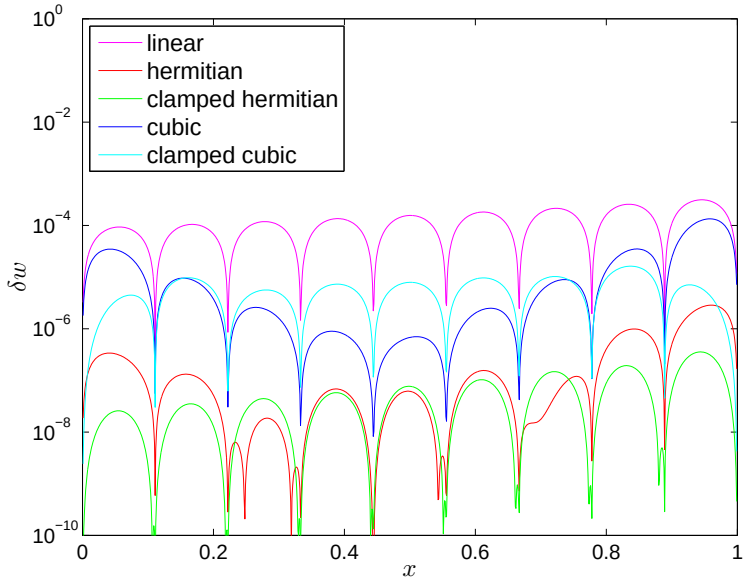

(a) *Pipe* segment

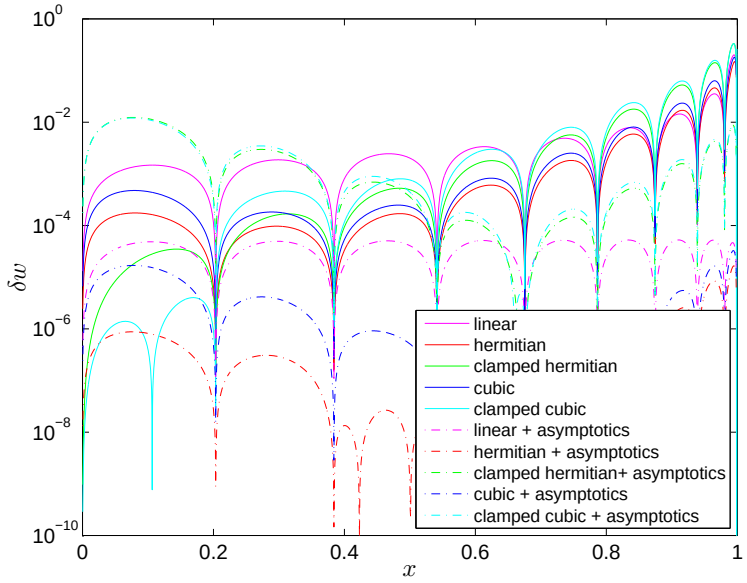

(b) *Crack* segment

Figure 91: Relative error obtained while extrapolating midpoints values between $N = 10$ grid point. Self similar solution based pipe and crack segments. It is possible to achieve accuracy of 10^{-4} or better for most types of interpolants over the entire interval.

A.4 MATLAB SINGLE FRACTURE CODE

A.4.1 *Simple Running Script*

```
%sample (simplified )running script
clear all;
clc;

a=1;%initial time
t=[0 100]; %computation interval

epsilon=1e-3;
N=100;
%%grid choice
% grid=RegularGrid(N,epsilon);
% grid=ArcTanhGrid(N,epsilon);
grid=QuadraticGrid(N,epsilon);

%choice of a benchmark
bench=BenchmarkSimilar(a);

%object that hold all initial conditins
ic=InitialCondition(grid,bench);

%%derivative approximation choice
% diffs=FiniteDifferences(grid);
diffs=AsymFD(grid,ic);
% diffs=Polynomial2nd(grid);
% diffs=DiffSpline(grid);

% methods for dealing with BC
left=leftBC1(ic);
right=rightBC1(ic);

%setting up the sysem
sys1=CrackSystemW(ic,left,right,diffs);

%computation
tic
    [sol]=sys1.solve(t);
toc

%optional results ploting
[X,T]=meshgrid(grid.xi(1:N),sol.x);
figure
ww=bench.w(T,X);
mesh(X,T,sol.y(1:N,:)');
mesh(X,T,abs(sol.y(1:N,:)'-ww)./ww);
figure
L=sol.y(N+1,:).^.5;
plot(sol.x,abs(L-bench.L(sol.x))./bench.L(sol.x),'r')
```

A.4.2 *Crack system w variable*

```
classdef CrackSystemW<handle

    properties,
        function_calls,xi,N,k,M,...
            left_BC,right_BC,ic,diffs;
    end

    methods
        %constructor
        %ic set of initial conditions
        %left_BC used for BC at x=0
        %right_BC used for BC at x=1
        %diffs used for dw/dx and d2w/dx2 approximation
        function ...
            this=CrackSystemW(ic,left_BC,right_BC,diffs)
            this.N=ic.grid.N;
            this.ic=ic;
            this.left_BC=left_BC;
            this.right_BC=right_BC;
            this.diffs=diffs;
            this.xi=ic.grid.xi;
            this.k=ic.k;
            this.M=ic.M;
        end


        function [sol]=solve(this,t_spam)

            %reset function calls counter
            this.function_calls=0;

            n=this.N;
            A=diag(ones(1,n+1),0)+... %tridiagonal part
                diag(ones(1,n),1)+...
                diag(ones(1,n),-1);
            A(:,end-2:end)=1;   %three extra columns
            A(1,3)=1;  %attributed to left BC

            options = ...
                odeset('RelTol',1e-8,'AbsTol',1e-8,...
                'Jpattern',A);

            sol=ode15s(@(t,w)ODE(this,t,w),t_spam,...
                [this.ic.w;this.ic.L_0^2],options);


        end

        function dw=ODE(this,t,w)

            this.function_calls=this.function_calls+1;
            %allows to escape form endless computation
```

```
            if(this.function_calls>100000)
52              throw(MException('Id:id','iterations ...
                    exeeded'));
            end

            % assign local variables
            n=this.N;
57          L_t=w(end)^.5;
            x=this.xi;

            %allocated output of operators A and B
            %{A_1,A_2,...,A_N,B}
62          dw=zeros(n+1,1);

            %computing derevative approximations
            this.diffs.preset(w);
            dwdx=this.diffs.calcFirstDer();
67          d2wdx2=this.diffs.calcSecondDer();

            %getting boundary derevative values, and ...
                asymptotics term w_0
            [dwdx(1),d2wdx2(1)]=...
                this.left_BC.get_left(t,L_t,w,dwdx,d2wdx2);
72          [w_0,dwdx(n),d2wdx2(n)]=...
                this.right_BC.get_right(t,L_t,w,dwdx,d2wdx2);

            %computes operator A
            dw(1:n)=this.k/this.M/L_t^2.*dwdx(1:n).*w(1:n).^3.*...
77              (1/3*w_0^3*x(1:n)./w(1:n).^3+3*dwdx(1:n)./w(1:n)...
                +d2wdx2(1:n)./dwdx(1:n))-this.ic.q_1(t,x(1:n));

            %computes operator B
            dw(end)=2*this.k/this.M/3*w_0^3;
82
        end
    end

end
```

A.4.3 *central FD*

```
classdef FiniteDifferences<handle
    %handle for computing Crack derevative
3   %central FD scheme with variable interval
    %length is used

    properties
        D,F,G,N,grid,dy;
8   end

    methods
        function this=FiniteDifferences(grid)
```

```
            this.N=grid.N;
            n=this.N-1;
            dxi=grid.dxi;

            %precompute constant parameters
            this.D=dxi(1:n-1);
            this.F=dxi(2:n);
            this.G=1./dxi(1:n-1)+1./dxi(2:n);
        end

        function preset(this,y)
            n=this.N;
            this.dy=diff(y(1:n));
        end

        function fstder=calcFirstDer(this)
            n=this.N;
            fstder=zeros(n,1);
            fstder(2:n-1)=1/2*(this.dy(2:n-1)...
                ./this.F+this.dy(1:n-2)./this.D);
        end

        function secder=calcSecondDer(this)
            n=this.N;
            secder=zeros(n,1);
            secder(2:n-1)=1/2*this.G.*(this.dy(2:n-1)...
                ./this.F-this.dy(1:n-2)./this.D);
        end
    end
end
```

A.4.4 *polynomial*

```
classdef Polynomial2nd<handle
    %handle for computing Crack derevative
    %approximation where derevative at x_i is given by ...
        2ax+b and 2a
    %as approximated by ax^2+bx+c on points x_i-1,x_i,x_i+1
    properties
        N,grid,A,B,C,E,F,dy;
    end

    methods
        function this=Polynomial2nd(grid)
            this.grid=grid;
            this.N=grid.N;

            %precompute constant parameters
            n=this.N;
            dxi=grid.dxi;
            this.A=1./(dxi(2:n-1)+dxi(1:n-2));
            this.B=dxi(1:n-2)./dxi(2:n-1);
```

```
            this.C=dxi(2:n-1)./dxi(1:n-2);
            this.E=1./dxi(1:n-2);
            this.F=1./dxi(2:n-1);
        end

        function preset(this,y)
            n=this.N;
            this.dy=diff(y(1:n));
        end

        function fstder=calcFirstDer(this)
            n=this.N;
            fstder=zeros(n,1);
            fstder(2:n-1)=this.A.*(this.dy(2:n-1)...
                .*this.B+this.dy(1:n-2).*this.C);
        end

        function secder=calcSecondDer(this)
            n=this.N;
            secder=zeros(n,1);
            secder(2:n-1)=2*this.A.*(this.dy(2:n-1)...
                .*this.F-this.dy(1:n-2).*this.E);
        end
    end
end
```

A.4.5 *spline*

```
classdef DiffSpline<handle
    %handle for computing Crack derevative
    %spline is constructed by spline() function
    %and subsequently its derevative given by fnder
    %is used

    properties
        N,x,pp;
    end

    methods
        function this=DiffSpline(grid)
            this.x=grid.xi;
            this.N=grid.N;
        end

        function preset(this,y)
            n=this.N;
            %spline is constructed
            this.pp=spline(this.x,y(1:n));
        end

        function fstder=calcFirstDer(this)
            n=this.N;
```

```
            fstder=zeros(n,1);
            %function for first derevative
            f=@(x)ppval(fnder(this.pp,1),x);
            %evaluation over grid x
            fstder(2:n-1)=f(this.x(2:n-1));
        end

        function secder=calcSecondDer(this)
            n=this.N;
            secder=zeros(n,1);
            %function for second derevative
            f=@(x)ppval(fnder(this.pp,2),x);
            %evaluation over grid x
            secder(2:n-1)=f(this.x(2:n-1));
        end
    end

end
```

A.4.6 *Asym FD*

```
classdef AsymFD<handle
    %handle for computing Crack derevative
    %using 2 terms asymptotics.
    %Asymptotic approximation is used to calculate most
    %of the value, thous better accuracy is expected.
    %The reminder is treated with central FD

    properties
        grid,N,A1,A2,B1,B2,xn1,xn2,alpha,beta,dy,f,fx,fxx,...
            A,B,C,D,F,G,xa,xb,xaa,xbb,xaaa,xbbb;
    end

    methods
        %constructor grid, first asym power, second ...
            asym power
        function this=AsymFD(grid,ic)
            %assign grid, N
            this.N=grid.N;
            this.grid=grid;
            a=ic.alpha; % first asym term power ...
                (usually 1/3)
            b=ic.beta; % second asym term power
            this.alpha=a;
            this.beta=b;
            %working tip parameters for finding asym terms
            x1=1-grid.xi(end);
            x2=1-grid.xi(end-1);
            this.A1=(x2^(a)-x2^(b)/x1^(b-a))^(-1);
            this.A2=-(x2/x1)^(b)*this.A1;
            this.B1=-this.A1/x1^(b-a);
            this.B2=1/x1^(b)-this.A2/x1^(b-a);
```

```
            this.xn1=x1;
            this.xn2=x2;

            %precomputing constant asym parameters
            x=grid.xi;
            this.xa=(1-x).^a;
            this.xb=(1-x).^b;
            this.xaa=-a*(1-x).^(a-1);
            this.xbb=-b*(1-x).^(b-1);
            this.xaaa=a*(a-1)*(1-x).^(a-2);
            this.xbbb=b*(b-1)*(1-x).^(b-2);

            %precomputing constant FD parameters
            dxi=grid.dxi;
            n=this.N-1;
            this.A=1./(dxi(2:n)+dxi(1:n-1));
            this.B=dxi(1:n-1)./dxi(2:n);
            this.C=dxi(2:n)./dxi(1:n-1);
            this.D=dxi(1:n-1);
            this.F=dxi(2:n);
            this.G=1./dxi(1:n-1)+1./dxi(2:n);
        end

        function preset(this,y)
            n=this.N;
            %finds asym terms on 2 last data points
            a=this.A1*y(n-1)+this.A2*y(n);
            b=this.B1*y(n-1)+this.B2*y(n);

            %calculates asym based approximation for
            %F dFdx and d2Fdx2
            this.f=a*this.xa+b*this.xb;
            this.fx=a*this.xaa+b*this.xbb;
            this.fxx=a*this.xaaa+b*this.xbbb;

            %difference of asym approximation and ...
                acctual value
            this.dy=diff(y(1:n)-this.f);
        end

        function fstder=calcFirstDer(this)
            n=this.N;
            fstder=zeros(n,1);
            fstder(2:n-1)=this.fx(2:n-1)... %asym ...
                derivative term
                +1/2*(this.dy(2:n-1)./this.F...%FD ...
                    derivative term
                +this.dy(1:n-2)./this.D);
        end

        function secder=calcSecondDer(this)
             n=this.N;
             secder=zeros(n,1);
             secder(2:n-1)=this.fxx(2:n-1)...%asym ...
                 derivative term
```

```
                    +1/2*this.G.*...            %FD ...
                        derivative term
                    (this.dy(2:n-1)./this.F-this.dy(1:n-2)./this.D);
            end
        end
    end
```

A.4.7 *regular grid*

```
    classdef RegularGrid
        %uniform grid
        properties
            N,xi,dxi,epsilon;
        end

        methods
            function this=RegularGrid(N,epsilon)
                this.N=N;
                this.epsilon=epsilon;
                this.xi=linspace(0,1-epsilon,N)';
                this.dxi=diff(this.xi);
            end
        end
    end
```

A.4.8 *BC x=0*

```
    classdef leftBC1
        %leftBC1 deals with BC at x=0

        properties
            q_0,k,M,x;
        end

        methods
            function this=leftBC1(ic)
                this.q_0=ic.q_0;
                this.k=ic.k;
                this.M=ic.M;
                %the first 3 points are extracted
                this.x=ic.grid.xi(1:3);
            end

            function ...
                [dwdx_0,d2wdx2_0]=get_left(this,t,L_t,w,¬,¬)

                %pumping rate q_o is proportional to first ...
                    derevative
                dwdx_0=-this.M/this.k*L_t/w(1)^3*this.q_0(t);
```

```
            x1=this.x(1);
            x2=this.x(2);
            x3=this.x(3);
            da=-1/2./(x2-x1);
            db=1/2*(1./(x2-x1)-1/(x3-x2));
            dc=1/2./(x3-x2);
            %aproximation of a special polynomial
            d2wdx2_0=(-2/x2*da+4/x2*this.q_0(t)*...
                this.M/this.k*L_t*w(1)^(-4)-6*x2^-2)*w(1)+...
                (-2/x2*db+6*x2^(-2))*w(2)+...
                (-2/x2*dc)*w(3);
        end
    end

end
```

A.4.9 *BC x=1*

```
classdef rightBC1
    %rigthBC1 deals with BC at x=1

    properties
        A1,A2,B1,B2,xn1,xn2,N,alpha,beta;
    end

    methods

        function this=rightBC1(ic)

            x1=1-ic.grid.xi(end);
            x2=1-ic.grid.xi(end-1);

            a=ic.alpha;
            b=ic.beta;

            this.alpha=a;
            this.beta=b;
            this.xn1=x1;
            this.xn2=x2;


            this.A1=(x2^(a)-x2^(b)/x1^(b-a))^(-1);
            this.A2=-(x2/x1)^(b)*this.A1;
            this.B1=-this.A1/x1^(b-a);
            this.B2=1/x1^(b)-this.A2/x1^(b-a);
            this.N=ic.grid.N;

        end

        function ...
            [w_0,dwdx_n,d2wdx2_n]=get_right(this,¬,¬,w,¬,¬)
```

```
33
                n=this.N;

                %finds w_0 and w_1
                A=this.A1*w(n-1)+this.A2*w(n);
38              B=this.B1*w(n-1)+this.B2*w(n);

                a=this.alpha;
                b=this.beta;
                w_0=A;
43
                %direct result of differentiating asymptotics
                dwdx_n=-a*A*this.xn1^(a-1)+...
                    -b*B*this.xn1^(b-1);

48              %direct result of differentiating asymptotics
                d2wdx2_n=a*(a-1)*A*this.xn1^(a-2)+...
                    b*(b-1)*B*this.xn1^(b-2);
            end
        end
53  end
```

A.4.10 *Benchmark Self-Similar*

```
    classdef BenchmarkSimilar
2       properties
            alpha,beta,w,V,L,dL,q_l,int_q_l,q_0,dwdt,Omega,k,M,a,w_0,...
                A,C,D,powers,sym_powers,L_inv,q_l_star,q_l_norm,dwdx,...
                Yb,YY,ql_star;
        end
7
        methods

            function obj = BenchmarkSimilar(a)

12              obj.a=a;

                kl=4;
                ke=1;
                q0=1;
17              qn=1;
                tn=1;

                xn=((kl*ke)/4)^(1/5)*qn^(3/5)*tn^(4/5);
                wn=qn*tn/xn;
22
                b0=1;
                b1=-1/16;
                b2=-15/224*b1;
                b3=-3/80*b2;
27              b4=-11/5824*b3;
```

```
            xi_s=1.3208446*(q0/qn)^(0.6);

            obj.Yb=@(x)0.6*xi_s^2*((1-x).^(1)...
                +b1/2*(1-x).^(2)+b2/3*(1-x).^(3)...
                +b3/4*(1-x).^(4)+b4/5*(1-x).^(5));


            Y=@(x)0.6*xi_s^2*(b0/1*(1-x).^(1)+b1/2*(1-x).^(2)+...
                +b2/3*(1-x).^(3)+b3/4*(1-x).^(4)+b4/5*(1-x).^(5));
            obj.YY=Y;


            dxYb=@(x)0.6*xi_s^2*(...
                -1 ...
                +2*1/16/2*(1-x).^(1)+...
                +3*15/224*-1/16/3*(1-x).^(2)...
                +4*3/80*-15/224*-1/16/4*(1-x).^(3)...
                +5*11/5824*-3/80*-15/224*-1/16/5*(1-x).^(4));

            obj.k=4;
            obj.M=1;
            obj.w=@(t,x)wn*(Y(x)).^(1/3).*(a+t).^(1/5);
            obj.dwdt=@(t,x)1/5*wn*(Y(x)).^(1/3).*(a+t).^(-4/5);
            obj.dwdx=@(t,x)...
                wn*1/3*(Y(x)).^(-2/3).*dxYb(x).*(a+t).^(1/5);
            obj.q_0=@(t)q0;
            obj.ql_star=@(t,x) t*0+x*0;
            obj.L=@(t)xi_s*xn*(a+t).^(4.0/5.0);
            obj.V=@(t,x)-obj.k/obj.M./obj.L(t).*...
                obj.w(t,x).^2.*obj.dwdx(t,x);
            obj.L_inv=@(x)(x./xi_s./xn).^(5.0/4.0)-a;
            obj.alpha=1.0/3.0;
            obj.beta=4.0/3.0;
            obj.Omega=@(t,x)quad(@(x)obj.w(t,x),1,x,10^-12);
            obj.q_1=@(t,x)0+0*t+0*x;

        end
    end

end
```

A.4.11 *Initial condition*

```
classdef InitialCondition
    %InitialCondition encapsulation of simulation ...
        parameters
    %   includes various parameters that might be used
    %   a proxy to benchmark in this particular ...
        implementation

    properties
        a,w,w_0,V,Omega,L_0,L_inv,k,M,q_0,...
```

```
                q_l,q_l_star,q_l_norm,int_q_l,C,...
                grid,bench,alpha,beta;
        end

        methods
            function this=InitialCondition(grid,bench)

                this.a=bench.a;
                this.L_0=bench.L(0);
                this.grid=grid;
                this.alpha=bench.alpha;
                this.beta=bench.beta;
                this.w=bench.w(0,grid.xi);
                this.V=bench.V(0,grid.xi);
                this.k=bench.k;
                this.M=bench.M;
                this.q_0=bench.q_0;
                this.q_l=bench.q_l;
                this.int_q_l=bench.int_q_l;
                this.q_l_star=bench.q_l_star;
                this.q_l_norm=bench.q_l_norm;
                this.L_inv=bench.L_inv;
                this.C=bench.C;
            end
        end

    end
```

A.5 JAVA MULTIFRACTURING CODE

The source code developed for multifracturing scenario is available for download from GitHub at: https://github.com/morswinb . It is still an experimental version that is likely to change and evolve, so please find any instructions and examples at the repository.

BIBLIOGRAPHY

[1] (2007). There will be blood. (Cited on page 2.)

[2] Adachi, J., Siebrits, E., Peirce, A., and Desroches, J. (2007). Computer simulation of hydraulic fractures. *International Journal of Rock Mechanics and Mining Sciences*, 44:739–757. (Cited on pages 11 and 12.)

[3] Adachi, J. I. and Detournay, E. (2002). Self-similar solution of a plane-strain fracture driven by a power-law fluid. *Int. J. Numer. Anal. Methods Geomech.*, 26:579–604. (Cited on pages 9 and 35.)

[4] Aiken, R. C. (1985). *Stiff computation.* Oxford University Press. (Cited on page 45.)

[5] Almasi, G., Gustavson, F. G., and Moreira, J. E. (2000). Design and evaluation of a linear algebra package for java. Technical report, Department of Computer Science, University of Illinois at Urbana-Champaign, Urbana, IL 61801. (Cited on page 188.)

[6] Artigas, P. V., Gupta, M., Midkiff, S. P., and Moreira, J. E. (2000). High performance numerical computing in java: Language and compiler issues. Technical report, IBM Thomas J. Watson Research Center, Yorktown Heights NY 10598-0218. (Cited on page 188.)

[7] Ashino, R., Nagase, M., and Vaillancourt, R. (2013). Behind and beyond the matlab ode suite. *Computers and Mathematics with Applications*, 40. (Cited on pages 52 and 103.)

[8] Behrmann, L. (1996). Quo vadis, extreme overbalance. (Cited on page 66.)

[9] Bull, J. M., Smith, L. A., Pottage, L., and Freeman, R. (2001). Benchmarking java against c and fortran for scientific applications. Technical report, The University of Edinburgh, Edinburgh Parallel Computing Centre, James Clerk Maxwell Building, The King's Buildings, The University of Edinburgh, Mayfield Road, Edinburgh EH9 3JZ, Scotland, UK. (Cited on page 188.)

[10] Bunger, A. P. (2013). Analysis of the power input needed to propagate multiple hydraulic fractures. *International Journal of Solids and Structures*, 50:1538–1549. (Cited on pages 12, 125, 136, 137, 140, 174, 185, and 186.)

[11] Bunger, A. P. and Detournay, E. (2008). Experimental validation of the tip asymptotics for a fluid-driven crack. *Journal of the Mechanics and Physics of Solids*, 56:3101–3115. (Cited on page 12.)

[12] Bunger, A. P. and Peirce, A. P. (2014). Numerical simulation of simultaneous growth of multiple interacting hydraulic fractures from horizontal wells. *Shale Energy Engineering*, pages 201–210. (Cited on pages 13 and 14.)

[13] Carbonell, R., Garagash, D., Savitski, A., Adachi, J., Bunger, A., Kovalyshen, Y., Madyarova, M., Kresse, O., Lecampion, B., and Gordelyi, E. (2014). Mechanics of hydraulic fractures. pages 201–210. (Cited on pages 8 and 10.)

[14] Carter, E. D. (1957). Optimum fluid characteristics for fracture extension. *American Petroleum Institute.*, pages 261–270. (Cited on pages 9, 11, 19, 20, and 111.)

[15] Cavallo, A. J. (2004). Hubberts petroleum production model: an evaluation and implications for world oil production forecasts. *Natural Resources Research*, 13:211–221. (Cited on page 5.)

[16] Cho, D. (2014). Hydraulic fracturing as a global cascade in networked systems. *CSEG RECORDER*, 39. (Cited on page 128.)

[17] Chuprakov, D., Melchaeva, O., and Prioul, R. (2013). Hydraulic fracture propagation across a weak discontinuity controlled by fluid injection. pages 157–181. (Cited on pages 145 and 147.)

[18] Cipolla, C., Weng, X., Mack, M., Ganguly, U., Gu, H., Kresse, O., C.Cohnen, and Schlumberger, S. (2011). Integrating microseismic mapping and complex fracture modeling to characterize fracture complexity. *SPE International*. (Cited on pages 12, 13, and 14.)

[19] Clifton, R. J. and Wang, J. J. (1988). Multiple fluids, proppant transport, and thermal effects in threedimensional simulation of hydraulic fracturing. *SPE*, 18198. (Cited on page 19.)

[20] Crittendon, B. C. (1959). The mechanics of design and interpertation of hydraulic fracture treatments. *arXiv*, 21:21–29. (Cited on page 4.)

[21] Damjanac, B. and Cundall, P. (2014). Application of distinct element methods to simulation of hydraulic fracturing in naturally fractured reservoirs. *Computers and Geotechnics (Preprint)*. (Cited on pages 13 and 14.)

[22] Davey, P. (2013). matlabcontrol. `https://code.google.com/p/matlabcontrol/`. (Cited on page 191.)

[23] Detournay, A. S. E. (2002). Propagation of a fluid-driven penny-shaped fracture in an impermeable rock: asymptotic solutions. *Int J Solids Struct*, 39(26):6311–6337. (Cited on page 9.)

[24] Dusseault, M. and McLennan, J. (2011). Massive multi-stage hydraulic fracturing: Where are we? (Cited on page 12.)

[25] Economides, M. and Nolte, K. (2000). *Reservoir Stimulation. 3rd edn.*, volume 222. Wiley, Chichester, UK. (Cited on pages 9, 11, 57, and 109.)

[26] Economides, M. J., Mikhailov, D. N., and Nikolaevskiy, V. N. (2007). On the problem of fluid leakoff during hydraulic fracturing. *Transp Porous Med*, 67:487–499. (Cited on page 117.)

[27] Einstein, A. (1905). Uber die von der molekularkinetischen theorie der warme geforderte bewegung von in ruhenden flussigkeiten suspendierten teilchen. *Annalen der Physik*, 322:549–560. (Cited on page 6.)

[28] Endre, S. and David, M. (2003). *An Introduction to Numerical Analysis*. Cambridge University Press. (Cited on page 50.)

[29] Garagash, D., Detournay, E., and Adachi, J. (2011). Multiscale tip asymptotics in hydraulic fracture with leak-off. *Journal of Fluid Mechanics*, 669:260–297. (Cited on pages 10 and 23.)

[30] Geertsma, J. and de Klerk, F. (1969). A rapid method of predicting width and extent of hydraulically induced fractures. *J Pet Tech*, 21:1571–1581. (Cited on pages 4 and 8.)

[31] Ghani, I., Kohen, D., Oussaint, R., and Passchier, C. W. (2013). Dynamic development of hydrofracture. *Pure and Applied Geophysics*, 170:1685–1703. (Cited on pages 13 and 14.)

[32] Hansen, C. P. (2012). Hummus and Magnets, 0x5f3759df. http://h14s.p5r.org/2012/09/0x5f3759df.html. (Cited on page 178.)

[33] Harrison, E., Jr., W. F. K., and McGuire, W. (1954). The mechanics of fracture induction and extension. *Petroleum Trans. AIME*, 201:252–263. (Cited on page 4.)

[34] Hubbert, M. K. (1956). Nuclear energy and the fossil fuels. *Drilling and Production Practice*, 95:9–11,21–22. (Cited on page 4.)

[35] Hubbert, M. K. and Willis, D. G. (1957). Mechanics of hydraulic fracturing. *J. Pet. Tech.*, 9:153–168. (Cited on page 4.)

[36] Id Software, Inc. (2012). Quake III Arena GPL source. https://github.com/id-Software/Quake-III-Arena. (Cited on page 179.)

[37] Jose I. Adachi, A. P. P. (2008). Asymptotic analysis of an elasticity equation for a finger-like hydraulic fracture.j. elast. *Journal of Elasticity*, 90:43–69. (Cited on page 23.)

[38] Kemp, L. F. (1990). Study of nordgren's equation of hydraulic fracturing. *SPE Production Eng.*, 5:311–314. (Cited on pages 10, 17, 21, 22, and 212.)

[39] Khristianovic, S. A. and Zheltov, Y. P. (1955). Formation of vertical fractures by means of highly viscous liquid. In *Proceedings of the fourth world petroleum congress*, pages 579–586, Rome. (Cited on pages 4 and 8.)

[40] Kovalyshen, Y. (2010). *Fluid-Driven Fracture in Poroelastic Medium.* PhD thesis, The University of Minnesota. (Cited on pages 10, 18, 19, 20, 109, and 172.)

[41] Kovalyshen, Y. and Detournay, E. (2009). A reexamination of the classical pkn model of hydraulic fracture. *Transport in Porous Media*, 81:317–339. (Cited on pages 10, 22, 90, 91, 92, 93, and 94.)

[42] Kresse, O. and Weng, X. (2013). Hydraulic fracturing formations with permeable natural fractures. pages 287–310. (Cited on pages 12, 13, 14, 19, 119, 133, 144, 145, and 147.)

[43] Kresse, O., Weng, X., Chuparkov, D., Prioul, R., and Cochen, C. (2013). Effect of flow rate and viscosity on complex fracture development in ufm model. pages 183–210. (Cited on pages 13, 14, and 128.)

[44] Kusmierczyk, P., Mishuris, G., and Wrobel, M. (2013). Remarks on application of different variables for the pkn model of hydrofracturing: various fluid-flow regimes. *International Journal of Fracture*, 2:185–213. (Cited on pages 10, 11, 13, 17, 18, 40, 57, and 125.)

[45] Kuzkin, V. A., Krivtsov, A. M., and Linkov, A. M. (2013). Proppant transport in hydraulic fractures: computer simulation of effective properties movement of the suspension. In *Proceedings of XLI International Summer School-Conference APM 2013*, Repino, St. Petersburg. (Cited on pages 6 and 119.)

[46] Kvarving, A. M. (2008). Natural cubic splines. http://www.math.ntnu.no/emner/TMA4215/2008h/cubicsplines.pdf. (Cited on page 217.)

[47] Laevsky, Y. (2011). Intel Ordinary Differential Equations Solver Library. https://software.intel.com/en-us/articles/intel-ordinary-differential-equations-solver-library. (Cited on pages 103 and 191.)

[48] Lash, G. G. and Engelder, T. (2009). Tracking the burial and tectonic history of devonian shale of the appalachian basin by analysis of joint intersection style. *Geological Society of America Bulletin*, 121:265–277. (Cited on page 12.)

[49] Lenoach, B. (1995). The crack tip solution for hydraulic fracturing in rock of arbitrary permeability. *Journal of the Mechanics and Physics of Solids*, 43:1025–1043. (Cited on page 20.)

[50] Lewis, J. P. and Neumann, U. (2004). Performance of Java versus C++. http://scribblethink.org/Computer/javaCbenchmark.html. (Cited on page 188.)

[51] Li, H. (2009). Solving Stiff ODEs. http://lh3lh3.users.sourceforge.net/solveode.shtml. (Cited on pages 191 and 192.)

[52] Li, L. C., Tang, C. A., Li, G., Wang, S. Y., Liang, Z. Z., and Zhang, Y. B. (2012). Numerical simulation of 3d hydraulic fracturing based on an improved flow-stress-damage model and a parallel fem technique. *Rock Mech Rock Eng*, 45:801–818. (Cited on page 12.)

[53] Lie, K. A. (2014). An introduction to the matlab reservoir simulation toolbox. ICMS, Edinburgh. SINTEF, PMPM Research Network. (Cited on page 187.)

[54] Linkov, A. M. (2011a). On efficient simulation of hydraulic fracturing in terms of particle velocity. *Int. J. Engng Sci*, 52:77–88. (Cited on pages 10, 17, 19, 21, 23, 30, 33, 38, 57, 76, 100, 212, and 215.)

[55] Linkov, A. M. (2011b). On numerical simulation of hydraulic fracturing. In *XXXVIII summer school-conference Advanced Problems in Mechanics-2011*, pages 291–296, Repino, St. Petersburg. (Cited on pages 10, 21, and 23.)

[56] Linkov, A. M. (2011c). Speed equation and its application for solving ill-posed problems of hydraulic fracturing. *ISSM 1028-3358, Doklady Physics*, 56:436–438. (Cited on pages 10, 17, 21, 23, 38, 39, and 40.)

[57] Linkov, A. M. (2011d). Use of a speed equation fornumerical simulation of hydraulic fractures. *arXiv:1108.6146*. (Cited on pages 10, 21, and 23.)

[58] Lister, J. R. (1990). Buoyancy-driven fluid fracture: the effects of material toughness and of low-viscosity precursors. *J Fluid Mech*, 210:263–280. (Cited on page 5.)

[59] Lister, J. R. and Kerr, R. C. (2012). Fluid-mechanical models of crack propagation and their application to magma transport in dykes. *Journal of Geophysical Research: Solid Earth*, 96:10049–10077. (Cited on page 5.)

[60] Mack, M. G. and Warpinski, N. R. (2000). *Reservoire stimulation*. Wiley-Blackwell, Chicester, 3rd edition. (Cited on page 10.)

[61] Mathias, S. A. and van Reeuwijk, M. (2009). Hydraulic fracture propagation with 3-d leak-off. *J Fluid Mech*, 80:499–518. (Cited on page 20.)

[62] Mathworks (2015). ode15s. http://www.mathworks.com/help/matlab/ref/ode15s.html. (Cited on pages 52 and 104.)

[63] McCarthy, J., Brayton, R., Edwards, D., Fox, P., Hodes, L., Luckham, D., Maling, K., Park, D., and Russell, S. (1960). *LISP I Programmers Manual*. Boston, Massachusetts. (Cited on page 187.)

[64] Mishuris, G. and Wrobel, M. (2013). On various strategies of numerical simulation of hydraulic fracturing. In *XLI summer school-conference Advanced Problems in Mechanics-2013*, Repino, St. Petersburg. (Cited on pages 21 and 192.)

[65] Mishuris, G., Wrobel, M., and Linkov, A. (2012). On modeling hydraulic fracture in proper variables: stiffness, accuracy, sensitivity. *arXiv*, 1203.5691v1. (Cited on pages 10, 11, 13, 17, 18, 19, 22, 23, 26, 30, 33, 38, 40, 46, 52, 57, 76, 88, 92, 100, 111, 212, and 213.)

[66] Mitchell, S. L., Kuske, R., and Peirce, A. P. (2007). An asymptotic framework for finite hydraulic fractures including leak-off. *SIAM J Appl Math*, 67(2):364–386. (Cited on page 109.)

[67] Moschovidis, Z. A. and Steiger, R. P. (2000). The mounds drill-cuttings injection experiment:final results and conclusions. In *IADC/SPE drilling conference*, New Orleans. Society of Petroleum Engineers. (Cited on page 5.)

[68] Negrut, D. (2010). ME751 Advanced Computational Multibody Dynamics. http://sbel.wisc.edu/Courses/ME751/2010/. (Cited on page 50.)

[69] Nonnekes, L. E., Cox, S. J., and Rossen, W. R. (2015). Effect of gas diffusion on mobility of foam for enhanced oil recovery. *Transport in Porous Media*, 106:669–689. (Cited on page 5.)

[70] Nordgren, R. P. (1972). Propagation of a vertical hydraulic fracture. *Society of Petroleum Engineers Journal*, 12. (Cited on pages 4, 8, 9, 18, 19, 20, 21, 90, 92, 125, 212, and 215.)

[71] Oancea, B., Rosca, I. G., Andrei, T., and Iacob, A. I. (2011). Evaluating java performance for linear algebra numerical computations. *Procedia Computer Science*, 3:474–478. (Cited on page 188.)

[72] Patel, A. (2012). 2d visibility. http://www.redblobgames.com/articles/visibility/. (Cited on page 140.)

[73] Pathmanathan, P. (2011). Numerical methods and object-oriented design. http://www.cs.ox.ac.uk/people/pras.pathmanathan/nmood_printable.pdf. (Cited on page 187.)

[74] Peaceman, D. W. (1977). *Fundamentals of Numerical Reserviour Stimulation*. Elsevier, New York. (Cited on page 2.)

[75] Peirce, A. P. and Bunger, A. P. (2013). Interference fracturing: Non-uniform distributions of perforation clusters that promote simultaneous growth of multiple hydraulic fractures. *SPE*. (Cited on page 128.)

[76] Perkins, T. K. and Kern, L. R. (1961). Widths of hydraulic fractures. *Journal of Petroleum Technology*, 13. (Cited on pages 4 and 8.)

[77] Pine, R. J. and Cundall, P. A. (1985). Applications of the fluid-rock interaction program (frip) to the modelling of hot dry rock geothermal energy systems. In *Proceedings of the international symposium on fundamentals of rock joints*, pages 293–302, Bjorkliden, Sweden. (Cited on page 5.)

[78] Prandtl, L. (1905). Varhandlungen des dritten internationalen mathematiker-kongress. (Cited on page 25.)

[79] Radhakrishnan, K. and Hindmarsh, A. C. (1993). Description and use of lsode, the livermore solver for ordinary differential equations. (Cited on page 191.)

[80] Rahman, M. M. and Rahman, M. K. (2010). A review of hydraulic fracture models and development of an improved pseudo-3d model for stimulating tight oil/gas sands. *Energy Sources*, 32:1416–1436. (Cited on page 11.)

[81] Rubin, A. M. (1995). Propagation of magma filled cracks. *Ann Rev Earth Planet Sci*, 23:287–336. (Cited on page 5.)

[82] Sabanis, S. (2015). Numerical methods and object-oriented design. http://www.drps.ed.ac.uk/14-15/dpt/cxmath11152.htm. (Cited on page 187.)

[83] Savitski, A. A. (2013). "unconventional challenges of hydraulic fracturing modeling". In *XLI summer school-conference Advanced Problems in Mechanics-2011*, pages 95–96, Repino, St. Petersburg. (Cited on page 12.)

[84] Schlumberger (2008). ThermalFRAC Shear-Tolerant Fracturing Fluid. http://content.yudu.com/A1rjzm/Autumn2008/resources/content/59.swf. (Cited on page 119.)

[85] Sneddon, I. N. (1946). The distribution of stress in the neighbourhood of a crack in an elastic solid. *Proc. R. Soc. Lond. A*, 187:229–260. (Cited on page 8.)

[86] Sneddon, I. N. and Elliot, H. A. (1946). The opening of a griffith crack under internal pressure. *Q Appl Math*, 4:262–267. (Cited on page 8.)

[87] Spence, D. A. and Sharp, P. (1985). Self-similar solutions for elastohydrodynamic cavity flow. *Proc. R. Soc. Lond. A*, 400:289–313. (Cited on pages 4, 10, and 21.)

[88] StackOverflow (2013). What is matlab good for? why is it so used by universities? when is it better than python? (Cited on page 187.)

[89] The GSL Team (2013). Gnu scientific liblary. https://www.gnu.org/software/gsl/manual/html_node/Ordinary-Differential-Equations.html. (Cited on page 191.)

[90] TIOBE Software (2015). Tiobe index. http://www.tiobe.com/index.php/content/paperinfo/tpci/index.html. (Cited on page 187.)

[91] Tsai, V. C. and Rice, J. R. (2010). A model for turbulent hydraulic hydraulic fracture and application to crack propagation at glacier beds. *Proc. R. Soc. Lond. A*, 115:1–18. (Cited on page 5.)

[92] U.S. Energy Information Administration (2015). U.S. NAtural Gas Gross Withdrawals. http://www.eia.gov/dnav/ng/hist/n9010us2m.htm. (Cited on page 5.)

[93] Valko, P. and Economides, M. J. (1995). *Hydraulic Fracture Mechanics*. Wiley, 1st edition. (Cited on pages 11, 114, and 117.)

[94] Voeckler, H. and Allen, D. M. (2012). Estimating regional-scale fractured bedrock hydraulic conductivity using discrete fracture network (dfn) modeling. *Hydrogeology Journal*, 20:1081–1100. (Cited on page 12.)

[95] White, F. M. (1998). *Fluid Mechanics*, chapter 6. McGraw-Hill, 4th edition. (Cited on page 133.)

[96] Wikipedia (2015a). Backward differentiation formula. (Cited on page 50.)

[97] Wikipedia (2015b). Hydraulic fracturing. (Cited on page 7.)

[98] Wikipedia (2015c). Jacobian matrix and determinant. (Cited on page 103.)

[99] Wikipedia (2015d). Natural gas. (Cited on page 3.)

[100] Wikipedia (2015e). Object oriented programming. (Cited on page 187.)

[101] Wikipedia (2015f). Peak oil. (Cited on page 4.)

[102] Wikipedia (2015g). Stiff equation. (Cited on page 44.)

[103] William, G. C. (1971). *Numerical initial value problems in ordinary differential equations*. Longman Higher Education. (Cited on page 50.)

[104] Wolfram (2015). van der pol equation. (Cited on page 44.)

[105] Wong, S.-W., Geilikman, M., and Xu, G. (2013). *The Geomechanical Interaction of Multiple Hydraulic Fractures in Horizontal Wells*, pages 661–677. Effective and sustainable hydraulic fracturing, INTECH. (Cited on page 128.)

[106] Wrobel, M. and Mishuris, G. (2014). Efficient pseudo-spectral solvers for the pkn model of hydrofracturing. *Fracture Phenomena in Nature and Technology*, pages 151–170. (Cited on pages 10, 11, 57, and 107.)

[107] Wrobel, M. and Mishuris, G. (2015). Particle velocity based universal algorithm for numerical simulation of hydraulic fractures. *arXiv:1412.5529*. (Cited on pages 10 and 11.)

[108] Xu, C. and Dowd, P. (2010). A new computer code for discrete fracture network modelling. *Computers and Geosciences*, 36:292–301. (Cited on page 12.)

[109] Zhang, X., Jeffrey, R. G., and Thiercelin, M. (2007). Escape of fluid-driven fractures from frictional beedding interfaces: A numerical study. *Journal of Structural Geology*, 38:478–490. (Cited on page 12.)